# Man-portable Vector Time Domain EMI Sensor and Discrimination Processing

MR-1443

Final Report

Submitted to

Strategic Environmental Research and Development Program (SERDP)

April 16, 2012

Revision **2.1**

By

U.S. Army Corps of Engineers Research and Development Center
Cold Regions Research and Engineering Laboratory (CRREL)
72 Lyme Road
Hanover, NH 03755

Principal Investigators
Ben Barrowes, Fridon Shubitidze, Pablo Fernandez and Kevin O'Neill
benjamin.e.barrowes@usace.army.mil

# REPORT DOCUMENTATION PAGE

*Form Approved*
*OMB No. 0704–0188*

The public reporting burden for this collection of information is estimated to average 1 hour per response, including the time for reviewing instructions, searching existing data sources, gathering and maintaining the data needed, and completing and reviewing the collection of information. Send comments regarding this burden estimate or any other aspect of this collection of information, including suggestions for reducing this burden to Department of Defense, Washington Headquarters Services, Directorate for Information Operations and Reports (0704–0188), 1215 Jefferson Davis Highway, Suite 1204, Arlington, VA 22202–4302. Respondents should be aware that notwithstanding any other provision of law, no person shall be subject to any penalty for failing to comply with a collection of information if it does not display a currently valid OMB control number. **PLEASE DO NOT RETURN YOUR FORM TO THE ABOVE ADDRESS.**

| 1. REPORT DATE *(DD–MM–YYYY)* | 2. REPORT TYPE | 3. DATES COVERED *(From — To)* |
|---|---|---|
| 04–11–2011 | Final | 05 March 2006 — 10 January 2010 |

**4. TITLE AND SUBTITLE**

Man-portable Vector Time Domain EMI Sensor and Discrimination Processing

**5a. CONTRACT NUMBER**

W74RDV63621961

**5b. GRANT NUMBER**

**5c. PROGRAM ELEMENT NUMBER**

**6. AUTHOR(S)**

Barrowes, Benjamin, E., and O'Neill, Kevin

**5d. PROJECT NUMBER**

MR-1443

**5e. TASK NUMBER**

**5f. WORK UNIT NUMBER**

**7. PERFORMING ORGANIZATION NAME(S) AND ADDRESS(ES)**

U.S. Army Corps of Engineers, Engineer Research and Development Center
Cold Regions Research and Engineering Laboratory (CRREL)
72 Lyme Road
Hanover, NH 03755

**8. PERFORMING ORGANIZATION REPORT NUMBER**

**9. SPONSORING / MONITORING AGENCY NAME(S) AND ADDRESS(ES)**

SERDP Program Office
901 North Stuart Street, Suite 303
Arlington, Virginia 22203-1821
(703) 696-2127

**10. SPONSOR/MONITOR'S ACRONYM(S)**

**11. SPONSOR/MONITOR'S REPORT NUMBER(S)**

**12. DISTRIBUTION / AVAILABILITY STATEMENT**

Approval for public release; distribution is unlimited.

**13. SUPPLEMENTARY NOTES**

The views, opinions and/or findings contained in this report are those of the authors and should not be construed as an official U.S. Government position, policy or decision, unless so designated by other documentation.

**14. ABSTRACT**

SERDP project MR-1443 entitled "Man-portable Vector Time Domain EMI Sensor and Discrimination Processing" is complete. This report contains the final design, engineering challenges, modeling advancements, and data analysis results from this project. This combination of vector receivers coupled with a laser positioning system resulted in a versatile prototype instrument delivering high quality, diverse data well suited to rigorous models of UXO and soil. New algorithms aimed at utilizing the high quality data from the MPV were developed including the Generalized Standardized Excitations Approach (GSEA) and Normalized Surface Magnetic Source (NSMS). Results from this project suggest a further need for high quality, hand held, production instruments in the time domain suited to UXO remediation efforts. The MPV2 instrument incorporates a redesign of the MPV concept.

**15. SUBJECT TERMS**

keywords; electromagnetic induction, handheld, frequency domain, rigorous models, inversion

| 16. SECURITY CLASSIFICATION OF: | | | 17. LIMITATION OF ABSTRACT | 18. NUMBER OF PAGES | 19a. NAME OF RESPONSIBLE PERSON |
|---|---|---|---|---|---|
| a. REPORT | b. ABSTRACT | c. THIS PAGE | | | Benjamin E. Barrowes |
| U | U | U | UU | 153 | 19b. TELEPHONE NUMBER *(include area code)* (603)646-4822 |

This report was prepared under contract to the Department of Defense Strategic Environmental Research and Development Program (SERDP). The publication of this report does not indicate endorsement by the Department of Defense, nor should the contents be construed as reflecting the official policy or position of the Department of Defense. Reference herein to any specific commercial product, process, or service by trade name, trademark, manufacturer, or otherwise, does not necessarily constitute or imply its endorsement, recommendation, or favoring by the Department of Defense.

# Contents

**1 Abstract** **iii**

**2 Objectives** **1**

**3 Background and Overview** **2**
3.1 Introduction . . . 2
3.2 The Instrument and Its Use . . . 4
3.3 This Report . . . 5

**4 MPV Hardware** **6**
4.1 The Sensor Head . . . 6
4.2 Laser positioning . . . 8
4.3 The Data Acquisition System . . . 9

**5 Data Acquisition Procedures** **12**
5.1 Data Acquisition Procedures for the MPV . . . 12
5.2 Transmitting and Recording Over Time . . . 13
5.2.a Time Patterns of Transmission . . . 13
5.2.b Signal-Conserving Interpolation . . . 14
5.3 MPV System Sensitivity . . . 16
5.3.a Effect of Transmitter Dimension . . . 16
5.3.b Relative Sensitivity . . . 18
5.4 Positioning . . . 19
5.4.a Positioning Checks . . . 22
5.5 Sensor Motion Issues . . . 26

**6 Data Acquired by the MPV** **29**
6.1 ERDC Teststand Data . . . 29
6.2 CRREL Testplot Data . . . 30
6.3 Sky Data . . . 31
6.3.a Sky Hanover . . . 31
6.3.b Sky Vancouver . . . 31
6.4 Topsoil Elevation Profiles . . . 31
6.5 Blind Test Data . . . 32
6.5.a Blind Test Suite 1 . . . 32
6.5.b Blind Test Suite 2 . . . 33
6.6 Dynamic Tests at CRREL . . . 33

**7 Models for Post-processing MPV Data** **43**
7.1 UXO Identification With the MPV . . . 43
7.2 Triaxial Dipole Models . . . 44
7.2.a Patterns in Dipole Inversions of MPV Data . . . 45
7.3 The Standardized Excitations Approach (SEA) . . . 53
7.3.a SEA Results . . . 57
7.3.b Conclusion . . . 60
7.4 HAP for Object Location Without Search . . . 62
7.5 The Normalized Surface Magnetic Source (NSMS) System . . . 65

7.5.a Concepts and Formulation . . . . . 66
7.5.b Tests . . . . . 68
7.5.c Sensitivities and Robustness . . . . . 70
7.5.d Conclusion . . . . . 73

**8 The MPV-II** **74**

**9 Publications** **78**

**APPENDICES**

**A Pre- and Post-Processing Software Package** **79**

**B ERDC Teststand Data Report** **79**

**C Laser Characterization** **107**

**D MPV Dynamic Response** **128**

**References** **138**

# 1 Abstract

SERDP project MR-1443 entitled "Man-portable Vector Time Domain EMI Sensor and Discrimination Processing" is complete. The original objectives of MR1443 consisted of both hardware and software goals. On the hardware side, the goal was to develop an innovative vector (multi-axis) handheld ultra-wideband (UWB) electromagnetic induction (EMI) sensor in the time domain, with precise 3-D positioning, for close interrogation of anomalies. This new instrument would allow a new higher level of UneXploded Ordnance (UXO) discrimination in the vicinity of a noteworthy magnetic response or in the presence of metallic clutter. Data processing software accompanying the new instrument would also be developed. The goal here was to develop clutter-tolerant signal processing for UXO discrimination using the data provided by the new sensor, based on new, high-fidelity, physically complete forward modeling (the Standardized Excitation Approach (SEA) and the Normalized Surface Magnetic Source (NSMS) approach), rigorous instrument characterization, and on new processing techniques.

We have constructed the Man-Portable Vector (MPV) instrument along with a positioning system with subcentimeter accuracy at a range of about 2 meters. This new instrument has been successfully used to acquire data both under lab conditions and in both static and dynamic modes. Results from all blind tests indicate the MPV can acquire diverse and accurate vector data with a signal to noise ratio (SNR) similar to or better than previous time domain (TD) handheld instruments. Single target inversion results for laboratory blind tests were 100% accurate.

Initially, positioning of the MPV sensor head was accomplished through a laser positioning system (see App. Sec. C). However, due to considerations such as the added weight, the bulky setup procedure, and the prospect of no support from the bankrupt vendor, a novel "beacon" positioning system, which uses the primary field of the MPV itself to locate the sensor head, was developed and successfully deployed. The MPV successfully acquires three axis data of the secondary field at five locations within the 75cm sensor head disk. Details of the MPV hardware development can be found in Sec. 4.

Our group has developed algorithms and models which accompanied the development of the MPV hardware. These algorithms include Support Vector Machine (SVM) classification models, extensions of the SEA, and improvements to the NSMS model. Details of these models and algorithms can be found in Sec. 7.

The MPV is now a fully functioning EMI instrument capable of vector sensing of magnetic anomalies while being well located within a limited range. For precise, cued interrogation of anomalies, the MPV provides diverse, accurate, time domain data of the secondary EMI field suitable for inversion and discrimination with high fidelity, rigorous models. At the same time, as the project progressed, we realized that the MPV instrument was simply too large and heavy to be used for a long period of time regardless of the data quality. Therefore, the MPV has been redesigned with these issues in mind. The resulting second generation instrument (MPV-II, see Sec. 8) is much lighter, easier to use, and is currently undergoing field testing under ESTCP project MR-201005.

## List of Acronyms (and page references to first use)

| | |
|---|---|
| 3-D | Three Dimensional – first used on page (iii) |
| ASI | Identifies the particular laser positioning system used – first used on page (8) |
| ATC | U.S. Army Aberdeen Test Center – first used on page (29) |
| CRREL | Cold Regions Research and Engineering Lab – first used on page (iv) |
| EMI | Electromagnetic Induction – first used on page (iii) |
| ERDC | Engineering Research and Development Center – first used on page (19) |
| ESTCP | Environmental Security Technology Certification Program – first used on page (iii) |
| GPS | Global Positioning System – first used on page (8) |
| MPV | Man-Portable Vector (subject of this final report) – first used on page (iii) |
| MQS | Magnetoquasistatic – first used on page (2) |
| MR | Munitions Response – first used on page (iii) |
| NSMC | Normalized Surface Magnetic Charge – first used on page (29) |
| NSMS | Normalized Surface Magnetic Source – first used on page (iii) |
| Rx | Receiver – first used on page (2) |
| SEA | Standardized Excitations Approach – first used on page (iii) |
| SERDP | Strategic Environmental Research and Development Program – first used on page (iii) |
| SNR | Signal-to-noise ratio – first used on page (iii) |
| SVM | Support Vector Machine – first used on page (iii) |
| TD | Time Domain – first used on page (iii) |
| Tx | Transmitter – first used on page (2) |
| USACE | United States Army Corps of Engineers – first used on page (29) |
| UWB | Ultra-wideband – first used on page (iii) |
| UXO | UneXploded Ordnance – first used on page (iii) |

**Keywords:** electromagnetic induction, handheld, time domain, rigorous models, inversion

**Acknowledgments:** This project was funded by the Strategic Environmental Research and Development Program (SERDP) under project MR-1443. We worked closely with contractors G&G Sciences and Dartmouth College for the duration of the project. Special thanks go to Jesse Stanley and Rosanne Stoops at CRREL who took much of the data presented here. Drs. Jeff Marqusee, Anne Andrews, and Herb Nelson, and the review committee for SERDP, provided support and constructive reviews during the course of the project.

# List of Figures


3.1 The MPV sensor system as implemented, including backpack with transmitter, power source, and DAQ. . . . . 3
3.2 Vertical gray plastic rods on the sensor head support the laser positioning receivers. 3
4.1 Sketch of the MPV from behind (top panel) and from above (bottom panel). . . . 6
4.2 Close-up view of one of the MPV cubes (R0 in this case) showing the three receiver coils. The numbers in the tape measure increase in the $-\hat{\boldsymbol{x}}_{\text{MPV}}$ direction. . 7
4.3 Detailed schematic of receiver cube. . . . . 8
4.4 Block Diagram of MPV Instrumentation. . . . . 10
4.5 MPV Data acquisition system (DAQ). . . . . 10
4.6 Picture of transmitter. . . . . 11
5.1 Current vs time in the MPV transmitter cycle, showing four stages of equal duration, delimited by vertical lines: A step-on, a step-off (top left inset detail), a negative step-on (bottom right inset semi-log detail), and another step-off. . . . . 14
5.2 Signal-conserving interpolation: . . . . . 15
5.3 Synthetic profile over a 4.875-in diameter steel sphere using an EM61 antenna configuration. The antenna parameters (transmitter and receiver turns) were adjusted to yield a peak response of 1100mv (1.1 x $10^6$ $\mu$v) as reported in [1]. . . . 17
5.4 The vertical field strength of the 3 systems studied measured as a function of depth beneath the center of the loops. Note that at shallow depths the MPV system has the largest primary field. . . . . 18
5.5 Synthetic profiles of the response for a 500$\mu$s time gate for the three systems under study, for a shallow test target (50 cm depth). The results show the clear advantage of using a system with a near point receiver (AOL and MPV systems) as compared with the EM61 system that uses a large (1m $\times$ 1m) receiver. . . . . 19
5.6 Same as previous figure but for a target depth of 1m, showing that the advantage in sensitivity for MPV system as compared with the EM61 has largely disappeared. 20
5.7 Test of the ASI positioning system on the MPV. Left, (a) shows the location of the ASI triangle (brown), location of the central receiver R1 (red), and the tilted $\hat{\boldsymbol{z}}_{\text{MPV}}$-axis (blue lines). Right, (b) Euler angles (dashed lines) in the yaw-pitch-roll convention. . . . . 22
5.8 Laser receiver triangle geometry. . . . . 23
5.9 Positioning system check in blind test measurements. . . . . 24
5.10 "Way-off" results for triangle double area, obtained in the dynamic MPV measurements . . . . . 25
5.11 With problem points weeded out using the first criterion, this figure should ideally be identical to Figure 5.9 (refer to its caption) but is not. . . . . 28
5.12 Same as Figure 5.11 but with a more stringent selection criterion. . . . . 28
6.1 Grid used for MPV test-stand measurements. Superimposed is a schematic diagram of the sensor head, shown in more detail in Figure 4.1. . . . . 30
6.2 Raw data for receivers R0 through R4, taken by the MPV on the test stand in Vicksburg MS, for an upright 81-mm projectile 45 cm below the sensor. Top three: Point-to-point values at the 10th time gate (0.168 ms) in the $z$, $x$, and $y$ directions. Bottom Three: Absolute value of signal at center of the grid vs time. . 35

6.3 Grid for the measurements carried out at Sky Hanover, with a typical setup for two 40-mm projectiles separated horizontally by 25 cm and a schematic outline of the sensor head, for reference. . . . . 36
6.4 Acquiring an elevation profile over topsoil at field site. . . . . 36
6.5 Overlaid MPV data from 19 different heights, ranging from 36 inches elevation down to contact with the soil. Shown is the $H_z$ response from cube 1. . . . . 37
6.6 Same as previous figure, but showing $H_x$ response from cube 1. . . . . 38
6.7 Response for sphere in soil for receiver cube 1, x-component, as a function of elevation, background subtracted. . . . . 38
6.8 Same as previous figure, but for receiver cube 1, y-component. . . . . 39
6.9 Same as previous figure, but for receiver cube 1, z-component. . . . . 39
6.10 Response for sphere in soil for receiver cube 3, y-component, as a function of elevation, background subtracted. . . . . 40
6.11 SNR (in dB) of the z-component of receiver 1 as a function of depth. Steel sphere was buried 5 cm below ground level (to center). . . . . 40
6.12 Data grid used for collection of 17 point data from CRREL parking lot. Positioning achieved by laser positioning system. . . . . 41
6.13 60 mm mortar placed alongside the MPV at the start of dynamic data acquisition. 42
7.1 Triaxial dipole fit results: BLU26 at H1. Blue line is data, green model, red is mismatch. . . . . 46
7.2 Triaxial dipole fit results, as in previous figure, but for the 105-mm at H1. . . . . 46
7.3 Triaxial dipole polarizability results for the 81-mm and 105-mm projectiles and the BLU26 bomblet. In each pair of plots, blind test results are on left, test stand results on right. Multiple lines of same color indicate results from different elevations of the sensor. . . . . 47
7.4 Same as previous figure, but for the 57 mm and 60 mm UXOs. . . . . 48
7.5 Polarizabilities derived from the Vancouver MPV data for a steel cylinder at various inclinations, taken at two depths, (a) and (b). Like the polarizabilities, the tilt angles (black shapes:measured, gray shapes: model predictions) are consistent as inclination changes. . . . . 49
7.6 Polarizabilities derived from Vancouver MPV measurements for aluminum and steel cylinders, at two depths, (a) and (b). . . . . 51
7.7 Inverted magnetic polarizabilities vs time, extracted from multi-object MPV measurements on a 105-mm UXO and a box of nails, over the $5 \times 5$ grid of Fig. 6.3, for two different box/UXO separations (25 and 40 cm). . . . . 52
7.8 Same as previous figure except that here the UXO is a 60-mm mortar. . . . . 52
7.9 Magnetic polarizabilities inverted from Vancouver one-target and two-target measurements. Case 45: two copies of the 6”$\times$3” cylinder from Fig. 7.6. Case 67 (solid lines): one of those cylinders and a smaller one of size 4”$\times$1.5”. Also shown, polarizabilities extracted from single-target data collected for those objects. . . . . 54

7.10 Solution definition (SD) data over spatial sweeps at a given time, for the 81-mm projectile including 14 out of 15 test-stand data sets. Top left: original signal (blue dash-dotted line), the SEA reconstructed signal (solid green line), and absolute value of the difference (red dashed line) at t = 0.207 ms. Top right: results for +z-hat target orientation at 35 cm depth. Bottom panels zoom in to show sample results for receivers R1 and R3. . . . . 58
7.11 Signals and mismatches between data and SEA model output, for optimized locations and orientations for each target in the CRREL test, at a single elevation. Blue line is data, green line prediction, red is mismatch. . . . . 61
7.12 Figures of merit (confidence), defined in (7.3.10), for the ten CRREL scenarios (5 targets, two elevations). The data-derived SEA identifies the targets correctly in all cases except one, being a close second for the 105-mm UXO at H2. . . . . 62
7.13 A magnetic dipole at $\mathbf{r}_d$, representing the target, and associated geometry. . . . . 63
7.14 Geometry of the NSMS model. . . . . 66
7.15 X-component of ERDC test stand data (red) for a 60 mm mortar and corresponding signal calculated by the NSMS (blue), for the first time gate from receivers 1 and 2. . . . . 69
7.16 Blind test results using the NSMS method, in which $Q(t)$ for unknown target #1 clearly matches that for the 81 mm and contrasts with the $Q(t)$ for alternatives in the library. . . . . 70
7.17 NSMC Blind Test Results 2 . . . . . 71
7.18 Same as in previous figure, here for Target #2 (left) and Target #3 (right). . . . . 71
7.19 ERDC test stand data acquisition grid of 89 points with MPV outline superimposed (*left*). $Q(t)$ from 5 single soundings acquired over a 60 mm mortar at the ERDC test stand (*right*). . . . . 72
7.20 NSMS model comparison to library for blind test #3, where vertical axis is $Q(t)$. The curve recovered in blind testing correctly matches that for the BLU-26, especially outside of the late-time noise region. . . . . 73
7.21 $Q_n(t_i)$ as a function of time for limited number of data locations. (*left*). $\phi$ vs number of observation points used (*right*). . . . . 74
7.22 $Q_n(t_i)$ as a function of time for increasing levels of noise injected into the EMI data. (*left*). $\phi$ for this case (*right*). . . . . 74
7.23 $Q_n(t_i)$ as a function of time for increasing levels of noise injected into the position of the MPV sensor head. (*left*). $\phi$ for this case (*right*), with positional error in meters. . . . . 75
7.24 Correct and misplaced locations for indicated noise levels. Blue circles are accurate values, red stars are noisy data. . . . . 76
8.1 The MPV-II sensor . . . . . 77
8.2 Magnetic polarizabilities for a 40 mm projectile, inverted from Yuma Proving Ground MPV-II data (markers), and also (solid and dashed lines) extracted from Sky Research Hanover data. . . . . 77
A.1 Main menu introductory screen to EMI.m. . . . . 79
A.2 Position of the MPV head for this data run of 30 seconds (300 positions). Arrows indicate tilt and rotation of MPV head. . . . . 135
A.3 $H_z$ data values for data run in Fig. A.2. . . . . 136
A.4 Adding the current target to the library in EMI.m. . . . . 137

A.5 Discriminate against the current library in EMI.m. . . . . 137

# List of Tables

1 Tabulated antenna properties of the three systems that were analyzed in this study. . 17
2 Correct answers for the blind-test data runs. . . . . 32
3 Inverted and measured depths and directions of a 12-in cylinder, with percentage depth discrepancy (a small component along $\hat{\boldsymbol{x}}$ is not shown) . . . . . 48
4 Inverted target locations and ground truth for selected Vicksburg measurements . . . 50
5 Inverted locations and ground truth for selected Vancouver two-target measurements 53
6 Correct answers for CRREL blind-test data runs. . . . . 65
7 NSMS model inversion results for position and orientation for CRREL blind test data. Numbers with an asterisk are arbitrary due to BOR considerations. . . . . 65

# 2 Objectives

The objectives of this project were to

- Develop an innovative vector (multi-axis) man-portable UWB electromagnetic induction (EMI) sensor in the time domain (TD), with precise 3-D positioning, for close interrogation of anomalies identified during broader surveying, i.e. for cued interrogation.
- Develop a new level of signal processing for UXO discrimination using the data provided by the new sensor, based on
  - Rigorous instrument characterization
  - New, high-fidelity, physically complete forward modeling of object responses (the Standardized Excitation Approach: SEA)
  - Innovative target models and parameterizations that support improved discrimination, particularly the Normalized Surface Magnetic Sources (NSMS) and the H-A-Phi (HAP) system
  - Application of cutting edge search, inversion, and classification techniques, including Differential Evolution (DE) and the Support Vector Machine (SVM).

With multiple vector receivers and either laser or beacon positioning, the new instrument should produce quality diverse data for superior, clutter-tolerant discrimination over rugged, non-trafficable terrain.

# 3 Background and Overview

## 3.1 Introduction

The presence of buried unexploded ordnance (UXO) in former battlefields and decommissioned firing ranges is a serious humanitarian and environmental problem worldwide [2, 3]. UXO cleanup is extremely expensive and laborious, possibly costing some $1.4 million per acre in the United States [4]. Expenses are driven in part by the fact that most environments that contain UXO are also cluttered with harmless items that get detected just as readily. For buried, more or less intact items, sensors are not able to detect explosive material per se. Thus, in the absence of further information, harmless items must be treated as dangerous. Thus the technical problem is not so much one of detection but of identification and discrimination.

Electromagnetic induction (EMI) sensing has been the most promising technology in the field, thus far. Operating in the magnetoquasistatic (MQS) frequency range (from 10's of Hz to 100's of kHz), EMI sensors emit a primary field that induces eddy currents and magnetic response in metallic bodies [5]. These in turn produce secondary magnetic fields that can be detected by the sensor's receivers. While in this frequency range the ground is essentially transparent, the technology and treatment of its data are not exempt from difficulties.

Induction sensing occurs at very low electromagnetic frequencies, which means that one must work at very low resolutions in most respects. This forfeits the possibility of imaging and one must search instead for patterns in response, inferred parameters and signatures in the data. Typically, this shortage of information is exacerbated by minimal spatial diversity of the measurements. Data often consist of a single field component measured at a single altitude at only a few points. Positional uncertainty also limits the precision and usefulness of detected signals. New-generation instruments like the Berkeley UXO Discriminator (BUD) [6, 7], TEMTADS [8], and the MetalMapper [9, 10] attempt to ameliorate this situation by providing arrays of transmitters and receivers in precisely known configurations. However, these systems are large and heavy and cannot be readily used in rough or treed terrain that does not allow vehicular access.

The Man-Portable Vector (MPV) sensor has been designed in response to the previous concerns. Realized by coworkers G&G Sciences, the MPV is a ultrawideband (UWB) time-domain handheld EMI instrument that measures all three vector components of the secondary field at five different locations in relation to the transmitter, including two different heights. Thus the instrument combines the virtues of monostatic sensing (Tx and Rx units attached and moving about together to different excitation and observation points) and multi-static sensing (distributed or spatially separated observations of a single field from a given excitation). It features user-adjustable temporal resolution and data-acquisition window, either in static or dynamic measurement configurations. Its laser positioning system tracks its location with sub-centimeter precision. Continuously recorded transmitter current can be used to cancel errors due to instrument drift. These features, along with its portability, make the MPV a versatile instrument that provides a wealth of high-quality information.

Our studies have shown that the MPV is indeed a capable tool for detection and identification of buried items. [11, 12], [13] MPV-collected data have been analyzed using the dipole model [14], the Standardized Excitation Approach [15] and a generalized version thereof [12], and the Normalized Surface Magnetic Source (NSMS) method [11, 16, 17] to detect and identify single- and multiple-target UXO scenarios in the laboratory and at various UXO sites. Future plans include the adaptation to the MPV of the Orthogonal Volume Magnetic Source model [18] and of spheroidal [19, 20] and ellipsoidal [21] analytic procedures. Overall, encouraged by the perfor-

Figure 3.1: The MPV sensor system as implemented, including backpack with transmitter, power source, and DAQ.

Figure 3.2: Vertical gray plastic rods on the sensor head support the laser positioning receivers.

mance and potential utility of the MPV, we have designed and realized a second generation of the instrument that is smaller, lighter, and better facilitated electronically and ergonomically (see Sec. 8).

### 3.2 The Instrument and Its Use

In summary, key benefits of the MPV are:

- By being man-portable, the MPV can be deployed at sites where terrain and vegetation prevent heavier, cart-based systems from being used. Also, one can tilt the sensor head such that the transmitter illuminates the buried target at multiple angles. Standard horizontal loop transmitters produce a strong vertical field when directly above the target. Horizontal field components only come into play when the transmitter is positioned at a standoff distance away. However, at such standoff distances, the magnitude of both Tx and Rx fields are reduced, producing lower signal-to-noise ratios in horizontal field components. By tilting the MPV one can take multiple "looks" at the target from a position close to it, obtaining greater diversity in excitation and response configurations, with desirable SNR and consequent benefits for discrimination [22].

- The MPV can measure the time decay of an anomaly over a broad range of user-specified times, from very early time (about 60 µs ), generally up to 25 ms after the primary field has been terminated. Very early time can be particularly useful for distinguishing small items, and the contrast between early and late time behavior enhances discrimination (see e.g. Sec. 7.5). Late time information has been shown to be very useful for estimating target size [23]. The sensor is equipped with a graphical user interface that controls time-related acquisition parameters, such as transmitter waveform characteristics and the recording time channels [24]. The MPV is the only available non cart-based system that can acquire multistatic, multi-component data on a wide and programmable range of time channels.

- The amount and diversity of data in each MPV "shot" reduce the number of soundings required for target localization and discrimination. The instrument's five receivers each simultaneously record three orthogonal components of the scattered field with exact relative positioning among receivers. We show below the ability to predict target depth, orientation, and intrinsic discrimination parameters using shots from a small number of points (see Sec. 7.5.c).

- The MPV is well suited for small target discrimination. Smaller caliber anomalies have localized response, varying especially rapidly over space when they are (typically) shallow. Air induction receiver coils measure a voltage by spatially averaging the secondary field from a target over the face of the loop. Therefore, large receivers tend to "smear out" the secondary field. The 10x10 cm receivers of the MPV are typically smaller than other multichannel sensors (for example the Geonics EM63 has 50x50 cm receiver) thus better suited to detecting and sampling the secondary field over small targets.

- The MPV has very stable EMI components. In field tests we observed negligible measurement drift and insensitivity to varying survey conditions (sun exposure, temperature). Time consuming, periodic recalibrations are not required for the MPV sensor. There is no offset due to electronic components owing to the transmitter current form and the receiver data

stacking scheme. In addition, transmitter current is monitored and recorded at all times during the survey, thus variation of excitation can be accounted for.

- The MPV data are well understood and characterized, and can be modeled very successfully using standard EMI theory together with innovative formulations (see Sec. 7). The ability to model accurately the MPV signal, in a variety of ways, from both compact metallic targets and magnetic soils is critical for facile, robust inversion and discrimination.

- The combination of multi-static, multi-component, and multi-time channel measurement capabilities of the MPV allow for the use of new and emerging soil compensation techniques (SERDP 1414 and 1573). The broad time range and sensitivity allow measurement of the characteristic decay of viscous remanent magnetic soil. The effect of soil can therefore be modeled and successful discrimination can be achieved even in the presence of magnetic soils [25, 26]. Further, in many instances soil effects may be strong in the received vertical field components but should be negligible in the horizontal components, which the instrument also receives.

- The MPV has an accurate portable positioning system that is applicable in diverse types of terrain. The initially implemented laser positioning system provided sub-cm accuracy, but also had a variety of drawbacks, as detailed below. Thus an additional system was devised and preliminary tests performed, using the transmitted field of the sensor itself as a beacon that can be tracked. Initial tests of MPV beacon positioning were successful at locating it with high accuracy (extension of SERDP project MR-1443). The magnetic moment of the MPV transmitter can be detected at a relatively large distance from the MPV. The position of the MPV could be predicted with sub-centimeter accuracy within a 5-m range, which is more than sufficient to cover any UXO anomaly, and not more than 3 cm error as far as 8 m away when the MPV was allowed to lay still for 10 s. The beacon system is implemented and will be relied upon in future uses and generations of the instrument.

### 3.3 This Report

The hardware for the MPV is presented in Sec. 4 while data acquisition processes and issues are described in Sec. 5. Section 6 reports on the specific, archived data sets acquired with the new instrument; pre-processing of data for positioning, binning, quality check etc is described in Appendix Sec. A. Section 7 contains results of modeling and discrimination work that progressed in tandem with the MPV hardware, including the triaxial dipole model, the Standardized Excitation Approach (SEA), the Normalized Magnetic Source approach (NSMS), and the HAP method for target localization without an optimization search. Section 8 describes the improved, second generation version of the instrument.

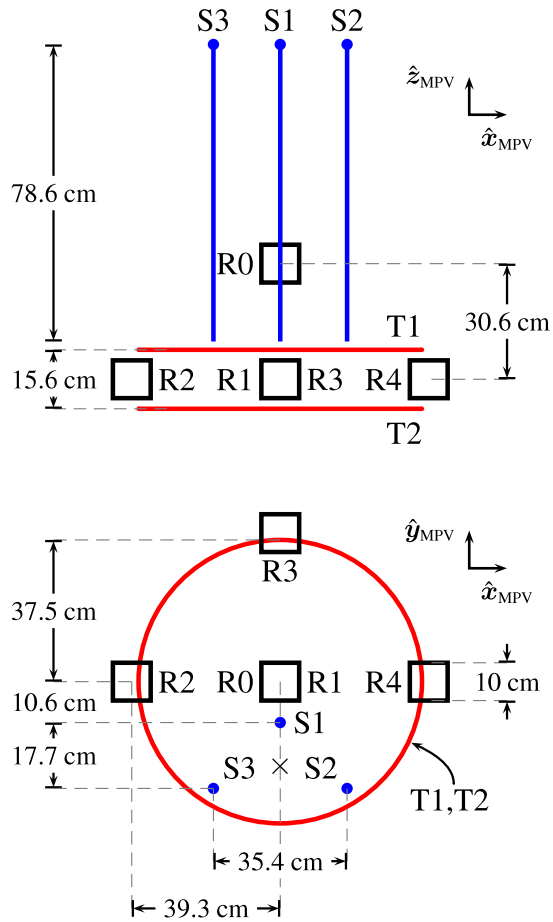


Figure 4.1: Sketch of the MPV from behind (top panel) and from above (bottom panel).

# 4 MPV Hardware

## 4.1 The Sensor Head

Overall, the system consists of the sensor head, including transmitter (Tx) coils, receiver (Rx) coils, and laser positioning receivers; a boom with support strap so that the head can be carried and maneuvered by the operator; and a backpack (see Fig. 3.1 and Fig. 3.2). The components in the backpack are the data acquisition computer in the white box, the transmitter in the blue box, and the laser laser positioning electronics at the bottom. The backpack weighs about 30 to 35 lb while the MPV instrument head and boom including the counterweight battery weigh about 15 to 20 lb. The instrument head and a backpack may be carried by separate people

The red circles in Fig. 4.1, of radius 37.5 cm, are the two transmitter coils whose use is described more fully in Section 5.2. The finite widths of about 4.8 cm of the stacked windings are not indicated in the diagram. The distance between the bottom of the upper transmitter and the top of the lower transmitter is 11.6 cm. The bottom of lower transmitter coil is 0.7 cm from the bottom surface of the plywood framework that houses it. Each Tx coil is composed of 14 helically wound copper-wire loops, each of which has diameter 2 mm and is vertically separated from its neighbors by approximately 1.5 mm end to end. These coils vertically bracket most of the receiver assembly,

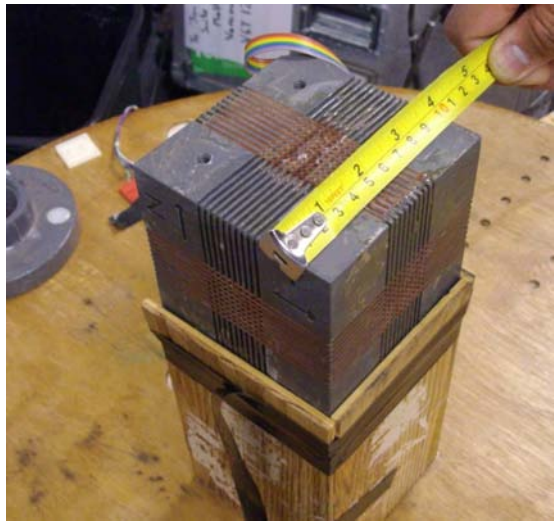

Figure 4.2: Close-up view of one of the MPV cubes (R0 in this case) showing the three receiver coils. The numbers in the tape measure increase in the $-\hat{\boldsymbol{x}}_{\text{MPV}}$ direction.

excepting unit R0.

The five black squares in Fig. 4.1 represent the receivers. In what follows we refer to the coordinate system shown in the figure as the "MPV" coordinates: the origin is at the center of receiver R1. Each of the other Rx units is separated from R1 by 39.3 cm: In the aforementioned coordinate system, R2 is displaced in the $-\hat{\boldsymbol{x}}_{\text{MPV}}$ direction, R3 in $+\hat{\boldsymbol{y}}_{\text{MPV}}$, and R4 in $+\hat{\boldsymbol{x}}_{\text{MPV}}$. The columns supporting the laser receivers are arranged in an isosceles right triangle above and to the "rear" of the head. They and the laser receivers at their tops are represented in the figure by blue lines and dots. Their functioning is described in Section 4.2,

A picture of a receiver cube is shown in Fig. 4.2 with detailed diagrams in Fig. 4.3. The cube is 10 cm on a side and contains three windings oriented in orthogonal directions, wound around a plastic core. The center points of each winding are coincident. Each receiver coil is wound helically on a set of 10 grooves etched on the surface of the cube; 36-gauge wire is used throughout. Each groove is 1.2 mm wide and is separated from its neighbors by 2.0 mm; thus each set of grooves has a total width of $0.12 \times 10 + 0.2 \times 9 = 3.0$ cm. From Faraday's law, the measured signal must be interpreted as the surface integral, over the coil area of each winding, of the time derivative of the secondary magnetic flux density. The dimensions of the MPV receiver coils have been chosen so the signals are as similar loop-to-loop as possible. The grooves corresponding to the $z$-coil (the horizontal one in Fig. 4.2) are 1.0 mm deep; each groove has 12 turns wound around it, giving the coil an effective flux-measuring area of $120 \times (10.0 - 0.1 \times 2)^2 = 11524.8$ cm$^2$. The $x$-coil, perpendicular to the tape measure in Fig. 4.2, is wound around 4.8-mm deep horizontal grooves and 1.0-mm deep vertical ones and contains 13 turns per groove; its effective area is $130 \times (10.0 - 2 \times 0.48) \times (10.0 - 2 \times 0.1) = 11517.0$ cm$^2$. Finally, the $y$-coil surrounds 4.66-mm deep grooves, and has 14 turns per groove, which gives it an effective area of $140 \times (10.0 - 2 \times 0.466)^2 = 11512.0$ cm$^2$.

In the inversions of Section 7.2.a we take all receivers to be $10 \times 10$ cm$^2$; we also implicitly divide out the number of loops and neglect the groove-to-groove separation. These effects are not too dramatic unless the target is very close to the sensor, as has also been found to happen with other EMI instruments [27].

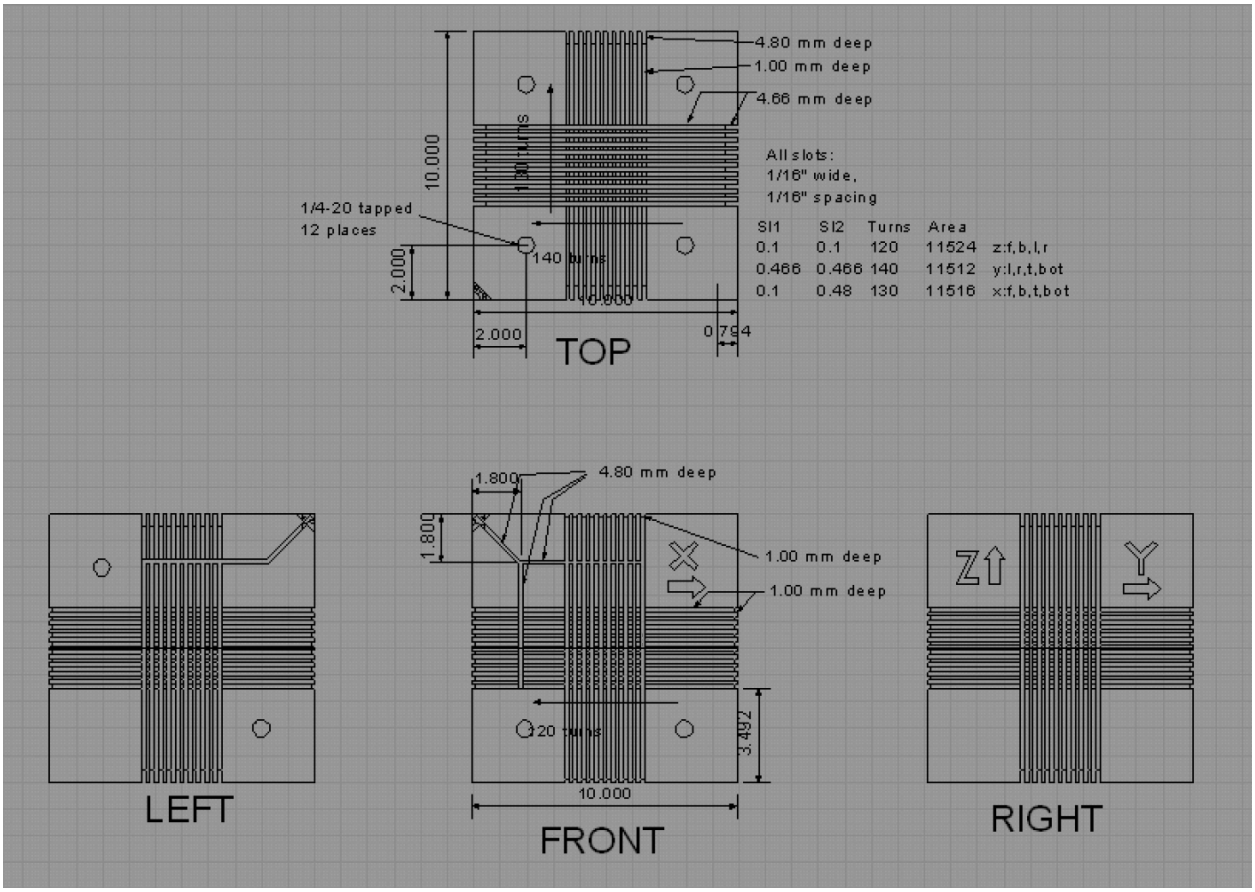


Figure 4.3: Detailed schematic of receiver cube.

The MPV records at a user-selectable number of time gates ranging from about 60 µs to typically 25 ms. Common settings include 30 or 35 logarithmically spaced gates, but the MPV can also sample more than 100 time channels (as in Section 6.1). The signals from the cubes are amplified and sampled in a data-acquisition system tethered to the sensor (the backpack in Fig. 3.1 and Fig. 3.2).

## 4.2 Laser positioning

Access to the full three-dimensional (3D) response of a target makes it necessary to have a full 3D positioning system that accounts for the location and all rotation angles of the sensor at any point. Some existing EMI sensors have used GPS for this purpose [6, 7, 28]. The generally available resolution, on the order of centimeters, may serve to record the whereabouts of anomalies but may not suffice to support discrimination.

The MPV is equipped with a laser positioning system that consists of 1) two transmitters, set up near the survey area, whose positions we assume are known; and 2) three receivers, S1, S2, and S3, whose locations are known with respect to a coordinate system (the "ASI") provided by the positioning device. The laser receivers are arranged in an isosceles right triangle of side 25 cm placed so that the line pointing from the centroid of the triangle to the right angle coincides with $\hat{\boldsymbol{y}}_{\text{MPV}}$ and the hypotenuse coincides with $\hat{\boldsymbol{x}}_{\text{MPV}}$. The centroid of the triangle is located 22.4 cm behind

receiver R0 (see Fig. 4.1.)

The picture of the final MPV configuration in Fig. 3.1 differs from the initial design concept in the vertical pillars provided to mount the laser navigation receivers. It proved necessary to move the laser receivers farther away from the surface of the head and its Rx units because they induced a significant background signal.

### 4.3 The Data Acquisition System

A block diagram of the MPV instrumentation is shown in Fig. 4.4. The heart of this system is a data acquisition system (DAQ) manufactured by National Instruments (Fig. 4.5). As configured for the MPV, the DAQ contains 16 channels of 16-bit Analog-to-Digital conversion, 8 bits of digital output, and five RS-232 Serial Ports. The DAQ contains a fully capable PC running Windows XP. It is capable of operation from either a DC or AC power source.

The transmitter is contained in a separate box as shown in Fig. 4.6. It is a proprietary design that generates a conventional TEM waveform under control of the DAQ. The digital output bits from the DAQ determine whether the transmitter is ON-POSITIVE, OFF, or ON-NEGATIVE. This transmitter was originally designed and fabricated under a contract to the Navy's Naval Explosive Ordnance Disposal Technology Division. It was replaced by a newer version and the Navy allowed its transfer to this project.

The three coils in each receiver cube are connected to a circuit board containing three channels of pre-amplification and anti-alias filtering. The amplified and filtered signals are sent to the DAQ for digitization. The three laser sensors are connected to nearby amplifiers, the signal from which is sent to a laser *'PCE'* box. Each *PCE* produces an RS-232 serial data stream that is sent to the DAQ.

The DAQ and the entire system is controlled by and monitored by a Touch Pad Console shown in Fig. 4.5 that is connected wirelessly to the DAQ. The console acts as the PC's primary console through the use of Remote Desktop.

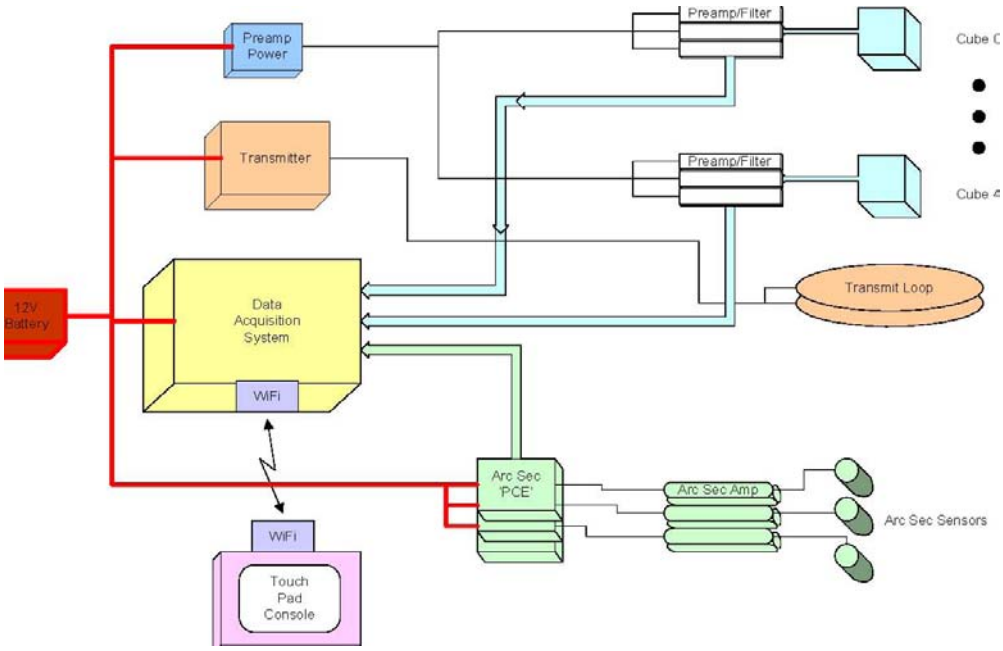


Figure 4.4: Block Diagram of MPV Instrumentation.

Figure 4.5: MPV Data acquisition system (DAQ).

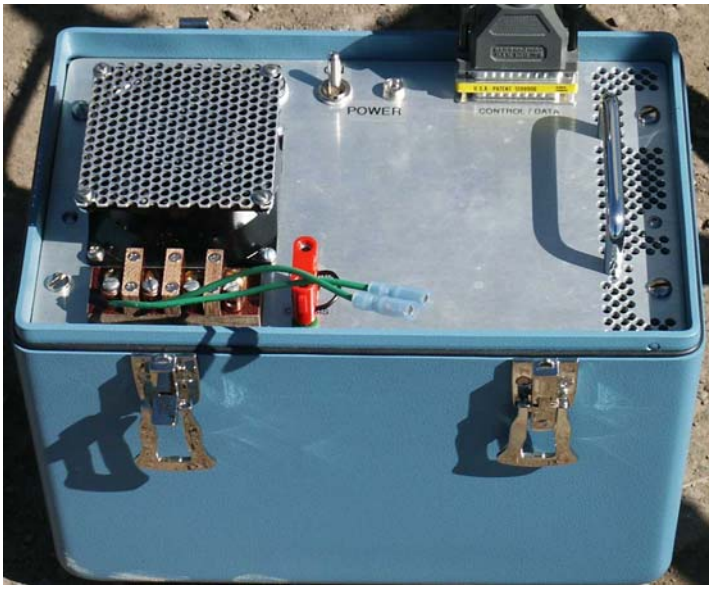


Figure 4.6: Picture of transmitter.

# 5 Data Acquisition Procedures, Issues, and Pre-processing

## 5.1 Data Acquisition Procedures for the MPV

Overall, the MPV can be operated in two distinct modes of operation: static data acquisition mode and dynamic data acquisition mode (Hybrid mode consists of switching between the two, as desired, on the fly). In both modes, the MPV acquires data at an interval of 10Hz for both positioning and magnetic field data. However in static data acquisition mode, the instrument is placed in a fixed location and the 10Hz data stacked, or averaged, for a user selectable amount of time. This data mode results in a higher SNR compared to dynamic data mode due the well known noise reducing effect of integration. Typically, the MPV will be (approximately) placed at gridpoints over a specific anomaly (e.g. in Sec. 7.5.c). One disadvantage of the static mode is sparsity of data compared to the dynamic acquisition mode. Using the MPV in dynamic mode results in 10Hz data collection points as the MPV is freely waved around above an anomaly. While the SNR is lower in this mode, the data is potentially more diverse because the instrument can be maneuvered to interrogate the anomaly from different angles and depths. The data are also more abundant: half a minute's worth of target illumination results in $300 \times 5 \times 3 = 4500$ data points, not including the number of time gates chosen for each.

Data collection procedures with the MPV consists of the following major steps: setting up the laser laser positioning system, configuring and testing the MPV transmitter setup, then acquiring data either in static, dynamic, or hybrid modes. The set up of the laser system consists of about 15 minutes of calibrating the system by acquiring positional information at more than six different locations. The distance between at least two of these location must be known and input into the calibration software, and all of these calibration positions must be within about 25 to 30 m of the laser transmitters. This calibration procedure is sometimes a bit of a trial and error process as documentation from the now defunct company which designed and manufactured the laser system is sparse. After this successful calibration procedure, the positioning information from the laser system is incorporated into the data stream of the MPV.

For statically acquired data, laser information is averaged over the entire data window. For dynamically acquired data, the laser system can provide positional information at a maximum rate of 10 samples per second which often corresponds to the MPV data acquisition rate. Due to this data sampling rate, the MPV instrument head speed is usually kept less than 1cm/sec in order to retain an accurate correspondence between the laser positional information and the EMI data from the MPV itself. Data acquisition can proceed within the triangle defined by the laser transmitters but not within three to five meters of any given transmitter. If any transmitter is moved, the calibration procedure must be repeated.

The laser positioning system does give excellent positional information after the calibration procedure when the system is operating correctly. However, in practice the laser system is less robust than we would hope, suffering from data dropouts, non uniform and inconsistent data paths between the three receivers, and inadvertent line of sight blockage. The laser positioning system incorporates four batteries as well, one in each of the three transmitters on tripods, and one on the backpack in the controller module. These batteries tend to last for a considerable amount of time, especially the transmitter battery which lasts more than eight hours on a single charge. However, it is difficult to know when the laser system is no longer providing data to the MPV data stream except by an alert operator noticing that the positional information is not being updated while data is being acquired. Our recommendations for future positioning measures have generally been implemented in the second generation of the instrument (Section 8).

Most sensors currently in use measure only the vertical component of the secondary field and exhibit cylindrical symmetry. The background subtraction then amounts (to first order) to the subtraction of two scalars. In the case of the MPV we must take into account the fact that in general the sensor is at a different orientation at every measurement point, and that the background run will most likely have been taken at a different set of points and yet another set of orientations. Then it becomes necessary to locate both sets of measurements in the same reference frame before we can subtract one from the other. The orientation also affects the locations of the sensor receivers, which are significantly displaced from the center. In general, background data and survey data are collected at different locations, so we perform nearest-neighbor interpolation to determine the background values at the points where the data were collected. Only then do we carry out the actual subtraction receiver by receiver, direction by direction, and time channel by time channel. Afterward subtracting the background in this way, we rotate the resulting background-subtracted field component data back to the MPV coordinate system and use the original reference point as the origin.

In terms of procedures linked to discrimination post-processing (e.g. using the NSMS of Sec. 7.5), the MPV can be used at field sites in the following manner. If something is known about the potential targets at a site, those representative targets can be characterized by the system by simply placing them on the ground and acquiring roughly one minute's worth of data followed by adding that target to the library using EMI.m. As the cued interrogation and excavation processes progress, the data from each new extracted UXO will also be characterized and inserted into the library in real time. At the same time, each new anomaly is compared to known targets in the library, a process which currently takes about 5 minutes. Thus, the library in current use will become site specific and will grow as the remediation process continues. Discrimination accuracies will improve along with the library.

## 5.2 Transmitting and Recording Over Time

The MPV data acquisition sequence begins with the transmitter which energizes the primary coils, and continues with the DAQ cards in the computer recording of the received signal from the five vector receiver cubes. The transmitter and receivers can be reprogrammed at any time during data acquisition to different operating parameters. Adjustable parameters include number of stacks, recording start time and end time, number of data windows, and how or if any real time plotting feedback is desired (see Sec. 4 and [29, 30] for further details). While this makes for a flexible and extremely useful system, the operator must be trained sufficiently on how to use the system or the data will be less useful. In standard operational mode, the operator of the DAQ equipment must cue the MPV instrument head operator verbally for each static or dynamic data shot.

### 5.2.a Time Patterns of Transmission

The transmitter works in the bipolar on/off cycle shown in Fig. 5.1. (The settings are in fact adjustable; here we restrict our attention to the numbers used most often in the measurements reported below.) A gradual but fairly rapid buildup of current occurs at the beginning of each cycle; after a couple of milliseconds the current plateaus and stabilizes at about 4.5 A. At 25 ms it is shut off abruptly and kept at zero for 25 ms more. Midway through the cycle the current is built up again, with the polarity reversed in order to limit the magnetization of the target during data collection and suppress long-lived eddy currents. Then it is shut off again at 75 ms for another 25 ms that conclude the cycle. Sharp spikes follow the shutoffs and, to a lesser extent, the onsets

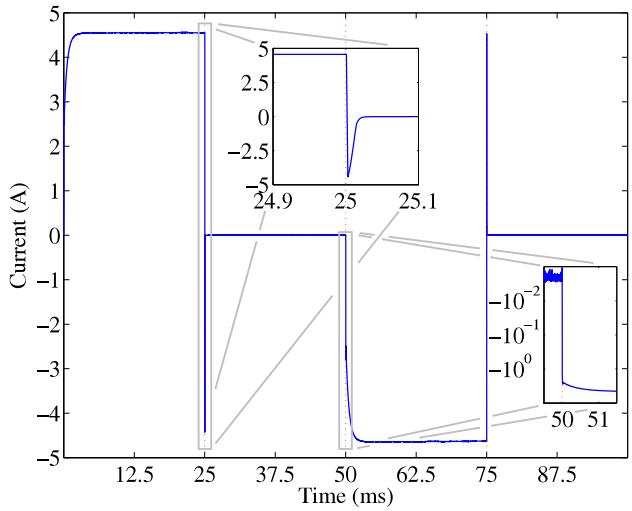


Figure 5.1: Current vs time in the MPV transmitter cycle, showing four stages of equal duration, delimited by vertical lines: A step-on, a step-off (top left inset detail), a negative step-on (bottom right inset semi-log detail), and another step-off.

of the buildup stages. The arithmetic and log $y$-axes in the inset bring out the small peak that occurs between the first, more abrupt rise and the damped one that ends in a stable value. In actual measurements only the step-on currents are recorded. The data acquisition system has a sampling rate of 2 μs; the plot thus contains $5 \times 10^4$ data points. Each point has resulted from stacking 100 measurements.

To make the data files more compact, only the current through the transmitter coils is measured during transmitter-on time; when the transmitter is turned off, only the voltages across the 15 receiver coils are recorded. The MPV thus gives a picture of the transmitter current when it is on, at different times than the receiver signals but sampled identically. The reason for sampling the transmitter current is to measure it near the end of its cycle, when it reaches its peak, because the drop from this value scales the magnitude of the driving signal that energizes a target: the driving field at the target ($d\mathbf{B}/dt$ from the transmitter current) is approximately an impulse with a magnitude proportional to the current in the transmitting loop just before it turns off. The data have to be normalized with respect to the transmitter current because the latter varies noticeably from point to point. Usually the measured voltage at each receiver coil is divided by the transmitted current read at the last time sample.

### 5.2.b Signal-Conserving Interpolation

The freedom of choosing the resolution in time must be supported by a means of translating between different binning schemes that will conserve the total signal collected by the sensor. The MPV sensor collects data during a 25-ms interval that begins at the instant the primary field is shut off. By choosing the number of channels into which the data are binned, the user dictates how much signal is captured in each time channel.

Each channel has a width equal to a fixed percentage $p$ of the time elapsed from $t = 0$ to the end of the previous channel. The channels corresponding to times earlier than $T_0 = 0.1$ ms are discarded, since the transients from the collapsing primary field are still significant. The solution

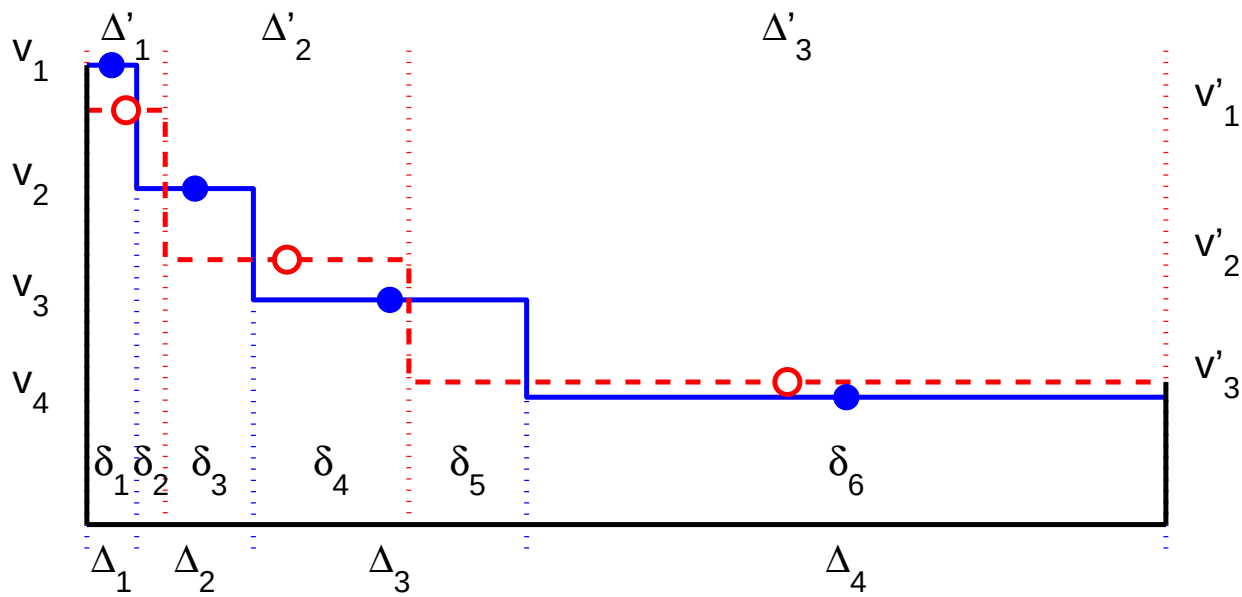


Figure 5.2: Signal-conserving interpolation:

definition data taken at the test stand have $p = 5\%$, corresponding to 107 usable time channels, while the CRREL measurements use $p = 17.5\%$ and 29 usable gates.

To convert back and forth between test-stand and CRREL measured values we use an interpolation method that guarantees conservation of signal. If the signal values and channel widths are respectively $v_i$ and $\Delta_i$ $(i = 1, \ldots, N)$ in one binning scheme, for a partition with widths $\Delta'_j$ $(j = 1, \ldots, N')$ we must find a set of interpolated signal values $v'_j$ such that

$$\sum_{i=1}^{N} v_i \Delta_i = \sum_{j=1}^{N'} v'_j \Delta'_j. \tag{5.2.1}$$

We first impose that the first and last bin edges coincide by making $T_0 = T'_0$ and $T_N = T'_N$ and then generate the union of the two partitions (their common refinement [31]), with widths $\delta_k$. Thus

$$\sum_{i=1}^{N} \Delta_i = \sum_{j=1}^{N'} \Delta'_j = \sum_k \delta_k = T_N - T_0. \tag{5.2.2}$$

The algorithm then determines the signal value $\tilde{v}_k \in \{v_i\}$ that corresponds to each $\delta_k$ and the range of intervals that exhausts each $\Delta'$—that is, the set $\mathbf{k}_j$ such that

$$\sum_{k \in \mathbf{k}_j} \delta_k = \Delta'_j. \tag{5.2.3}$$

The procedure is straightforward and is carried out by looping over the positions of the bin edges and determining $\tilde{v}_k$ and the elements of $\mathbf{k}_j$ point by point. One can then compute the interpolated signals using

$$v'_j = \frac{1}{\Delta'_j} \sum_{k \in \mathbf{k}_j} \tilde{v}_k \, \delta_k. \tag{5.2.4}$$

Figure 5.2 provides an illustration: Given the field values $v_i$ (filled circles) over a set of (solid line) bins of widths $\Delta_i$ and a second set of (dashed) bins $\Delta'_j$, we must find the (open circle) values $v'_j$ obeying 5.2.1 so that the total signal collected by the sensor is conserved. The interpolation procedure finds the ordinates according to 5.2.4 so that, in this example, $\tilde{v}_1 = v_1$, $\tilde{v}_2 = \tilde{v}_3 = v_2$, $\tilde{v}_4 = \tilde{v}_5 = v_3$, $\tilde{v}_6 = v_4$, and $\mathbf{k}_1 = \{1,2\}$, $\mathbf{k}_2 = \{3,4\}$, $\mathbf{k}_3 = \{5,6\}$.

## 5.3 MPV System Sensitivity

The question of sensitivity of the MPV system can be addressed at two levels. Since the system is based on hardware from an existing system (the AOL system), we can easily assess the sensitivity of the MPV relative to that of the AOL system. Estimating the relative sensitivity against the EM61 is a bit harder because the precise electrical characteristics of the EM61 (i.e., the number of turns on the transmitter and receiver and the receiver gain) are kept semi-confidential[1]. Here, we base our sensitivity calculations for the EM61 on measurements and calculations published by Barrow, Khadr, and Nelson [1]. The target was a 4.875 in diameter steel sphere located at a depth of 15 cm below the plane of the EM61 transmitter coil. Their data shows a peak response of 1100 mv for a centerline profile directly over the sphere. Using this observed response and assuming a current of 6A (specified current for the EM61), we have calculated (see Fig. 5.3) that a transmitter with 30 turns carrying 6A and a receiver with approximately 11 turns will generate a peak anomaly of 1100 mv over the target[2].

Having thus established parameters for the EM61, we can now compare responses for three different systems: a) the EM61; b) AOL (central z-receiver); and c) the MPV system (central z-receiver). In Table 1, we list the essential characteristics of the 3 systems. Our calculations have been normalized to unit transmitter current. All three systems are capable of transmitting the 6A current specified for the EM61. The AOL transmitter, in fact, can transmit considerably more than 6A. However, we normally operate it conservatively at around 6A because, until recently, it has been a "one-of-a-kind" instrument. Note that we have provided noise estimates for each of the instruments. Those noise figures were taken from Snyder and George [32]. With regard to the EM61 noise levels, Snyder and George report a noise level of 3.7 mv for the EM61HP over the same target set that they observed a noise level of 14 uv/A with the AOL system. In the case of the EM61, our experience and that of others suggests that typical noise levels for the standard EM61 with a 500 $\mu$s time gate is on the order of 1-2 mv or about $\mu$v/A. Since the MPV will be using standard AOL receiver cubes, we can expect noise levels similar to those observed and documented in the AOL system.

### 5.3.a Effect of Transmitter Dimension

We consider first the effect of primary field strength. The reader may note in Table 1, that with equal current in the three systems the EM61 transmitter has the largest transmitter moment (I $\times$ Area $\times$ Turns). Transmitter moment is directly proportional to the strength of the primary field and so a large moment is always desirable. However, at distances less than a characteristic transmitter

[1] One of the team investigators (Snyder) measured the self-inductance of the transmitter and lower receiver loop for a $1m \times 1m$ EM61. Using these measurements, he calculated that the transmitter loop has 30 turns and the receiver loop has 10 turns. Thus the effective area of the receiver is 10m$^2$ times the gain.

[2] Barrow et. al. used $\mu_r = 500$ and $\sigma = 10^7 S/m$, respectively, as the relative permeability and conductivity of the steel when calculating theoretical responses.

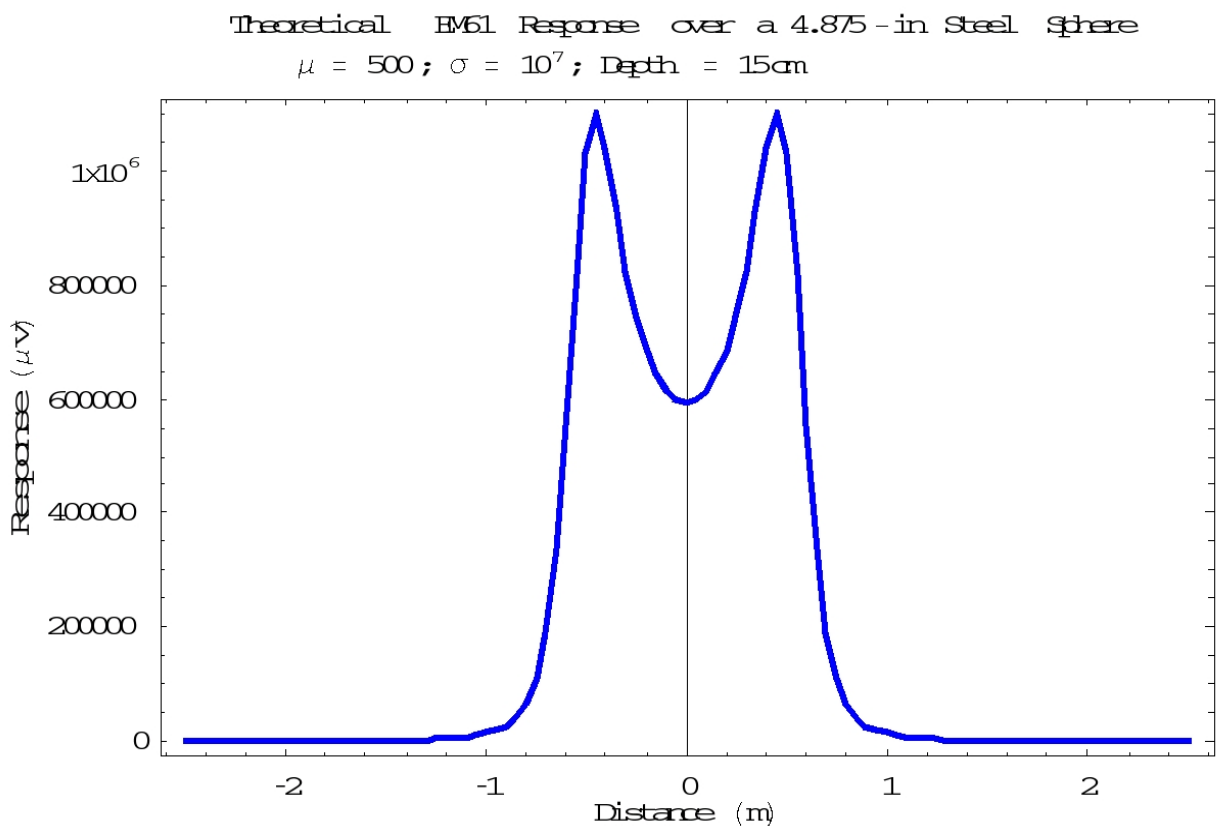


Figure 5.3: Synthetic profile over a 4.875-in diameter steel sphere using an EM61 antenna configuration. The antenna parameters (transmitter and receiver turns) were adjusted to yield a peak response of 1100mv (1.1 x $10^6$ $\mu$v) as reported in [1].

| System | Tx Size | Tx Turns | I (Amps) | Rx Size | Est. Noise ($\mu$V/A) |
|---|---|---|---|---|---|
| EM61 | 1m $\times$ 1m | 30 | 1 | 1m $\times$ 1m | 200 |
| AOL | 1m $\times$ 1m | 16 | 1 | 0.1m $\times$ 0.1m | 20 |
| MPV | 0.75m diam. | 28 | 1 | 0.1m $\times$ 0.1m | 20 |

Table 1: Tabulated antenna properties of the three systems that were analyzed in this study.

dimension (e.g., diameter or side length), we see that the field of the smaller MPV transmitter is actually larger than the 1mx1m AOL transmitter( see Fig. 5.4)[3].

TEM signal strength is directly proportional to the magnitude of the inducing field. Therefore, Fig. 5.4 suggests that the transients induced with the MPV transmitter will actually be larger than those induced with the larger AOL transmitter at distances of less than about 0.75m. At greater distances, the AOL transmitter with its larger dimension and slightly larger moment has the larger field. The field of the EM61 is included in Fig. 5.4 for perspective. Because it has nearly twice the number of turns as the AOL transmitter, it has the largest field over the entire depth range.

[3]The number of turns in the MPV transmitter has been increased to 28 from 16 on the AOL transmitter. If the reader does the math, he or she can verify that the length of wire in the two coils is the same to the nearest even turn.

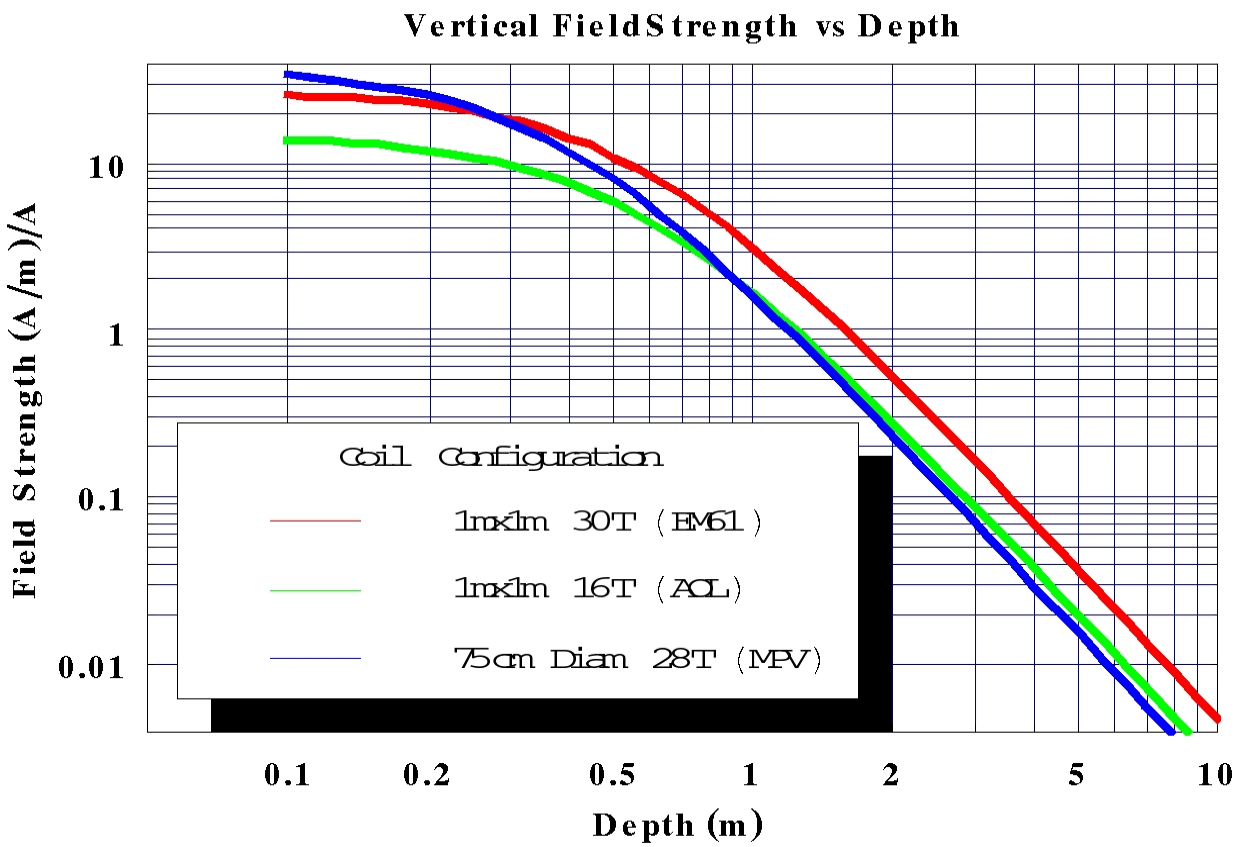


Figure 5.4: The vertical field strength of the 3 systems studied measured as a function of depth beneath the center of the loops. Note that at shallow depths the MPV system has the largest primary field.

#### 5.3.b Relative Sensitivity

We can estimate relative sensitivity for the three systems in Table 1 by calculating their response to a common object. For this purpose, we have used the sphere model cited in Barrow, et. al. [1]. We have placed it at a depth of 50 cm below the plane of the transmitter and calculated profiles similar to that shown in Fig. 5.3. The profiles represent the response from a 500 $\mu$s EM61 gate (start = 400 $\mu$s; end = 900 $\mu$s). The profiles for the three systems calculated over the same target are shown in Fig. 5.5. The MPV system (with the lowest moment) shows the highest peak response. The higher response is partly due to the larger primary field that the MPV transmitter has in its near field (distances of less than 0.75m). However, a second reason is that we are using a small receiver. For shallow targets, the field is highly localized and a small receiver such as the 10cm AOL cube measures a high local field when centered over the target. In contrast, the large 1m x 1m EM61 receiver **averages** its field over a 1m$^2$ area, which reduces its response. In a sense, we have "stacked the deck" here in order to show the MPV in its most favorable operating mode – when looking for shallow targets. But that is what a handheld system is for – isn't it? The advantage in using the MPV configuration disappears for deeper targets. In Fig. 5.6, we show the comparative responses over the same target buried at a depth of 1m. In this case, the anomaly amplitudes of the three systems are about equal.

Using the noise estimates from Table 1, we note that the signal-to-noise ratio (SNR) for the

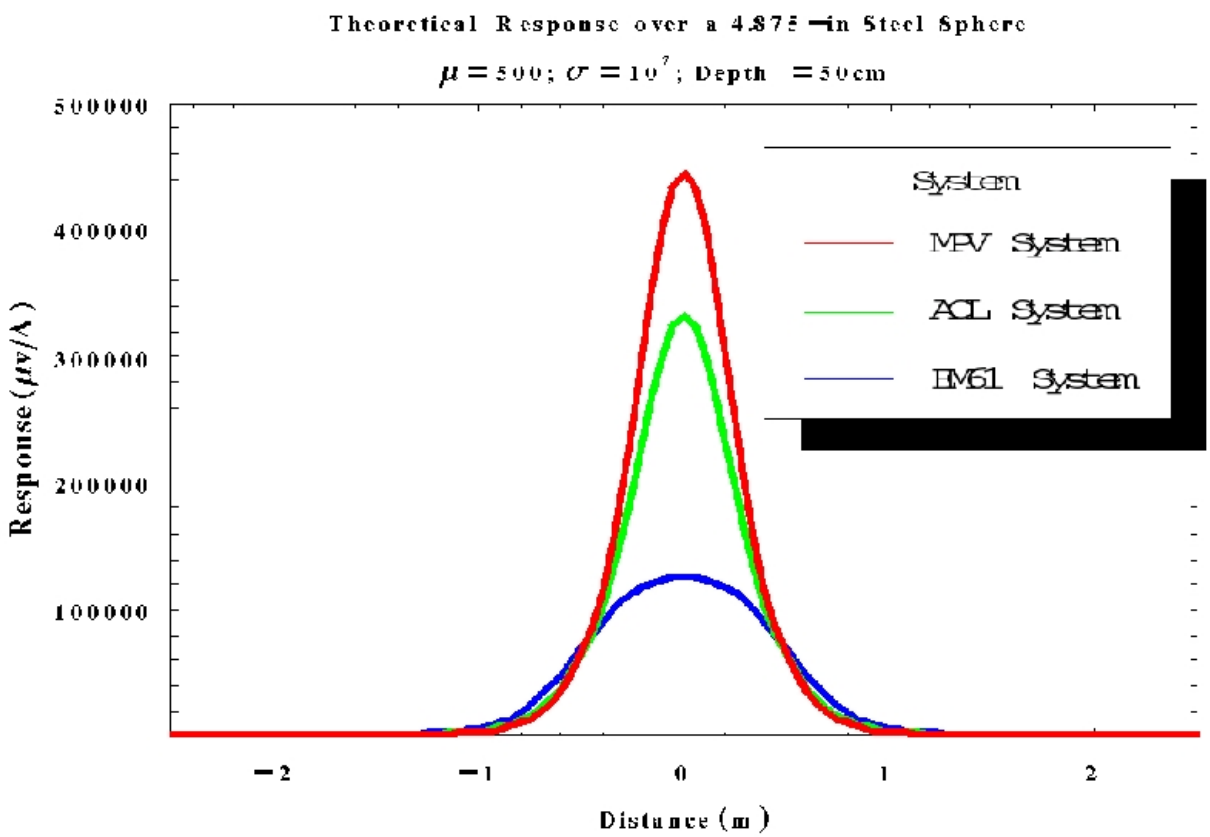


Figure 5.5: Synthetic profiles of the response for a 500$\mu$s time gate for the three systems under study, for a shallow test target (50 cm depth). The results show the clear advantage of using a system with a near point receiver (AOL and MPV systems) as compared with the EM61 system that uses a large (1m $\times$ 1m) receiver.

MPV can be more than 20 dB better than that of the EM61 for these shallow targets ($SNR_{EM61}$=57dB; $SNR_{MPV}$=93dB). However, as noted above, the differences in relative signal amplitude diminish with deeper targets.

## 5.4 Positioning

The original plan in this project was to use a laser navigation system currently owned by the performers. However, future technical support for this system has become worse than uncertain. To complete the immediate project tasks, contractors G&G sciences teamed with ERDC/CRREL and, after some experimentation, trial, and error, was successful in acquiring positional data from the existing ArcSecond laser system. As configured in those applications that were successful, the data provides positional information every one hundred milliseconds and is operated using the computer within the MPV data acquisition system. This method provides the intentional consequence that the time stamp on the positional information is from the same clock that provides time stamps in the data acquisition system. Thus, post processing these two data streams avoids the common problem of trying to match up data time stamps with navigational time stamps.

This “work-around” implementation allowed completion of one of the project objectives: an MPV with on-board, (potentially) precise positioning. However, given the difficulties encountered

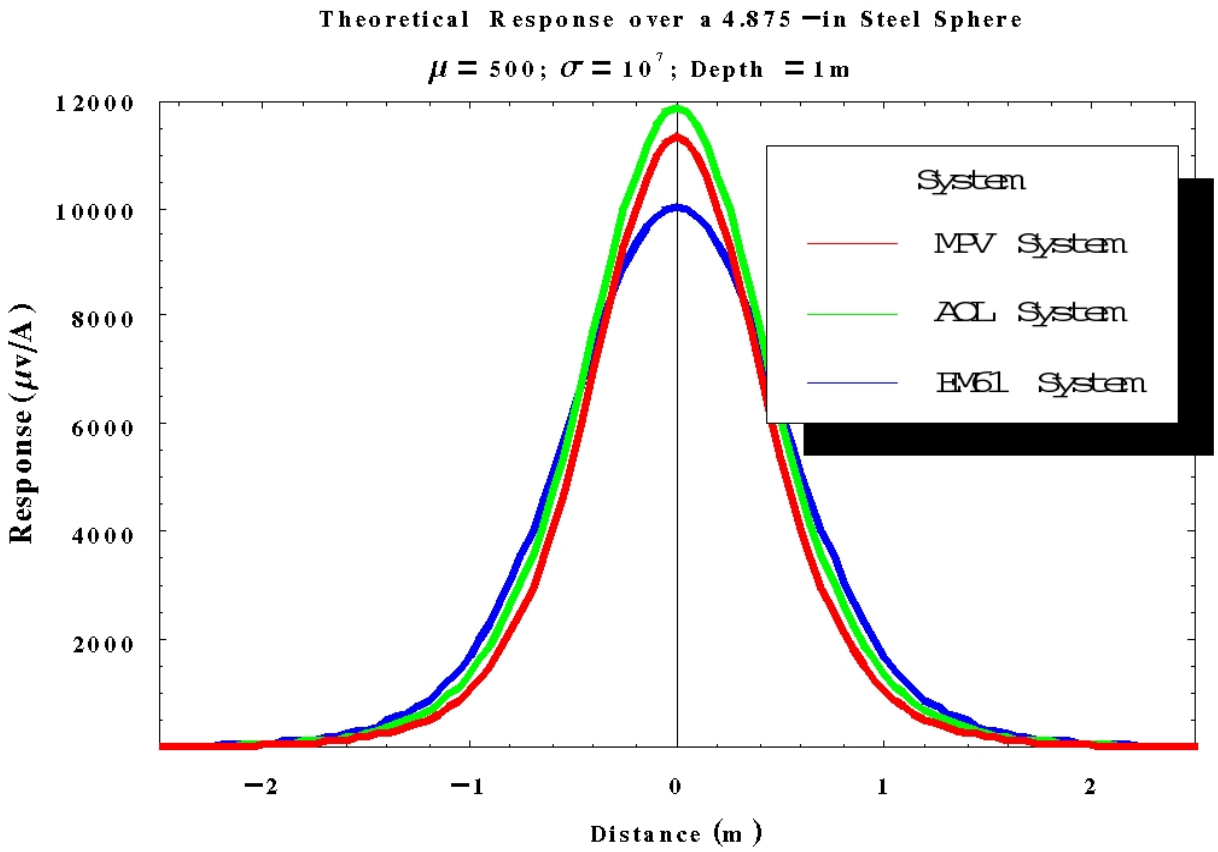


Figure 5.6: Same as previous figure but for a target depth of 1m, showing that the advantage in sensitivity for MPV system as compared with the EM61 has largely disappeared.

in using the system under dynamic survey conditions and also its lack of support, future systems should utilize alternative positioning approaches, especially for instruments meant to be more than just unique research tools. It is possible that laser systems available in the future may offer advantageous positioning tools. However, the possibility pursued successfully in the second generation MPV-II (Section 8) utilizes a "beacon" positioning system, which requires no additional technology beyond the sort of transmitters and receivers already in use in the sensor. In the beacon system, external receivers at known locations track the MPV transmitter. This requires calculation of sensor head location and orientation based on the primary field as received at the positioning receivers. However this can be done readily. In what follows we describe the accomplishments of this project using the laser positioning system that was at hand, as well as the evaluation of that system.

Treatment of the laser positioning data requires transformation of quantities in terms of the local orientation of the sensor head and laser receivers, ultimately producing quantities in a reference or global coordinate system (see Fig. 4.1 and Sec. 4.2 for system geometry, coordinate system specification, and associated notation). To proceed, note that the MPV unit vectors can be

expressed as [33]

$$\hat{\boldsymbol{x}}_{\text{MPV}} = \frac{\mathbf{r}_{\text{S2}} - \mathbf{r}_{\text{S3}}}{|\mathbf{r}_{\text{S2}} - \mathbf{r}_{\text{S3}}|}, \tag{5.4.1a}$$

$$\hat{\boldsymbol{y}}_{\text{MPV}} = \frac{\mathbf{r}_{\text{S1}} - \frac{1}{2}(\mathbf{r}_{\text{S2}} + \mathbf{r}_{\text{S3}})}{|\mathbf{r}_{\text{S1}} - \frac{1}{2}(\mathbf{r}_{\text{S2}} + \mathbf{r}_{\text{S3}})|}, \tag{5.4.1b}$$

$$\hat{\boldsymbol{z}}_{\text{MPV}} = \hat{\boldsymbol{x}}_{\text{MPV}} \times \hat{\boldsymbol{y}}_{\text{MPV}}, \tag{5.4.1c}$$

which in turn yield the rotation matrix (also called "direction cosine matrix, or DCM")

$$\mathsf{R} = \begin{bmatrix} \hat{\boldsymbol{x}}_{\text{MPV}} \cdot \hat{\boldsymbol{x}} & \hat{\boldsymbol{x}}_{\text{MPV}} \cdot \hat{\boldsymbol{y}} & \hat{\boldsymbol{x}}_{\text{MPV}} \cdot \hat{\boldsymbol{z}} \\ \hat{\boldsymbol{y}}_{\text{MPV}} \cdot \hat{\boldsymbol{x}} & \hat{\boldsymbol{y}}_{\text{MPV}} \cdot \hat{\boldsymbol{y}} & \hat{\boldsymbol{y}}_{\text{MPV}} \cdot \hat{\boldsymbol{z}} \\ \hat{\boldsymbol{z}}_{\text{MPV}} \cdot \hat{\boldsymbol{x}} & \hat{\boldsymbol{z}}_{\text{MPV}} \cdot \hat{\boldsymbol{y}} & \hat{\boldsymbol{z}}_{\text{MPV}} \cdot \hat{\boldsymbol{z}} \end{bmatrix}. \tag{5.4.2}$$

where the unsubscripted unit vectors refer to a chosen global system. At each step the DCM can be polished (i.e., made "more orthogonal") by iterating [34]

$$\mathsf{R}_{n+1} = \tfrac{1}{2}\left(\mathsf{R}_n + (\mathsf{R}_n^{\text{T}})^{-1}\right), \tag{5.4.3}$$

starting from the initially measured $\mathsf{R}_0$. Usually three iterations are sufficient. From the DCM we can compute the Euler angles in the yaw-pitch-roll convention [35], modified so that $\hat{\boldsymbol{x}} \to \hat{\boldsymbol{y}}$, $\hat{\boldsymbol{y}} \to \hat{\boldsymbol{x}}$, $\hat{\boldsymbol{z}} \to -\hat{\boldsymbol{z}}$ [33]:

$$\phi = \arctan \frac{\hat{\boldsymbol{y}}_{\text{MPV}} \cdot \hat{\boldsymbol{x}}}{\hat{\boldsymbol{y}}_{\text{MPV}} \cdot \hat{\boldsymbol{y}}} \qquad \text{Yaw}, \tag{5.4.4a}$$

$$\theta = \arcsin\ \hat{\boldsymbol{y}}_{\text{MPV}} \cdot \hat{\boldsymbol{z}} \qquad \text{Pitch}, \tag{5.4.4b}$$

$$-\psi = \arctan \frac{\hat{\boldsymbol{x}}_{\text{MPV}} \cdot \hat{\boldsymbol{z}}}{\hat{\boldsymbol{z}}_{\text{MPV}} \cdot \hat{\boldsymbol{z}}} \qquad \text{Roll}. \tag{5.4.4c}$$

A relevant measurable parameter is the "tilt angle" of the MPV, defined by

$$\gamma = \arccos\left(\hat{\boldsymbol{z}}_{\text{MPV}} \cdot \hat{\boldsymbol{z}}\right), \tag{5.4.5}$$

which in terms of the Euler angles is

$$\cos\gamma = \cos\psi \cos\theta. \tag{5.4.6}$$

This expression is independent of yaw and has a different interpretation for cases with pure pitch than in cases with pure roll, allowing us to check the correctness of each angle separately.

Next we locate the MPV and its receivers. The ASI triangle is centered at the point

$$\mathbf{R}_c = \tfrac{1}{3}\left(\mathbf{r}_{\text{S1}} + \mathbf{r}_{\text{S2}} + \mathbf{r}_{\text{S3}}\right), \tag{5.4.7}$$

and from the information in Fig. 4.1 we can locate every other point on the sensor. For example, the "center" of the MPV (i.e., the position of receiver R1) is

$$\mathbf{r}_{\text{R0}} = \mathbf{R}_c + 22.4\,\hat{\boldsymbol{y}}_{\text{MPV}} - ((81.5 - 5.9/2) + 21.8/2)\,\hat{\boldsymbol{z}}_{\text{MPV}}\ \text{cm}. \tag{5.4.8}$$

Fig. 5.7 shows an example measurement. With the MPV initially flat, the experimenter lifted the right-hand side ($\hat{\boldsymbol{x}}_{\text{MPV}}$) of the sensor to an angle of about 20 degrees and then, always with a

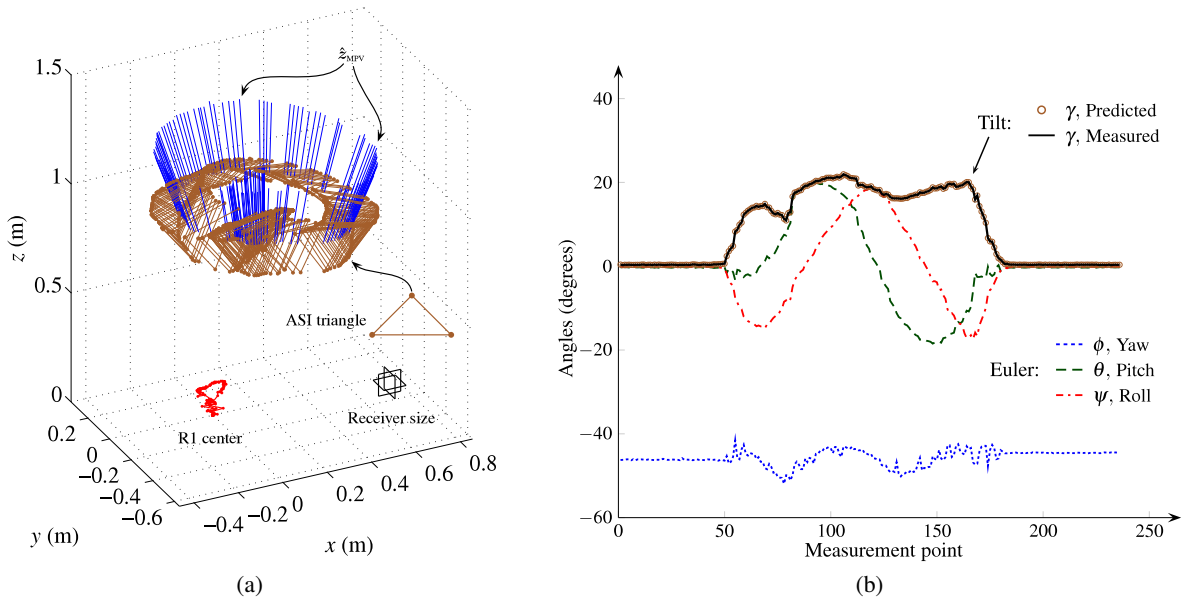


Figure 5.7: Test of the ASI positioning system on the MPV. Left, (a) shows the location of the ASI triangle (brown), location of the central receiver R1 (red), and the tilted $\hat{\boldsymbol{z}}_{\text{MPV}}$-axis (blue lines). Right, (b) Euler angles (dashed lines) in the yaw-pitch-roll convention.

point on the bottom rim of the instrument in contact with a flat surface, and the opposite side in the air at about the same initial angle, in one smooth motion performed the cycle

$$\begin{aligned} \hat{\boldsymbol{x}}_{\text{MPV}} \text{ up} \longrightarrow \quad \hat{\boldsymbol{y}}_{\text{MPV}} \text{ up} \longrightarrow -\hat{\boldsymbol{x}}_{\text{MPV}} \text{ up} \\ \longrightarrow -\hat{\boldsymbol{y}}_{\text{MPV}} \text{ up} \longrightarrow \quad \hat{\boldsymbol{x}}_{\text{MPV}} \text{ up,} \end{aligned}$$

and at the end laid the MPV flat again, pointing in the initial direction. Altogether, this motion somewhat resembles that of a slowly spinning coin. Fig. 5.7a shows the location of the ASI triangle as the sensor moved, taken directly from the MPV readings. The protruding lines (not to scale) represent the unit vector $\hat{\boldsymbol{z}}_{\text{MPV}}$, which, as expected, is tilted at an approximately constant angle and is seen to trace a circle. The dots at the bottom show the receiver R1, which barely moves during the process. Fig. 5.7b depicts the Euler angles as computed from (5.4.4). The agreement between expressions (5.4.5) and (5.4.6) for the tilt angle $\gamma$ shows that the pitch, yaw, and roll are calculated correctly.

### 5.4.a Positioning Checks

Rotation of the raw data for analysis and for background subtraction, as described above, are detailed in [30]. However, due to the instability and occasional drop out of the laser data from the data stream, further processing must be performed on the data before modeling and inversion. Here we describe some positioning problems that have arisen in the analysis of dynamic MPV data, whose value is compromised by the uncertainties introduced by the laser positioning system. At the end of this section we include a short Matlab program that could be used after a typical run to alert the user when the data must be retaken.

The three laser receivers attached to the MPV sensor are placed on an isosceles right triangle of side 25 cm. The relevant dimensions are shown in Figure 5.8. There are some immediate consequences:

1. Let $\mathbf{r}_1 = \mathbf{R}_3 - \mathbf{R}_2$, $\mathbf{r}_2 = \mathbf{R}_3 - \mathbf{R}_1$, and $\mathbf{r}_3 = \mathbf{R}_2 - \mathbf{R}_1$. Since the triangle is isosceles, it must always be true that $r_2 = r_3 = 25$ cm.

2. More relations follow from the fact that the angle $\angle_1 = \pi/2$. From the Pythagorean theorem we must have $r_1^2 = r_2^2 + r_3^2$. Equivalently, $\mathbf{r}_2 \perp \mathbf{r}_3$ or $\mathbf{r}_2 \cdot \mathbf{r}_3 = 0$. Moreover,

$$\frac{\mathbf{r}_1 \cdot \mathbf{r}_3}{r_1 r_3} = -\frac{\sqrt{2}}{2} \quad \text{and} \quad \frac{\mathbf{r}_1 \cdot \mathbf{r}_2}{r_1 r_2} = \frac{\sqrt{2}}{2} \tag{5.4.9}$$

3. Finally, (twice) the area $\Delta$ of the triangle is given by

$$2\Delta = |\mathbf{r}_1 \times \mathbf{r}_2| = |\mathbf{r}_1 \times \mathbf{r}_3| = |\mathbf{r}_3 \times \mathbf{r}_2| = 25^2 = 625 \text{ cm}^2. \tag{5.4.10}$$

**5.4.a.(1) Blind-test data** All of these three conditions were satisfied quite nicely in the "blind tests" and the corresponding characterization measurements (see Sec. 6). Figure 5.9 shows the results for a particular instance (Target 5, the 60-mm UXO, at height H2).

**5.4.a.(2) Dynamic-measurement data** On the other hand, when we consider the recent dynamic measurements we get very different results. We will illustrate our findings using the measurements taken over the 57-mm UXO but we note that all other sets of measurements show the same sort of anomalies. First, there are some very "wild" points, as shown in Figure 5.10, which plots the triangle double areas as found from (5.4.10). Some results are two orders of magnitude larger than expected.

We have built into our code a criterion to weed out these points:

```
R3R1=Thr-One;R3R2=Thr-Two;
Area3=cross(R3R1,R3R2,2);Area3=sqrt(dot(Area3,Area3,2));
Answer=25^2;probb=find(abs(Area3-Answer)>Answer);
```

In other words, we decide that those points with $|\mathbf{r}_1 \times \mathbf{r}_2| - 2\Delta > 2\Delta$ (more than 100% discrepancy) are problematic. Even in that case, however, there are some bad points that are still kept in, as Figure 5.11 shows. We modify the criterion so it will be more stringent:

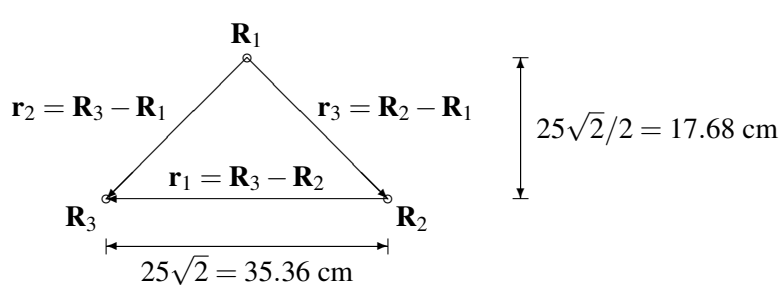


Figure 5.8: Laser receiver triangle geometry.

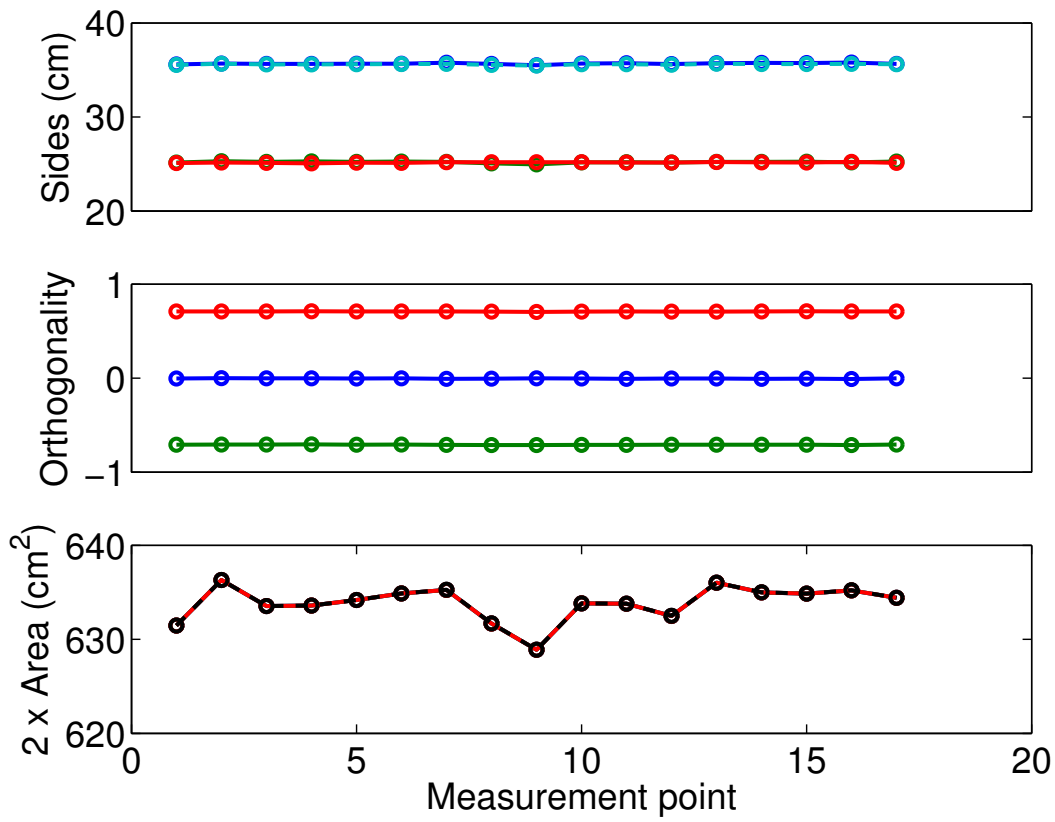


Figure 5.9: Positioning system check in blind test measurements. • TOP PANEL: the hypotenuse (dark blue) of the triangle has mean length 35.68 cm and is seen to equal the square root (light blue, mean 35.60 cm) of the sum of the squares of the catheti (green and red), whose means are respectively 25.20 cm and 25.16 cm. • MIDDLE PANEL: The blue line is the cosine of the angle between $\mathbf{r}_2$ and $\mathbf{r}_3$, whose mean is $-0.004$. The green and red lines, corresponding to the cosines of the other two angles, have means $-0.708$ and 0.709. • BOTTOM PANEL: The double area of the triangle is found by using all three expressions of (5.4.10) (solid lines) and by multiplying the length of the two catheti (dashed line). They all coincide and have as mean 634 cm, which is off from the exact result by 1.4%.

```
Answer=25^2/2;probb=find(abs(Area3-Answer)>Answer);
```

Note, however, that this criterion is outright wrong: the triangle is required to have half its real area.

Figure 5.12 shows that, even with this "improved" criterion, the results are clearly not what we would expect them to be:

1. The triangle sides fluctuate noticeably from point to point; the supposed hypotenuse turns out to be the smallest of the sides; the "theoretical" hypotenuse (the sum of the squares of the catheti) is stable enough, but is significantly larger than 35 cm.

2. The cosines of the angles between the sides also change from point to point. Most troubling, however, is the fact that the sides forming a right angle turn out to be close to parallel.

3. The (double) area as measured is half the expected value, and has a standard deviation of $\sim 14\%$.

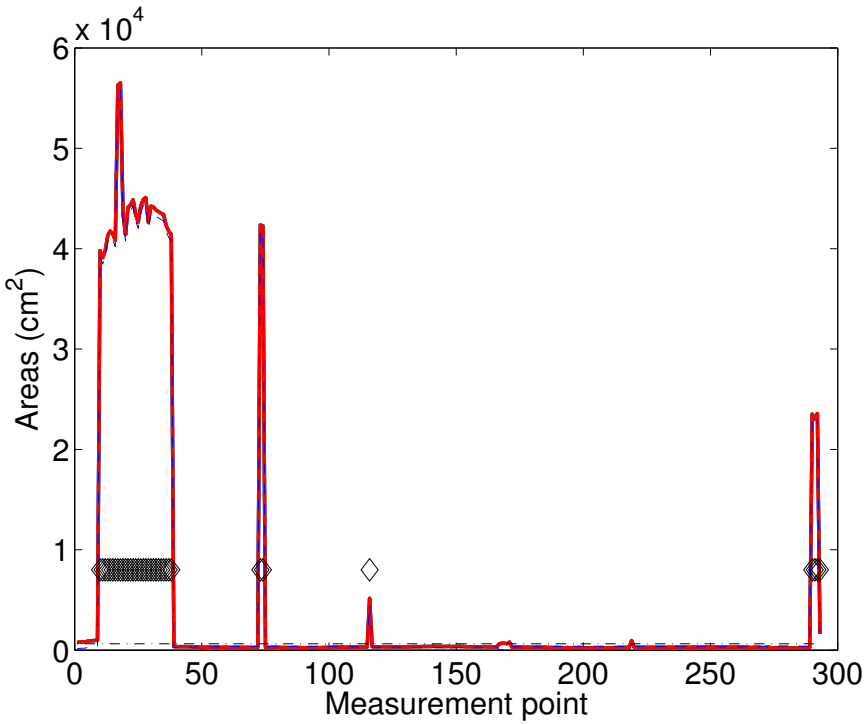


Figure 5.10: "Way-off" results for triangle double area, obtained in the dynamic MPV measurements

These problems may be due to the placement of the laser transmitters. In the blind tests, the $z$-coordinate was consistently around $-30$ cm for all receivers, while in the dynamic measurements it is smaller (and alternating in sign).

**5.4.a.(3) Quality-check routine** The following Matlab routine can provide a quality check after each measurement, alerting the user if the data are unreliable.

```
%  Read data file
[dname dpath di]=uigetfile('.csv','Choose data file',...
                           'location',[100 100]);
datall=csvread([dpath dname],1,15);datall(:,end)=[];
%  Positions
One=datall(:,2:4);Two=datall(:,6:8);Thr=datall(:,10:12);
%  Delete lines consisting of only zeros
Allpts=find(sum([One Two Thr],2));
One=One(Allpts,:);Two=Two(Allpts,:);Thr=Thr(Allpts,:);
R2R1=Two-One;R3R1=Thr-One;R3R2=Thr-Two;
%  Lengths of the sides; Pythagorean relation
Check1=sqrt(dot(R3R2,R3R2,2));
Check2=sqrt(dot(R3R1,R3R1,2));
Check3=sqrt(dot(R2R1,R2R1,2));
hyp=sqrt(Check2.^2+Check3.^2);
%  Check orthogonality
```

```
Checko1=dot(R2R1,R3R1,2)./Check3./Check2;
Checko2=dot(R2R1,R3R2,2)./Check3./Check1;
Checko3=dot(R3R1,R3R2,2)./Check2./Check1;
%  Triangle double areas
Area1=cross(R2R1,R3R1,2);Area1=sqrt(dot(Area1,Area1,2));
Area2=cross(R2R1,R3R2,2);Area2=sqrt(dot(Area2,Area2,2));
Area3=cross(R3R1,R3R2,2);Area3=sqrt(dot(Area3,Area3,2));
Answer=25^2;
%  Find problem points
proba=find(abs(Area3-Answer)>Answer);
```

### 5.5 Sensor Motion Issues

This section addresses the question of how to handle sensor head movement during data collection and during post processing. Prior instruments known to us have not had to address this issue in detail because either 1) the sensor head did not move during data acquisition, or 2) the data acquisition window was narrow enough so that sensor head movement was negligible during the window. Experience suggests that positioning must be known within a centimeter or so in order to allow reasonable inversions of UXO, dipole-like targets, where it is assumed that a given decay-curve time response is a discrete sample of the spatial response. A moving sensor head requires consideration of data-acquisition time-response windows as well as considerations of navigation-system time-response windows.

In the case of the TD MPV, length of the data acquisition window relative to the distance the sensor moves during that window is such that these issues must be addressed. Since we can control both sensor-head movement and the data-acquisition time window, we can trade off measurement speed and sensor movement speed. A data point is recorded by the DAQ on the MPV system from a so-called "block." Selectable block lengths (at present) are 33.333 ms, 0.1s, 0.3s, 0.9s, and 2.7s. Each block consists of a series of cycles (aka "repeats" within a data collection window) of a standard time-domain signals (on-pos, off, on-neg, off) with equal on and off times. The number of cycles within each block as dictated by a selected "repeats" parameter that can be 1,3,9,27,81,243, or 729. The selection of block lengths and repeats is deliberate to cause the fundamental frequency of the frequency to be odd sub-harmonics or odd harmonics of 90 Hz. Thus it is possible to have a decay curve that is as slow as 675 ms (2.7s/1/4) or as fast as 11.4$\mu$s (0.0333s/729/4), corresponding to measurement-windows or blocks of 2.7s and 33.333 ms. These are limits established by software and are not hardware limitations. For the MPV DAQ, additional targeted capabilities are acquisition in measurement windows of 10 ms, 3.33 ms and 1.11 ms.

To address sensor head movement during data acquisition, there are two approaches: The first involves simply shortening the block time as stated above. If we assume a maximum sensor head velocity of 30 cm per second, then to maintain subcentimeter accuracy, the maximum time allowable for the acquisition of one block is 33.3 milliseconds. In particular, the ten millisecond block length should provide excellent positional accuracy on the order of 3 or 4 mm. This approach results in CPU overhead due to the increased number of shorter blocks, and poorer SNR due to shorter averaging times (fewer repeats within a given block).

The other approach involves a continuous data acquisition mode. In this mode, one collects and stores decay data without stacking. The sensor head movement issue is dealt with dynamically in experimental post processing. This allows "adaptive" and/or "spatial" stacking (averaging, filter-

ing, smoothing, polynomial matching, spline interpolation...) to maximize SNR for a decay curve assumed to be a spatial sample. Versions of this approach that are superior under any particular circumstances can be programmed into modifications of the software within the data acquisition system.

We note that sensor head movement during EMI data acquisition is not the only issue to be addressed. Movement of the navigation sensors and the response of the navigation system while moving is also an issue. Under any particular survey conditions, one simple test that can be used to study all of these movement issues at once is to measure the response from a small shallow target. Baseline data is taken by statically collecting spatially discrete data points. Then dynamic data for both the navigation system and the data acquisition system can be compared to the baseline data.

As the system now stands, it is apparent that we can always restrict movement speed enough to allow collection of quality data. Sensor head movement issues relating to the positioning system in the second generation MPV-II (Sec. 8) become, in effect, the same as those for the EMI data. This is because the positioning Rx units in the MPV-II beacon system are similar to those on the sensor head itself. They respond to the same Tx field, and their data streams are controlled by and routed into the same DAQ.

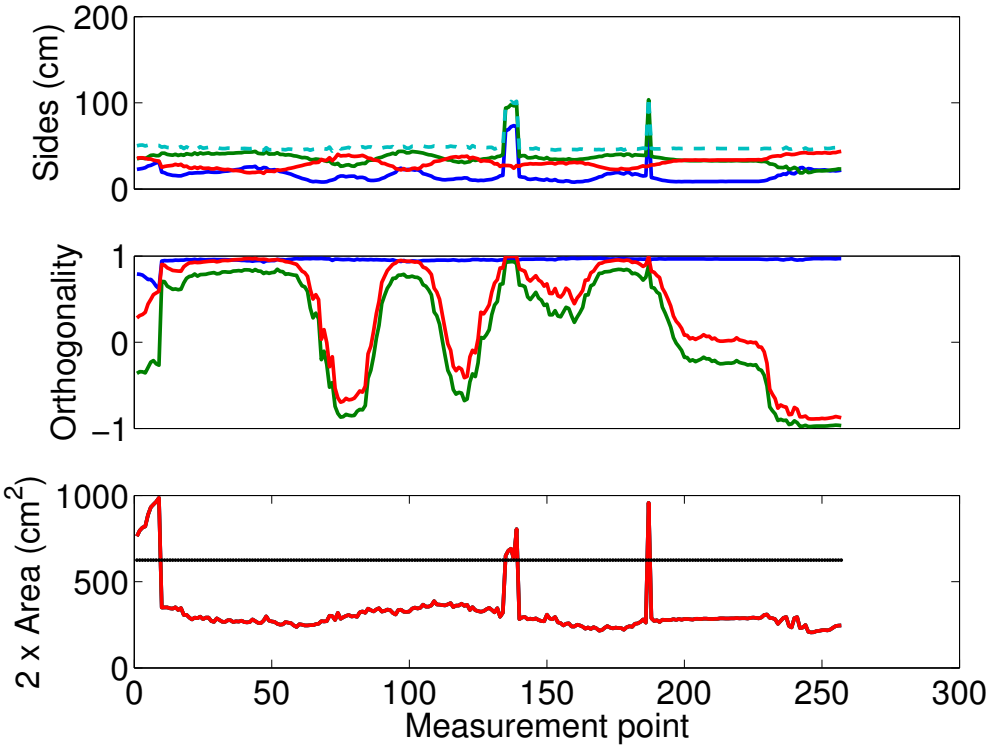


Figure 5.11: With problem points weeded out using the first criterion, this figure should ideally be identical to Figure 5.9 (refer to its caption) but is not.

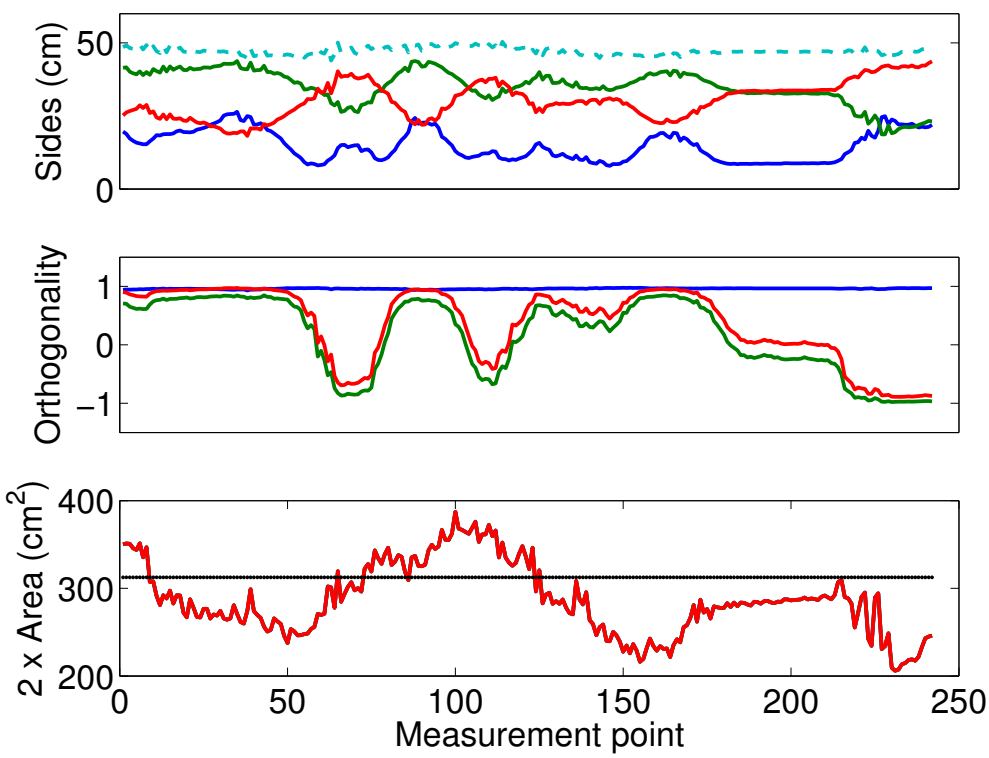


Figure 5.12: Same as Figure 5.11 but with a more stringent selection criterion.

# 6 Data Acquired by the MPV

The data sets acquired from the MPV instrument to date are enumerated below.

1. ERDC test stand runs, led by researchers from G&G Sciences, carried out in February and March of 2007 at the USACE ERDC Waterways Experiment Station (WES) in Vicksburg, Mississippi.
2. CRREL backyard static mode "testplot" runs, late 2007.
3. Elevation profile data acquired over representative topsoil at and near CRREL.
4. Blind test suite #1. These runs were designed in response to a request for data to test our modeling capability for dipole and non-dipole target representation.
5. Blind test suite #2. These runs included some scrap, some canonical items such as spheroids, and some multi-target configurations.
6. Data acquired in dynamic mode over US Army Aberdeen Test Center (ATC) and Camp Sibert targets in June 2008 (see Sec. 6.6 below).
7. Data acquired at Sky Research's Ashland Oregon site (detailed in FY09 ESTCP proposal from Sky and CRREL).
8. Data acquired by Sky Research at their Vancouver BC offices for baseline cases, employing UXO-sized cylinders and multiple objects in various orientations.
9. Data acquired by Sky Research at their Hanover NH site, all cases involving multiple objects, including both UXO and scrap, some previously characterized via ERDC test stand measurements.

These data are available on request. For reference, some details follow.

## 6.1 ERDC Teststand Data

Data were taken at the ERDC test stand over several ATC inert UXO and canonical targets. We had originally planned to acquire detailed data on all the ATC set for up to five orientations, 3 depths, and over a grid spanning about a meter. Time constraints and equipment issues forced us to narrow our scope. In the end, we acquired sufficiently detailed data over five UXO: 57 mm, 60 mm, 81 mm, 105 mm, and the BLU-26, to characterize them with our high fidelity physics based models: the normalized surface magnetic charge (NSMC) and standardized excitations approach (SEA). We were also able to acquire data over a 4 in. steel sphere, and a prolate spheroid. The measurement scheme employed an 89-point grid sketched in Fig. 6.1. Each run started at point $\mathbf{x}_1$ on the upper left corner and followed the blue line until point $\mathbf{x}_{89} = 190\hat{\boldsymbol{x}} + 80\hat{\boldsymbol{y}}$ cm on the lower right corner; each was preceded and followed by calibration measurements, some 180 cm away from the center.

The test stand at WES has a usable measurement area of about 3 by 4 m. On this machined fiberglass platform, a sensor was mounted on a computer-controlled robotic arm with motion positioned to an accuracy of about 1 mm. The sensor was attached firmly enough so that its orientation was nominally constant throughout. The targets are placed so that their depth known to within 1

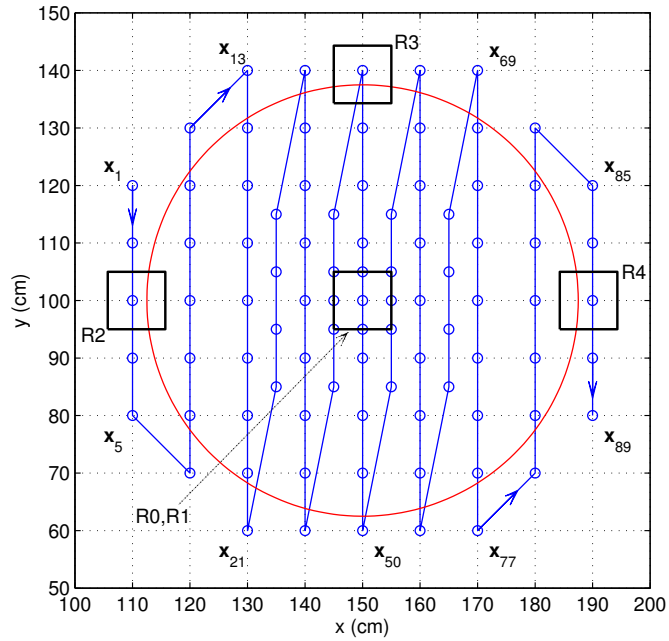


Figure 6.1: Grid used for MPV test-stand measurements. Superimposed is a schematic diagram of the sensor head, shown in more detail in Figure 4.1.

cm. (There is, however, a noticeable systematic error in the horizontal position: the targets are displaced from the origin about 3 cm in the $+\hat{x}$ direction and 1 cm in the $-\hat{y}$ direction.) The background was measured at one faraway point before and after each data run. The sensor was firmly attached to the robotic arm so that its orientation was nominally constant throughout. For a complete description of the data acquisition process and the data itself see Appendix B.

Fig. 6.2 shows an example of the raw (though background-subtracted) data collected on the test stand. In the inversions of the next section we discard the first 15 time channels of the 122 that were used in this set of measurements. The measurements were repeated 27 times per data point and thus lasted for 2.7 s. The data has been normalized by the current at every point, and a background field taken some 180 cm away with no targets present (and smaller by four orders of magnitude) has been subtracted. The signals are clearly discernible until they decay below $10^{-5}$ mV/A, at which point they are overwhelmed by noise.

## 6.2 CRREL Testplot Data

Investigators from G&G Sciences and from the USACE ERDC Cold Regions Research and Engineering Laboratory (CRREL) took measurements on the same test stand targets in October of 2007. They acquired both static and dynamic data over 15 target combinations in the CRREL test plots. These targets included much of the ATC set, several items of scrap, several multi target configurations, and some spherical targets. After calibrating the laser laser positioning system, we collected “static” data by a placing the MPV onto multiple locations around each target set. We then collected “dynamic” data by waiving the instrument around each target set at different heights and orientations.

It quickly became clear to us that there was some problem with the background for all of the

test plots. This background was on the order of two or three orders of magnitude larger than backgrounds due to soil that we had seen in the past. Furthermore, this background was essentially the same from plot to plot, even though the soils in each plot contrasted significantly. This background signal also increased as we approached the walls of the test plots. We concluded that the structural rebar in the the concrete floor and walls of the test plots were contaminating our data (despite its depth of some 2 m). The response was so large because the rebar mesh essentially formed a conducting plane of metal. Data acquired over soil nearby but outside the testplot showed no such contamination. Therefore, regrettably, the entire data set acquired with the MPV over the CRREL test plots had to be discarded. Instead, measurements (e.g. the blind test data described below) were taken nearby, in a parking area, where no anomalous background was noted.

## 6.3 Sky Data

### 6.3.a Sky Hanover

Personnel from Sky Research, Inc. carried out a series of measurements at their Hanover, New Hampshire, branch in March of 2009. This set of measurements differs from the others in that the sensor was placed upside-down on an adjustable support assembly and left in place throughout the data collection process. The targets, on a door atop a stack of milk crates, were moved around in the pattern shown (Fig. 6.3) on a $5 \times 5$ measurement grid with 20 cm point-to-point separation (Note that the coordinate axes are flipped, as the sensor head was inverted).

All measurements involved two-target configurations and employed 30 time channels. Two stacks, each with 27 repetitions, were used, for a measurement duration of 5.4 s per data point. Some of the targets—the 60-mm, 81-mm, and 105-mm shells from the preceding section—had already been characterized at Vicksburg. A 40-mm projectile was also studied in this run, as were a ferrous ellipsoid and a box of nails to represent clutter.

### 6.3.b Sky Vancouver

Another set of measurements taken by Sky Research staff took place at their Vancouver, British Columbia, location in February and March of 2010. The objects studied in this data run were not actual munitions but a diverse sampling of cylinders of sizes and material properties typical of UXO. Several one- and two-target scenarios were studied, along with attitude configurations similar to the one of Fig. 5.7 and time-on measurements to get a complete picture of the waveform (as presented in Fig. 5.1). An assortment of grids were used during the measurements, the most common being a $7 \times 7$ grid with 15-cm separation, though for the multi-object measurements the favored grid was $7 \times 6$. Unlike previous measurements, these resulted from grids navigated in zigzag, with the instrument moving in the same direction across every transect. A typical measurement included 27 repetitions (for a measurement time of 2.7 s per data point) and contained 35 time channels. In our inversions we discard the first of these.

## 6.4 Topsoil Elevation Profiles

In October 2007 elevation profiles were taken over different types of soils at a field site in West Lebanon, NH. Each soil was built up in a 1 m tall four meter diameter mound, smoothed out the top. MPV data were acquired without using the laser positioning system at successive heights starting at ground level, incrementing by 2 in (blueboard thickness) up to the 36 in in height (see

| Target | ID | $x_0$ (cm) | $y_0$ (cm) | $z_0$ (cm) | $\phi$ (°) | dip (°) | Height |
|---|---|---|---|---|---|---|---|
| 1 | 81-mm | −23.26 | 22.5 | 56.16 | 0 | −18.3 | H1 |
| 2 | 105-mm | −20.26 | 22.5 | 69.14 | 180 | -18.6 | H2 |
| 3 | BLU26 | 0.00 | 22.5 | 41.56 | 0 | 0.0 | H1 |
| 4 | 57-mm | 5.22 | 22.5 | 58.19 | 180 | 306.6 | H2 |
| 5 | 60-mm | 0.00 | 22.5 | 54.02 | 0 | 270.0 | H1 |

Table 2: Correct answers for the blind-test data runs.

Fig. 6.4). The overlaid responses from these 19 measurement over a typical topsoil found in New England is shown in Fig. 6.5. As can be seen from the figure, there was a very little variation in the MPV data as a function of height. For this soil, we concluded that the general shape of the response seen in the figure was due to the instrument and not the soil because the responses are not height dependent.

We then repeated this procedure after placing a 3 in. steel sphere about 5 cm deep midway between receiver cubes No. 1 and 3. The results are shown in Figs. 6.7–6.10. In these figures, lines of greater magnitude indicate that the MPV was closer to the ground in its elevation profile. Asterisks indicate a negative value for the data. These data have also had the background subtracted. Figure 6.10 is provided as a contrast to Fig. 6.8 showing the sign change due to the target being in between the two receivers.

If we assume a time independent noise floor of about $10^{-4}$, then we can calculate the signal to noise ratio as a function of depths and time. Figure 6.11 shows the SNR as a function of depth for a few time gates. It is notable that the MPV can see a 3 in. target at around 80 centimeters deep (up to around 1ms), roughly corresponding to the 11x detection depth goal.

## 6.5 Blind Test Data

### 6.5.a Blind Test Suite 1

Data for our first blind tests consisted of data over 3 spheres (steel, brass, and aluminum, all 3" diameter) and 5 other targets. We collected this data in the parking lot near the CRREL testplots. During the data collection, we employed the laser system for positioning, though we used a grid as a rough estimate when we moved the MPV instrument itself. Data were taken at two heights, separated by 10 cm or two blue board thicknesses. At each height and after acquiring background data, we took a total of 17 measurement in a four by four grid followed by a single shot located precisely on the grid. We used this last data point to define a global coordinate system for each set of 17 data points. The locations and orientation of the five targets are in Table 2. A depiction of the location of the three laser sensors as a function of position during a sample data acquisition run is given in Fig. 6.12.

The data was taken at CRREL without the knowledge or assistance of any of our team at Dartmouth. This data was then handed off to the Dartmouth colleagues as a blind test. The NSMC model was then used to invert for the position and orientation of the target using the total (integrated) NSMC as a discriminant: the targets were classified according to the best match of the total NSMC with that obtained for items in a library constructed from WES test stand data. We also applied our SEA TD model to discriminating between these targets. For particulars of our inversion processing and attendant results, see Section 7.

#### 6.5.b Blind Test Suite 2

A second round of blind testing took place in November 2007. First we acquired 17 data shots at a single elevation for two spheroids, two ellipsoids, and four pieces of frag. These first measurements served as an addition to the signature library. Next, we arranged these items, as well as the spheres and the five UXO we had libraries for already, into 10 configurations. Some of these were multi target configurations, and some were single targets. This data was then provided to the Dartmouth analysts, again for blind tests of inversion capabilities (Section 7).

### 6.6 Dynamic Tests at CRREL

Tests of data acquisition by the MPV in dynamic mode were performed in June 2008. We acquired data over 30 different targets, each placed in turn initially at the same reference location relative to the MPV instrument head. After placing the target next to the MPV, we would lift the sensor and move it around over the target for about 30 seconds, resulting in 300 data points each containing 15 different data traces. Figure 6.13 shows a picture of the initial target placement and equipment set up.

The position of the MPV instrument head as a function of time is shown in Fig. A.2 where the arrows at each location indicate sensor head tilt and orientation. Total time for each target took in total about 2 minutes including the actual acquisition time of 30 seconds. The items labeled H# are scrap items from Former Camp Sibert. This data serves as characterization ("Solution Definition") data for the NSMS and SEA algorithms.

The targets were:

1. Spheroid S2, Nose North (NN)
2. Spheroid A2, NN
3. 20mm, NN
4. Rockeye, NN (thin rod at nose)
5. 81mm, NN
6. H259 label up pointing N
7. H569 label up pointing N
8. Ellipsoid EA-2 flat pointing N
9. Ellipsoid ES-1 flat pointing N
10. H83 NN (thin rod at nose)
11. H854 NN (thin rod at nose)
12. H117 flat (nose up)
13. H571 flat (nose up)
14. Hollow shell 42-029, NN
15. Intact 4.2 in, NN (thin rod at back)

16. Rockeye, Nose North
17. Spheroid S2, 45 deg NE
18. H83, Nose Up (flat)
19. 42-029, Nose East
20. Spheroid A2, Nose East
21. H569, label up pointing East
22. 57-mm, Nose South
23. Intact 4.2 in, Nose South
24. 60-mm, Nose West
25. H117 flat (nose down)
26. 60-mm, Nose 45 deg SE
27. H569, label down pointing South

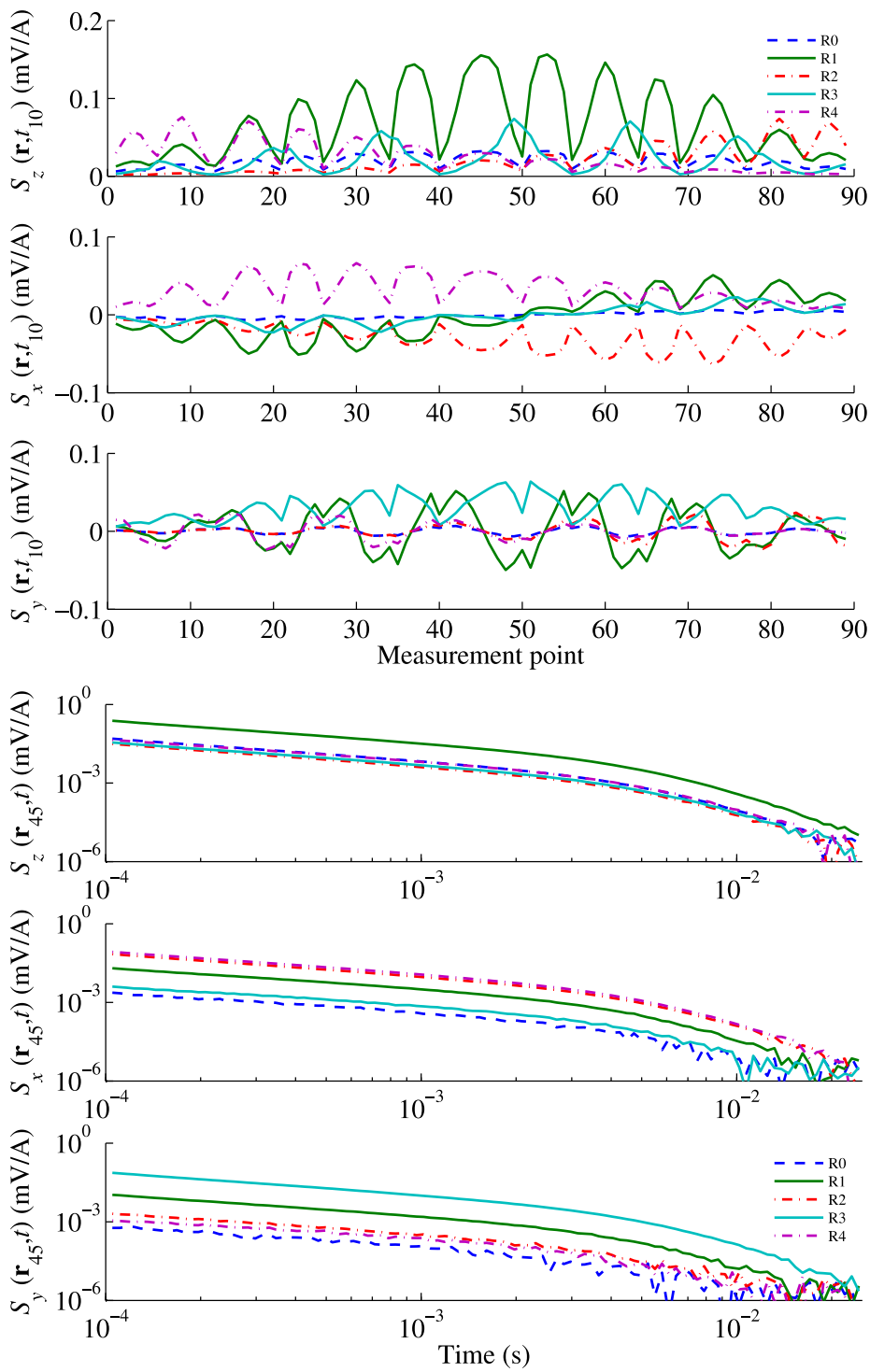


Figure 6.2: Raw data for receivers R0 through R4, taken by the MPV on the test stand in Vicksburg MS, for an upright 81-mm projectile 45 cm below the sensor. Top three: Point-to-point values at the 10th time gate (0.168 ms) in the $z$, $x$, and $y$ directions. Bottom Three: Absolute value of signal at center of the grid vs time.

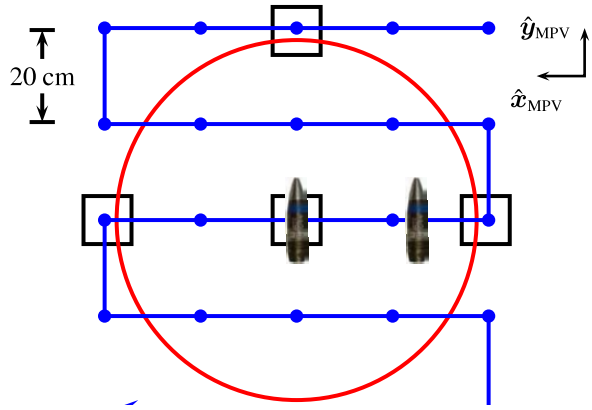


Figure 6.3: Grid for the measurements carried out at Sky Hanover, with a typical setup for two 40-mm projectiles separated horizontally by 25 cm and a schematic outline of the sensor head, for reference.

Figure 6.4: Acquiring an elevation profile over topsoil at field site.

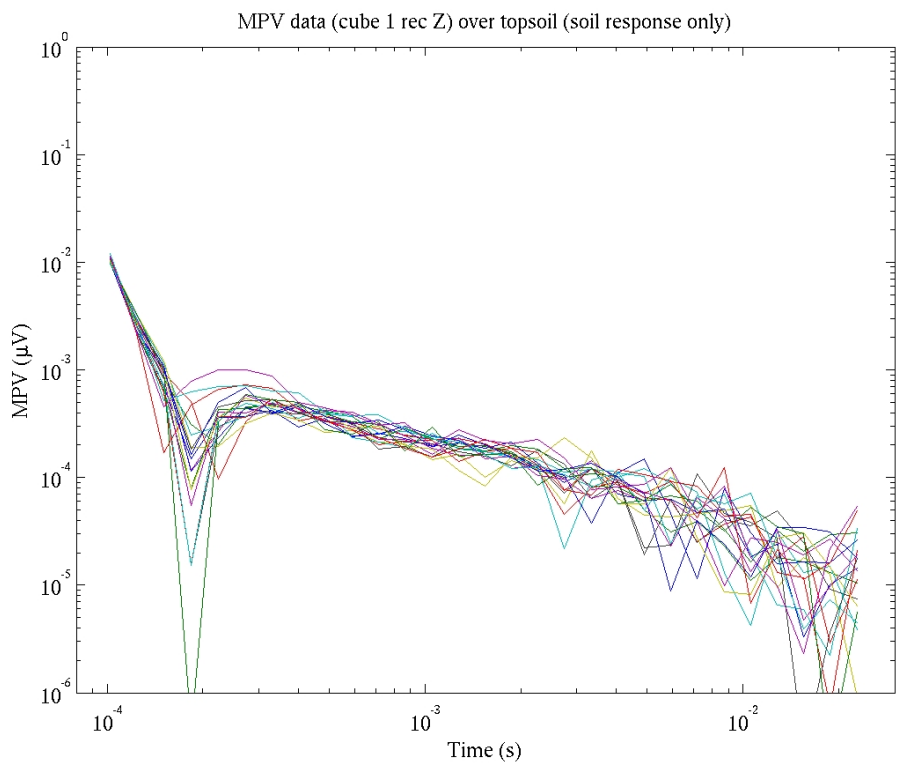


Figure 6.5: Overlaid MPV data from 19 different heights, ranging from 36 inches elevation down to contact with the soil. Shown is the $H_z$ response from cube 1.

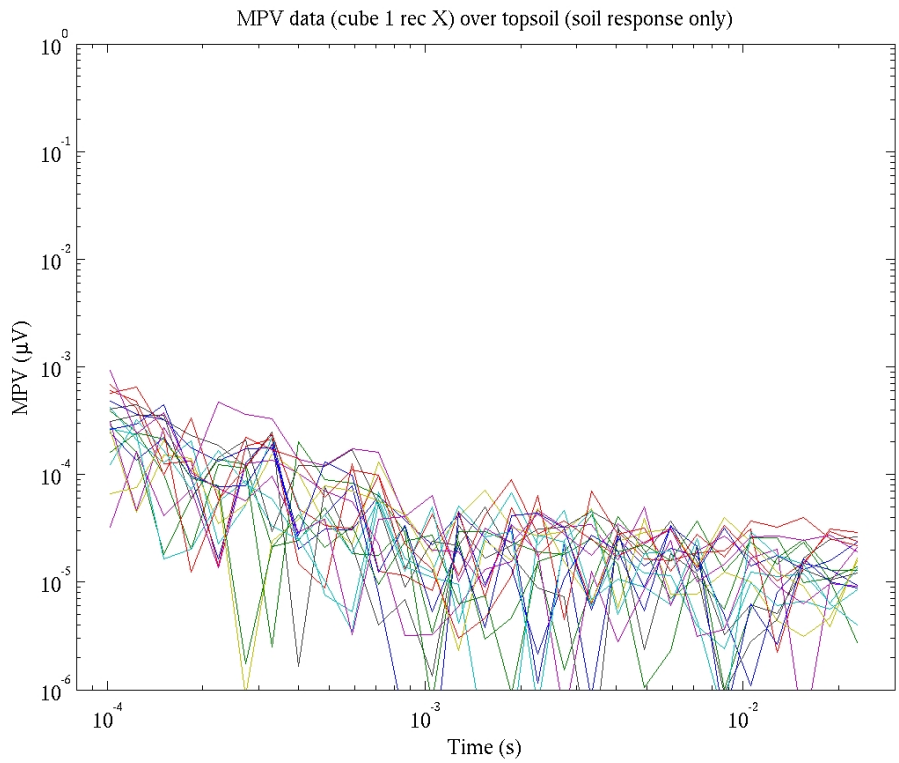


Figure 6.6: Same as previous figure, but showing $H_x$ response from cube 1.

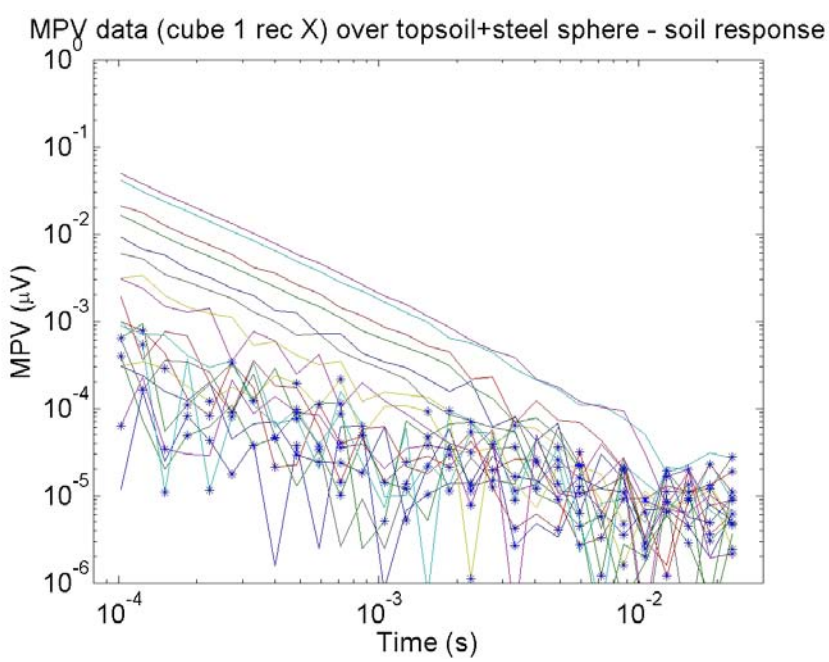


Figure 6.7: Response for sphere in soil for receiver cube 1, x-component, as a function of elevation, background subtracted.

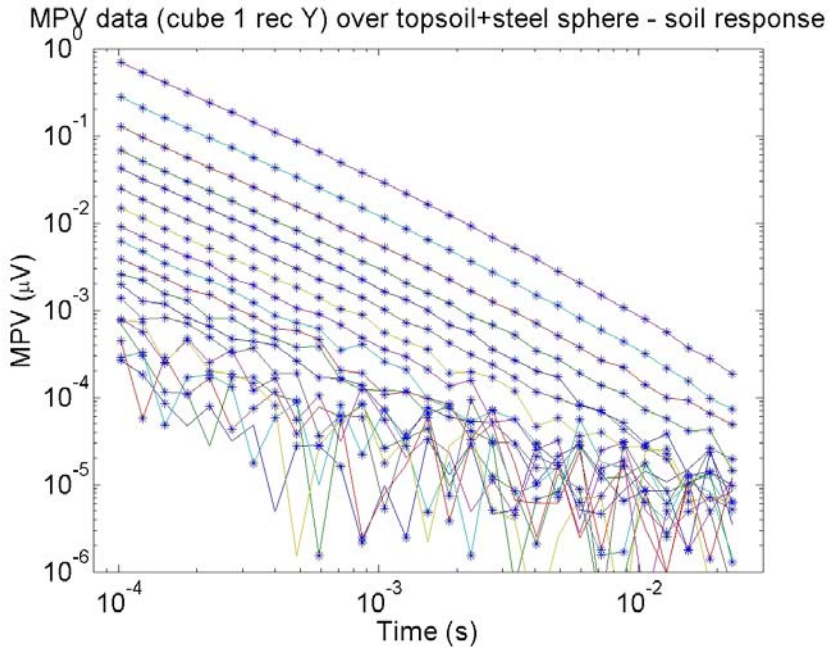


Figure 6.8: Same as previous figure, but for receiver cube 1, y-component.

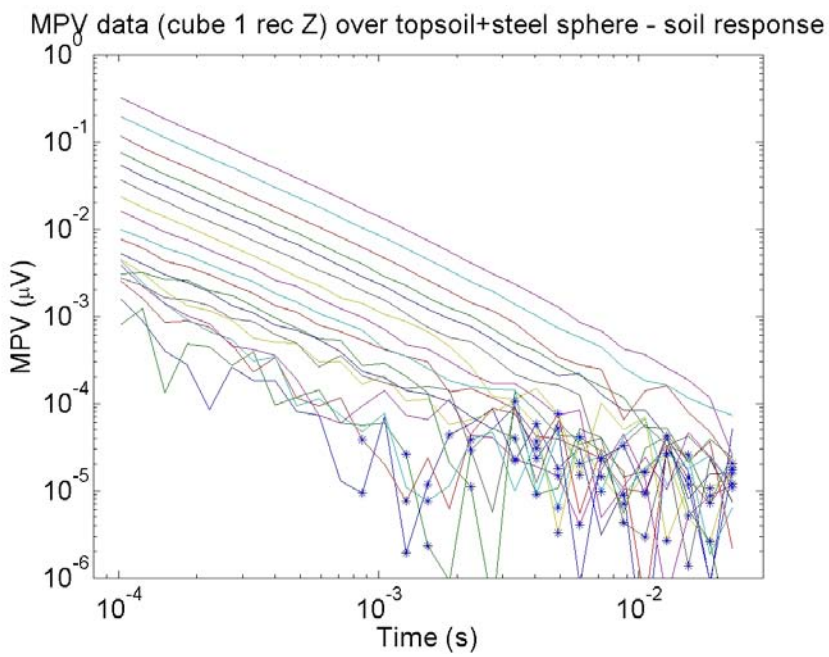


Figure 6.9: Same as previous figure, but for receiver cube 1, z-component.

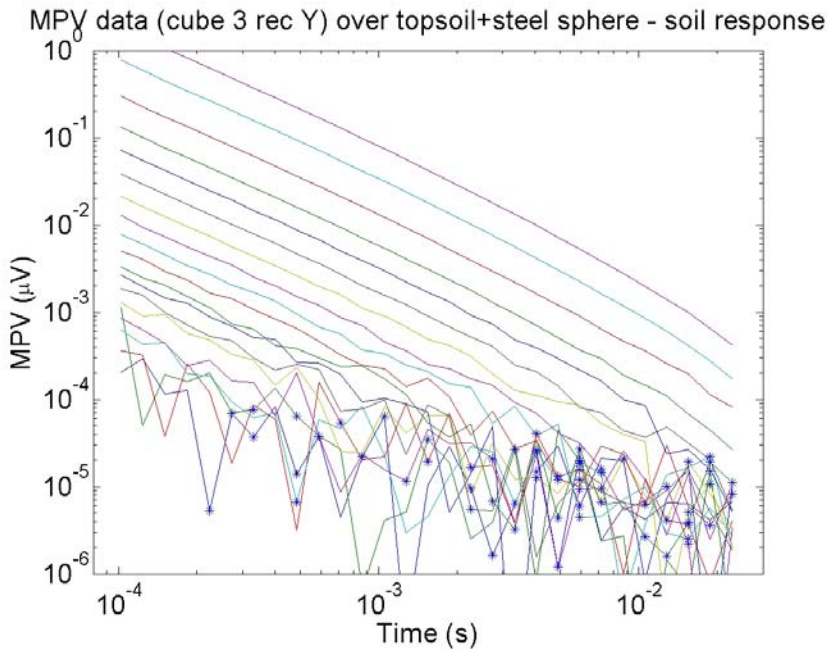


Figure 6.10: Response for sphere in soil for receiver cube 3, y-component, as a function of elevation, background subtracted.

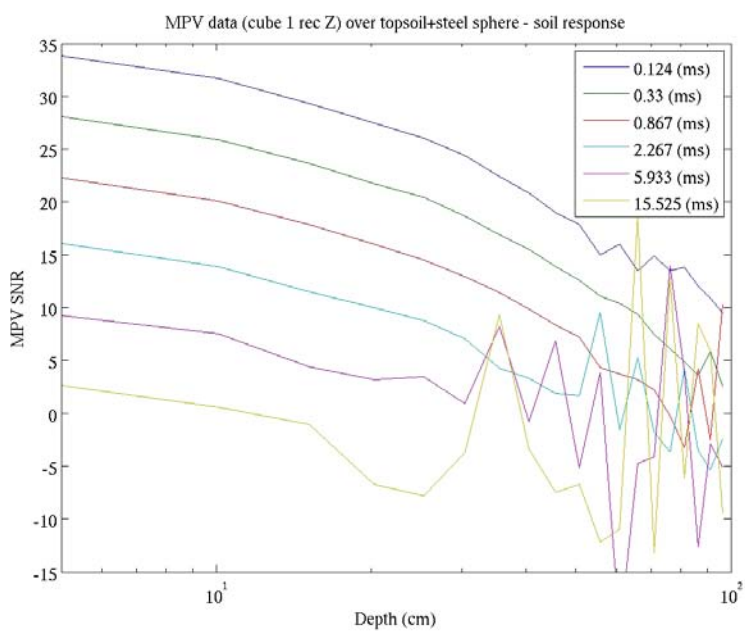


Figure 6.11: SNR (in dB) of the z-component of receiver 1 as a function of depth. Steel sphere was buried 5 cm below ground level (to center).

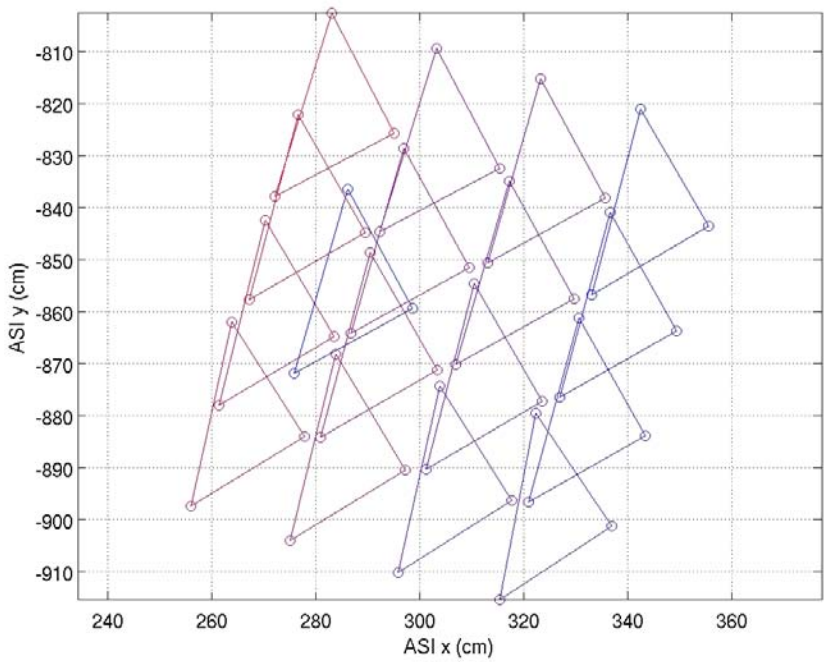


Figure 6.12: Data grid used for collection of 17 point data from CRREL parking lot. Positioning achieved by laser positioning system.

Figure 6.13: 60 mm mortar placed alongside the MPV at the start of dynamic data acquisition.

# 7 Models for Post-processing MPV Data

## 7.1 UXO Identification With the MPV

Signals from the MPV instrument may be modeled and analyzed using a large variety of EMI modeling approaches, including infinitesimal tri-axial dipole models ([36–40]), the Standardized Excitations Approach (SEA, [41–45]), and analytical spheroidal models [46–52]. The Normalized Surface Magnetic Source (NSMS) method, of which the Normalized Surface Magnetic Charge (NSMC) method is a specialization, is particularly noteworthy for its innovativeness, efficiency, and success ([53–60]). Each model yields different parameters that can contribute to the discrimination process; we will investigate the models' performance with respect to the data constraints and the advantages of applying each. The SEA and NSMS models represent a new class of model for high-fidelity descriptions of metallic target responses. They have the important characteristic of having tunable fidelity, i.e. the coarseness of the models is selectable, from a formulation that is basically dipolar in nature to an exact description limited only by the data quality. Dipole parameters correspond roughly to the lowest order SEA or NSMC response coefficients.

We first attempt discrimination using a triaxial dipole model, which has worked well with other instruments, both in the frequency domain and in the time domain [22, 36–39, 61]. This method characterizes the target using a symmetric polarizability tensor [62]. As we shall show (Sec. 7.4), while limited in its physical adequacy, this model can produce good estimates of object location and orientation without computationally demanding searches.

We also adapt the data-derived standardized excitation approach (SEA) [63–65] to the time domain, specifically for the MPV. The SEA incorporates the finite size of the target under interrogation and the fact that a nonuniform primary field may vary significantly over that length scale. It also produces good results when the sensor is so close to the object that additional response moments beyond the dipole become significant, or when the target is large or heterogeneous enough that it cannot be described by a single dipole [40]. In the first, crucial step of the SEA, we decompose the primary field of the sensor into standardized excitation modes. This lets us separate the electromagnetic response of an object from the particulars of position and orientation, these being accounted for by the particular, case-dependent coefficients of the modal expansion. For the most part, we have developed the SEA in the frequency-domain, e.g. [66], in which domain it has been combined with Support Vector Regression [67] to predict the depth of buried UXO [68]. The method has only been adapted to the time domain for one instrument[69] , the Geonics EM63 [28]. Here we formulate and implement it for the new MPV.

We have also developed the Normalized Surface Magnetic Source (NSMS) in the TD, applicable specifically to the MPV. The method provides a faster and more flexible method than the SEA (Sec. 7.3) and appears to offer comparable or better accuracy. Its fundamental innovation lies in the implementation of a "response rule" associated with responding equivalent magnetic sources arrayed mathematically around an object. Using these effectively posits an equivalent object, consisting of these sources. The normalized values of these surface sources provides an archived set of NSMS values for a particular target enables one to compute its possible responses quickly. Perhaps much more important, one can obtain from the distributed NSMS values a simple, unified measure of the object's pattern of response. In particular, one integrates scalar NSMS values over the mathematically enclosing surface to obtain the total NSMS, $Q$, of a target. While still a single (time, frequency dependent) parameter, this reflects the particular heterogeneities of the object better than the simple dipole models. Because it is a characteristic of the object, it can also serve as as a discriminant.

Explanations of the formulation of each model, their implementation specifically for the MPV, and their testing against data appear in the following sections.

### 7.2 Triaxial Dipole Models

A popular and useful model for UXO discrimination replaces the buried target by one or more triaxial point dipoles, either in the frequency domain [36, 37] or in the time domain [38]. The dipole model has been found to fit measured data adequately when bodies are small enough so that the primary field can be assumed uniform along their extent, when they are far enough away from the sensor so that higher moments vanish, and when their composition is homogeneous enough that there are no contrasting signals from different parts of the object [39, 40].

In the dipole model, a given target centered at $\mathbf{r}'$ is considered to respond to a primary field in the manner of a point dipole at that location, of moment $\mathbf{m}$:

$$\mathbf{H}^{\mathrm{sc}}(\mathbf{r}) = \frac{1}{4\pi R^5}\left(3\,\mathbf{R}(\mathbf{R}\cdot\mathbf{m}) - R^2\,\mathbf{m}\right), \tag{7.2.1}$$

which means that the receiver $\mu$ will measure a signal

$$S_{\mu\nu}(\mathbf{r}_j, t_k) = \int_{\mathrm{R}\mu(\mathbf{r}_j)} ds_{\mathrm{R}\mu}\hat{\boldsymbol{n}}_\nu \cdot \left(\frac{\mu_0}{4\pi R^5}\left(3\mathbf{R}(\mathbf{R}\cdot\dot{\mathbf{m}}(t_k)) - R^2\dot{\mathbf{m}}(t_k)\right)\right) \tag{7.2.2}$$

in the $\nu$-th direction, where $\mathbf{R} = \mathbf{r} - \mathbf{r}'$, $\mathbf{r}$ is an observation point, and $R = |\mathbf{R}|$. As required by Faraday's law, we interpret the measured signal as the integration of the time derivative of the secondary magnetic flux density over the receiver loop with normal $\hat{\boldsymbol{n}}_\nu$ over its area; hence the dot denoting time differentiation of the dipole moment. The factor $\mu_0$ relating magnetic field and magnetic flux density is absorbed into $\dot{\mathbf{m}}$. Also hidden in $\dot{\mathbf{m}}$ are any other time-dependent linear operations that the sensor may have carried out on the secondary field.

Perhaps the key assumption in the dipole model is the "response rule," to the effect that the dipole moment of the target is given by the product $\mathbf{m} = \mathsf{B}\cdot\mathbf{H}^{\mathrm{pr}}$, where $\mathbf{H}^{\mathrm{pr}}$ is the primary field generated by the MPV and impinging on the target at $\mathbf{r}'$. The target polarizability tensor $\mathsf{B}$ can be decomposed into an orientation-dependent part and an intrinsic, time-dependent part:

$$\mathsf{B} = \mathsf{R}_d \cdot \Lambda(t) \cdot \mathsf{R}_d{}^{\mathrm{T}}, \tag{7.2.3}$$

where $\mathsf{R}_d$ is the Euler rotation matrix, whose elements are found as part of the optimization. For clarity, one often wishes to align the coordinate system with the principal directions or axes of the target. In this case the rotation matrices become unitary and $\mathsf{B}$ is diagonalized, with its principal values on the diagonal.

It is possible to express the time dependence of the principal polarizability elements $\beta_i$ by using a simple parametrization in a power law combined with an exponential decay[38, 70]:

$$\dot{\beta}_i = k_i\, t^{-b_i}\, e^{-t/g_i}. \tag{7.2.4}$$

We can use the results given by this approximation as a starting guess for the more demanding SEA technique, which we discuss below.

Figures 7.1 and 7.2 show example fits with this model. Curves show signal at a chosen time plotted vs measurement point on the horizontal axis. The blue solid lines represent the measured

data at point $j$, $H^{\text{sc}}_{\text{meas.}}(j)$, while the green solid lines show the predictions of (7.2.1), $H^{\text{sc}}_{\text{model}}(j)$. The red dashed line shows the difference between the two. Each figure contains four plots: In the first plot there are three panels showing gates 1–3, the second plot's three panels show gates 8–10, etc. Figure 7.1 shows the result for the BLU26 bomblet, the smallest object in the collection, whose signal is deluged by noise even at intermediate times. The plots in Figure 7.2 are for the 105 mm projectile, the largest of the objects in our collection, whose signal continues to be clearly discernible at the very end of the measurement. Overall, one notes that the mismatch is relatively small when signals are strong.

Figures 7.3 and 7.4 show the polarizability elements that result from fits such as those in the previous figures. Each plot shows the three dipole moments of the target, sorted in ascending order. In all cases we see that all three elements tend to coincide at very early times but that, for most of the time range considered, one of the elements becomes larger than the other two, which tend to coincide. This is a consequence of BOR symmetry. In each set of two plots, the left one exhibits the results obtained by investigators in blind tests (Multiple curves of the same color indicate results for elevations H1 and H2) . The plot on the right in each pair shows results for the same cases but based on data from the test stand runs. The similarity between the right and left plots for each case is notable.

Further exercises exploiting the inferred polarizabilities also encourage pursuit of the data for discrimination purposes. Plots of magnitudes of axial vs transverse polarizabilities show distinct clustering for 57 mm, 60 mm, 81 mm, 105 mm, and the BLU UXO. Values from blind test cases (Sec. 6.5) fall within the correct cluster for each.

Overall, beyond the virtues or limitations of the model itself, the MPV data shows itself to be consistent with a physically sensible construction involving frequently used parameters; and patterns of those parameters support the pursuit of instrument, data, and models for discrimination purposes.

### 7.2.a Patterns in Dipole Inversions of MPV Data

**7.2.a.(1) Single Target** We first look at some one-target inversions performed on the Vancouver MPV data. In one example, a solid steel cylinder of length 12" (30.48 cm) and diameter 3" (7.62 cm) was placed on a pivot with controllable dip angle. Data were collected on a $7 \times 7$ grid described previously with the cylinder pointing 15°, 30°, 60°, and 75° degrees below the horizontal; this was done for two different target depths. Fig. 7.5 and Table 3 display the results of the inversion for each case, including the reconstructed depth and the unit vector associated with the dominant eigenvalue; the $\hat{\boldsymbol{x}}$ component is always an order of magnitude smaller and is not displayed. (The table also displays the results of two additional measurements carried out at a 45° dip angle.) In all cases the agreement between measured and inverted locations and orientations is reasonable (as we can see from the last column, which displays the percent discrepancies in depth defined by $|h_{\text{meas}} - h_{\text{inv}}|/h_{\text{meas}} \times 100$). The polarizability elements are consistent case to case and show the usual power-law/exponential decay [38, 71]. Two of the elements, the "transverse" ones, are very similar to each other and thus reflect the azimuthal symmetry of the object. Note that there is an ambiguity in the orientation resulting from the cylinder's up-down symmetry. These results, while reassuring, are not wholly unexpected for a geometrically and materially homogeneous object of modest dimensions relative to the sensor and test configuration.

In contrast, we can use the MPV data and our dipole inversion to investigate how the material properties of an object affect its EMI response. Fig. 7.6 shows the responses of two cylinders of

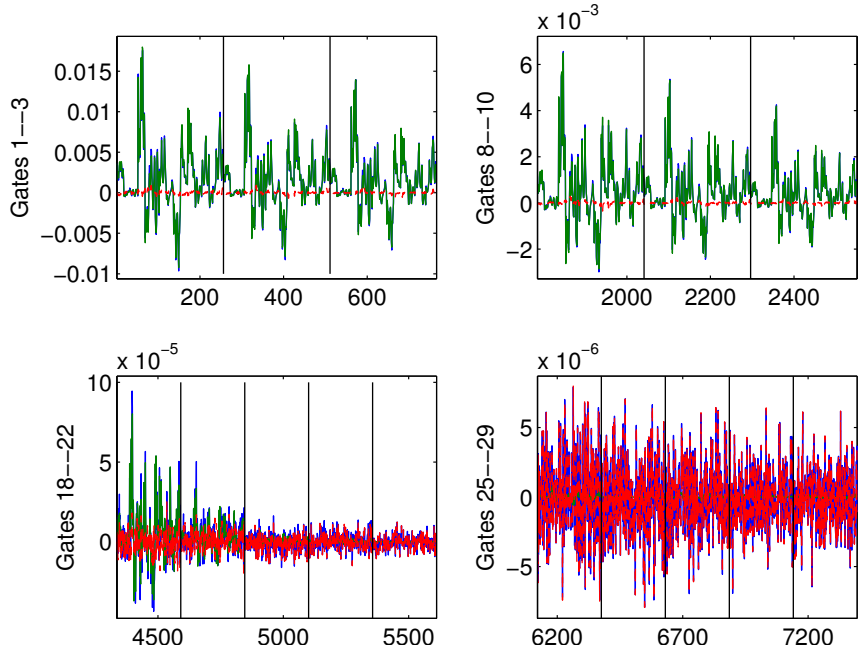


Figure 7.1: Triaxial dipole fit results: BLU26 at H1. Blue line is data, green model, red is mismatch.

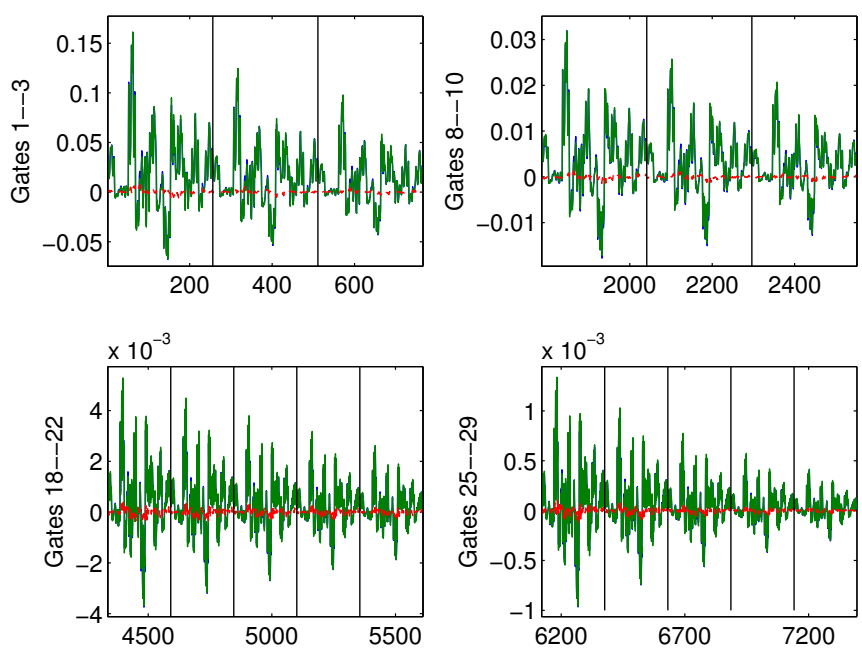


Figure 7.2: Triaxial dipole fit results, as in previous figure, but for the 105-mm at H1.

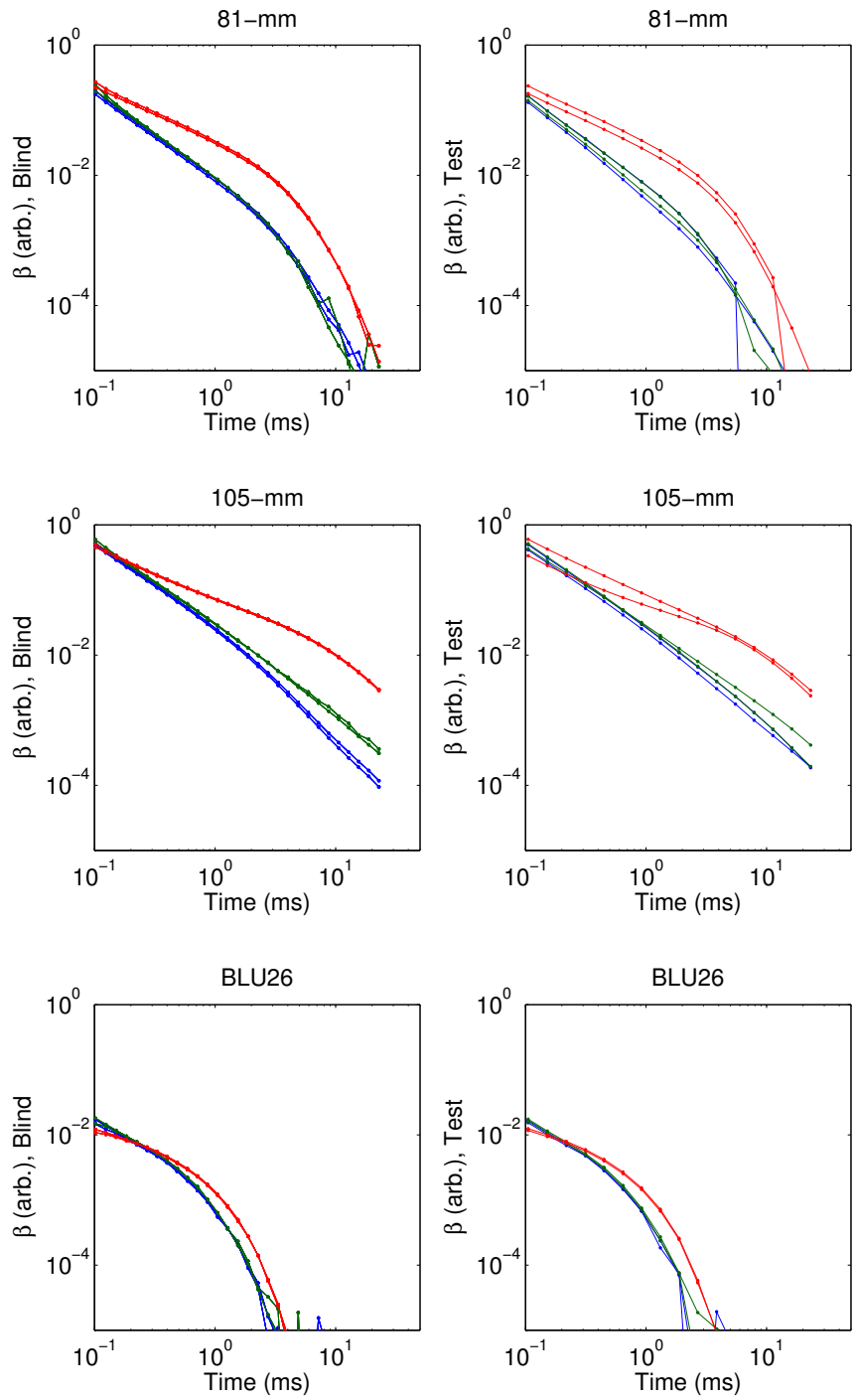


Figure 7.3: Triaxial dipole polarizability results for the 81-mm and 105-mm projectiles and the BLU26 bomblet. In each pair of plots, blind test results are on left, test stand results on right. Multiple lines of same color indicate results from different elevations of the sensor.

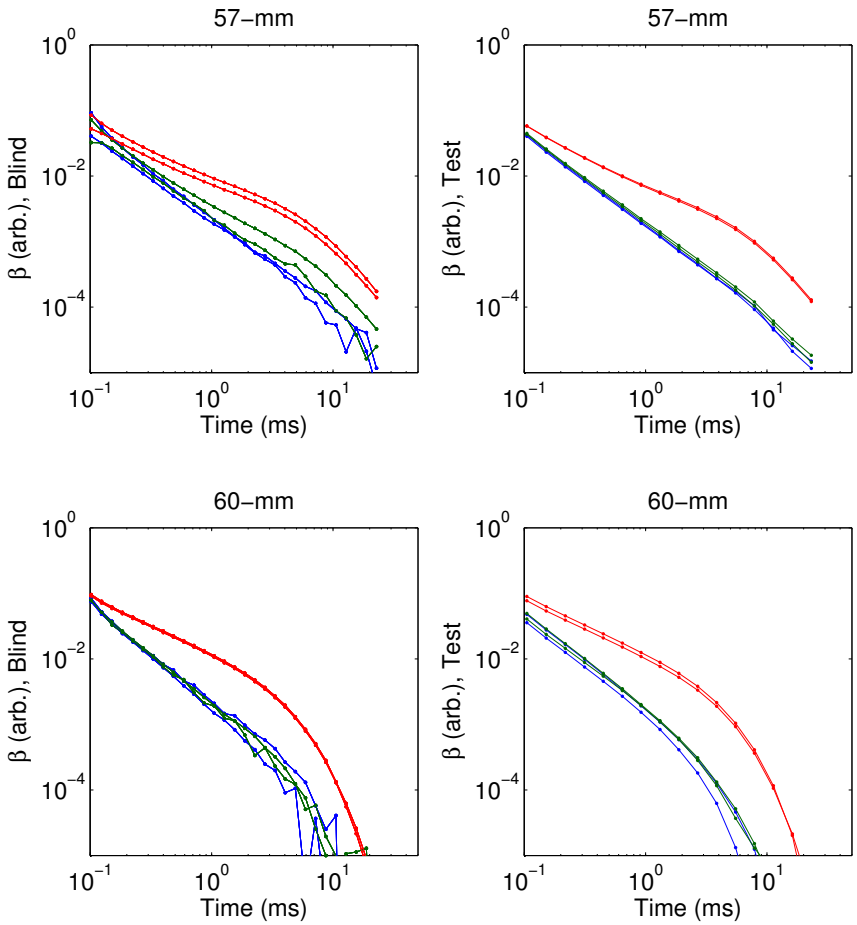


Figure 7.4: Same as previous figure, but for the 57 mm and 60 mm UXOs.

Table 3: Inverted and measured depths and directions of a 12-in cylinder, with percentage depth discrepancy (a small component along $\hat{\boldsymbol{x}}$ is not shown)

| Dip (°) | $\hat{\rho}_{\text{meas}}$ | $\hat{\rho}_{\text{invr}}$ | $h_{\text{meas}}$ (cm) | $h_{\text{invr}}$ (cm) | Discr. (%) |
|---|---|---|---|---|---|
| 15 | $+0.96\hat{\boldsymbol{y}}-0.26\hat{\boldsymbol{z}}$ | $+0.96\hat{\boldsymbol{y}}-0.27\hat{\boldsymbol{z}}$ | 41.18 | 44.24 | 7.43 |
| 30 | $+0.87\hat{\boldsymbol{y}}-0.50\hat{\boldsymbol{z}}$ | $+0.85\hat{\boldsymbol{y}}-0.52\hat{\boldsymbol{z}}$ | 41.80 | 43.26 | 3.49 |
| 45 | $-0.71\hat{\boldsymbol{y}}+0.71\hat{\boldsymbol{z}}$ | $+0.77\hat{\boldsymbol{y}}-0.64\hat{\boldsymbol{z}}$ | 50.69 | 51.75 | 2.09 |
| 60 | $-0.50\hat{\boldsymbol{y}}+0.87\hat{\boldsymbol{z}}$ | $-0.45\hat{\boldsymbol{y}}+0.89\hat{\boldsymbol{z}}$ | 43.90 | 42.66 | 2.82 |
| 75 | $-0.26\hat{\boldsymbol{y}}+0.97\hat{\boldsymbol{z}}$ | $-0.23\hat{\boldsymbol{y}}+0.97\hat{\boldsymbol{z}}$ | 44.99 | 42.96 | 4.51 |
| 15 | $+0.96\hat{\boldsymbol{y}}-0.26\hat{\boldsymbol{z}}$ | $+0.96\hat{\boldsymbol{y}}-0.26\hat{\boldsymbol{z}}$ | 25.18 | 28.01 | 11.24 |
| 30 | $+0.87\hat{\boldsymbol{y}}-0.50\hat{\boldsymbol{z}}$ | $+0.84\hat{\boldsymbol{y}}-0.54\hat{\boldsymbol{z}}$ | 25.80 | 26.78 | 3.80 |
| 45 | $-0.71\hat{\boldsymbol{y}}+0.71\hat{\boldsymbol{z}}$ | $-0.67\hat{\boldsymbol{y}}+0.74\hat{\boldsymbol{z}}$ | 27.19 | 25.50 | 6.22 |
| 60 | $-0.50\hat{\boldsymbol{y}}+0.87\hat{\boldsymbol{z}}$ | $-0.39\hat{\boldsymbol{y}}+0.92\hat{\boldsymbol{z}}$ | 27.40 | 25.33 | 7.55 |
| 75 | $-0.25\hat{\boldsymbol{y}}+0.97\hat{\boldsymbol{z}}$ | $-0.19\hat{\boldsymbol{y}}+0.98\hat{\boldsymbol{z}}$ | 28.99 | 25.72 | 11.28 |

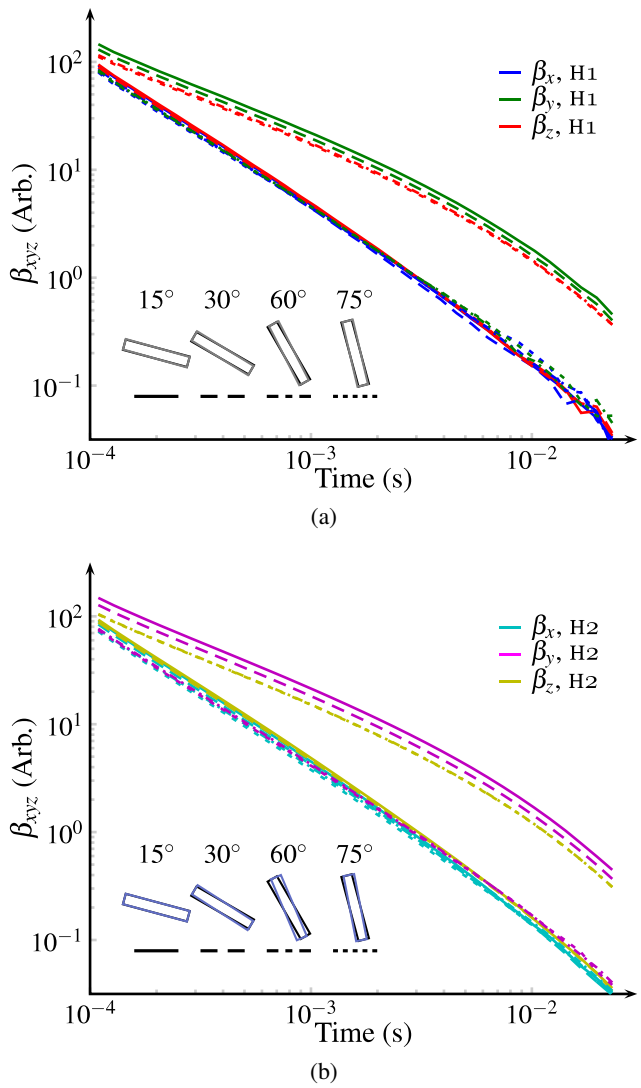


Figure 7.5: Polarizabilities derived from the Vancouver MPV data for a steel cylinder at various inclinations, taken at two depths, (a) and (b). Like the polarizabilities, the tilt angles (black shapes:measured, gray shapes: model predictions) are consistent as inclination changes.

Table 4: Inverted target locations and ground truth for selected Vicksburg measurements

| | Model (cm) | | | Ground truth (cm) | | |
|---|---|---|---|---|---|---|
| UXO | $x$ | $y$ | $z$ | $x$ | $y$ | $z$ |
| 105-mm | 3.94 | 3.87 | 61.71 | 0 | 0 | 60 |
| 105-mm | 3.79 | 3.40 | 42.52 | 0 | 0 | 40 |
| 60-mm | 3.85 | −1.35 | 46.71 | 0 | 0 | 45 |
| 60-mm | 3.52 | −1.78 | 26.85 | 0 | 0 | 25 |

identical size—length 6" and diameter 3"—placed at similar "depths." (Two different experiments, at different depths and dip angles, are shown.) One of the cylinders is made of steel and the other is made of aluminum. Two features of the polarizability elements of nonferrous bodies stand out: ($a$) The longitudinal polarizability element is smaller than the two transverse ones for a nonferrous body, the opposite of what happens with a ferrous object [72]; and ($b$) The polarizability elements of the aluminum cylinder are smaller than those of the steel cylinder by about an order of magnitude. The latter can be explained by the fact that the amplitude of the time derivative of the magnetic flux through the receivers—the quantity measured by the MPV—depends on the material properties of the target in the combination [73] $\sim a/\sigma$, where $a$ is a characteristic length and $\sigma$ is the conductivity. The conductivity of aluminum is $\sigma_{\text{Al}} = 36.9$ MS/m, some six times that of steel, $\sigma_{\text{Steel}} = 5.9$ MS/m [74]. On the other hand, the higher conductivity allows the shallow induced eddy currents to linger on for a bit longer before their eventual exponential decay. This is also clearly visible from the figure.

**7.2.a.(2) Two Targets** Figs. 7.7 and 7.8 show the inverted polarizabilities from some of the measurements taken at Sky Hanover and described in Section 6.3. In both cases a UXO is placed in the field of view of the MPV alongside a full 5-lb box of nails (see Fig 7.8), to serve as clutter. In Fig 7.7 the UXO is a 105 mm shell and in Fig 7.8 it is a 60-mm mortar round; in all cases the munitions are horizontal. Each figure shows two different scenarios, with the box of nails placed 25 and 40 cm away (in the $x$-direction) from the ordnance and at the same depth. The figures show the inverted time-dependent polarizabilities. Multi-target dipole processing is explained in [14].

In all cases the "first" object (solid lines) is readily identified as the corresponding UXO from its decay profile (To confirm this we also plot the polarizabilities inverted from two independent one-target measurements carried out three years before). The largest ("longitudinal") polarizability element of the UXO is $\beta_y$ in every case, consistent with the fact that the munition is horizontal and pointing in the $\hat{\mathbf{y}}_{\text{MPV}}$-direction. The transverse polarizability elements of the first object are again very similar, as expected from a body with azimuthal symmetry. To support the foregoing statements we have included in the figures (as dots) the inverted polarizabilities of the 105-mm and 60-mm UXO in two independent single-object characterization measurements taken over the 89-point grid at Vicksburg (Sec. 6.1). The inverted locations are displayed and compared to the ground truth in Table 4. (The systematic error of almost 4 cm in the $x$-coordinate had already been noted by the researchers who took the data [75].)

The "second" object (shown with dashed lines) produces a signal whose three elements are clearly different. This is to be expected, since the box has much less symmetry than the munitions. The polarizability elements from the second object decay much faster than those of the first, even though at early times they are of comparable magnitude (and can even be larger, as in Fig. 7.8).

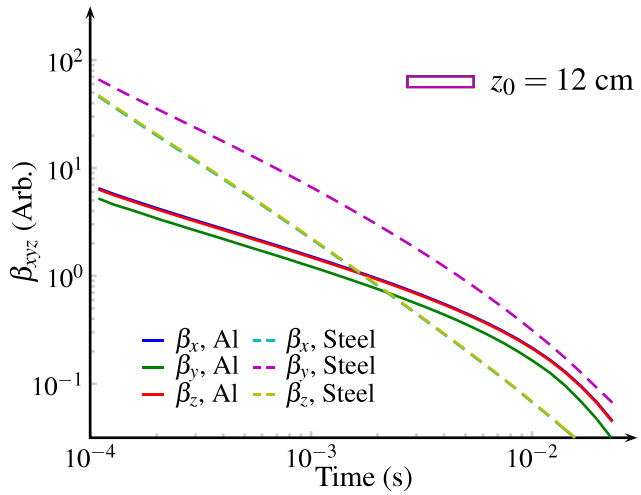


(a)

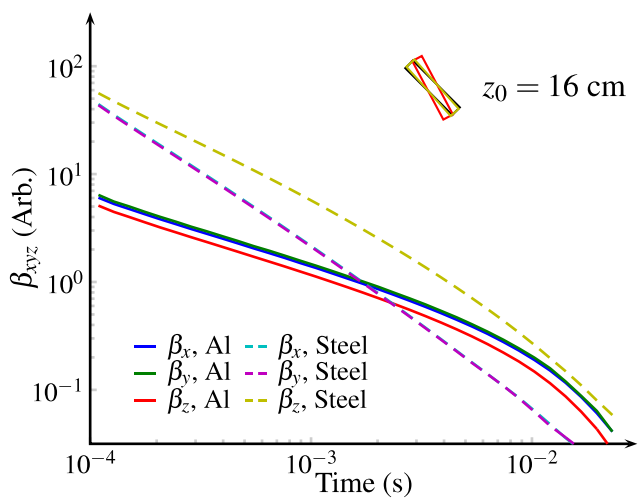


(b)

Figure 7.6: Polarizabilities derived from Vancouver MPV measurements for aluminum and steel cylinders, at two depths, (a) and (b).

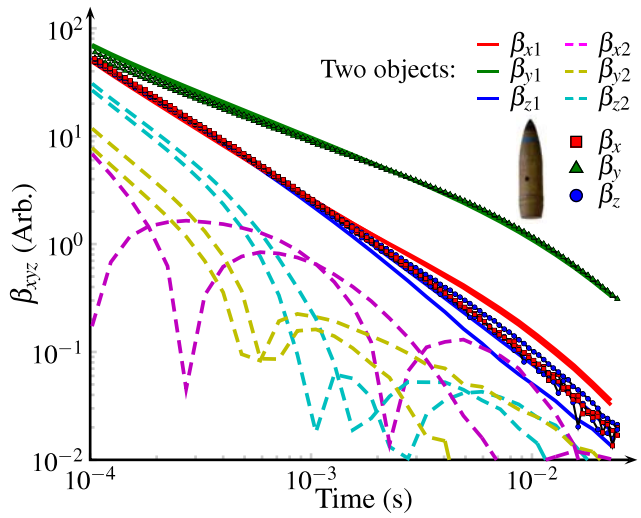


Figure 7.7: Inverted magnetic polarizabilities vs time, extracted from multi-object MPV measurements on a 105-mm UXO and a box of nails, over the $5 \times 5$ grid of Fig. 6.3, for two different box/UXO separations (25 and 40 cm).

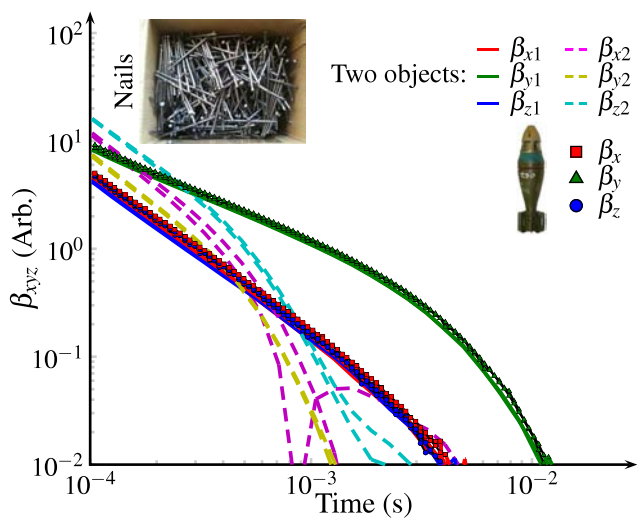


Figure 7.8: Same as previous figure except that here the UXO is a 60-mm mortar.

Table 5: Inverted locations and ground truth for selected Vancouver two-target measurements

| | Model (cm) | | | | Ground truth (cm) | | | |
|---|---|---|---|---|---|---|---|---|
| ID | $z_1$ | $z_2$ | $dz$ | $dy$ | $z_1$ | $z_2$ | $dz$ | $dy$ |
| 45 | 56.5 | 57.9 | 1.4 | 50.0 | 52.5 | 52.5 | 0.0 | 50.0 |
| 67 | 41.8 | 34.2 | 7.6 | 50.0 | 38.5 | 31.0 | 7.5 | 50.0 |

This behavior can be explained using EMI phenomenology [71, 76]: the metal in the box is packed in a loose and highly irregular manner, occupying a fairly large but not compact volume. (Its dimensions are $\approx 11 \times 11 \times 14$ cm$^3$ and its weight is 5 lb or 2.3 kg, which makes it intermediate between the two projectiles. To give a sense of the packing fraction we note that a steel cube of those dimensions would weigh some 30 lb.) At early times, when the eddy currents induced by the sensor are superficial, the response is sizable; later on, as the currents diffuse, they are hampered by the relatively large hollow spaces between the nails and dwindle quickly.

We note that the results are not as consistent measurement-to-measurement for the box as they are for the projectile. (Note in particular the appearance of sign flips.) The fact that the box has sharp corners makes it difficult to model it using a dipole. Also, in this experiment the sensor remained stationary while the targets were moved: the separation between the objects changes from point to point, however minutely, and the uncertainties accumulate; moreover, the nails within the box also move, however imperceptibly, from point to point, which also augments the inversion error. When the objects are placed at different depths, the results deteriorate somewhat for the box but are consistent for the UXO.

For a final example we return to the Vancouver measurements. Fig. 7.9 shows the polarizability elements extracted from two different two-target experiments. The dashed lines represent "Case 45," where two copies of the 6" cylinder studied in Fig. 7.6 were placed 50 cm apart at a depth of 52.5 cm. The solid lines correspond to "Case 67," where one of the 6" cylinders shared the field of view of the MPV with a smaller and thinner cylinder (length 4" and diameter 1.5"). For comparison we have included the polarizability elements of each of the cylinders as inverted from single-target data collected for those objects. The measurements are again quite consistent. Table 5 compares the inverted object locations to the measured ground truth. A small systematic error appears, in that the predicted depth is always slightly larger than the measurements.

We have seen in this section that the MPV provides data of a quality that allows for consistent identification of targets at depth. Using the MPV one can also discern distinct contributors to composite signals from two objects in proximity to one another.

### 7.3 The Standardized Excitations Approach (SEA)

The section above uses a simple point entity to represent the EMI response of geometrically and materially heterogeneous objects. In this section we develop a system formulated in terms of the response of the entire object, including all internal interactions, geometrical and material heterogeneity, near and far field effects. In short, with sufficient care one can include all influences that determine the data without knowing explicitly what those influences are. Having developed the model for a particular object, ideally perhaps taken as representative of a class of objects, e.g. 105 mm projectiles, one can only apply it to that (class of) object, but with relatively fast program execution for arbitrary configurations of object and (the same) sensor. There are ways to use an SEA model that calculates an object's response to one sensor to obtain what would be obtained using

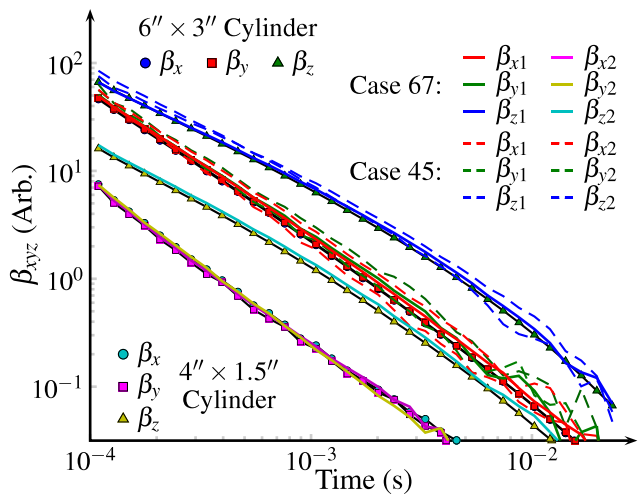


Figure 7.9: Magnetic polarizabilities inverted from Vancouver one-target and two-target measurements. Case 45: two copies of the 6”×3” cylinder from Fig. 7.6. Case 67 (solid lines): one of those cylinders and a smaller one of size 4”×1.5”. Also shown, polarizabilities extracted from single-target data collected for those objects.

another sensor. However we do not pursue that here.

The model rests on use of a set of standardized excitations in the formulation, and hence is called the Standardized Excitations Approach (SEA). At the heart of the method, one defines some set of spatially distributed basic excitations that can be used to describe any EMI primary field. In the mathematical sense, one selects a basis for expressing the primary field. The field transmitted by any of our instruments, impinging on an object in any location relative to it, is expressed as a weighted superposition of these basic excitations. At the heart of the method, one determines the response of the object to a primary field corresponding to a unit magnitude each of these standard excitations. Then, for any (other) particular sensor-object configuration, the complete solution is readily obtained just by superposition: A particular superposition of basic excitations in the primary field produces the same superposition (weighting) of the corresponding responses. We and our co-workers have pursued this in various forms in the frequency domain. The news here is the development and application of the method in the time domain. For details of the method’s development, implementation, and application see [41–45].

Presented as a list of steps, one obtains the SEA model for any particular object and sensor as follows:

1. Select a set of basic standardized excitation fields such that, for any sensor-target configuration, the primary field can be expressed as a linear combination (weighted superposition) thereof;

2. Determine the basic responses of the object, i.e. to unit magnitudes of each of these basic excitations;

3. In any specific case, decompose the primary field into a weighted sum of the basic excitations, then calculate the response with the correspondingly weighted sum of basic responses.

In equations,

1. Select a basis $\{\Psi_j^{PR}(\mathbf{r})\}$ so that at any point in time the primary field may be expressed in terms of it, via the coefficients $b_j$:

$$\Psi^{PR}(\mathbf{r},t) = \sum_j b_j \Psi_j^{PR}(\mathbf{r}) \tag{7.3.1}$$

2. Express the response field over time $\Psi_j^s(\mathbf{r},t)$ to a unit magnitude of each $(j^{th})$ excitation $\Psi_j^{PR}(\mathbf{r})$ as

$$\Psi_j^s(\mathbf{r},t) = \sum_k S_{j,k}(t)\Phi_k^s(\mathbf{r}) \tag{7.3.2}$$

   where the $\Phi_k^s(\mathbf{r})$ are functions that form a basis for the secondary field and the $S_{j,k}(t)$ are parameters to be determined.

3. Construct the ultimate solution, i.e. complete response field as

$$\Psi^s(\mathbf{r},t) = \sum_j b_j \Psi_j^s(\mathbf{r},t) = \sum_j b_j \sum_k S_{j,k}(t)\Phi_k^s(\mathbf{r}) \tag{7.3.3}$$

In practice, coming up with the basis for the secondary field, $\{\Phi_k^s\}$, is not very difficult. For example, if the $S_{j,k}(t)$ are conceived of as magnetic charges arrayed about the target location, then $\Phi_k^s$ is simply the field produced by the $k^{th}$ charge needed to produce the response to a unit value of the $j^{th}$ fundamental excitation. Time dependence enters the formulation through $S_{j,k}(t)$. That is, the $\Psi_j^{PR}(\mathbf{r})$ provide the spatial structure of the excitation field at some reference point in time, e.g. just before Tx current shutoff. The $S_{j,k}(t)$ then track the effect through time of that component of excitation.

As also explained below, once a framework of $\{\Psi_j^{PR}\}$ has been selected, the $b_j$ are readily obtained in any particular circumstances; and, given the $\{\Phi_k^s\}$, the essential calculation resides in determination of the $S_{j,k}(t)$. These fundamental response parameters need be determined only once, as they never change. They are inherent characteristics of the object's response to the sensor being considered. Only the applicable linear combination weights $b_j$ change, case by case, depending on the sensor-object configuration. Computationally, obtaining the SEA model for an object basically means solving (7.3.3), having first obtained real or computed data (left hand side) together with the applicable computed $b_j$ for the corresponding primary field(s). At a given time value, one thus needs a sufficient number of samples of $\Psi^s(\mathbf{r},t)$ to solve for the chosen set of $S_{j,k}(t)$ values. The computational runs in which one obtains the $S_{j,k}(t)$ for subsequent use are termed solution definition (SD) runs.

In passing, we note that the overall SEA procedure is much like what has been done in radar problems for a long time. In that realm, one might determine the response of an object to a collection of unit-magnitude plane waves, each striking the object from a different angle. Any real incident beam can then be constructed by some particular superposition of these plane waves. The scattered field will be a superposition of the responses to each of the constituent waves, according to the same superposition. However in EMI there are no waves. Otherwise put: There has been no immediately obvious way to express arbitrary EMI excitation fields as a sum of basic, universal reference components. So, at least in terms of conceptual challenges, the decisions behind and the execution of the first step above are the most crucial elements of the procedure.

Our investigations have produced different ways to perform effective field decompositions in the EMI realm that are in many ways simpler than those for radar, often requiring fewer terms. One can use various representative distributions of simple magnetic sources surrounding the object contemplated, e.g. fictitious magnetic charges or dipoles, to produce corresponding excitation fields. In this case, $\Psi_j^{PR}$ constitutes the field from a unit or reference magnitude of the $j^{th}$ set of sources, and $b_j$ provides scaling for other magnitudes required for that source (set). Alternatively, one can bypass sources and simply use sets of functions that form a complete basis. In this case, the $b_j$ are simply functional coefficients. Here we choose the latter alternative and proceed in terms of functions that are solutions in spheroidal coordinates to the Laplace equation that governs the primary potential field.

A crucial step here is the recognition that mathematical origin for these functions should be at the target, not at the sensor, ground surface etc. This contrasts with the analogous radar case in which plane waves are used: They may have an origin anywhere (or, loosely speaking, nowhere) with no effect on the formulation. However, being highly non-uniform, spheroidal modes need to be anchored to the object under consideration, to provide both consistency and appropriate detail for complete representation of arbitrary excitations around the target. Spheroidal modes are also chosen simply because spheroidal coordinate systems conform more readily to the kinds of shapes we are interested in, therefore fewer terms will be required.

In application here we exploit the fact that the fields are irrotational. They can be described by a scalar potential that obeys the Laplace equation whose fundamental solution in a prolate spheroidal system ($-1 \le \eta \le 1$, $1 \le \xi < \infty$, $0 \le \phi < 2\pi$) centered at the scatterer is the superposition [77]

$$\Psi_j^{PR}(\mathbf{r}) = \frac{1}{2} H_0 d \sum_{m=0}^{\infty} \sum_{n=m}^{\infty} \sum_{p=0}^{1} b_{pmn} P_n^m(\eta) P_n^m(\xi) T_{pm}(\phi), \tag{7.3.4}$$

where the subscript $j$ here enumerates admissible combinations of $(m,n,p)$. The $P_n^m(\cdot)$ are associated Legendre functions and the $T_{pm}(\cdot)$ are trigonometric:

$$T_{pm}(\phi) = \begin{cases} \cos m\phi, & p = 0, \\ \sin m\phi, & p = 1. \end{cases} \tag{7.3.5}$$

We choose the scale factor $H_0 = 1$. The interfocal distance for a prolate spheroid with semiminor and semimajor axes $a$ and $b$ is $d = 2\sqrt{b^2 - a^2}$; the surface of the spheroid is the set of points $\xi = \xi_0 \equiv 2b/d$. For computational purposes, we choose a value $\xi_0$ to produce a surface surrounding the object so that one may obtain the $b_j$ values by matching the primary field over the corresponding surface. It should be emphasized: the target is not being approximated geometrically as a spheroid. The surrounding surface is only used as a convenient computational construct over which necessary calculations may be performed.

It is easiest to perform the decomposition on the normal magnetic field over the spheroid, employing the fact that

$$H_\xi(\mathbf{r}) = -\hat{\boldsymbol{\xi}} \cdot \nabla \psi(\mathbf{r}) = -\frac{1}{h_\xi} \frac{\partial \psi(\mathbf{r})}{\partial \xi}, \tag{7.3.6}$$

where the metric coefficient

$$h_\xi = \frac{d}{2} \sqrt{\frac{\xi_0^2 - \eta^2}{\xi_0^2 - 1}}. \tag{7.3.7}$$

The orthogonality of the Legendre and trigonometric functions [78] yields

$$b_{pmn} = -\frac{\int_{-1}^{1} d\eta\, P_n^m(\eta) \int_0^{2\pi} d\phi\, T_{pm}(\phi)\, h_\xi H_\xi}{\frac{1}{2}\alpha\pi H_0 d\, \frac{2}{2n+1} \frac{(n+m)!}{(n-m)!} \left.\frac{\partial P_n^m(\xi)}{\partial \xi}\right|_{\xi_0}}, \tag{7.3.8}$$

where $\alpha = 2$ for $p = m = 0$ and $\alpha = 1$ otherwise. Thus, at least after one has computed the integral of the primary field over the spheroid's surface, it can be used in a closed form expression for the primary and secondary field linear combination weights. To compute the integral in (7.3.8) we use for each transmitter coil the exact expression for the field of a circular current in terms of complete elliptic integrals[79] then apply Gauss-Legendre quadrature and the periodic trapezoid rule[80].

In solving for the $b_j$ one must truncate the sequence intelligently and also probably (depending on the case) deal with some ill-conditioning. The latter arises from the fact that typically only a few low modes of excitation will be important. The matter is easily dealt with by common sense in the truncation and by Tikhonov regularization [67, 81]. The same may be said about solution for the fundamental response parameters $S_{j,k}$. In searches, as opposed to direct solutions for the quantities, we also may add a "tradeoff" term to the objective function that reduces overfitting by tempering the norm of the solution vector.

In all cases cited here, the fundamental response parameters are fictitious magnetic charges arrayed in rings around the target location.To obtain these, we first obtain test stand data for targets of interest. After computing the $b_j$ that apply to each sensor/target configuration, one substitutes them into the magnetic field equivalent of (7.3.3), with the test stand data inserted on the left hand side. Having solved for - and stored - the fundamental response parameters, one can deal with any other target-sensor configuration by simply recomputing $b_j$ in accordance with the new primary field values over the target. These are then applied with the archived $S_{j,k}$ in the equivalent of (7.3.3). In target search and discrimination exercises, one speculates on targets and their positions relative to the sensor, then uses these procedures to calculate the signals that would result, for comparison to observations. Alternatively, one can examine the response parameters themselves for the purposes of classifying targets (e.g. [82]). In principle, this is attractive because it can be shown that, for some formulations (such as the one above), the $S_{j,k}$ are unique. That is, a particular EMI response will correspond uniquely to a particular set of these parameters. Any difference in those parameters necessarily implies a different object. At present, computational demands limit the practicality of this approach and we do not pursue it further here.

### 7.3.a SEA Results

The following experiments illustrate TD SEA model validity and, in conjunction with it, prediction/discrimination potential for the MPV. More details on validation and testing of the MPV TD SEA are reported elsewhere [15]. In our first set of experiments we verify the consistency of the model using test stand data exclusively. For all UXOs in the test set, we obtain a complete (temporally and spatially diverse) data set of response measurements at cataloged positions and orientations. Corresponding values of $b_j$ are readily obtained. We then consider each UXO from the list and solve for the values of $S_{j,k}$ in (7.3.3), inserting the target's data in the left side of (7.3.3) from all data runs, save one. Finally, we use the resulting $S_{j,k}$ to predict the field at the depth and orientation of the absent data set and compare the prediction to the actual signal. As an example

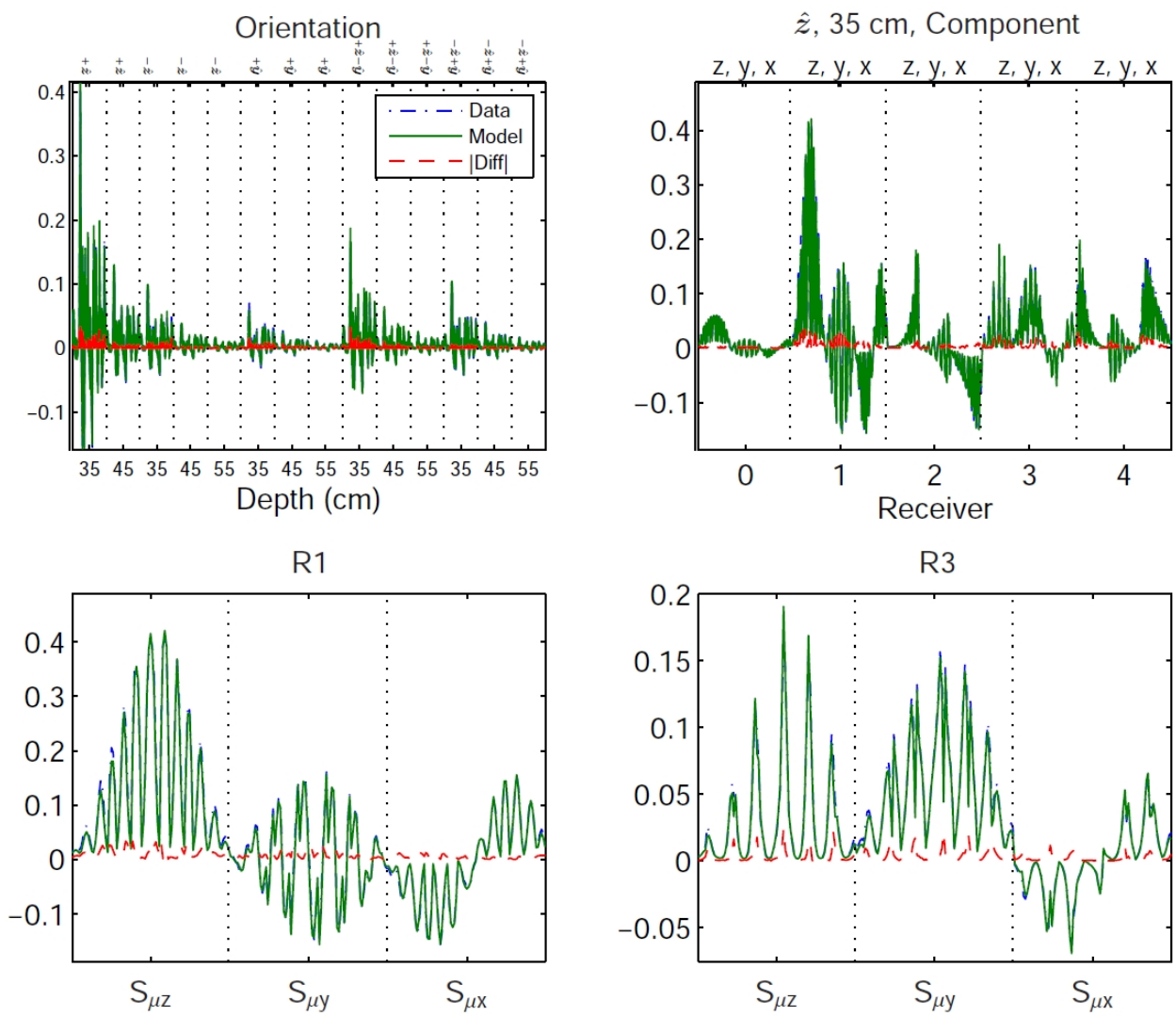


Figure 7.10: Solution definition (SD) data over spatial sweeps at a given time, for the 81-mm projectile including 14 out of 15 test-stand data sets. Top left: original signal (blue dash-dotted line), the SEA reconstructed signal (solid green line), and absolute value of the difference (red dashed line) at t = 0.207 ms. Top right: results for +z-hat target orientation at 35 cm depth. Bottom panels zoom in to show sample results for receivers R1 and R3.

consider the 81-mm munition. The complete test stand data suite for this object contains 15 files comprising three depths (35, 45, and 55 cm) and five orientations (nose pointing toward $+\hat{\boldsymbol{z}}$, $-\hat{\boldsymbol{z}}$, $+\hat{\boldsymbol{y}}$, $+\hat{\boldsymbol{z}}-\hat{\boldsymbol{y}}$, and $-\hat{\boldsymbol{z}}+\hat{\boldsymbol{y}}$). The file corresponding to the UXO oriented toward $+\hat{\boldsymbol{z}}$ at a depth of 55 cm is left out. We use 15 excitation modes and 12 sources for $S_{j,k}$. The number of modes is chosen so that the primary field is reproduced with less than 1% error along a meridian of the surrounding spheroid at $\xi_0$ where sensor and projectile are closest to one another in the SD configuration [83].

Figure 7.10 shows in varying levels of detail the original signal array $\mathbf{S}'$ for the 14th time channel (centered at $t = 0.207$ ms), the signal $\mathbf{S}$ reconstructed via (7.3.3), and the absolute value of the difference between the two, from the SD runs. We note that, given the choices made in

the numerical formulation and the parameter constraints employed, not all portions of the SD are represented as well as these plots might suggest. Next we compare the model prediction to the measured data in the test case that we excluded from the SD. The normalized discrepancy between measured and predicted signal in this example is $[(\mathbf{S}-\mathbf{S}')\cdot(\mathbf{S}-\mathbf{S}')/\mathbf{S}'\cdot\mathbf{S}']^{1/2} \approx 7.0\%$ over all 107 time channels.

In our next experiment we invert test stand data to extract equivalent charge values, i.e. $S_{j,k}$, that we then use to test predictions against subsequently obtained CRREL measurements. As described in Section 6, the CRREL measurements consist of 10 data files: each of the five targets, at a fixed location and orientation, was interrogated at two instrument elevations (H1 and H2 with $\mathrm{H2}-\mathrm{H1} = 10.2$ cm). To extract the SEA parameters we take the complete suite of test stand data for each object, which can include as many as 15 scenarios (for the 81-mm projectile) and as few as 3 (for the BLU-26 bomblet), and invert to find the charge amplitudes. In all cases we use 4 modes and 5 sources, which accelerates the inversion at the expense of some accuracy; we assume the UXO have different enough profiles that it is possible to discriminate between them at that level of precision. For simplicity we also obtain computed signals by approximating the integral of fields over the receiver loop area simply as the product of the field at the center of the receiver times the receiver's area.

For discrimination, for each of these targets we carry out a pattern-matching procedure: Assuming that each target has to be one of the five candidates, the SEA model produces possible responses for each candidate target. An optimization search determines the location and orientation of each candidate that provides the best fit to the test data, and the goodness of observed and calculated signal match is examined. The candidate target that produces the smallest misfit we take to be the target in question. In the optimization we minimize the objective function

$$\mathrm{Obj} = (\mathbf{S}-\mathbf{S}')\cdot(\mathbf{S}-\mathbf{S}') \tag{7.3.9}$$

using a subspace trust region Newton method [84]. The implementation allows the user to impose bounds on the parameters, and we take advantage of this feature: taking the calibration point as the origin in each case, we constrain the $x$-position of the UXO to lie between $-30$ and 30 cm, the $y$-position between $-10$ and 50 cm, and the depth between zero and 70 cm. As starting guesses we use the results of the triaxial dipole searches carried out on each file. We use all measurement points, directions, receivers, and time gates; each data file thus contains $17\times 15\times 29 = 7395$ points.

Figure 7.11 shows the results of fits for the CRREL targets at H1. The point-by-point differences between the recorded and (best) predicted signals changes noticeably from candidate to candidate. By inspection one can generally infer the correct target. To express this quantitatively, we compute

$$\mathrm{Confidence} = \left[1-\left[\frac{(\mathbf{S}-\mathbf{S}')\cdot(\mathbf{S}-\mathbf{S}')}{\mathbf{S}'\cdot\mathbf{S}'}\right]^{1/2}\right]\times 100 \tag{7.3.10}$$

as a figure of merit. This quantity is defined so it is 100% for a perfect match and decreases as the discrepancy between measured and modeled data increases. Figure 7.12 shows the figures of merit for all 10 CRREL files. The method predicts correctly for both elevations that Target 1 is the 81-mm munition and that targets 3 to 5 are respectively the BLU-26 bomblet, the 57-mm projectile, and the 60-mm mortar. The second target (the 105-mm projectile) is barely identified correctly relative to the 81-mm though it distinguishes itself more clearly from the other items. This may be due to the small number of configurations in which the 105 mm, a large and complex object,

was interrogated: we had only six SD cases for it, compared with 15 for the 81 mm. In any case, the results show that the probability of the correct target in fact being the 105 is quite high within the field of candidates. Examination of data and SEA predictions for position and orientation also shows that they are quite consistent for the most part, including the 10-cm gaps in $z_0$ due to the shift in instrument elevation.

#### 7.3.b Conclusion

In this project we have adapted the data-derived Standardized Excitation Approach to handle the mono/multistatic time-domain data generated by the MPV sensor. The calculations must address inherent challenges in the data analysis due to the vector character of the detected signal and the high level of detail with which the sensor can measure time decays. These arise regardless of the forward model one uses for detection, identification, and discrimination.

Particularly when the fundamental response coefficients for an object are obtained from appropriate data, the SEA model is "physically complete." This rests on the belief, easily substantiated, that both the formulation and reality contain only MQS fields, the physics of which is very well defined and readily quantified. Any and every detectable factor and effect will be included in the model's predictions. This is because the model user begins by exploiting information pertaining to locations closest to the object, to obtain the fundamental response parameters. Cases beyond the solution definition ones will simply involve following the same collection of fundamental response fields, in appropriate combinations, to more distant points. Whatever entered into the picture closest to the target (SD runs) will necessarily be extended to more distant points, where higher order effects generally fade in any case. The only approximations involve discretization and truncation of series, which can be performed rationally, with appropriate safeguards and checks. By concentrating first on the most demanding near field during SD, one inherently addresses requirements that represent an upper bound on the those that will apply to subsequent calculations.

We have seen that the combination of sensor and method provides consistent estimates for the location and orientation of a set of targets and can discriminate between the different objects, though we note that the discrimination ability is not perfect at this point. This may be a consequence of a) insufficient SD data, as mentioned above; b) loss in accuracy in very low order quadrature in integrals of fields over the Rx surfaces; and c) by performing the inversion with a smaller set of modes and sources in order to make the optimization tolerably fast. These and other factors result from choice of computational convenience and strategy, which can be upgraded.

The material above indicates that the MPV TD SEA can be used for forward modeling in inversion and classification codes that draw upon a library of known ordnance types for signal pattern matching. Upgrading to more thorough treatment of some aspects, such as responding equivalent source type and distribution, tends to increase computational demands, e.g. execution time. This may limit model usefulness for real-time application and could lead to rather long time requirements even for non-real-time post-processing.

We have shown elsewhere (e.g. [82]) that in some SEA formulations one can use inferred SEA response parameters as a basis for rigorous discrimination, as opposed to performing pattern matching of data against fields predicted by the SEA. While in some ways this goes more to the '"heart of the matter" in terms of identifying an object's particular response, it is at this time relatively laborious, challenging, and little tested. Our present recommendation for parameter based discrimination is to pursue NSMS instead (Sec. 7.5). The latter becomes more flexible and efficient by adding to the SEA framework a "response rule." This generates a particular kind of

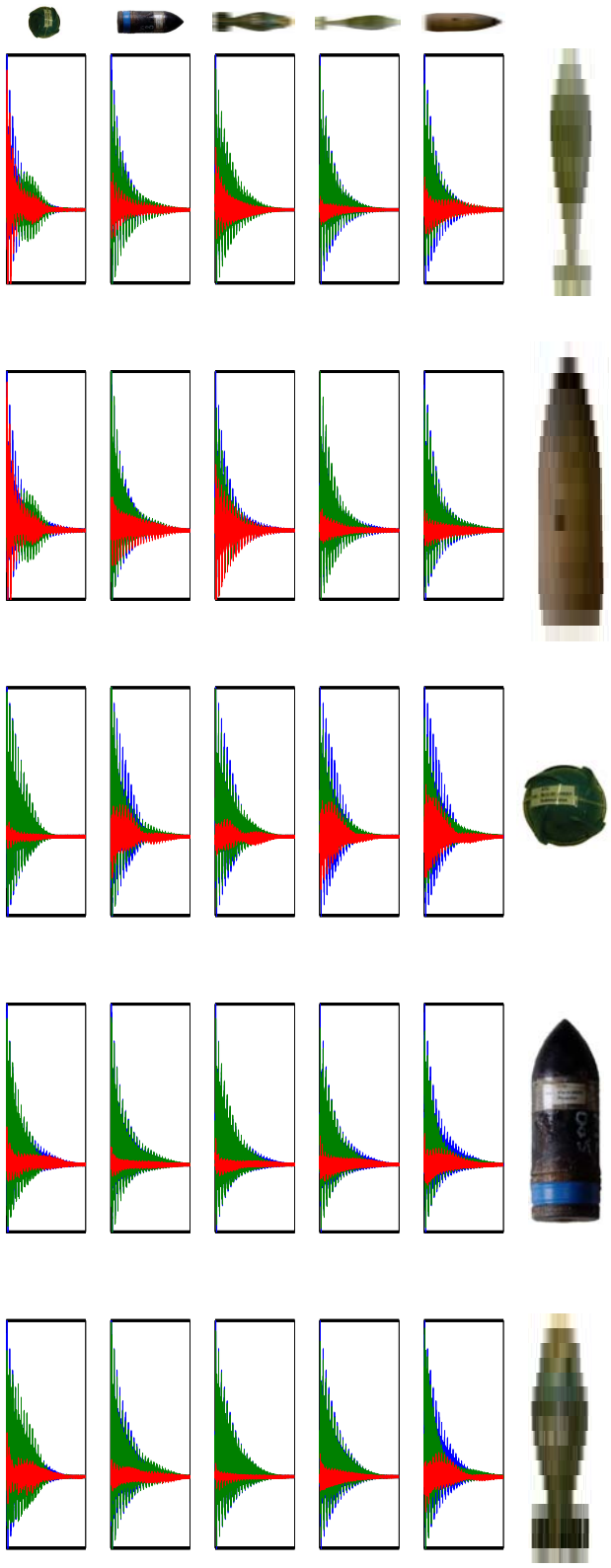

Figure 7.11: Signals and mismatches between data and SEA model output, for optimized locations and orientations for each target in the CRREL test, at a single elevation. Blue line is data, green line prediction, red is mismatch.

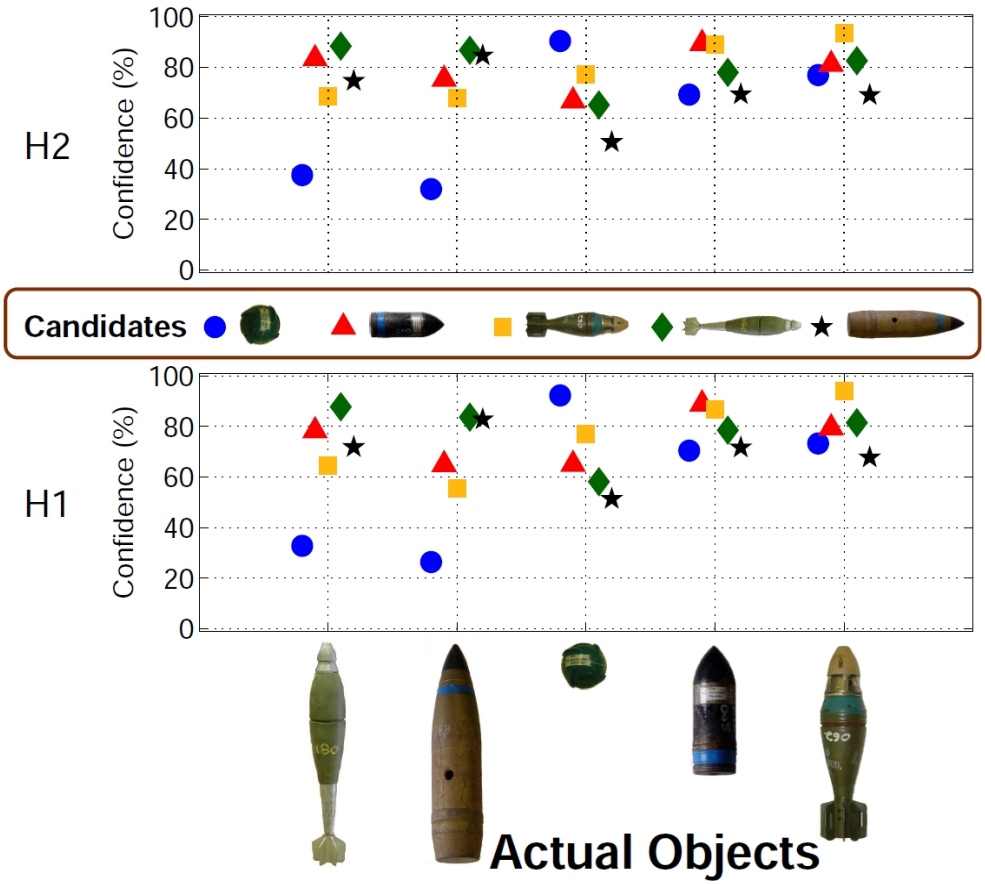


Figure 7.12: Figures of merit (confidence), defined in (7.3.10), for the ten CRREL scenarios (5 targets, two elevations). The data-derived SEA identifies the targets correctly in all cases except one, being a close second for the 105-mm UXO at H2.

responding equivalent sources around the target that are easily calculated in specific instances and which, in their sum, reflect the character of the object.

Finally, we note that somewhat more sophisticated formulations of the TD SEA may be developed, with possible increases in computational efficiency. For example, the "generalized SEA" [85] provides perhaps a more natural characterization of a magnetic scatterer in terms of radial dipole sources rather than charges. In this version of the model it is unnecessary to enforce the vanishing of the total charge, as is required by the divergence free MQS fields. Moreover, if one uses the vector potential instead of the magnetic field, the double integration over the receiver area becomes a line integral, decreasing (though not dramatically) the computational effort [12, 86].

## 7.4 HAP for Object Location Without Search

In order to classify subsurface metallic objects using the digital geophysical data, the object's location and orientation first typically need to be determined. In EMI, the primary magnetic field penetrates inside a metallic object to some degree and induces eddy currents/magnetic dipoles within it. These induced magnetic dipoles then produce a secondary or scattered field outside the object that is measured by a receiver. Representing the target's response in the lowest order,

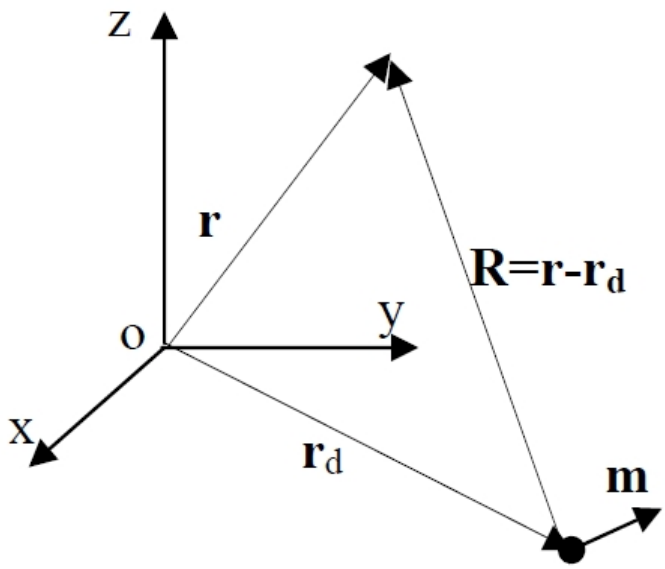


Figure 7.13: A magnetic dipole at $\mathbf{r}_d$, representing the target, and associated geometry.

i.e. using a single magnetic dipole, the magnetic field **H**, scalar $\psi$ and vector **A** magnetic field potentials can be written as ([79]):

$$\mathbf{H} = \frac{1}{4\pi R^3}\left(\frac{3\mathbf{R}(\mathbf{R}\cdot\mathbf{m})}{R^2} - \mathbf{m}\right) \tag{7.4.1}$$

$$\psi = \frac{(\mathbf{R}\cdot\mathbf{m})}{4\pi R^3} \tag{7.4.2}$$

$$\mathbf{A} = \mu_o \frac{(\mathbf{m}\times\mathbf{R})}{4\pi R^3}, \tag{7.4.3}$$

where **R=r-r**$_d$ , and the vectors **r** and $\mathbf{r}_d$ are the observation and source/dipole's location vectors respectively (see Fig. 7.13). Taking [Eq. (7.4.1)]·**R** and using (7.4.2) it can be shown that:

$$\mathbf{H}\cdot\mathbf{R} = \frac{1}{4\pi}\frac{1}{R^3}\left(\frac{3\mathbf{R}(\mathbf{R}\cdot\mathbf{m})}{R^2} - \mathbf{m}\right)\cdot\mathbf{R} = 2\frac{(\mathbf{R}\cdot\mathbf{m})}{4\pi R^3} = 2\psi \tag{7.4.4}$$

Similarly, upon taking [Eq. (7.4.1)]×**R** and using (7.4.3), we have

$$\mathbf{H}\times\mathbf{R} = \frac{1}{R^3}\left(\frac{3\mathbf{R}(\mathbf{R}\cdot\mathbf{m})}{R^2} - \mathbf{m}\right)\times\mathbf{R} = -\frac{[\mathbf{m}\times\mathbf{R}]}{R^3} = \frac{-\mathbf{A}}{\mu_o} \quad . \tag{7.4.5}$$

Now, taking **H**×[Eq. (7.4.5)] gives

$$\left[\mathbf{H}\times\frac{-\mathbf{A}}{\mu_o}\right] = \mathbf{H}\times[\mathbf{H}\times\mathbf{R}] = \mathbf{H}(\mathbf{H}\cdot\mathbf{R}) - \mathbf{R}|\mathbf{H}|^2 = 2\mathbf{H}\psi - \mathbf{R}|\mathbf{H}|^2 \tag{7.4.6}$$

From (7.4.5) we can solve for **R**

$$\mathbf{R} = \frac{2\mathbf{H}\psi + [\mathbf{H}\times\mathbf{A}/\mu_o]}{|\mathbf{H}|^2} \tag{7.4.7}$$

Under the assumption that of a single dipolar source, the dipole's location vector **R** can be expressed in terms of only three global secondary field quantities and is independent of the frequency or time. The magnetic dipole moment can be found by taking $\mathbf{R}\times$[Eq. (7.4.3)] and using (7.4.2)

$$\mathbf{m} = 4\pi R\left(\mathbf{R}\psi - [\mathbf{A}/\mu_o \times \mathbf{R}]\right) \tag{7.4.8}$$

where **R** is determined from Eq. (7.4.7) (see Fig. 7.13). Because the quantities sought are expressed in terms of **H**, **A**, and $\psi$, we term the method the HAP. For more details, see [87–90].

Note that for an isolated dipolar source, only a single instance of **H, A**,and $\psi$ is needed to uniquely determine **R** and **m**. At the same time, one must indeed obtain all three of these quantities at a point to execute the calculation. However our sensors measure only (a quantity proportional to) **H**. While subsequent to this work more efficient methods were developed, here collections of fictitious sources are inferred that correspond to the observed **H** and then provide all other details of the field, including **A**,and $\psi$.

The MPV can be seen as a mixed mono/multi-static sensor. That is, when the sensor is at a given location, it takes spatially distributed samples of a single secondary field (multi-static measurement), by virtue of its array of vector receivers . However, as the device moves, it records data pertaining to distinct and different secondary fields, each corresponding to a different excitation of the target. To the extent that the Rx units are attached to the Tx, move with it, and record signals around it, this is tantamount to monostatic sensing. For the purpose of reconstructing the potential fields corresponding to **H** at a point, the underlying monostatic nature of the device dominates the considerations: One cannot continue the **H** field around a measurement point by inferring a collection of sources such as would apply in traditional analytic continuation or in the SEA system presented above, both of which apply to single, spatially distributed fields. Instead, one must infer a distribution of fictitious sources that serve as a synthetic responder equivalent to the object. These sources must respond as the object does to a variety of excitations, with observations of each response limited to only a few points. To deal with this, one can employ here a variant of the Normalized Surface Magnetic Source (NSMS) system, which is explained in the next section.

In the NSMS as normally applied, one proceeds by hypothesizing equivalent sources around or even within a surface that encloses the responding object. As in the single dipole model, these respond in proportion to the local intensity of the primary field that impinges on them. They are determined so that, collectively, they respond as the overall object does. However, to proceed in that way one must know the object location, which is precisely what we are trying to estimate here. The solution applied here was to assume a distribution of dipole responders over a flat layer located according to convenience between the object and the sensor. Thus here we construct an "equivalent object" consisting of a flat plane instead of (e.g.) an enclosing spheroidal surface/volume at some specific subsurface location. Alternatively viewed, the planar source distribution "encloses" the responding object (entire subsurface half space and target it contains), with negligible source magnitudes required in distant locations and depths. See e.g. [87]. While computing the NSMS-based HAP is somewhat involved in that, using more or less all of the data, one must infer an entire 2-D array of equivalent sources, it is also efficient in that one need only do that once to obtain separate object position estimates from all data points.

An alternative method for inferring **A**,and $\psi$ around a data point that is efficient and in some ways more direct involves differencing **H** values between nearby points. To do this one takes the gradient of

$$\mathbf{H}\cdot\mathbf{R} = 2\psi \tag{7.4.9}$$

This produces an equation only in terms of **H** and its derivatives, which can be solved for $\mathbf{r}_d$. Exploitation of the divergence-free, curl-free nature of **H** allows one to express some **H** derivatives in terms of others, further simplifying the computations. As only the NSMS method was employed in the results of this project, we do not pursue the derivative based method further here.

The comparisons between inverted (Table 7) and true values (Table 6) for position and orientation of the CRREL data set objects (Sec. 6.5) show that the predicted values in general are very close with true values. In some instances values flip or are arbitrary, without error contribution, because of symmetries.

| Target | ID | $x_0$ (cm) | $y_0$ (cm) | $z_0$ (cm) | $\phi$ (°) | dip (°) |
|---|---|---|---|---|---|---|
| 1 | 81-mm | −23.26 | 22.5 | 56.16 | 0 | −18.3 |
| 2 | 105-mm | −20.26 | 22.5 | 69.14 | 180 | −18.6 |
| 3 | BLU26 | 0.00 | 22.5 | 43.21 | 0 | 0.0 |
| 4 | 57-mm | 5.22 | 22.5 | 51.45 | 180 | 306.6 |
| 5 | 60-mm | 0.00 | 22.5 | 54.50 | 0 | 0.0 |

Table 6: Correct answers for CRREL blind-test data runs.

| Target | ID | $x_0$ (cm) | $y_0$ (cm) | $z_0$ (cm) | $\phi$ (°) | dip (°) |
|---|---|---|---|---|---|---|
| 1 | 81-mm | -21.2 | 23.6 | 56.56 | 0 | −2 |
| 2 | 105-mm | - 6.0 | 23.7 | 67.57 | 170 | −20.8 |
| 3 | BLU26 | 0.25 | 21.8 | 47.55 | *0 | *180 |
| 4 | 57-mm | 0.75 | 21.6 | 58.19 | 0 | 320.4 |
| 5 | 60-mm | 0.67 | 19.3 | 54.02 | *3 | 0 |

Table 7: NSMS model inversion results for position and orientation for CRREL blind test data. Numbers with an asterisk are arbitrary due to BOR considerations.

### 7.5 The Normalized Surface Magnetic Source (NSMS) System

The Normalized Surface Magnetic Source (NSMS) method has been developed to provide a faster and more flexible method that the SEA (Sec. 7.3) or the generalized SEA [89]. It appears to offer comparable or better accuracy while faithfully representing a target's response. Its fundamental innovation lies in representing the target by using distributions of a particular kind of magnetic equivalent source over a surface mathematically enclosing the object. At the heart of the method, a "response rule" is associated with these sources. This connects the impinging primary field to the specific intensity of each responding source. Having inferred the value of each surface source entity that applies to excitation by a unit value of the primary field (i.e. the "normalized" source value), one can then compute responses for any other intensity of excitation by simple scaling.

An archived set of NSMS values for a particular target enables one to compute its possible responses quickly and thus perform the kind of pattern matching discrimination that was displayed in Sec. 7.3. Perhaps much more important, one can obtain from the distributed NSMS values a simple, unified measure of the object's pattern of response. In particular, one integrates scalar NSMS values over the mathematically enclosing surface to obtain the total NSMS, $Q$, of a target. While still a single (time, frequency dependent) parameter, this reflects the particular heterogeneities of the object better than the simple dipole models. Because it is a characteristic of the object, it

can also serve as as a discriminant. $Q$ may be parametrized by a Pasion Oldenburg type model and/or combined with other parameters, for example from the dipole model, in order to further characterize a target and classify it based on its EMI response[88].

When extracting $Q$ from controlled data for the purpose of model development, the location of the target is generally known *a priori*. However, when the target's position and orientation are not known, then inverse algorithm has to combine inversions not only to determine which target is present, but where that target is. This is a combination of a linear and nonlinear processes and is often time consuming. To this end, we apply the HAP method (Sec. 7.4) to estimate object location and orientation very quickly. Then, using this information at least as a first order estimate, one can then quickly perform the linear process of solving for the NSMS values. Assuming applicability of the HAP, in what follows we concentrate on the NSMS formulation, implementation, and application for object characterization, without emphasis on its possible role for locating a target.

### 7.5.a Concepts and Formulation

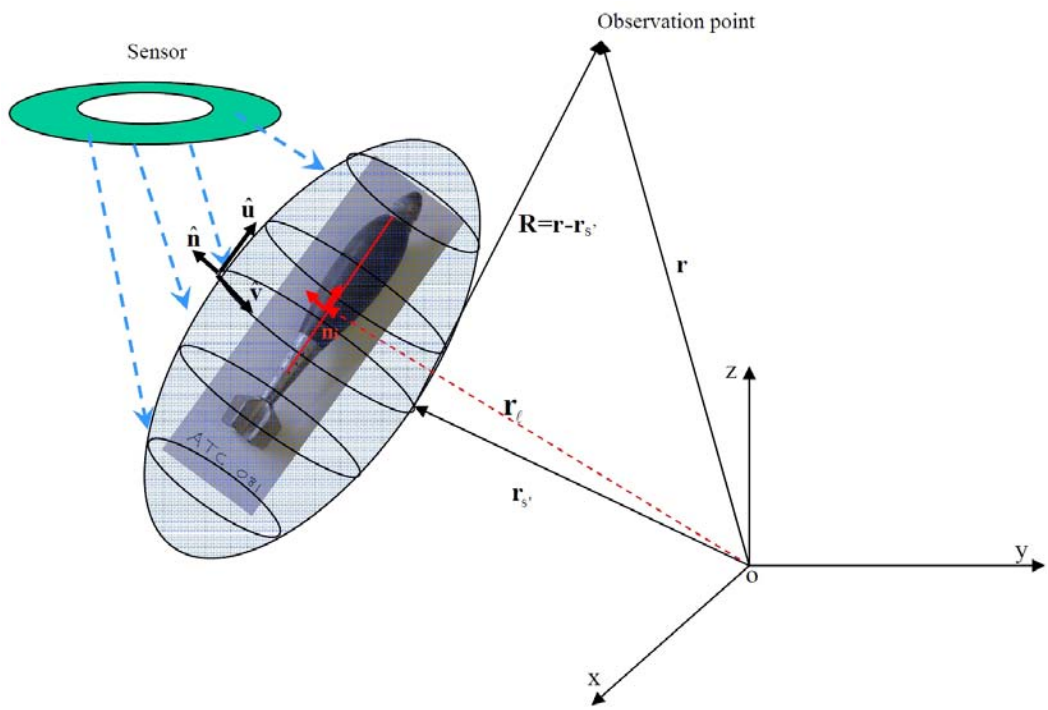


Figure 7.14: Geometry of the NSMS model.

In the NSMS approach, the response of an object is produced by a distribution of equivalent magnetic sources over a surface mathematically enclosing the object, as in Fig. 7.14. In general form the response is written in terms of a surface density of equivalent magnetic sources, $\sigma(\tau, \mathbf{r}_{s'})$, as

$$\mathbf{H}^{sc}(\tau, \mathbf{r}) = \int_S G(\mathbf{r}, \mathbf{r}_{s'})\, \sigma(\tau, \mathbf{r}_{s'}) ds' \tag{7.5.1}$$

where $\mathbf{r}$ is the observation point, $\mathbf{r}_{s'}$ is the source point, and for the moment we do not designate explicitly the exact physical and vector/tensor nature of the quantities in the integrand, nor the

operation between them, as this will vary according to the formulation. The variable $\tau$ designates time ($t$) in the time domain, and frequency ($f$) in the frequency domain. In much if not most of our earlier, frequency domain work (e.g. [53–60, 91]), $\sigma(f,\mathbf{r}_{s'})$ represented equivalent surface magnetic charge density. The identity of $G(\mathbf{r},\mathbf{r}_{s'})$ was then the specific Green function required to translate the charges at $\mathbf{r}_{s'}$ into the consequent field contributions at $\mathbf{r}$. Distributed with appropriate positive and negative values, the charges could form generalized dipole type structures and thus produce the required fields. In any given instance, the actual values for the source density were taken to be proportional to the local intensity of the normal component of the primary field.

$$\sigma(f,\mathbf{r}_{s'}) = \Omega(f,\mathbf{r}_{s'})\,H_n^{pr}(f,\mathbf{r}_{s'}) \tag{7.5.2}$$

The quantity $\Omega(f,\mathbf{r}_{s'})$ is effectively a normalized surface magnetic charge quantity, producing by itself the effect of a unit magnitude of $\sigma(f)$ at $\mathbf{r}_{s'}$. Substituting 7.5.2 into 7.5.1 with known values on the left hand side enables one to solve for $\Omega(f,\mathbf{r}_{s'})$ in discretized form, and thereby obtain a model for the object. See [53–59] for details of formulation, implementation, and application of a charge-based NSMS (= NSMC) for UXO problems.

While in some ways the NSMS is reminiscent of the SEA, it is fundamentally different because of the introduction of what is essentially a response rule, i.e. 7.5.2. This uses $\Omega(f,\mathbf{r}_{s'})$ to relate input and output, i.e. to provide values in a given instance for the essential response parameters $\sigma(f,\mathbf{r}_{s'})$. Thus, in contrast to the SEA, the NSMS constructs in effect an equivalent object whose response is determined by the values and distribution of $\Omega(f,\mathbf{r}_{s'})$, together with any particular pattern of excitation. Thus, at root, is has much in common with the infinitesimal dipole model, with the important addition that here the spatial distribution of the $\Omega(f,\mathbf{r}_{s'})$ will reflect the heterogeneity of the object. Further, while 7.5.2 provides point by point relations between excitation and response, to some significant extent the distribution and values of the $\Omega(f,\mathbf{r}_{s'})$ reflect the response of the whole object. This is because their values are determined from a system of equations with many different observations on the left hand side of 7.5.1, from which the values of all $\Omega(f,\mathbf{r}_{s'})$ are obtained simultaneously, acting collectively, so to speak.

The NSMS model pursued here is cast in the time domain ($\tau = t$). In addition, the surface sources $\sigma(f,\mathbf{r}_{s'})$ are taken to be distributed dipoles, these being more complete, point by point, as magnetic field sources. While the use of charges can suffice, they must combine in such a way as to produce, ultimately, dipole-like structures: They must be distributed so that opposite signs are separated and also sum to zero, as there are no net or isolated magnetic charges in nature. Altogether, for the distributed dipole based formulation, 7.5.1 becomes

$$\mathbf{H}^{sc}(t,\mathbf{r}) = \int_S \frac{1}{4\pi\mu_0 R^3}\mathbf{m}(t,\mathbf{r}_{s'})\cdot(3\hat{\mathbf{R}}\hat{\mathbf{R}} - \bar{\bar{\mathbf{I}}})ds', \tag{7.5.3}$$

where $\hat{\mathbf{R}}$ is the unit vector along $\mathbf{R} = \mathbf{r} - \mathbf{r}_{s'}$ (see Fig. 7.14), and $\bar{\bar{\mathbf{I}}}$ is the identity dyad. The induced magnetic dipole $\mathbf{m}(t,\mathbf{r}_{s'})$ on the surface at $\mathbf{r}_{s'}$ point is related to the primary field via the analog of 7.5.2.

$$\mathbf{m}(t,\mathbf{r}_{s'}) = \Omega(t,\mathbf{r}_{s'})\,H_n^{pr}(\mathbf{r}_{s'})\,\hat{\mathbf{n}}(\mathbf{r}_{s'}) \tag{7.5.4}$$

where $\Omega(t,\mathbf{r}_{s'})$ is normalized amplitude of the magnetic dipole density, i.e. the polarizability density, at $\mathbf{r}_{s'}$ point on the spheroidal surface. In this formulation, only dipole elements normal to the

enclosing surface, i.e. in the $\hat{\mathbf{n}}(\mathbf{r}_{s'})$ direction are used. $H_n^{pr}(\mathbf{r}_{s'})$ is a reference value of the impinging primary field at a point in time prior to Tx shutoff, to which subsequent responses through time will be proportional, in the specific pattern given by $\Omega(t,\mathbf{r}_{s'})$.

Overall, the secondary field is represented in terms of $\Omega(t,\mathbf{r}_{s'})$ as:

$$\mathbf{H}^{sc}(t,\mathbf{r}) = \int_S \frac{1}{4\pi\mu_0 R^3}\Omega(t,\mathbf{r}_{s'})H_n^{pr}(\mathbf{r}_{s'})\left(\hat{\mathbf{n}}(\mathbf{r}_{s'})\cdot(3\hat{\mathbf{R}}\hat{\mathbf{R}}-\bar{\bar{\mathbf{I}}})\right)ds' \tag{7.5.5}$$

One defines the equivalent object by solving this equation for $\Omega(t,\mathbf{r}_{s'})$ for known cases in which the primary field $H_n^{pr}(\mathbf{r}_{s'})$ can be calculated and the values of $\mathbf{H}^{sc}(t,\mathbf{r})$ are known.

For discrimination purposes, a single variable equal to the total normalized responsiveness is proposed, i.e. here the polarizability density integrated over the enclosing surface. This is a global measure of $\Omega$ for the entire object and is thus less subject to numerical fluctuation than the individual $\Omega(t,\mathbf{r}_{s'})$ values:

$$Q(t) = \int_S \Omega(t,\mathbf{r}_{s'})ds' \tag{7.5.6}$$

In passing, we note that one can perform a similar but vectorial integral of surface magnetic dipole values to obtain single (vector) dipole values for the entire object, symbolically indicated by the red arrows in Fig. 7.14. In this sense, this NSMS formulation can be reduced where convenient to a version of the single dipole model.

Our above-cited studies indicate that the total NSMS $Q$ will be invariant for a given object, in the sense that different computational constructs (e.g. surrounding surfaces) and different primary fields produce the same value. Once the amplitudes of the NSMS are determined, the scattered EM fields can be calculated extremely quickly and accurately. Thus the NSMS model can be used for signal pattern matching as was performed with the SEA (Sec. 7.3). Perhaps more important, as $Q$ and its time history are characteristic of an object, that quantity can itself be used as a discriminator. One can either identify the target by comparing its $Q$ to that of a library of known items, or one can use it to make generic decisions as to whether an object is or is not UXO-like.

#### 7.5.b Tests

To illustrate applicability of the NSNS technique together with the new approach for estimating a buried object's location and orientation, the methods were tested against actual TD MPV sensor data from the ERDC test stand (Sec. 6.1). The data were collected on an 89 point grid for objects at different orientations and depths. The response of each object was represented via the NSMS with five discretized circumferential belts of sources. First, accuracy of the NSMS technique was tested against the well controlled test-stand data for a 60 mm UXO. Figure 7.15 shows comparisons between computed and actual data at fixed time gates for the x components of the scattered magnetic fields as measured by 5 vector receivers on the MPV. The results clearly show that the NSMS can produce the EMI response of a 60 mm UXO from a wide range of vantage points with little error.

After tests such as the above provided confidence in the accuracy and reliability of the NSMS formulation, the technique was applied to the TD-MPV CRREL blind test data (see Sec. 6.5. Measurement setup and background subtraction procedures are also described in more detail in [30]). Based on the ERDC test stand data set, the total NSMS Q(t) values were determined for each item that could appear in the blind test suite. Then, for the blind tests, target EMI responses were

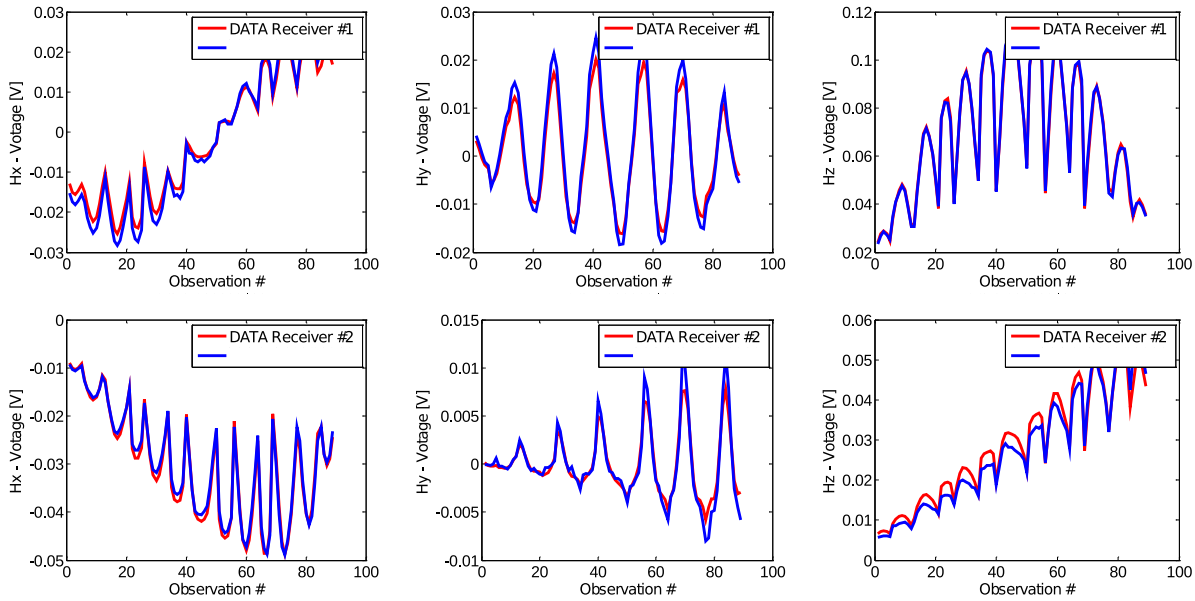


Figure 7.15: X-component of ERDC test stand data (red) for a 60 mm mortar and corresponding signal calculated by the NSMS (blue), for the first time gate from receivers 1 and 2.

measured over 34 grid points split over two elevations, with one elevation providing data for the test described here. The first part of the test consisted of applying the new HAP method (Sec. 7.4) to determine each object's location and orientation.The general success in this realm is indicated in Table 6 and Table 7 in the previous section. With the target locations and orientations calculated, $Q(t)$ for each unknown item was calculated and compared to that of each of the five library UXO items. The comparison between $Q(t)$ for target#1 and for the library UXOs is shown in Fig. 7.16.The test stand $Q(t)$ patterns by themselves show that the total NSMS is a scaler determinant that is directly related to the object size and its material properties. The larger objects tend to produce larger overall $Q(t)$ values while the complete pattern over time is influenced by object composition. Note also that the broadband (large range from earliest to latest time) of the MPV provides useful information: without the contrast between early and late time portions of the curves, one might not be able to distinguish between the 60 mm and the 57 mm.

Inclusion of $Q(t)$ for a non-permeable sphere emphasizes the sensitivity of total NSMS to composition. The AL sphere is about the same size as BLU-26, which is made with permeable steel. In early time, when induced currents do not penetrate the object deeply, the responses by the two objects are on the same order. However in late time they diverge strongly. Overall, the spread of curves over different orders of magnitude for objects with different characteristics allows some discrimination: the inverted $Q(t)$ for target #1 matches correctly that for the actual target and contrasts clearly with those for the other items. Given the difference in configurations in the test stand and blind test measurement setups, this illustrates that the $Q(t)$ is independent of the target's location and orientations. Rather, it is a characteristic of the object. The subsequent plots, Fig. 7.17 and Fig. 7.18 show that the algorithm identified correctly all remaining targets.

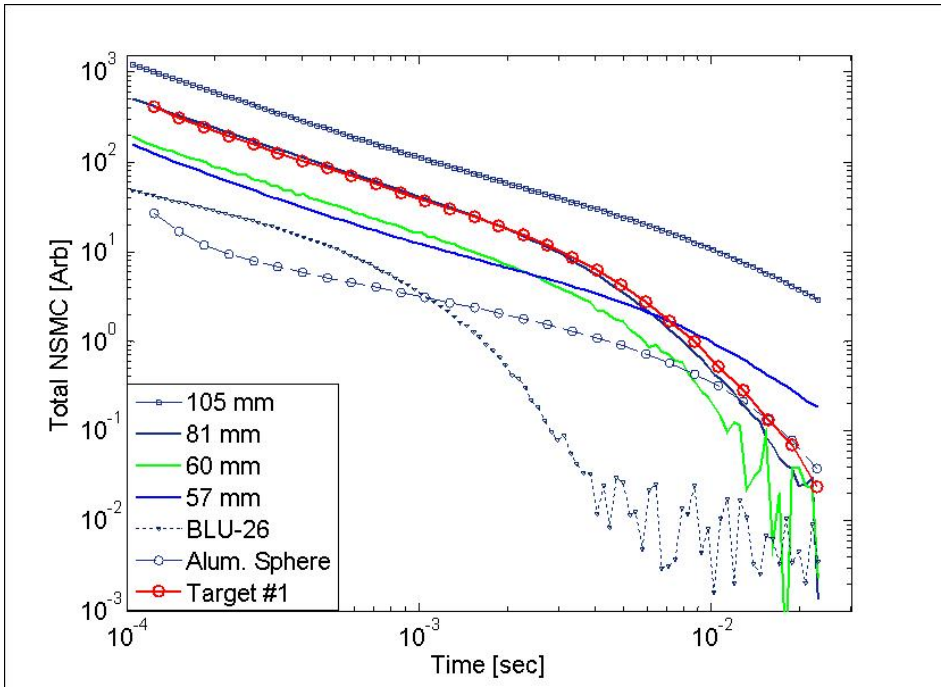


Figure 7.16: Blind test results using the NSMS method, in which $Q(t)$ for unknown target #1 clearly matches that for the 81 mm and contrasts with the $Q(t)$ for alternatives in the library.

### 7.5.c Sensitivities and Robustness

Several factors might limit the usefulness of MPV data under real world conditions including an excess of usable data, noise in the EM and position data, and insufficient coverage of anomalies. In this section, we investigate the impact these factors might have on the accuracy of discrimination results based on both static and dynamic MPV data. We investigate the effect of using only a subset of the data, and inject various levels of noise into the position of the MPV in order to gauge the robustness of the discrimination results. Results suggest that remarkably few data points are required for accurate discrimination; the vector receivers and low hardware noise of the MPV lead to robust results even with sparse data or noisy positional data.

**7.5.c.(1) Data Density** The number of data points at a given SNR required to obtain reliable inversion results is a prominent question. In dynamic mode especially, often 300 data points (30 seconds worth) result from even a brief interrogation. This actually translates into 300 $\times$ 5 Rx units $\times$ 3 vector components $\times$ 30 or so time gates = 135,000 data elements for each such interrogation. As a first test we investigate how many data shots are necessary, at least under pristine conditions, to accurately recover the TD-NSMS parameters, in particular, $Q(t)$. $\Omega(t, \mathbf{r}_{s'})$ values were obtained for a 60 mm mortar using only one data shot (15 data points from 3 vector components at 5 receivers). Because in this instance only five NSMS unknowns were used in the model to characterize the UXO, the number of data points for the each sensor position is more then number of responding sources in the formulation. Therefore, mathematically, a single sounding of the MPV data should be enough for UXO discrimination.

During the measurements the UXO was oriented horizontally at 45 cm and vertically at 24.5 cm

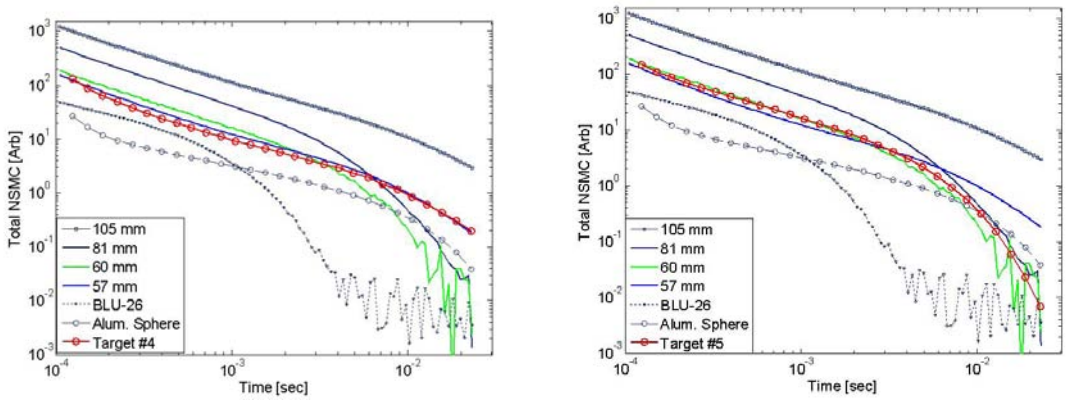


Figure 7.17: NSMS $Q(t)$ comparison between results in the library and those inferred for blind test Target #4 (left) and Target #5 (right), showing good matches for the 57 mm and 60 mm targets, respectively.

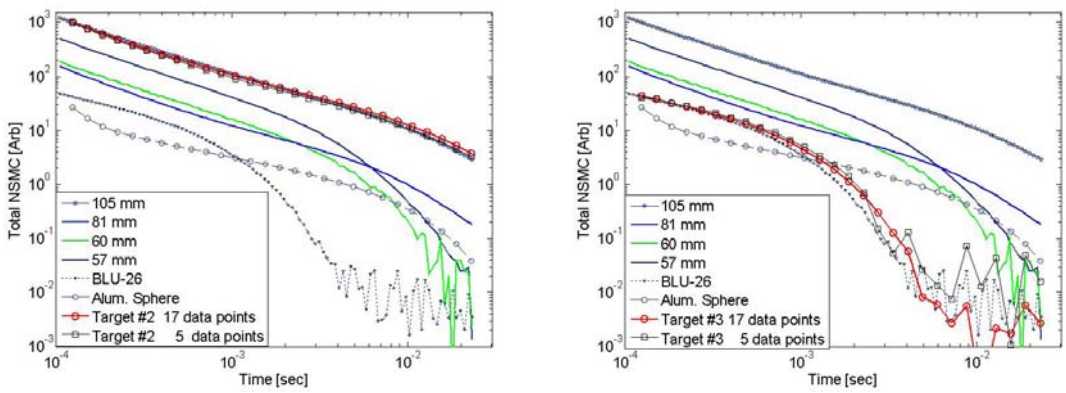


Figure 7.18: Same as in previous figure, here for Target #2 (left) and Target #3 (right).

producing two 89 point sets data (see Fig. 7.19, left). The analysis then used only single soundings from sensor positions 8, 25, 43 (vertical target), 43 (horizontal target), and 44. $Q(t)$ from each sounding appears in Fig. 7.19, right. The comparisons shows that the single sounding $Q(t)$ is robust in that it is generally stable in the face of substantial changes in vantage point.

Figure 7.20 shows the $Q(t)$ for blind test #3 when the target was the BLU-26. In addition to using 17 data points to calculate $Q(t)$, we also used a subset of the blind test data consisting of only five data shots ($\Rightarrow$75 data points). $Q(t)$ obtained using only five measurement shots instead of the full data set still allows and unambiguous and correct classification. These results are encouraging in that they show good limited-data performance even for a relatively small and deep target.

Continuing along these lines, Figure 7.21 contains plots that illustrate the effect of removing more and more observation points from the data on which $Q_n(t_i)$ is based ($1 < n < 34$). Random points were removed except the center shot which was kept until it was the last remaining point. Other than that, the position of the target was known and unchanged during all the analyses, and signals were more or less as high SNR as possible. The quantity $\phi$ also provides a metric to gauge goodness of fit, being essentially an average percent error:

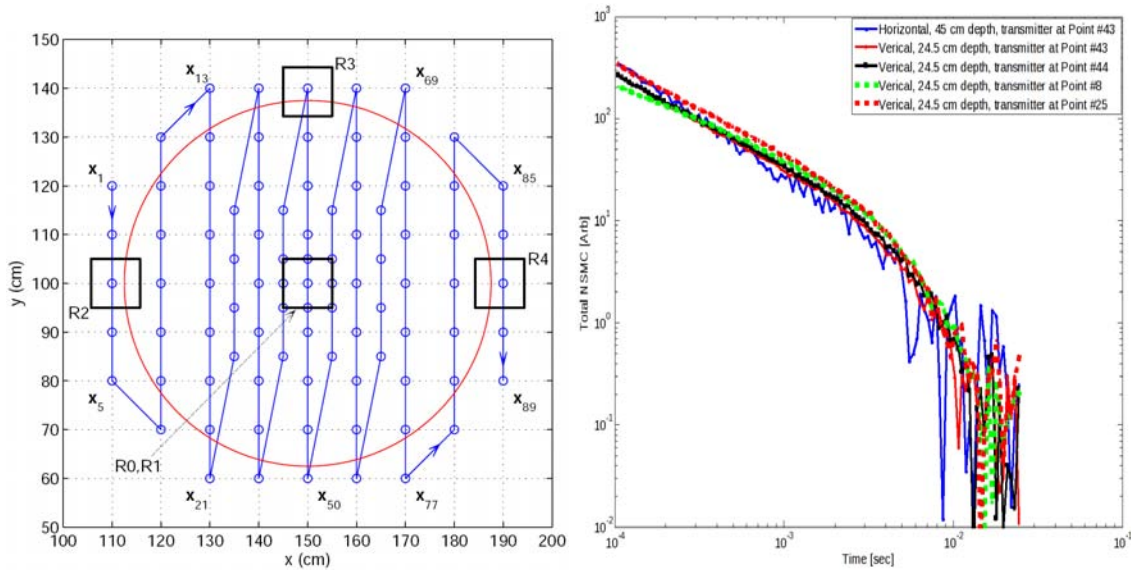


Figure 7.19: ERDC test stand data acquisition grid of 89 points with MPV outline superimposed (*left*). $Q(t)$ from 5 single soundings acquired over a 60 mm mortar at the ERDC test stand (*right*).

$$\phi = \sum_{i=1}^{N} \left| \frac{Q_0(t_i) - Q_n(t_i)}{Q_0(t_i)} \right| / N * 100\% \tag{7.5.7}$$

where $N$ is the number of measurements, $Q_0(t_i)$ is the original function based on the complete, high SNR data.

The left plot in Fig. 7.21 shows notably stable $Q(t)$ curves as the number of points is greatly reduced, for four example targets. The right plot in Fig. 7.21 shows $\phi$ as a function of how many data points were used with a linear fit. These results provide an estimate of the amount of data necessary to achieve a desired level of accuracy for the TD-NSMS based on MPV measurements.

**7.5.c.(2) Noise Sensitivity** Electromagnetic noise was injected into the raw EMI data in increasing levels, and the effect on $Q_n(t_i)$ is shown in Fig. 7.22. Three orders of magnitude of noise level were used, as $\psi_{EM} = \{3.79e^{-4}, 4.28e^{-3}, 4.83e^{-2}\}$ was the magnitude of a zero mean uniform distribution of range $(-\psi/2, \psi/2)$ respectively. The largest $\psi_{EM}$ was chosen to be 2% of the maximum received signal from the 105mm in this data. The figure shows that resulting average percent error varies linearly with the amount of noise injected with targets that exhibit a higher SNR such as the 105 mm shell being effected the least (Fig. 7.22, right). (Here, $n$ in $Q_n$ indicates noise). The effect of the added noise on SNR depended very much on the target and configuration, i.e. on the strength of the underlying signal to which noise was added. For perspective, note that, for most targets over most of the time range, the $Q(t)$ values are within about two orders of magnitude of one another. When the added noise affects SNR such that $Q(t)$ for the 105 mm is distorted at least over the late time portion of its response, then the other responses will be notably distorted

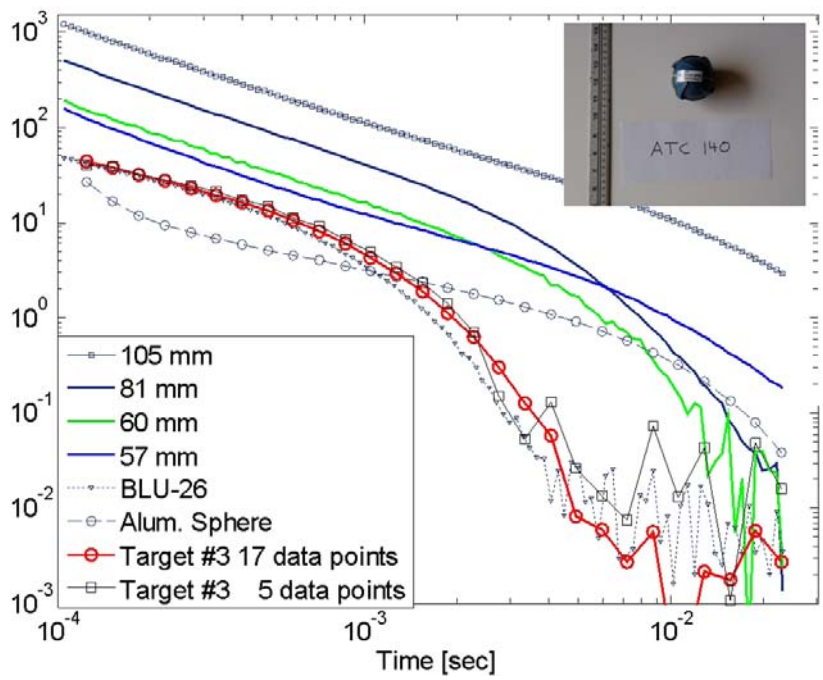


Figure 7.20: NSMS model comparison to library for blind test #3, where vertical axis is $Q(t)$. The curve recovered in blind testing correctly matches that for the BLU-26, especially outside of the late-time noise region.

over a much larger time range. The late-time, low-magnitude signal from the BLU-26 will also be affected notably by noise approximately an order of magnitude less than that.

Random noise was also injected into the position of the MPV from point to point, with otherwise "clean" data. Figure 7.23 shows some examples of the resulting $Q_n(t_i)$ as random positional noise was added from a flat distribution $(-\psi/2, \psi/2)$ with error limits in meters

$$\psi_{pos} = \{8.86e^{-3}, 7.85e^{-2}, 2.34e^{-1}, 4.83e^{-1}, 6.95e^{-1}\} \tag{7.5.8}$$

The accuracy of $Q(t)$ is remarkable when all data acquisition locations are potentially misplaced by as much as $23.4/2$ cm in any direction (see Fig. 7.24).

Future work would logically look as well at the effect of including only $H_z$ instead of all vector components, as well as the effect of considering data from fewer receiver cubes.

### 7.5.d Conclusion

We have adapted the NSMS model to the geometry, data format, and time domain nature of the MPV. Data acquired at the ERDC test stand at Vicksburg showed a high SNR under controlled acquisition conditions and showed promise for implementing the NSMS model to discriminate between UXO. Subsequent data taking at ERDC CRREL showed the TD-NSMS can successfully be used as a discriminant in blind tests for the MPV. Only a few shots, each consisting of 15 data traces, are required to find a good estimate of the TD-NSMS. The TD-NSMS is relatively robust, retaining its ability to accurately and consistently discriminate single UXO targets when significant EMI and positional noise is injected.

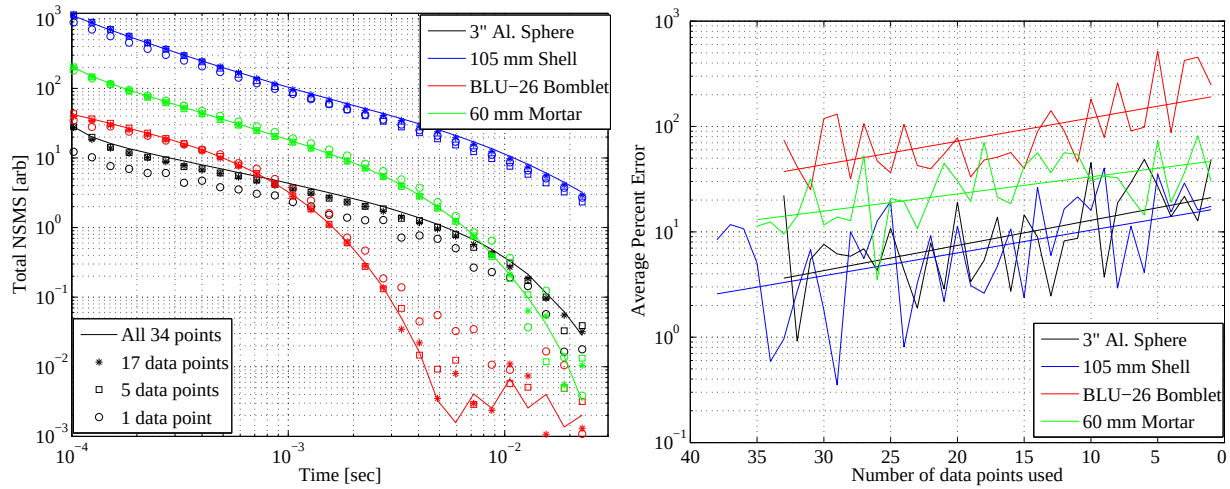


Figure 7.21: $Q_n(t_i)$ as a function of time for limited number of data locations. (*left*). $\phi$ vs number of observation points used (*right*).

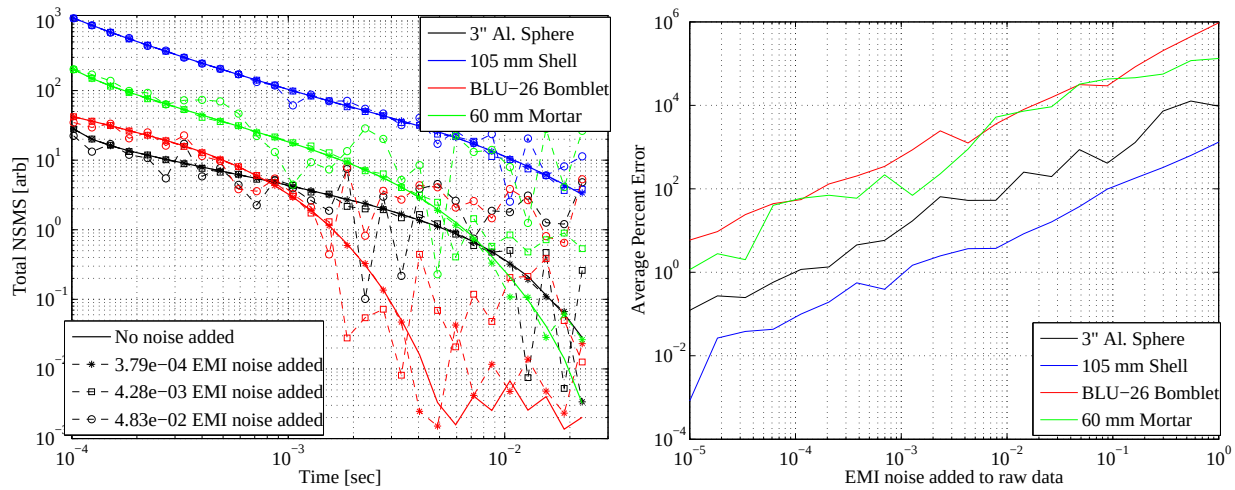


Figure 7.22: $Q_n(t_i)$ as a function of time for increasing levels of noise injected into the EMI data. (*left*). $\phi$ for this case (*right*).

# 8 The MPV-II

Experience with the MPV as realized motivated development of a second generation version, the MPV-II. The most compelling consideration was that the size, weight, and geometry of the original MPV (MPV-I) strained its description as readily portable. The multiple receivers and transmitters both contributed to this issue; and for desirable clearances, the boom was attached to the head in a way that placed the latter too far from the operator. The data acquisition system was also separated from the rest of the apparatus, to relieve the back of the operator, but then required a tether. Other issues centered on the laser positioning system. As described in Section 4.2, it has satisfactory precision over a short baseline but was found to require rather too much attention. It failed to

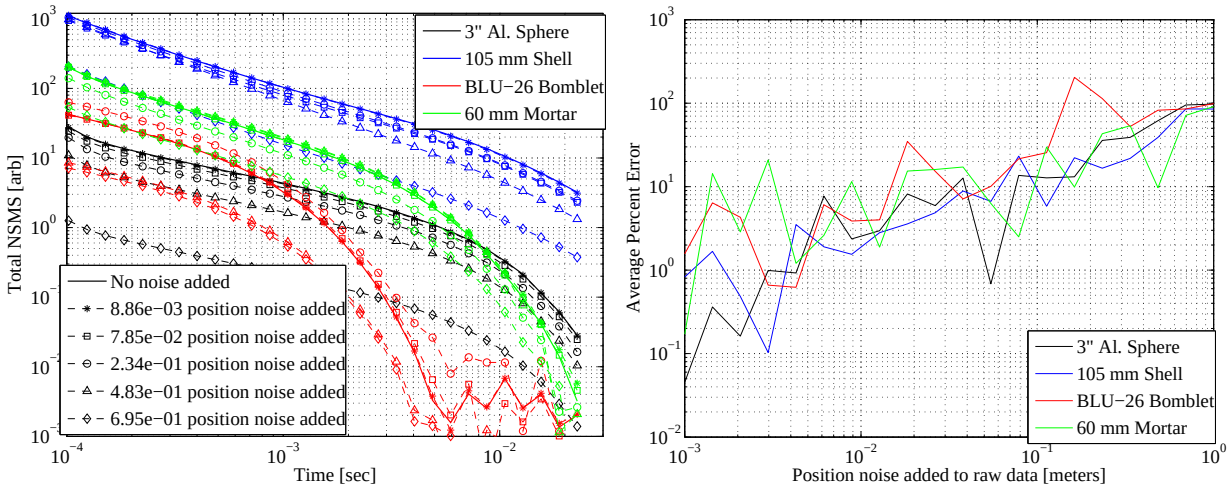


Figure 7.23: $Q_n(t_i)$ as a function of time for increasing levels of noise injected into the position of the MPV sensor head. (*left*). $\phi$ for this case (*right*), with positional error in meters.

produce usable data when one of the laser transmitters was obscured, which means that the system may lose much of its usefulness in treed landscapes. Further, the particular laser system employed is no longer supported and is not likely to be available commercially in the future. Finally, the top receiver, R0, was purposely situated above the base plane of the head, to provide signals with sufficient contrast to those from the other receivers. However in practice this often meant that it produced a problematically weak signals. Extending considerably from the region where the boom was attached, it combined with the elevated laser receivers to increase the overall unwieldiness of the device. All this outweighed the gain in data diversity that had originally motivated its inclusion in an elevated position.

With these issues in mind, a new version dubbed the MPV-II was designed and developed and has been realized by G&G Sciences (Fig. 8.1). The Rx cubes are smaller, with 8-cm sides as opposed to 10 cm and with a coil width of 3 cm. They are closer together, with a center-to-center separation of 18.44 cm (down from 39.3 cm). The new system has one transmitter coil instead of two, thus reducing much Tx weight. The 21-turn, 7.74 cm deep coil has diameter 49.68 cm (one-third smaller than the original) and is centered with respect to the receiver assembly. In all, the weight of the new device is about 12 lbs, which makes it less than half as heavy as the 23-lb original MPV. The ergonomic enhancements go beyond the reduction in size and weight. The sensor head of the new instrument is only about a foot away from the operator and the setup is also more balanced. The iPad based based operation allows wireless communication with the data acquisition system and an enhanced user interface.

For positioning, the MPV-II has a two-tiered system. The first level consists of a real-time-kinematic (RTK) GPS system [92] with a horizontal uncertainty of $\pm 2$ cm. The device also incorporates an electronic compass that gives its three-dimensional attitude at all times. For enhanced accuracy, and for situations in which there is no GPS access, a new positioning system was also devised. It uses the primary field of the transmitter as a beacon that is tracked by external receivers whose position is known, e.g. by virtue of the GPS system. Availability of the data from the compass/inclinometer assists the inversion of the beacon signals for position and orientation. The

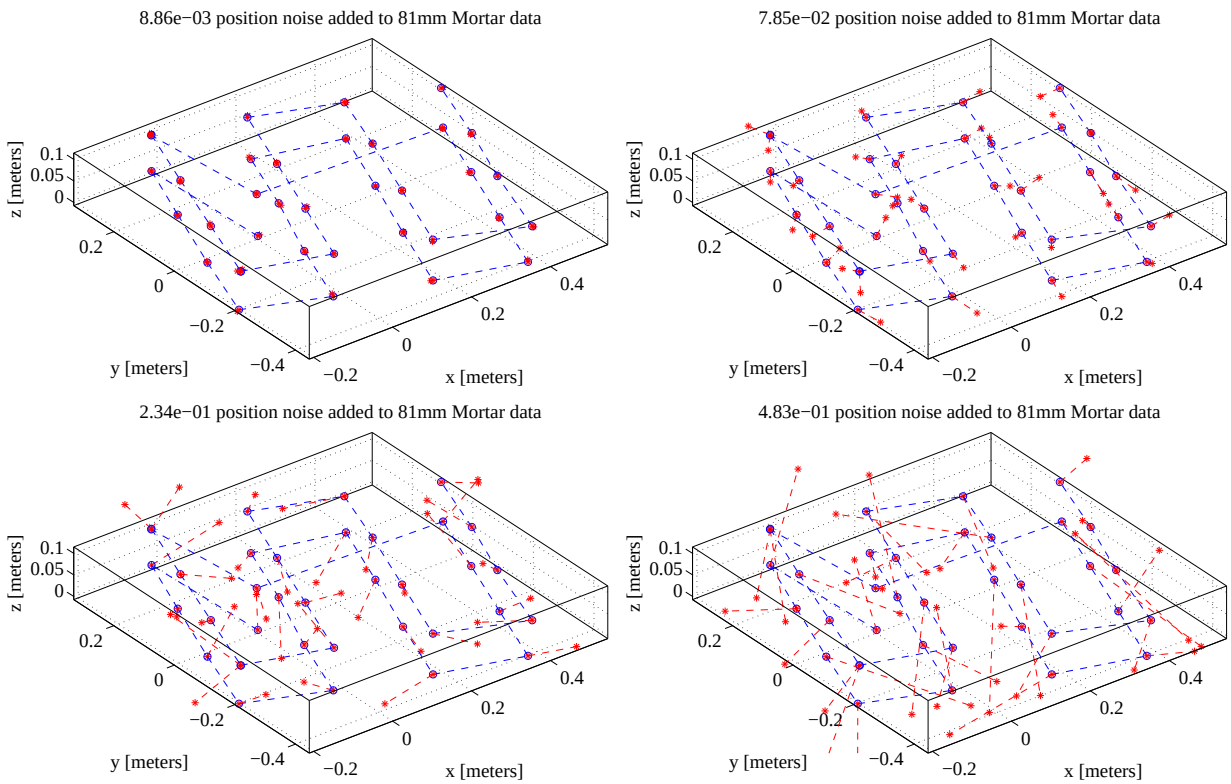


Figure 7.24: Correct and misplaced locations for indicated noise levels. Blue circles are accurate values, red stars are noisy data.

beacon data, collected during Tx on time, is collected by two receivers separated by 149.35 cm and (at this point) tethered to the sensor head. This is similar to the positioning system for the GEM-3D+ frequency-domain sensor [27]. A final difference between the MPV-I and the MPV-II is that the zeroth receiver has become the fifth: it is now located behind R1 on the same horizontal plane as the others (the new device has receivers labeled R1 - R5). This new configuration of receivers should facilitate the experimental computation of field gradients. Fig. 8.1. shows the compactness of the new head design, the iPad near the operator's hands, and the beacon Rx units in front of him on a horizontal beam on the ground.

Fig. 8.2 shows an example dipole inversion from MPV-II measurements. The data were collected at the Yuma Proving Ground in Arizona in October of 2010. A 40-mm projectile was buried 22 cm below the ground, oriented vertically, nose down. The MPV-II was placed horizontally flat at a set of nine points on the ground, as per Fig. 8.1, not on a grid. The inverted depth and dip angle are respectively 22.8 cm and 268°. For comparison, Fig. 8.2 shows polarizabilities derived instead from Sky Hanover measurements. These employed two such projectiles 25 cm away from the sensor and separated by 40 cm. The polarizabilities are very close in all three cases, encouraging confidence in both the instrument and the inversion procedure.

Figure 8.1: The MPV-II, with a smaller (50 cm diam) and lighter head, a single transmitter coil, a beacon positioning system that adds no hardware to the head, and iPad based communication with the remote data acquisition system.

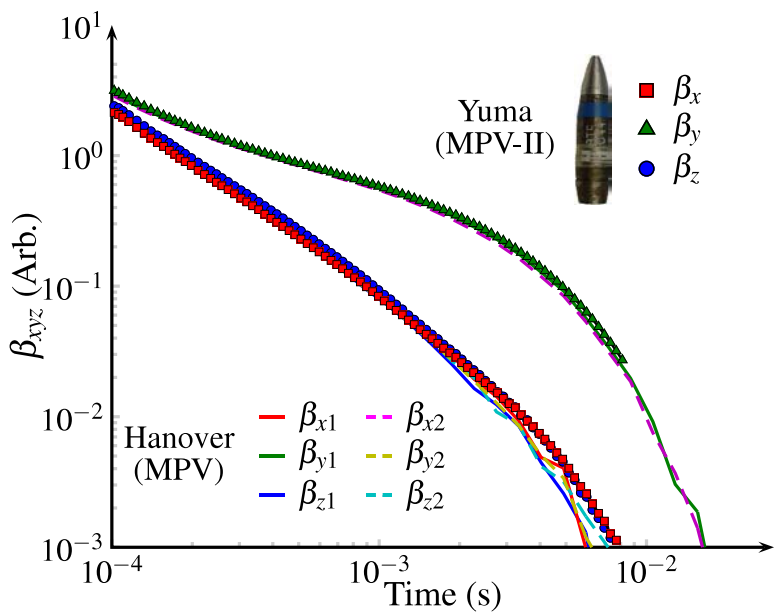


Figure 8.2: Magnetic polarizabilities for a 40 mm projectile, inverted from Yuma Proving Ground MPV-II data (markers), and also (solid and dashed lines) extracted from Sky Research Hanover data.

# 9 Publications

Publications produced in whole or part with funds from this project during FY06 are [45, 53, 54, 82, 90, 91, 93–98].

# A Pre- and Post-Processing Software Package

We have developed a Matlab based GUI (dubbed EMI.m) which incorporates the post-processing described above. This program combines the post-processing and data analysis steps into a single interface. Figure A.1 shows the introductory screen, which is followed by the preprocessing screen of EMI.m. Here background is subtracted from the data and trouble points e.g. in the positioning may be removed. Feedback is provided immediately in the form of positional tracking information (Fig. A.2) and raw data plots (Fig. A.3). After these steps, the NSMS model can characterize the target and either add it to the current library (Fig. A.4), or invert against the current library (Fig. A.5) yielding a ranking of nearby targets according the our discrimination parameter Q (the total NSMS). This GUI incorporates our models into a coherent package and is in addition to similar software such as UXOLab.

# B ERDC Teststand Data Report

Figure A.1: Main menu introductory screen to EMI.m.

**TECHNICAL NOTE 2007-2**

# DATA REPORT

# TESTS OF MPV AT VICKSBURG

# FEBRUARY 26 TO MARCH 2, 2007

**April 2, 2007**

**In support of**

**COLD REGIONS RESEARCH AND ENGINEERING LABORATORY**
72 Lyme Rd.
Hanover, NH 03755-1290

**by**

**David C. George and Joan L. George**
G&G Sciences Inc.
873 23 Road
Grand Junction, CO 81505
(970) 263 9714
dgeorge@ggsciences.com

# INTRODUCTION

The purpose of this report is to provide background, conditions, and detailed descriptions of data that was collected with the MPV during a field trip to the Waterways Experiment Station (WES) in Vicksburg, MS.

WES has a UXO test stand that was specifically constructed to provide facilities needed to determine the EM spatial response of UXO targets. This stand is non-conductive and provides automated and calibrated movement of a system being tested over a UXO target.

The objective of this field trip was two fold. The first objective was to collect ***static*** data for a series of UXO targets. In these tests, the MPV was moved to a position and stopped there while a data point was collected. These static data will be used by CRREL as reference response for the Standardized Excitation Approach (SEA) method. The second objective was to collect ***dynamic*** data. In these tests, the MPV was placed in continuous movement during data collection. This objective was chosen because there has been concern about the distortion that is caused by movement of the MPV while a stacked data point is being acquired. Since the MPV is to be a portable and hand-held device, any effect caused by sensor movement is important.

This field trip was a success. High quality data, both static and dynamic, were collected. The only significant failure in these tests was to collect static data for as many targets as desired. Static data consists of collecting many data points for a single target at a single orientation and a single depth. There are many targets, many orientations, and several depths. The result is that the data set becomes huge, and inadequate time was planned for the original scope. Data could not be collected as fast as hoped, so fewer target/orientation/depth cases were acquired than originally planned.

The dynamic data that were collected are higher quality than expected. Until we arrived at WES, we were unaware of the capability of the test stand to provide continuous movement at constant speed, coupled with the capability to produce coordinates of position. The dynamic data we collected should be able to be used to make an initial estimate of the effects of sensor movement during data acquisition.

We received able and energetic help from WES personnel. This level of cooperation and assistance was not expected.

This report is divided into two sections. The first section describes activities during the trip and the physical setup of the equipment on the WES test stand. The second section describes the data sets that were collected. In this section, descriptions are divided between static and dynamic data sets and between acquisition and review. Description of the acquired data is the heart and the basic objective of this report. The data were all reviewed. A description of this review is included to indicate the (small) extent to which any of these data have been analyzed. Also included are observations and judgments of the personnel who collected the data in the context that these observations might have bearing on the analysis of the data.

The data are posted in a non-publicly-exposed FTP folder on G&G's web site at ftp://ggsciences.com. The data consist of a series of (*.tem) files as described herein. The files have all been converted as well to Matlab (*.mat) files. Access to this site is via user name and password separately communicated.

# ACTIVITIES AND SETUP

The personnel conducting this field survey were David George and Joan George. Dave's responsibility was to guide activities, to set up and maintain the MPV equipment, and to assure and check the quality of the data. Joan's responsibility was to operate the equipment and to maintain a detailed field log.

## Schedule, Activities, Accomplishments

This information is shown in Table 1.

**Table 1 Summary of activities and accomplishments**

| | |
|---|---|
| Friday, February 23 | Depart Grand Junction |
| Sunday, February 25 | Arrive Vicksburg |
| Monday, February 26 | Check in to WES. Fabricate and install 'truss' to mount MPV head to test stand trolley. Set up MPV and work out hardware communications. In conjunction with Cliff Morgan, modify software on both DAQ and Test-Stand-Controller to pass stop/go |

| | |
|---|---|
| | signals and coordinates. Collect simple test data sets and estimate speed of data collection. Evening: design static data point grid. |
| Tuesday, February 27 | Additional tests to test grid, communications, data. Begin static data collection ~ 11am. Complete:<br>• 60 mm mortar 5 orientations, 3 depths,<br>• Blu-26 bomblet 1 orientation, 3 depths.<br>Set up dense grid and 81 mm mortar for attempted overnight run. |
| Wednesday, February 28 | Dave travels to Washington D.C. for I.P.R. and returns evening. Complete:<br>• 81 mm mortar, 5 orientations, 3 depths,<br>• 57 mm projectile, one orientation, 3 depths.<br>Progress slowed briefly for VIP tour of UXO test stand. |
| Thursday, March 1 | Weather severe (same storm that killed students in Alabama high school). Progress halted several times in morning. Had difficulty suspected to be water related but eventually resolved to components and/or connections in transmitter.<br>Complete:<br>• 57 mm projectile, two more orientations, 3 depths,<br>• 4 inch steel sphere, 3 depths,<br>• Prolate spheroid, 1 orientations, 3 depths; 2 orientations, 2 depths. |
| Friday, March 2 | Modify software communications to be useful for dynamic tests. Platform speeds were ~ 0.05, 0.1, 0.2, and 0.5 m/s. Complete following tests:<br>• Using profiles directly over 4 inch sphere<br>  ○ Four speeds for one block time and repeat setting<br>  ○ Four block times while maintaining one decay length at fast speed<br>  ○ Three fast block times/repeats at fast speed<br>  ○ Full waveform data storage for differing block times at fast speed<br>• Using profiles directly over 60 mm mortar, 45º nose down<br>  ○ Four speeds for one block time and repeat setting<br>• Using 2m x 2m grid over 50 mm mortar 45º nose down<br>  ○ Four speeds for one block time and repeat setting<br>Continue static tests. Complete:<br>• 105 mm projectile, 3 orientations, 2 depths<br>• 20 mm shell, 1 orientation, 2 depths |
| Saturday, March 3 | Depart Vicksburg. |

## Experimental Setup

A block diagram of the setup is shown in Figure 1, and pictures of the facility and setup are shown with detailed captions in Figures 2 through 6.

For these tests, the MPV was stripped. The ArcSecond sensor mounting assembly was removed and the handle was removed. This left only the MPV *head,* i.e. the transmitting and receiving coils, their preamps, and their cabling. A special suspension truss was fabricated by WES personnel to attach the MPV to the trolley in the test stand. The DAQ was placed on the test stand out of the way of the trolley/MPV. The DAQ system contains a PC running Windows XP.

The test stand control room is located about 30 or 40 meters from the test stand. To allow control of our DAQ system remotely, we usually use a wireless link and Remote Desktop. In this case, the wireless link was not reliable, so we connected a remote terminal to the DAQ via a hard-wired Ethernet link. This link is part of the test-stand wiring; we added a cross-over cable to avoid connecting through a router.

An important point of the setup is that communications were established between the DAQ and the test stand controller. These communications were via an ASCII serial link. For static data, the serial link provided the capability for the test stand to tell the DAQ software when it was time to collect a data point and the capability for the DAQ to tell the test stand when it was done with a data point so that the test stand could move the MPV head and trolley to the next position. The link also allowed the test stand to tell the DAQ the coordinates of each measurement point. For dynamic data, the communications allowed the test stand to produce streaming data similar to that produced from a GPS receiver. These data were read and interpreted by the DAQ software as if they were from a GPS receiver in the same manner that is used for any dynamic (continuous) surveying.

To establish the serial communications required software modifications and adaptations of both the software within the DAQ and the software within the test stand. WES employee Cliff Morgan willingly and ably provided the software modifications needed for the test stand.

A final piece of setup information is included in Figure 7. It shows the dimensions of MPV sensors as they were used for these tests.

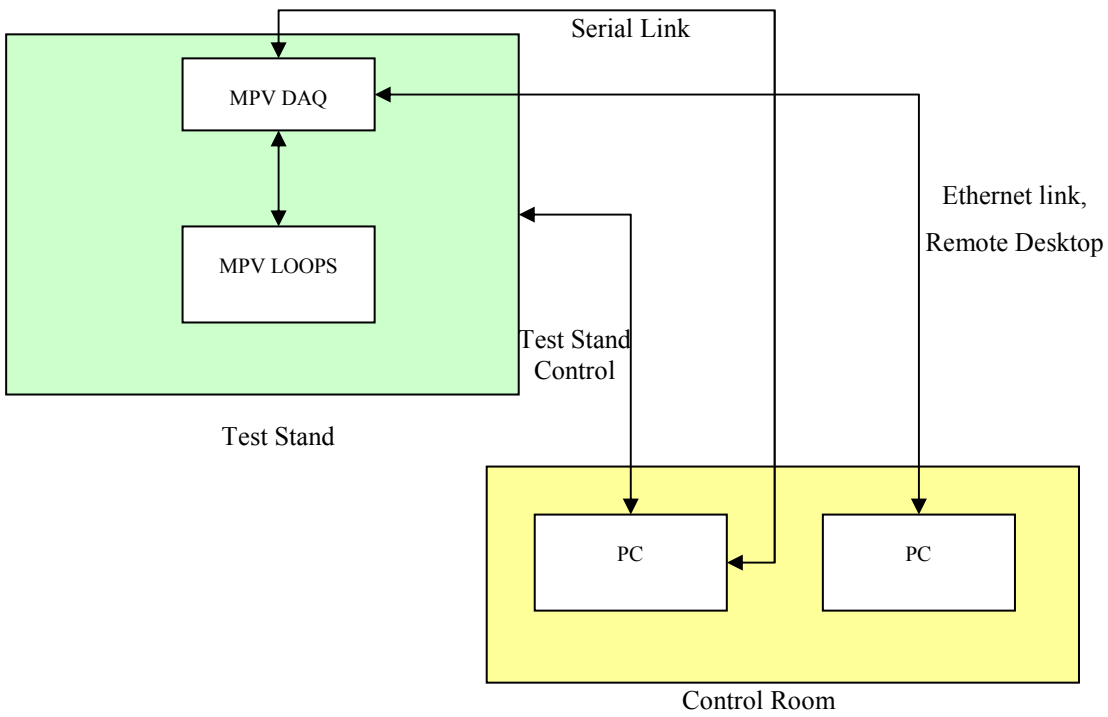


**Figure 1 Block diagram of test setup. The test stand is controlled by a PC. It communicated to the MPV DAQ through a serial link. The MPV DAQ was controlled remotely by a PC connected through a hard-wired (cross-over) Ethernet link.**

**Figure 2 Vicksburg UXO Test Stand. The test stand contains no metal except at the periphery. Motors controlling movement of the trolley are in the boxes that look like bird houses. The trolley moves by remote control in two dimensions. The target carrier is under the deck. This carrier can be raised and lowered using remote control. Cables to/from the control room run from the boxes located at the bottom of the stairs.**

**Figure 3 MPV head mounted on test stand trolley. The DAQ is in the background. For these tests, the DAQ was powered by AC. The battery supplied power for the transmitter and the pre-amplifiers. The bricks and lever arm on top of the trolley were added to attempt to reduce sway in left/right (+X/-X) direction. The wood suspension truss for the MPV was fabricated by WES employee Charles Hahn.**

**Figure 4 Another view of MPV and DAQ on the test stand.**

**Figure 5 Picture of target carrier under test stand deck. The carrier is raised and lowered by remote control. The carrier was tilted and rotated manually. Target depths were manually measured from the target to the MPV.**

**Figure 6 Picture of control room including the test stand creator and helpful WES employee Cliff Morgan.**

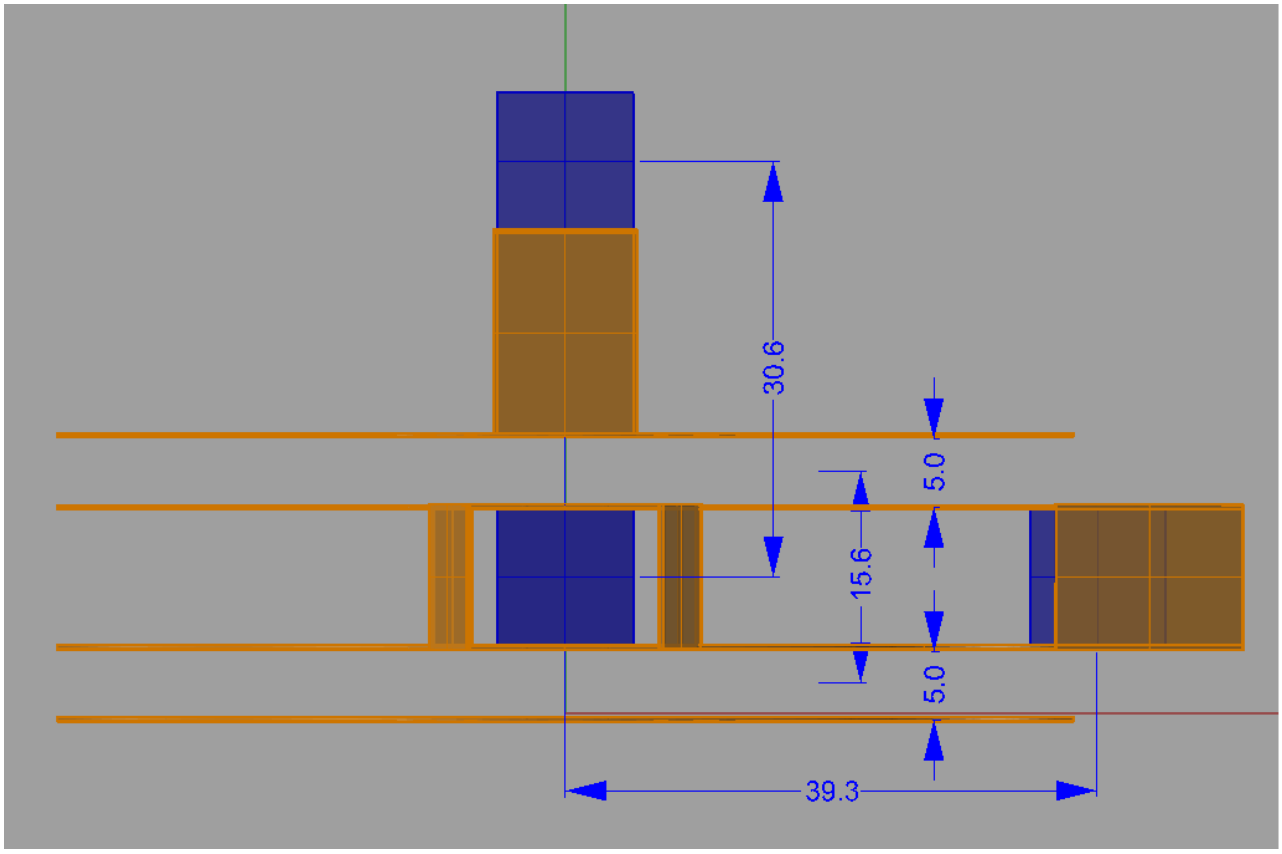


**Figure 7 Critical dimensions of MPV head. Dimensions in cm. Cube numbering for these experiments is: Cube 0: upper center; Cube 1: lower center; Cube 2: left (-X); Cube 3: forward (+Y); Cube 4: right (+X).**

# OBSERVATIONS AND DISCUSSION

## Static Data Sets

### Data Acquisition

For static acquisition, a target was placed, its depth measured, and a series of data points on a specific grid were acquired. The data points were all stored in a single (*.tem) file.

#### Procedure

After the first day of set-up, test runs, and determination of speed at which we expected to be able to acquire data, a measurement grid was created. This grid is shown in Figure 8. The figure also shows an outline of the MPV for visual reference. A set of data points was collected into a file. The number of data points and their contents are shown in Table 2.

Each data set included a measurement of background at grid position (0,0) and measurement of the response of a calibration target at grid position (0,100). The calibration target was an aluminum ring, 2 inch outside diameter, 1.5 inch inside diameter, 0.0625 inch thick, placed 32 cm below the bottom of the MPV head.

The targets were set up at grid position (150,100). Depth was measured from the bottom of the MPV head to the geometric center of the target. The targets were pre-marked for geometric center. After setting up target, procedure was to check target depth and to initiate an automated data collection sequence.

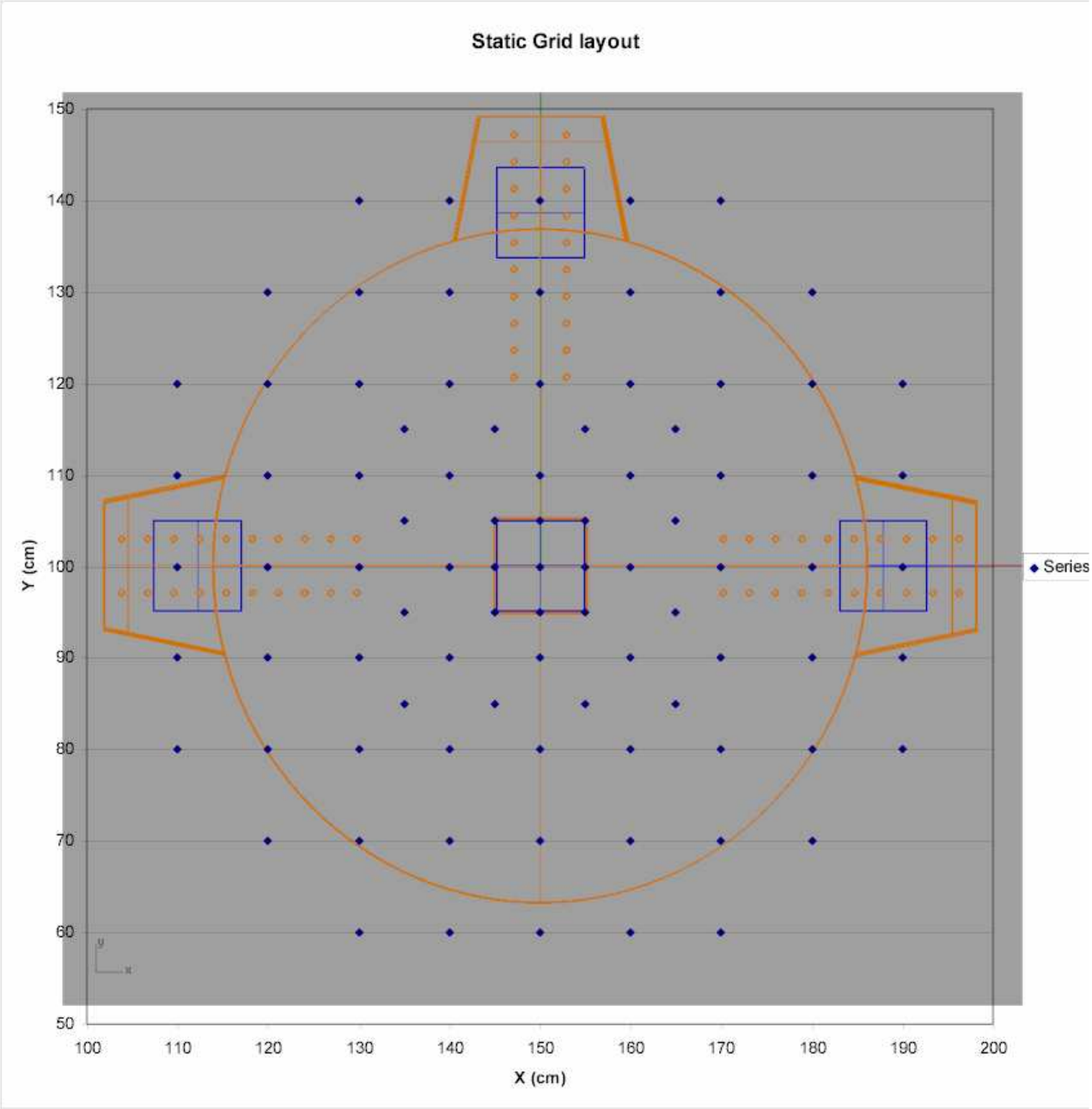


**Figure 8 Grid layout used for static measurements. Target was located at the center of the grid.**

**Table 2**

Data points in standard static data set

| Data Point Number | Description |
|---|---|
| 1 | Al ring calibration at (0,100) |
| 2 | Background at (0,0) |
| 3 - 91 | 89 points on grid as in Figure 8 |
| 92 | Background at (0,0) |
| 93 | Al ring calibration at (0,100) |
| 94 | Background at (0,0) |

### Discussion

The data are documented in summary Table 1 and more specifically in the large Table 4 in the appendix. The most significant element in Table 4 is the file name. This name matches the files that are posted on the FTP site. Table 4 contains names of files that were incomplete or bad that are not posted on the web site.

## Data Review

Since each data file contains roughly 100 data points, and each data point contains 15 transients (5 cubes, three components, with ~120 time-gates per transient), data review is challenging because of the huge amount of data. To quality check the data, we developed procedures in Matlab to make a display of all the transients for one grid.

### Procedure

Each (*.tem) data file was converted to a Matlab (*.mat) file using the facility in our program TEMView. A sample of the contents of the Matlab file is shown in Table 3.

A Matlab m-file, *ShowTransients.m* was developed. This file and its associated function files are also posted on the FTP site. This Matlab file produces a display like that shown in Figure 9. One display shows the Z, Y, and X received transients for a single cube, at each of the grid positions over the target. For the display of the transient, the transient decay curves are first cropped to time gates > 100 µs. Then the transients are converted to a companded amplitude where both positive and negative amplitudes greater than some threshold voltage (50 µV in this case) are converted to log(amplitude) maintaining sign, and amplitudes less than the threshold are used as is. This display provides a way to easily see the sign of the transients and to emphasize signals where signal to noise ratio is poor.

For detailed inspection of transients, program TEMView was used. This program provides a graphical view of transients. Graph scales and axes can be controlled, display of transients for any combination of cubes and components can be controlled, and successive data points can be overlaid. One simple display is shown in Figure 10.

All of the data files were reviewed using this procedure.

**Table 3 Description of variable produced by converting a TEM file to a Matlab file.**

| Variable in Matlab workspace | Sample size | Matlab memory usage | Variable type | Description |
|---|---|---|---|---|
| AcqMode | 1x94 | 752 | double | Indicates mode of data acquisition: 0=Full Waveform, 1= Decay Waveform, 2=Decimated (Gated) Waveform |
| BlockT | 1x94 | 752 | double | Block time: 0.0333, 0.1, 0.3, 0.9, or 2.7 sec |
| CPUms | 1x94 | 752 | double | Not used |
| DeIt | 1x94 | 752 | double | Sampling period: 2 us for the MPV |
| DtyCyc | 1x94 | 752 | double | Always 0.5 |
| Elev | 1x94 | 752 | double | Not used |
| GPSUTC | 1x94 | 752 | double | Time in seconds, for dynamic measurements |
| GateHOff | 1x94 | 752 | double | Time to first gate |
| GateWid | 1x94 | 752 | double | Width of gates, in us |
| Gates | 122x1 | 976 | double | Gate centers in us |
| Heading | 1x94 | 752 | double | Not used |
| Lat | 1x94 | 752 | double | Not used for static measurements. X coordinate for dynamic measurements |
| LineNo | 1x94 | 752 | double | Not used |
| LocalX | 1x94 | 752 | double | X coordinate for static measurements. Not used for dynamic measurements |
| LocalY | 1x94 | 752 | double | Y coordinate for static measurements. Not used for dynamic measurements |
| LocalZ | 1x94 | 752 | double | Not used |
| Lon | 1x94 | 752 | double | Not used for static measurements. Y coordinate for dynamic measurements. |
| Mag1 | 1x94 | 752 | double | Not used |
| Mag2 | 1x94 | 752 | double | Not used |
| MagDly1 | 1x94 | 752 | double | Not used |
| MagDly2 | 1x94 | 752 | double | Not used |
| Pitch | 1x94 | 752 | double | Not used |
| PtNo | 1x94 | 752 | double | Point number: sequential in file beginning with 1. |
| Roll | 1x94 | 752 | double | Not used |
| Rx | 94x1x5 | 1428800 | cell | Cell array containing received data. For N data points, this is an {N,1,5} cell array. Each cell contains a (Ngates,3) matrix. The third dimension is cube number. |
| S1_X | 1x94 | 752 | double | Not used |
| S1_Y | 1x94 | 752 | double | Not used |
| S1_Z | 1x94 | 752 | double | Not used |
| S1ms | 1x94 | 752 | double | Not used |
| S2_X | 1x94 | 752 | double | Not used |
| S2_Y | 1x94 | 752 | double | Not used |
| S2_Z | 1x94 | 752 | double | Not used |
| S2ms | 1x94 | 752 | double | Not used |
| S3_X | 1x94 | 752 | double | Not used |
| S3_Y | 1x94 | 752 | double | Not used |
| S3_Z | 1x94 | 752 | double | Not used |
| S3ms | 1x94 | 752 | double | Not used |
| TxI | 94x1 | 102272 | cell | Cell array containing transmitter current data. For N data points, this is an {N,1} cell array. Each cell conatins a (Ngates,1) matrix. |
| nRepeats | 1x94 | 752 | double | Number of repeats |
| nStk | 1x94 | 752 | double | Number of stacks |

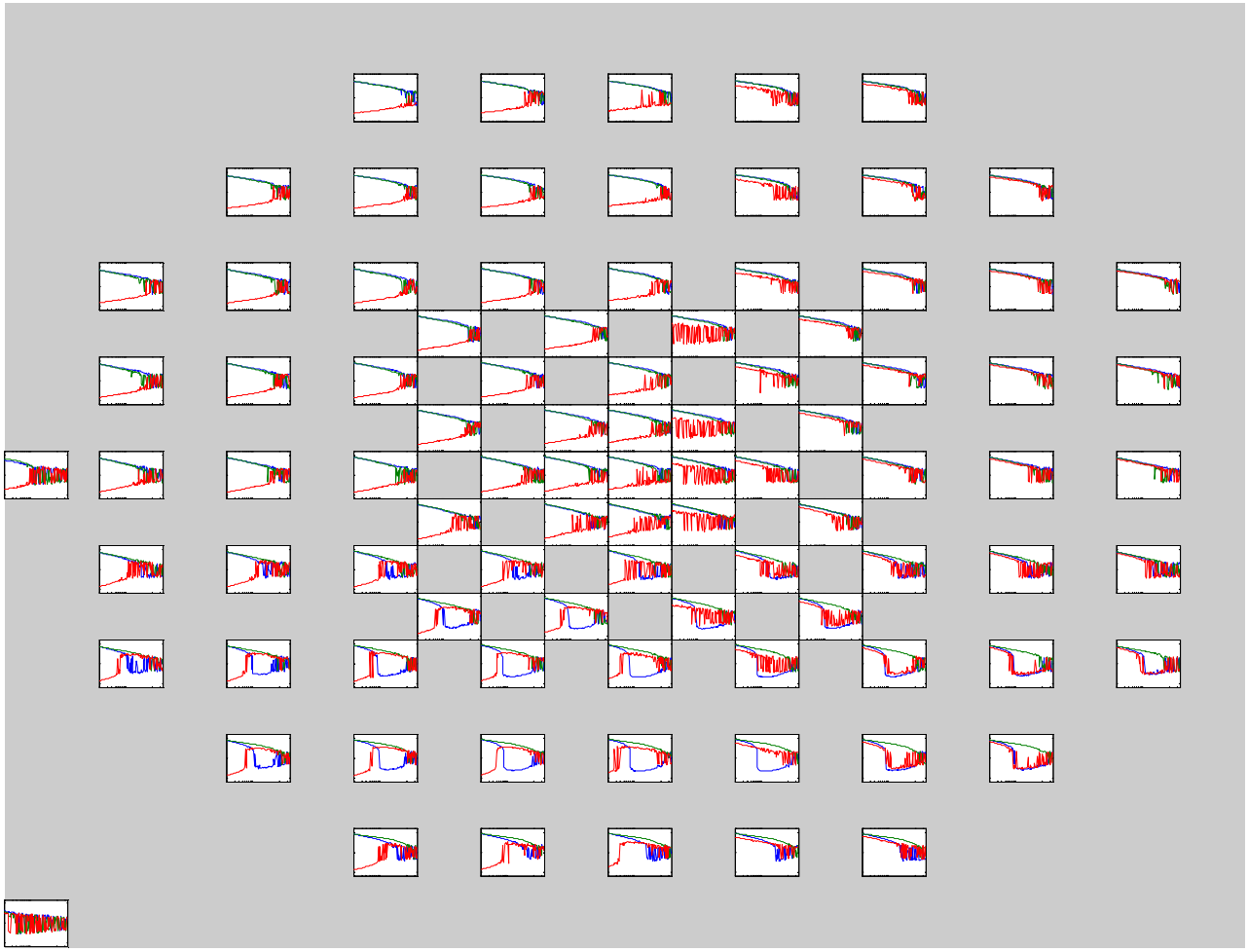

**Figure 9 Picture of file used for review of static data. One figure was made for each cube. Each subplot shows Z(blue), Y(green), and X(red) components plotted on a companded scale, linear for magnitude less than 50 uV and logarithmically for larger magnitude. Decay curves are plotted for gates from 100 uS to 25 mS.**

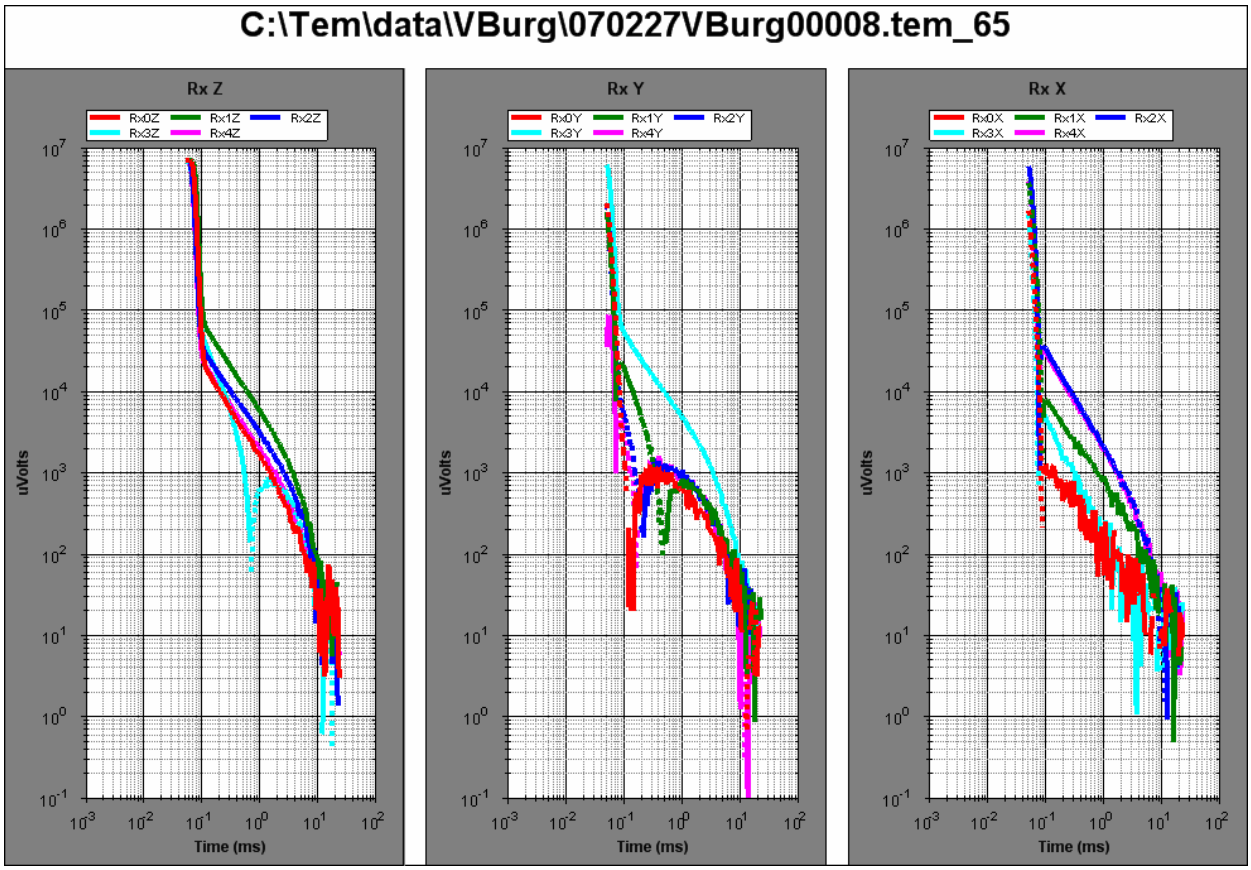


**Figure 10 Sample display of signals using TEMView. Positive signals are shown with solid trace. Negative signals are shown with dashed trace.**

**Discussion**

Comments on these data are made in the column labeled *Analyst Notes* in the detailed table in the Appendix.

# Dynamic Data Sets

The effects of collecting data dynamically are a complicated convolution of movement of the sensors and data acquisition parameters (block time, decay length, DAQ performance). For dynamic testing, we devised a brief set of tests that can hopefully be used to establish the importance (or unimportance) of some of these effects. Most of the tests involved continuously collecting data points as the MPV moved along a profile directly over a target. Movement speed and acquisition parameters were varied in preset patterns. For completeness, we performed one test where the MPV moved along a predetermined path/grid covering a 2x2 meter area over the target.

## Data Acquisition

To complete these tests, we developed software that could read and average a stream of coordinates produced by the test stand. The test-stand software was modified so this string resembled a standard $GGA string from a GPS receiver. Then we were able to use most of the software that we usually use to track data produced by a GPS receiver, but in this case it was produced by the test stand.

The test stand produced data coordinates at the rate of about 5 positions/second. This is a little bit slower than our usual GPS setting of 10 or 20 positions per second but it is useful.

We used data block times covering the range of capabilities of the MPV (0.033s to 2.7s). Shorter block times should be useful to collect reasonably undistorted data in a dynamic environment. Longer block times should offer the opportunity to study distortion of decay transient shapes due to movement.

### Procedure

For these tests, the procedure was similar to static tests. A physical geometry was established and data parameters were set. Then an automated data collection sequence was initiated and all data points from this sequence were stored in one file.

### Discussion

For the dynamic data sets, the reference coordinate of the test stand was changed. In these data, the aluminum calibration ring is located at (100,200) and the target is located at (250,200). Furthermore, while static coordinates are contained in the LocalX and LocalY variables in the data sets, dynamic coordinates are contained in the Lat and Lon variables.

For these dynamic data, acquisition clock times and coordinates are key elements. Due to a software error, the DAQ clock time coordinated with actual acquisition of a transient was not saved. However, CPU clock time coordinated with acquisition of a GPS string (a test stand string in this case) is available in the Matlab variable GPSCPUTime. The GGA string from the test-stand controller contained a UTC clock time, similar to UTC clock time in a GGA string, and this time was recorded. But in this case, UTC clock time was actually the CPU clock time of the test stand controller and contained only one second resolution.

## Data Review

Review of these dynamic data is challenging. As well, analysis of these data will be even more challenging.

### Procedure

The procedure for an extremely brief review of these data was:

- Convert to Matlab using the same procedure as for static data. However, in the initial conversion, GPSTime was not included. So the dynamic data files were re-converted after adding that refinement. The additional variable is GPSCpuTime and it is the number of seconds since midnight.
- Convert the decay transients to a single number by integrating the decay curve for decay times > 100 µs.
- Compute magnitude of the decay for each cube by adding Z, Y, and X components in quadrature.
- Filter the time file and Y coordinate file to estimate true time/coordinates.

A sample is shown in Figure 11.

### Discussion

The procedure used to review this data is by no means an attempt to analyze the data. The analysis was undertaken primarily to assure that the data could be useful for these studies. There are at least two issues associated with these data. The first is latency in terms of acquiring a data point and storing it in combination with its spatial coordinates. If the spatial coordinates lag the acquired data, then a profile will appear at an incorrect position. Two profiles across a target, done in opposite directions will easily show if latency is an issue. This is the approach shown here.

The second issue is distortion of decay transients because they are not acquired in a fixed position. Preview of the static data shows that spatial variations are rapid versus coordinate, changing substantially sometimes for movements of a couple centimeters. No effort was made to review or display this issue from these data.

Latency in these data is a combination of latency in the test stand software, in the serial communications link, and in the DAQ. Although latency was observed, amount of latency in MPV alone is not easy to determine. Yet an upper limit on latency can probably be determined.

The position output rate from test stand was about 5 readings/s. At the MPV's faster data collection speeds, this resulted in repeated coordinates for two or more data points. Therefore, analysis requires that the reported and recorded coordinates be somehow interpolated or smoothed in order to obtain an estimate of position at the time of the measurement.

The Matlab m-file, ShowTransientsDynamic.m, is used to attempt to show the presence of latency. Part of its output is shown in Figure 11. The data file for this plot was 070302VBurg00015.mat. This is a data file of four speeds over a 60mm Mortar at 35cm depth, using a block time of 0.1 s. The data show clear latency at the faster speeds but show that data are probably OK at speeds of 10 cm/s or less.

Further comments are included in Table 4 in the appendix.

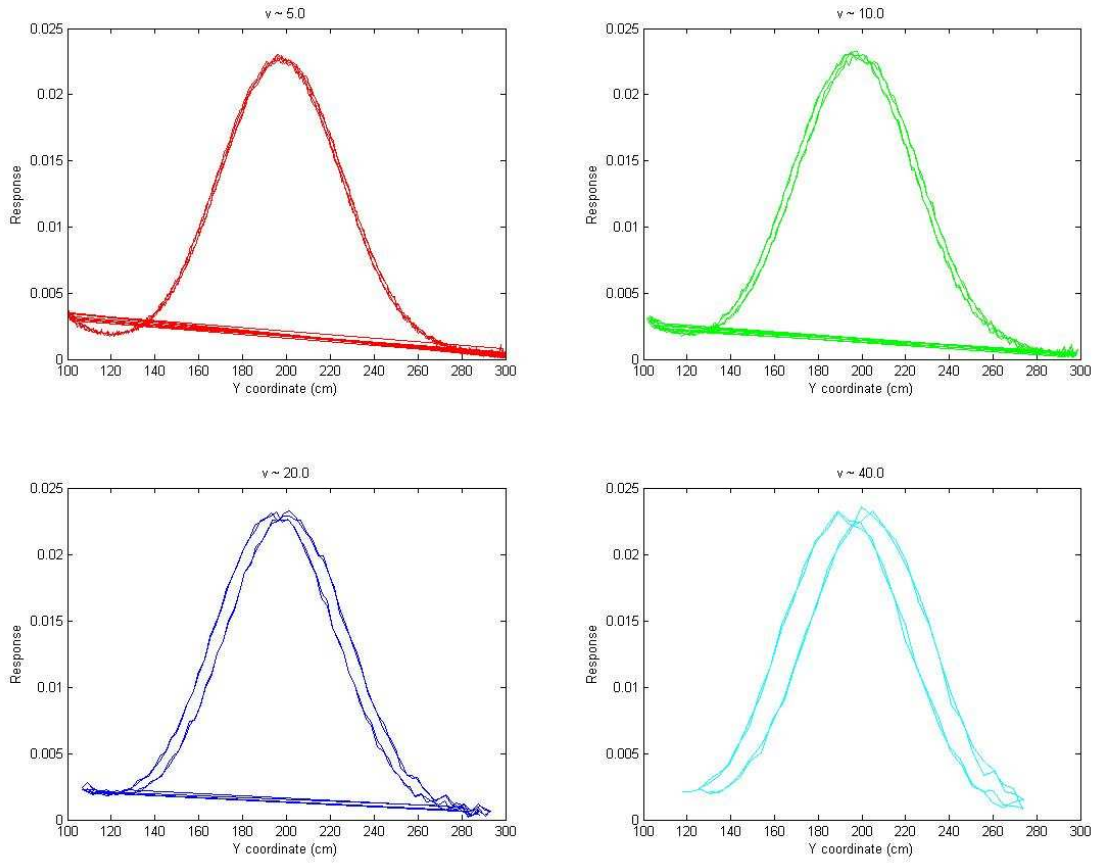


**Figure 11 Latency demonstrated from up and back profiles over a 60mm mortar at 35 cm depth. Velocities are in cm/s.**

# ACKNOWLEGEMENTS

We were ably and generously assisted by WES personnel Cliff Morgan principally, and Charles Hahn as needed. Charles fabricated the wood suspension truss that attached the MPV to the test stand trolley, helped by allowing us to continue measurements when Cliff was absent, and transported Joan to WES when Dave traveled to Washington for the IPR. Cliff was willing to work long hours and, as well, provided competent technical insight and observation. Importantly, Cliff willingly made modifications to the test stand control software to allow it to communicate with the software in our DAQ. He also prepared and checked the *trajectory files* that were used to establish movement and positioning of the test-stand trolley during these tests.

# APPENDIX

**Table 4**

Detailed descriptions of acquired data files.

| *Orientation* | *Depth (cm)* | *Filename* | *Start (MST)* | *End (MST)* | *Notes* | *Analyst Notes* |
|---|---|---|---|---|---|---|
| | | | | | | |
| ***Background*** | | | | | | |
| NA | NA | 070227Vburg00002 | 8:20 AM | 8:34 AM | 7 sec/point. Only half of points recorded. 2" Trailer ball for calibration target. | x' in this column represents checkmark that data file has been reviewed. |
| NA | NA | 070227Vburg00003 | 8:46 AM | 8:50 AM | Bad file, collecting every other point, caused by changing stacks to two | |
| Background with all points | | | | | Calibration source is Aluminum ring at (0,100) | |
| NA | NA | 070227Vburg00004 | 9:22 AM | 9:38 AM | 94 data points. | x |
| horizontal nose +Y | 25 | 070227Vburg00005 | 9:51 AM | 10:08 AM | | x |
| **STATIC TESTS** | | | | | | |
| **Response for 60 mm mortar** | | | | | | |
| horizontal nose +Y | 25 | 070227Vburg00006 | | | Bad file | Data lost for 25 cm depth |
| horizontal nose +Y | 35 | 070227Vburg00007 | 10:15 AM | 10:25 AM | finished 5 minutes early? | Missing one part of grid: missing stations for x = 110. |
| horizontal nose +Y | 45 | 070227Vburg00008 | 10:30 AM | 10:46 AM | | x |

| | | | | | | |
|---|---|---|---|---|---|---|
| vertical nose up | 25 | 070227Vburg00009 | 10:58 AM | 11:08 AM | Time for grid seemed quick. Possibly movement at each point? | Data appears visually OK. |
| vertical nose up | 35 | 070227Vburg00010 | 11:17 AM | 11:33 AM | | Appears there may be a slight misalignment in x direction since x transient does not have good null on centerline. Misalignment says target is to +x side of centerline by a cm or two. |
| vertical nose up | 45 | 070227Vburg00011 | 11:37 AM | 11:52 AM | | x |
| vertical nose down | 24.5 | 070227Vburg00012 | 12:04 PM | 12:20 PM | | x |
| vertical nose down | 34.5 | 070227Vburg000013 | 12:24 PM | 12:40 PM | | x |
| vertical nose down | 44.5 | 070227Vburg00014 | 12:41 PM | 12:56 PM | | x |
| 45 deg nose up -Y | 25 | 070227Vburg00015 | 1:10 PM | 1:26 PM | | x |
| 45 deg nose up -Y | 35 | 070227Vburg00016 | 1:30 PM | 1:45 PM | | x |
| 45 deg nose up -Y | 45 | 070227Vburg00017 | 1:46 PM | 2:02 PM | | x |
| 45 deg nose down +Y | 25 | 070227Vburg00018 | 2:18 PM | 2:34 PM | | x |
| 45 deg nose down +Y | 35 | 070227Vburg00019 | 2:36 PM | 2:54 PM | Dave on test stand taking photos | x |
| 45 deg nose down +Y | 45 | 070227Vburg00020 | 2:56 PM | 3:12 PM | | x |
| **Response of BLU-26 bomblet** | | | | | | |
| horizontal | 25 | 070227Vburg00021 | 3:23 PM | 3:38 PM | copper band horizontal | x |
| horizontal | 35 | 070227Vburg00022 | 3:39 PM | 3:55 PM | copper band horizontal | x |
| horizontal | 45 | 070227Vburg00023 | 3:55 PM | 4:12 PM | copper band horizontal | x |

| | | | | | | |
|---|---|---|---|---|---|---|
| horizontal nose +Y | 50 | 070227VburgBigGrid | 4:52 PM | ? | 2791 points collected (one partial grid) prior to apparent comm error. | |
| | | | | | | |
| **Response of 81 mm mortar** | | | | | | |
| vertical nose up | 35 | 070228Vburg00001 | 7:39 AM | 7:55 AM | 7:45 AM Cliff and Chuck SW of test stand setting up show and tell. | x |
| vertical nose up | 45 | 070228Vburg00002 | 7:57 AM | 8:13 AM | EM-63 was used during run near test = must rerun. In between runs 2 & 3, Chuck swapped out serials cable connected to our laptop in trailer and picked up cable on ground between test stand and trailer. | Data appear by eye to be useful -- would be a good repeat against file 070228VBurg0003. EM63 appears to have caused some noise but not a lot. |
| vertical nose up | 45 | 070228Vburg00003 | 8:15 AM | 8:31 AM | Rerun of above. Then, show and tell for Colonel = delay start of next run. | |
| vertical nose up | 55 | 070228Vburg00004 | 9:02 AM | 9:18 AM | | x |
| vertical nose down | 35 | 070228Vburg00005 | 9:26 AM | 9:42 AM | | x |
| vertical nose down | 45 | 070228Vburg00006 | 9:46 AM | 10:02 AM | 95 data points | x |
| vertical nose down | 55 | 070228Vburg00007 | 10:08 AM | 10:24 AM | | x |
| horizontal nose +Y | 35 | 070228Vburg00008 | 10:30 AM | 10:46 AM | | x |
| horizontal nose +Y | 45 | 070228Vburg00009 | | | empty file, double clicked "Acquire"? | |

| | | | | | | |
|---|---|---|---|---|---|---|
| horizontal nose +Y | 45 | 070228Vburg00010 | 10:47 AM | 10:57 AM | 93 data points, acquisition time only 10 minutes, error at end of run. Data appears OK. | x |
| horizontal nose +Y | 55 | 070228Vburg00011 | 10:59 AM | 11:14 AM | | x |
| 45 deg nose up -Y | 35 | 070228Vburg00012 | 11:25 AM | 11:40 AM | Cliff has code problems prior to run | x |
| 45 deg nose up -Y | 45 | 070228Vburg00013 | 11:45 AM | 12:00 PM | 95 data points | x |
| 45 deg nose up -Y | 55 | 070228Vburg00014 | 12:02 PM | 12:17 PM | | x |
| 45 deg nose down +Y | 35 | 070228Vburg00015 | 12:23 PM | 12:39 PM | | x |
| 45 deg nose down +Y | 45 | 070228Vburg00016 | 12:40 PM | 12:56 PM | | x |
| 45 deg nose down +Y | 55 | 070228Vburg00017 | 12:58 PM | 1:13 PM | | x |
| **Response of 57 mm projectile** | | | | | | |
| vertical nose up | 25 | 070228Vburg00018 | 1:18 PM | 1:34 PM | | x |
| vertical nose up | 35 | 070228Vburg00019 | 1:36 PM | 1:51 PM | | x |
| vertical nose up | 45 | 070228Vburg00020 | 1:53 PM | 2:09 PM | | x |
| | | | | | RH = high this morning. Threat of severe thunderstorms. Set up with backpack sitting on platform, not hanging (higher) over side, same approx. X location. | |
| **Characterize RF spectrum** | | | | | DCG talked to Ben at IPR yesterday; they agreed on fewer orientations and depths - no nose down for 57 mm. | |

| | | | | | | |
|---|---|---|---|---|---|---|
| | | 070301VBurgfft00001 | | 6:45 AM | Bad data file | Data lost, |
| **Response of 57 mm projectile, continued** | | | | | | |
| horizontal nose -Y | 25 | 070301VBurg00001 | 6:59 AM | 7:15 AM | Dave notices BG in third and fourth decade. Investigates. No obvious metallic source. Wipe off top of 0 sensor, no change in signal. Decide to proceed with measurement series. | Data appear by eye to be useful. |
| horizontal nose -Y | 35 | 070301VBurg00002 | 7:37 AM | 7:53 AM | Watch for noise spikes in these decays, lightning to west | Data appear useful. |
| horizontal nose -Y | 45 | 070301VBurg00003 | 7:54 AM | 8:13 AM | | Data appear useful but some X components pretty noisy. |
| 45 deg nose up -Y | 25 | 070301VBurg00004 | 8:17 AM | 8:33 AM | | x |
| 45 deg nose up -Y | 35 | 070301VBurg00005 | 8:35 AM | 8:51 AM | | Cube 3X often noise in this and other data sets. |
| 45 deg nose up -Y | 45 | 070301VBurg00006 | 8:53 AM | ? | 35 points | |
| 45 deg nose up -Y | 45 | 070301VBurg00007 | ? | 9:09 AM | 58 points | Matlab files 00006 and 00007 merged into 070301VBurg00006_7.mat |
| **Response of Steel Sphere** | | | | | | |
| NA | 25 | 070301VBurg00008 | 9:16 AM | 9:32 AM | | x |
| NA | 35 | 070301VBurg00009 | 9:33 AM | 9:49 AM | Stop for rain, put poncho over MPV | Data appear OK |
| NA | 45 | 070301VBurg00010 | | | Empty file, hit "acquire" twice | |
| NA | 45 | 070301VBurg00011 | 10:15 AM | 10:30 AM | | Cube 0 data pretty noisy |
| **Response of Prolate Spheroid** | | | | | | |

| | | | | | | |
|---|---|---|---|---|---|---|
| vertical | 25 | 070301VBurg00012 | 10:41 AM | 10:56 AM | Thunder, move MPV to center. ~12:15 PM Dave tucks plastic bag around backpack, which is still near edge of platform | Response is very large but not clipped. |
| vertical | 35 | 070301VBurg00013 | | | Dave stops run | |
| vertical | 35 | 070301VBurg00014 | 12:30 PM | 12:45 PM | Dave up on platform during run to look for cause of transient to 5th decade | Early, large transient on Z channel. Eventually traced to transmitter difficulties and coupling of primary that was slow to turn off. |
| **Difficulties in rain storm** | | | | | | |
| | | 070301VBurgWet00001 | | | MPV at (0,0), on cradle, tarp on | |
| | | 070301VBurgWet00002 | | | at (0,0), on cradle, tarp off | |
| | | 070301VBurgWet00003 | | | on tall kitchen trash can above grid, but no change | |
| | | 070301VBurgWet00004 | | | no change, remove 2" blue painter's tape from outside of loops, also remove 2 wire ties holding umbilicus | |
| | | 070301VBurgWet00005 | | | same as Wet00004 | |
| | | 070301VBurgWet00006 | | | back on cradle, turn heater on SW of MPV | |
| | | 070301VBurgWet00007 | | | No good, heater too close | |

| | | | | | | |
|---|---|---|---|---|---|---|
| | | 070301VBurgWet00008 | | | Heater off, out of the way. Same transient, even though wood is drying out some. Remove heater and core. | |
| | | 070301VBurgWet00009 | ~2:10 PM | | No change, put heater back on | |
| | | 070301VBurgWet00010 | 2:30 PM | | Another test | |
| | | 070301VBurgWet00011 | 2:31 PM | | transmitter off | |
| | | 070301VBurgWet00012 | 2:32 PM | | transmitter on | |
| | | 070301VBurgWet00013 | 2:35 PM | | worked on transmitter. Interchanged 2 resistors, tightened 1 connection. NOTE: remainder of 070301 data are collected with transmitter disassembled on platform | |
| | | 070301VBurgWet00014 | 2:56 PM | | transient is lower | |
| | | 070301VBurgWet00015 | 2:58 PM | | at (0,100) | |
| | | 070301VBurgWet00016 | 3:01 PM | | at (0, 0). Decide to start ellipsoid series over | |
| **Response of Prolate Spheroid Continued** | | | | | | |
| vertical | 25 | 070301VBurg00015 | 3:06 PM | 3:23 PM | | x |
| vertical | 35 | 070301VBurg00016 | 3:24 PM | 3:39 PM | | x |
| vertical | 45 | 070301VBurg00017 | 3:50 PM | 4:06 PM | | x |
| horizontal Y | 30 | 070301VBurg00018 | 4:21 PM | 4:37 PM | | x |
| horizontal Y | 40 | 070301VBurg00019 | 4:38 PM | 4:53 PM | | x |
| 45 deg nose up -Y | 30 | 070301VBurg00020 | 5:17 PM | 5:33 PM | | x |
| 45 deg nose up -Y | 40 | 070301VBurg00021 | 5:36 PM | 5:52 PM | Bring backpack and transmitter into to trailer for night. Park MPV at center | x |

| | | | | | | |
|---|---|---|---|---|---|---|
| | | | | | | |
| **DYNAMIC TESTS** | | | | | Test stand origin changed to (100, 100), so AL ring is located at (100, 200), and target is at (250,200). | |
| | | | | | | |
| **Test software communications and registrations** | | | | | | |
| NA | 34.5 | 070302VBurg00001 | 8:48 AM | | Test in debug environment | |
| **Test effects of speed for one block time and repeats** | | | | | | |
| | 4 repeat profiles each speed (two up and back) | | | | | |
| NA | 34.5 | 070302VBurg00002 | 9:19 AM | | Decimated wave form | |
| **Test effects of block time while maintaining same decay length, using a symmetric target, at a fast speed** | | | | | | |
| | Eight repeat profiles each setting (four up and back), fast speed (> 0.4 m/s) | | | | | |
| NA | 34.5 | 070302VBurg00003 | 9:46 AM | 9:50 AM | 0.1s blk, 1 rpt | Need to smooth coordinates because tem collection interval faster than coordinate interval |
| NA | 34.5 | 070302VBurg00004 | | | Abort | Unknown problem in these files. Fastest data (0.1s blk) seems to show more latency. Difficulty with multiple points, see text. |
| NA | 34.5 | 070302VBurg00005 | 9:51 AM | 9:55 AM | 0.3s blk, 3 rpt | |
| NA | 34.5 | 070302VBurg00006 | 9:56 AM | 10:00 AM | 0.9s blk, 9 rpt | |
| NA | 34.5 | 070302VBurg00007 | | | Abort | |
| NA | 34.5 | 070302VBurg00008 | 10:02 AM | 10:06 AM | 2.7s blk, 27 rpt | |
| **Demonstrate best possible response using short block times with small variations in decay length** | | | | | | |
| | Eight repeat profiles each setting (four up and back), fast speed (> 0.4 m/s) | | | | | |

| | | | | | | |
|---|---|---|---|---|---|---|
| NA | 34.5 | 07002VBurg000009 | 10:08 AM | 10:12 AM | 0.33s blk, 1 rpt | Clear latency in these files |
| NA | 34.5 | 070302VBurg00010 | 10:13 AM | 10:16 AM | 0.1s blk, 9 rpt | |
| NA | 34.5 | 070302VBurg00011 | 10:18 AM | 10:21 AM | 0.03s blk, 3 rpt | |
| **Collect full waveform data at fast speed with differing block times** | | | | | | |
| NA | 34.5 | 070302VBurg00012 | 10:22 AM | 10:25 AM | Full wave form, 0.1s blk | These data sets were not reviewed |
| NA | 34.5 | 070302VBurg00013 | 10:27 AM | 10:29 AM | Full wave form, 2.7s blk | |
| NA | 34.5 | 070302VBurg00014 | 10:34 AM | 10:38 AM | Full wave form, 0.9s blk | |
| **Test effects of speed using short block times over 60mm mortar at four different speeds** | | | | | | |
| | Four repeat profiles each speed (two up and back) | | | | | |
| 45 deg nose down +Y | 35 | 070302VBurg00015 | 10:49 AM | 10:55 AM | | Latency apparent but need more work to display difference vs speed |
| | | | | | | |
| **Demonstrate response of 60 mm mortar over a 2x2 m grid at varying survey speeds** | | | | | | |
| 45 deg nose down +Y | 35 | 070302VBurg00016 | 11:10 AM | 11:24 AM | Slow speed, 0.1s blk 1 repeat | |
| 45 deg nose down +Y | 35 | 070302VBurg00017 | 11:25 AM | 11:34 AM | Med speed | |
| 45 deg nose down +Y | 35 | 070302VBurg00018 | 11:34 AM | 11:41 AM | Med speed | |
| 45 deg nose down +Y | 35 | 070302VBurg00019 | 11:42 AM | 11:47 AM | Fast speed | |
| Response of 105 mm projectile | | | | | | |
| | | | | | | |
| **STATIC TESTS CONTINUED** | | | | | | |
| **Response of 105mm projectile** | | | | | | |
| horizontal nose -Y | | 070302VBurg00020 | 12:04 PM | | Abort | |
| horizontal nose -Y | | 070302VBurg00021 | 12:06 PM | | Abort | |
| horizontal nose -Y | | 070302VBurg00022 | 12:08 PM | | Abort | |

| | | | | | | |
|---|---|---|---|---|---|---|
| horizontal nose -Y | 40 | 070302VBurg00023 | 12:09 PM | 12:25 PM | | x |
| horizontal nose -Y | 60 | 070302VBurg00024 | 12:27 PM | 12:43 PM | | x |
| 45 deg nose up -Y | 40 | 070302VBurg00025 | 12:53 PM | 1:13 PM | | x |
| 45 deg nose up -Y | 60 | 070302VBUrg00026 | 1:22 PM | 1:37 PM | | x |
| vertical | 40 | 070302VBurg00027 | 1:43 PM | 1:58 PM | | x |
| vertical | 60 | 070302VBurg00028 | 1:59 PM | 2:14 PM | | x |
| **Response of 20 mm shell** | | | | | | |
| 45 deg nose down +Y | 25 | 070302VBUrg00029 | 2:21 PM | 2:36 PM | | Signals pretty noisy |
| 45 deg nose down +Y | 35 | 070302VBUrg00030 | 2:36 PM | 2:52 PM | | ditto |

# C Laser Positioning System Characterization

# TECHNICAL REPORT

For

**Contract #W913E5-06-C-0003**

# PRECISION POSITION AND ATTITUDE MEASUREMENTS: An evaluation of the integration of the ArcSecond "Indoor GPS" System into the MPV

Submitted to

**Technical Point of Contact**
**Dr. Kevin O'Neill**
U. S. Army Engineer R&D Center,
Cold Regions R&E Laboratory
72 Lyme Road
Hanover, NH 03755-1290
(603) 646-4312
Kevin.Oneil@erdc.usace.army.mil

By

**D. D. "Skip" Snyder**
**Snyder Geoscience, Inc**
671 Crescent Ct
Grand Junction, CO 81505

Point of Contact: Donald D. Snyder
Telephone: (970) 254-0330
Email: skips@bresnan.net

July 16, 2007

# 1 Introduction

The man-portable vector (MPV) TEM system is a TEM system consisting of a single transmitter loop and 5 tri-axial receiver cubes that sample the secondary field at 4 points in the plane of the transmitter loop and at a 5$^{th}$ point on the axis of the transmitter loop and elevated above it. The system is being developed by G&G Sciences, Inc. under contract with the U. S. Army Engineer R&D Center (Cold Regions Research & Engineering Laboratory).

The MPV is designed to be deployed at the end of a hand-held boom for acquiring precision TEM data for target classification using dynamic-mode data acquisition. That is, the antenna assembly will be swept over an area of interest rather than used to acquire data statically at discrete data points. However, regardless of whether the data are statically or dynamically acquired, a number of authors have established through the use of numerical models and experimental data that the accuracy of the sensor position and attitude for high quality target parameter extraction must be "sub-centimeter" [1-3]. The MPV system seeks to achieve the requisite accuracy in sensor attitude and position through the use of a Metris/ArcSecond (ASI) laser positioning system. This system can provide millimeter level position accuracies with static measurements and sub-centimeter accuracies for dynamic measurements [4, 5]. The MPV hardware system includes an array of 3 ASI receivers that are rigidly attached to the transmitter coil. Because the positions of the ASI receivers with respect to the MPV geometry are precisely known, one can compute the position and attitude of the MPV antenna array in the ASI work space. G&G Sciences, Inc has integrated the acquisition of the ASI positioning data into its acquisition software so that each data point acquired by the MPV includes the positions of the 3 ASI sensors attached to the MPV antenna array.

In this report, I evaluate the ASI system in the context of providing accurate estimates of sensor location and attitude. Because this evaluation was conducted using the MPV data acquisition software, the work also confirms that ASI positioning system has been correctly integrated into the MPV hardware and its acquisition software. And secondly, the results provide experimental verification of the mathematics that I have developed for reduction of the ASI data from a set of 3 positions (9 data values) to a single position plus three attitude angles (heading, pitch, and roll). The experiments and results described here are limited to static measurements, mainly due to the requirement that I submit a report by the end of July. This leaves open the question how well the system performs under dynamic conditions. Such an evaluation will require a motorized transport system with at least 2 axes of motion. Such a facility is available at Huntsville. And the USGS has recently completed a transport shuttle located at the Federal Center in Denver.[1] If budget and time permit, it will be desirable to conduct a series of dynamic experiments at one of these facilities.

In the section 2 of the report, I describe the 3-ASI-receiver geometry and its relationship to the MPV antenna. In order to conduct the static experiments with mm precision, I constructed a planar position template (platform) and a circular mounting base for the 3 receivers. The results of the experiments are presented in section 3.

[1] David Wright, USGS, personal communication.

# 2 Experiment Description

Figure 1 shows a functional block diagram of the MPV. It is not my intent to describe the system in detail. However, the diagram in Figure 1 provides context for discussion. As shown in the Figure, the MPV includes three ASI receivers and their associated PCE Modules. These ASI assemblies receive and process laser signals received generated by 3 satellite transmitters and periodically report the receiver position via 3 RS232 data channels. MPV data points are acquired in time blocks that contain an integer number of base transmitter periods (Repeats). In the dynamic acquisition mode, the block period is frequently set to 0.1s and the Repeat factor is set to 9 (base period = 90Hz).[2] The acquisition software stores the average position of each receiver over the intervening block period. The operator can set a Stack Counter when he/she desires an average over several blocks. In the results reported here, the block period was always 0.1s and most of the results are reported for a stack count of 1. The ASI system was setup for a 10 Hz report rate.[3]

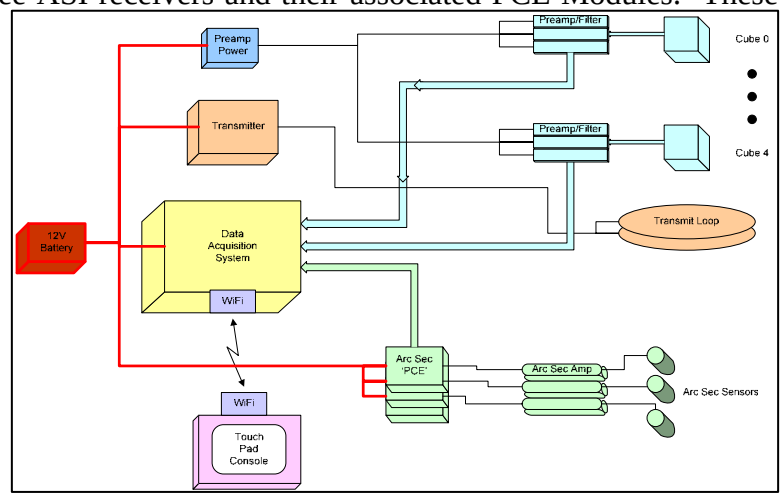


Figure 1: A functional block diagram of the MPV system. The diagram shows how the (3) ASI sensor/PCE assemblies are integrated into the overall data acquisition system (blue boxes).

## 2.1 ASI Sensor Geometry

The 3 ASI receivers are arrayed in the form of an isosceles right triangle as illustrated in Figure 2. The plane of the triangle is made parallel to the plane of the transmitter loop. The sensor array is mounted so that the vertex of the 90° angle is the vertex closest to the center of the transmitter loop and the perpendicular bisector from that vertex to the base of the triangle is on the loop's axis of bilateral symmetry. By our coordinate convention, therefore, the bisector is parallel with the platform y-axis and, consequently, the base of the triangle is parallel with the platform x-axis.

## 2.2 Experimental Apparatus

In order to verify that the MPV system has indeed been properly integrated with the ASI receiver array and (as well) to provide an assessment of the intrinsic precision with which the resulting system can be used to measure position and attitude, it was necessary to construct an apparatus for locating the MPV or other test fixture upon which the ASI sensor array is mounted with a precision commensurate with the precision of the stated ability of the ASI system (i.e., mm

[2] The MPV acquisition software (TEMAcquire) allows its operator to select block periods as small as 33.3ms and as long as 2.7s (spaced at multiplicative intervals of 3 – i.e., 33.3, 100,300,900,2700 ms). Similarly, the Repeat factor can be set to 3, 9, 27, and 81.

[3] The ASI documentation indicates that the PCE report rate can be set as high as 40Hz. The high report rate would be desirable for dynamic acquisition.

precision). My location platform or template consists of a heavy duty frame constructed of pressure-treated 4”x4”’s. I used a half-sheet of ¾”x4’x8’ as a floor. I assembled the frame and the attached the floor first with screws. Then, I drilled ½” holes and pegged the whole structure together with a number of ½” oak dowels. Each dowel was glued in place with aliphatic resin glue. The screws were then removed leaving a 4’x4’ platform containing no metal. The platform is shown in Figure 3. Using a half sheet of 3/16” pegboard as a template, we drilled a uniform grid of holes 9/16” holes into the platform on 4” centers. I believe that the holes are located with a precision of ±2 mm.

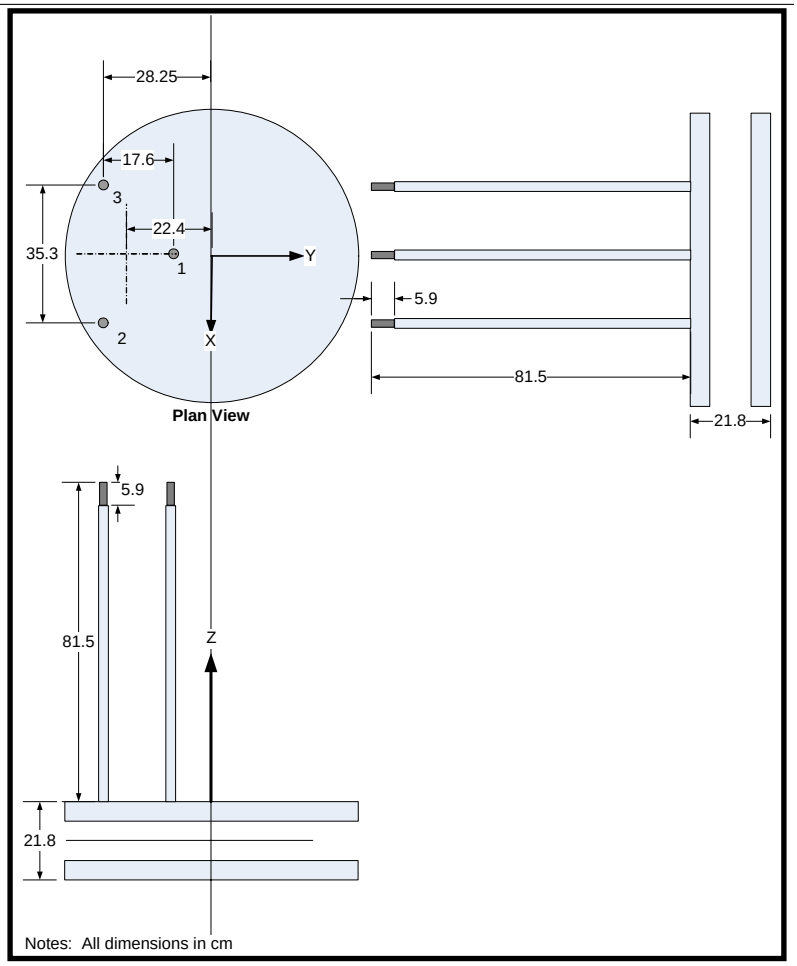


Figure 2: Dimensioned drawing showing the location of the 3 ASI receivers with respect to the MPV transmitter loop.

I mounted the 3-receiver sensor array to a circular base (2-ft diameter) constructed of ¾” plywood reinforced at its outer diameter with an 2” annular ring and at its center with 6” diameter circular piece both of the same ¾” plywood material. The pieces were laminated together using aliphatic resin glue. The resulting base has a double thickness of ¾” plywood (1¼” nominal thickness) on the outer edge and at its center and has a single thickness in an annular ring on the underside of the ring. This annular depression was sufficient to provide clearance for the threaded couplings used to attach the 3 legs of the ASI receiver mounting structure. The circular base was drilled through the center and a long ½” dowel was driven through the resulting hole. The centering dowel precisely locates the ASI array

Figure 3: Photo showing the precision location template and the ASI sensor holder used during the experiments described in this report.

fixture when it is inserted into one of the holes drilled through the platform. I estimate that the fixture is located to within ±3 mm (±2 mm random error in the position of the indexing holes and ±1 mm between the hole diameter (5/16 in) and the locating dowel (1/2 in)). Finally, the PVC legs of the ASI sensor holder were mounted such that the center of area (located along the perpendicular bisector of the base at 1/3 the triangle's height) coincided with the center of the circular base. The resulting experimental ASI assembly is located at one of the indexed locations on the template base in Figure 3.

Figure 4: Photo showing platform position index holes. The level and the Brunton compass were used to set the platform at a known strike and dip.

The template base is (approximately) a plane. And therefore, by a process of cross-leveling in one of the primary grid directions and elevating in the other, I can introduce a known angle between the ASI coordinate system and the platform coordinate system (see Figure 4). With any known inclination of the location template, a 360° rotation of the sensor base will produce a periodic oscillation of the 3 attitude angles.

## 2.3 Data Acquisition and Reduction

Prior to acquiring position data with the MPV system, it is first required that the ASI system be setup. The setup procedures are detailed in the ***Indoor GPS User's Guide*** prepared by Metris/ArcSecond [5]. Once the transmitter "constellation" has been set up, the system setup is accomplished using the ASI utility software program ***WorkSpace.*** Additional information about the operation of the ASI hardware and Workspace can be found in the ***Constellation Operations Manual***, a manual in preparation by the USACE at Huntsville.[4]

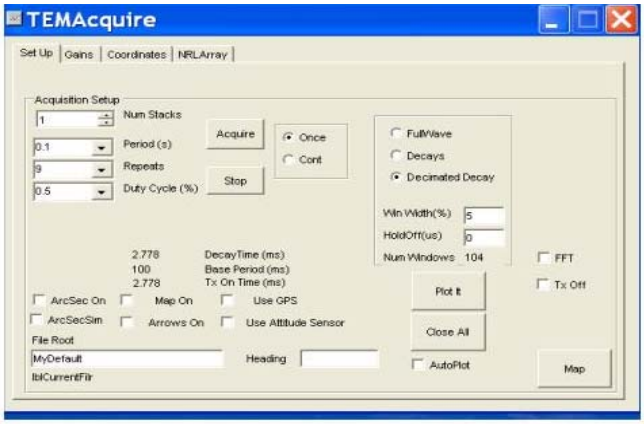


Figure 5: Screen view of the TEMAcquire GUI. The GUI allows the operator to select ArcSecond positions by checking the ***ArcSec On*** checkbox located in the lower left side of the screen.

**Acquisition** - After a valid setup file[5] has been generated, the data acquisition was accomplished with the MPV acquisition program (TEMAcquire). Figure 5 shows a screen capture of the TEMAcquire GUI. To activate acquisition of ArcSecond data, one simply checks the "ArcSec On" checkbox. For the experiments I describe in the next section, the position of the ASI sensor array that is shown mounted to its circular base and positioned on the location template in Figure 3 one simply needs to press the ***Aquire*** button and a data point file with the root name (in the case of the screen shown in Figure 5) of ***MyDefault*** plus an 5 digit fiducial (e.g., "00001") and the extension "*.tem is stored (a file name of ***MyDefault00001.tem*** ). Of course if the ASI receiver array is attached to the antenna platform, the data point would also include the 16 transients corresponding to the 15 receiver loops plus a transient channel that monitors the transmitter loop current. For the purposes of the tests described here, however, I was only interested in the ASI position data attached to each of the files we generate when we click the ***Acquire*** button.

**Reduction** - At the present time, TEMAcquire simply stores the (x,y,z) positions of the three ASI receivers. It required several post-acquisition processing steps to analyze and display the results shown in the next section. These steps are:

1. **Extract Position Data from *.TEM Files:** The *.tem files are binary files. All downstream processing was performed in ***Mathematica***. I wrote a Windows program called TEM_ArcSecond that will extract the positions of the 3 ASI sensors from a *.tem file and write them to an *.csv text file. I show a screen capture of the TEM_ArcSecond GUI in Figure 6.

[4] The constellation Operations Manual was sent to me by Scott Millhouse after I completed the testing described in this report. Many questions that I had as a result of my work with the ArcSecond system are answered in that manual.

[5] The MPV software expects an ASI setup file named ***crrel.3di*** to be located in the directory c:\tem\data on the MPV data acquisition computer.

2. **Translate Coordinate System:** The coordinates saved by TEMAcquire are in the ArcSecond coordinate system.[6] For the experiments described in this report, I am interested in a local coordinate system with an origin either at the location of the sensor base or at one of the grid points of the location template.

3. **Rotate Coordinates:** I rotated coordinates after translation into a system in which local y is parallel to the columns of the position index grid, and (presumably by construction) the local x coordinate is parallel with the rows of position index grid.

4. **Calculate Position and Attitude:** After the ArcSecond coordinates have been translated and rotated, I calculated position and attitude using algorithms described in the Appendix.

5. **Other Processing Steps:** The first four steps were applied to all data. Other steps were applied as required for the particular experiment. When required, I discuss those steps in the next section.

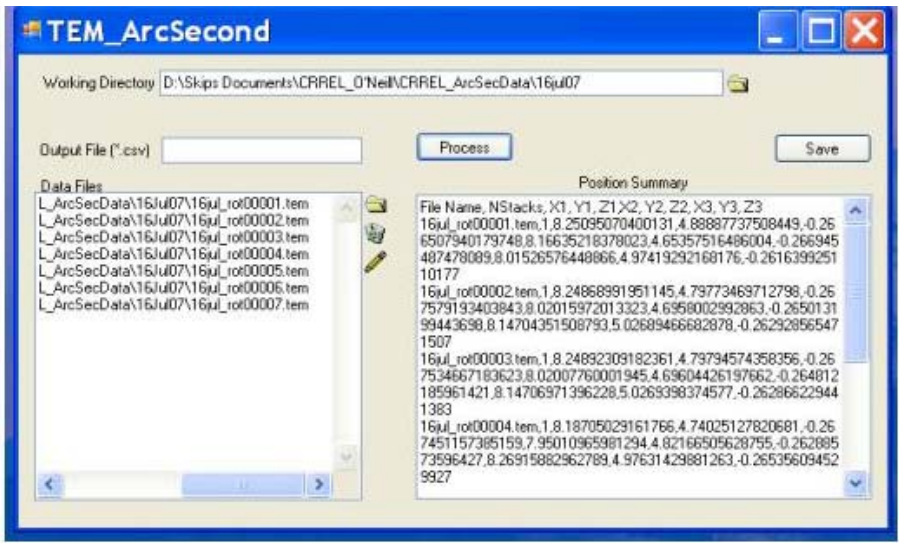


Figure 6: Screen capture of the TEM_ArcSecond GUI. The text box on the left contains the names of the *.tem files to be processed. The text box on the right is a view of the resulting *.csv data that will be saved.

[6] The ArcSecond coordinate system is determined by the setup file generated after setting up the 3 transmitters. It is an orthogonal xyz coordinate system with z vertical, x determined by the baseline between transmitters 1 and 2, and y is such that it is orthogonal to ArcSecond x and z and forms a right-handed coordinate system.

# 3 Experiments

All data were acquired in the static mode. The basic data acquisition parameters were set for a block period T = 0.1s. Unless otherwise indicated the data were acquired with a stack count of 1. I used a higher stack count to see how a time average of the ASI positions improved the measurement statistics.

The experiments fall into two classes:

1. **Translation Experiments:** In these experiments, the sensor holder I acquired data with the sensor holder occupying a 5 x 5 grid of points on 8" (20.32 cm) centers. The rotational orientation of the sensor holder was held constant.
2. **Rotation Experiments:** In these experiments, I acquired data at a single grid point while rotating the sensor head about its axis a total of 360° in steps of 45°.

## 3.1 Translation

The first set of data I acquired was a translation experiment conducted by measuring the 25-pt grid over a level location template. The results of this experiment are shown in Figure 7. I performed the same experiment with the plane pitched up in the y direction, respectively, at angles of 4.4° and 8.2°. I have provided a summary of the RMS errors for position and attitude measurements for the three translation experiments in Table 1.

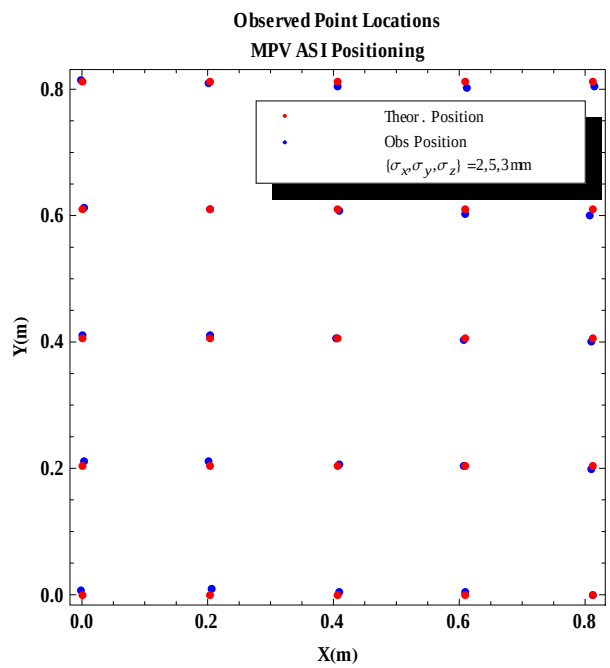


Figure 7: Plot showing the true location (red dots) and observed locations for a translation experiment over a level plane. The RMS errors in position is on the order of millimeters.

Table 1: Table of RMS position and heading errors for 3 translation experiment conducted on the location platform for three different (average) dips (0°, 4.4°, and 8.2°).

| Experiment | RMS Position Error (mm) | | | Attitude (Plane Fit) | | | ATI Mean Attitude & RMS Error | | | | | |
|---|---|---|---|---|---|---|---|---|---|---|---|---|
| | X(cm) | Y(cm) | Z(cm) | Hdg | Pitch | Roll | Hdg | err | Pitch | err | Roll | err |
| Translation - Level | 2 | 5 | 3 | 0.0 | 0.0 | 0.7 | -1.7 | 0.4 | -0.3 | 0.3 | 0.7 | 0.2 |
| Translation - dip 1 | 2 | 3 | 2 | 0.0 | 4.4 | 0.9 | -1.7 | 0.4 | 4.2 | 0.3 | 0.8 | 0.2 |
| Translation - dip 2 | 4 | 13 | 4 | 0.0 | 8.2 | 0.5 | -0.9 | 1.2 | 8.0 | 0.4 | 0.4 | 0.4 |

## 3.2 Rotation Experiments

By means of a systematic rotation of the sensor array about its vertical axis, which presumably passes through the center of the circular sensor base described in Section 2, we accomplish three things:

1. **Establish centroid position** – Because it was necessary to remove the 3 ASI sensors and their associated preamplifiers from proximity to the MPV transmitter and receiver cubes, the sensors are mounted on PVC legs at a height of 81.5cm above the top of the transmitter loop. In mounting the sensor legs to the base, I took great care to establish that the 3 sensors are at the same height to within an error of ±1 mm. I am thus assured that the plane through the sensitive point of the 3 receivers is reasonably parallel with the plane of the transmitter. However, this does not establish that a vector perpendicular to the two planes will pass through the center of area of the legs and also the center of area of the sensors. If there is any eccentricity (which there is!), it will be established by the rotation experiment.
2. **Validation of** the **algorithms –** These experiments serve to validate the algorithms that I developed to reduce the raw ASI data to position and attitude angles. Those algorithms and formulas have been included in the Appendix.
3. **Determination of Attitude Angle Sensitivity and Errors**

**Centroid Position** – I conducted two rotation experiments. The first one was conducted on the level plane, the second on the plane with a dip of 4.2° dip in the negative local y direction. The results of the first rotational experiment are shown as polar plots in Figure 8. Figure 8A represents results from a data set where the stack count was 1. Figure 8B is for a data set where the stack count was set to 8. In the Figure, the red circle represents the mean radius of the 9 positions used to generate the point plots. There is clearly a systematic error that represents an eccentricity between the axis of rotation and the center of area of the three ASI receivers. That eccentricity is 9 mm. It is also clear by comparing Figures 8A and 8B that stacking even a few positions significantly reduces the scatter of the data.

**Algorithm Validation –** When the rotation experiment is conducted on a dipping plane, the three attitude angles (heading, pitch, and roll) are modulated by the angle of rotation of the sensor and this modulation has a period of 360°. In Figure 9, I summarize the observed modulation of each of the attitude angles as a function of the angle of sensor array rotation. The points represent the observed attitude angles. The solid magenta curve represents the theoretical attitude angles based on an assumed dip (along the y-axis) of 4.2°. Those curves indicate that

the algorithm used to compute the heading, pitch, and roll is valid in each of the 4 quadrants defined by the attitude angles. The actual algorithm that I used is detailed in the Appendix.

**Attitude Angle Sensitivity and Errors (Translation) –** In Table 1, I have provided summary statistics for the attitude angles as derived from the translation experiments. In those experiments, I measured position and attitude at 25 discrete points with the attitude held constant.[7] The random errors in heading reported for the level surface and the surface when dipping at 4.4°[8] are consistent with my personal estimate of how well I can orient the sensor array. The random heading error for the platform when dipping at 8.2° increased dramatically. I believe (without experimental verification) that this increase in error may be due to poor lighting and haste on my part. My experiments with this setup were conducted last. It was getting late in the day (~8:30 pm) and there was a thunderstorm in the area. Table 1 also establishes that there is a systematic error in the heading of -1.7° (assuming that the results for a dip of 8.2 are suspect). The systematic error in roll most likely indicates that the platform cross-level was slightly off.

**Attitude Angle Sensitivity and Errors (Rotation) –** I have tabulated the error statistics for the three rotation experiments (Table 2): a) Rotation on a level reference plane; and b) Rotation on two dipping (4.4° and 8.2°) reference planes. These statistics characterize the errors between the observed attitude angles and the theoretical attitude angles based on the rotation angle of the sensor head and the attitude of the plane as determined from a least squares fit of 25 grid points measured on its surface (Table 1). Consistent with the summaries for the translation experiments, the rotation experiments suggest that the random errors in the three attitude angles are on the order of ±0.5°. The systematic error in the heading angle is significant and is probably due to a small twist in the sensor holder. This error, if confirmed when the sensor array is mounted on the MPV, can be easily corrected. The systematic errors in both pitch and roll are statistically insignificant.

Table 2: Statistics summarizing systematic and random errors observed with three rotation experiments. All data were acquired with a stack count of 1.

| Experiment | Heading (deg) | | Pitch (deg) | | Roll (deg) | |
|---|---|---|---|---|---|---|
| | Mean Error | Std Dev | Mean Err | Std Dev | Mean Error | Std Dev |
| Rotation - Level Plane | -2 | 0.6 | -0.4 | 0.7 | 0.2 | 0.7 |
| Rotation - 4.2 deg dip | -0.7 | 0.6 | -0.2 | 0.5 | 0.2 | 0.6 |
| Rotation - 8.2 deg dip | -0.5 | 0.5 | -0.2 | 0.3 | 0.1 | 0.3 |

[7] The constant attitude is based on the assumption that the location platform is truly planar and that the ASI sensor holder was oriented along the y-axis. I estimate that I as able to orient the sensor head to within an error or ±2mm using angular index lines marked on the circumference of the circular sensor base. This means that the random error of orientation that I introduced is approximately ±0.3°. The standard deviation

[8] I am using the dip as estimated by fitting a plane through the mean sensor locations.

# Rotation Experiment: Level Plane

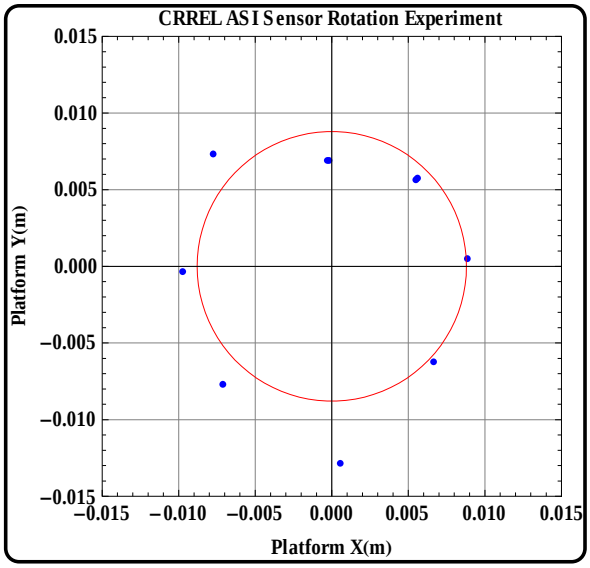


A) Stack Count = 1

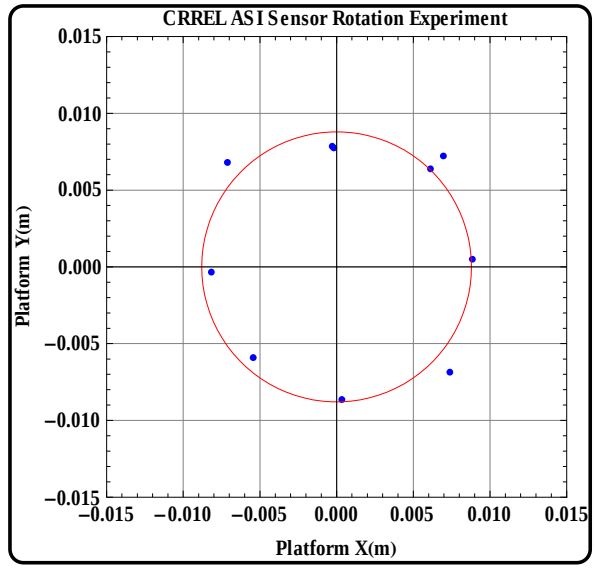


B) Stack Count = 8

Figure 8: The results of a 360° sensor rotation about a common point on a level plane. The points represent the average horizontal position of the 3 ASI sensors (after removal of the mean). The sensor head was rotated in increments of 45° starting at 0° (y-axis). The red circle has a radius equal to the average radius of those (9) positions. In point of fact, the red circle represents a fit to the data points of a circle with a least mean square error criterion. The right hand panel corresponds to a repeat of the experiment on the left during which the acquisition stack counter was set to 8.

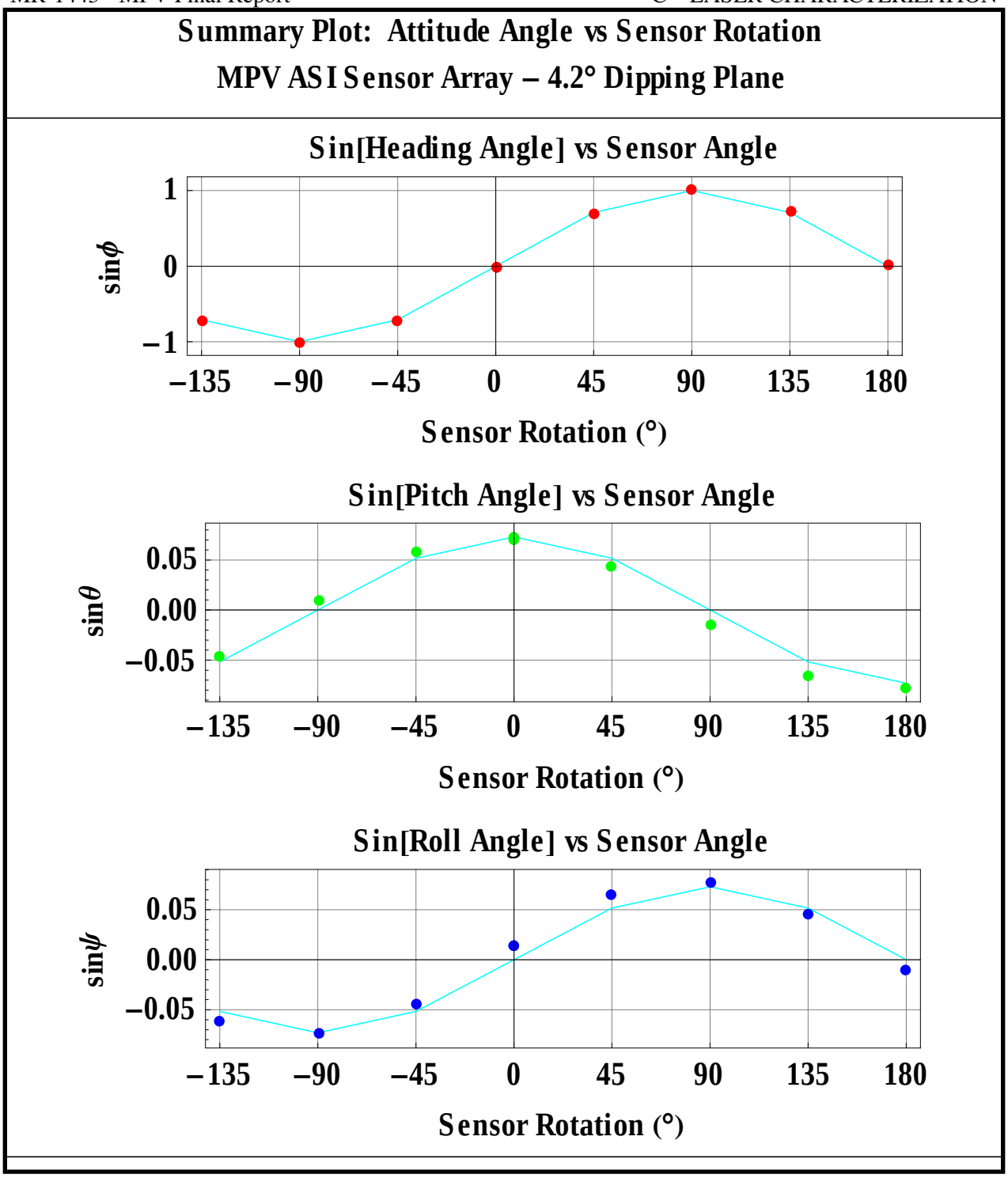


Figure 9: Plot of the sine of the attitude angles (heading, pitch, and roll) as a function of sensor head rotation angle for a plane with a dip of 4.2°. The points represent observed data. The magenta curve represents the theoretical attitude angles assuming a dip of 4.2° in the y direction.

# 4 Conclusions and Recommendations

The experiments described in this report confirm that the ASI system has properly been integrated into the MPV data acquisition system. All of the data I have used to illustrate this report have been captured with the MPV acquisition software set for a data block period of 0.1s while the ASI system was set for a report rate of 10 Samples/sec. So the statistics reported in Tables 1 and 2 indicate that positions can be resolved with "sub-centimeter" accuracy and the attitude angles are resolved with an accuracy of approximately ±0.5°. Of course these error predictions are for static data points. If the sensor head is moving at say 1 m /s, the head will move 10 cm during the acquisition of a single data block. And over this period of time, we capture only a single ASI data point with a 10 Hz report rate. Scott Millhouse informed me that the 10 Hz report rate of the ASI system is "***the most reliable***", that there are ***"frequent drop-outs when the system is set for 20 Hz"***, and that he has ***"never seen the system operate at its specified maximum report rate of 40Hz."*** It will be desirable to operate the ASI system with a report rate of 20 Hz or even 40 Hz when acquiring dynamic data. At least then we will have some sense of the average position of spatial aperture corresponding to the motion of the MPV sensor head during the acquisition period.

There are two significant deficiencies in the work presented here:

1. **No Dynamic Tests**: A good dynamic test will require a motorized gantry.
2. **ASI Receiver Array Mounted on Special Test Fixture:** Ideally these tests should have been conducted with the ASI sensor array mounted to the MPV antenna array. However, the smaller circular mounting base made it practical to precisely locate the antenna array and to rotate it about its center of area. To run the experiments I described in this report with the ASI sensor mounted on the MPV antenna would have required a much more elaborate test fixture and taken significantly longer. I believe that most, if not all, of the objectives were achieved without resorting to a more elaborate test fixture.

**Recommendations for Improvements**:

1. **Increase the dimensions of the ASI receiver triangle**. The height of the ASI receivers is required because the receivers and the associated preamplifiers produce a measurable TEM response when they are placed any closer. The height to base ratio (i.e., 81.5/35.3) creates a structure that can easily bend a few millimeters when, for example, the pre-amplifier cables are pulled taught. The base of the receiver triangle can easily be increased to 65 cm thus making the structure more stable. Furthermore, while in the process of relocating the position of the ASI receiver array, it should be located so that the center of area of the receiver triangle falls on the axis of symmetry of the transmitter loop. The larger dimensions of the ASI sensor will also improve the sensitivity of the attitude calculations.
2. **Procure/Manufacture longer ASI receiver cables.** The cables running between the ASI preamplifiers and the PCE's need to be much longer. These cables are terminated with Limo connectors. They should be available from Metris/ArcSecond.
3. **Repackage the preamplifiers to reduce their EM response.** The amplifiers are mounted in phenolic tubing with aluminum bulkheads at either end. These bulkheads could be

manufactured out of non-conductive material and a substitute connector that is less responsive can be selected. A simpler approach may be to increase the length of the cable running between the ASI sensor and the preamplifier. This approach would allow the preamplifier to be relocated away from the sensor array. Unfortunately, engineering considerations will probably preclude moving the preamplifier any farther away from its sensor.

# 5 References

[1] B. Barrow, Nagi Khadr, and Thomas Bell, "Evaluation of Laser Based Position for Characterization of EMI Signals from UXO," in SAGEEP 2006, Seattle, WA, 2006, p. 10.

[2] K. O'Neill, and Jay Bennett, "New Man-Portable Vector (MPV) Time Domain (TD) Electromagnetic Induction (EMI) Sensor and Physically Complete Processing Approaches for UXO Discrimination Under Realistic Field Conditions," Hanover, NH: USACE-CRREL, 2004, SERDP Proposal No. 05-UXO03-012.

[3] J. T. Smith, H. Frank Morrison, "Estimating Equivalent Dipole Polarizabilities for the Inductive Response of Isolated Conductive Bodies," IEEE Trans. on Geosc. & Rem. Sens., vol. 42, pp. 1208-1214, 2005.

[4] Metris, "Large-Scale Metrology and Measuring Solutions: Geophysical Mapping," 2007, http://www.indoorgps.com/Applications/geoMapping.aspx

[5] ArcSecond_Inc, "Indoor GPS User's Guide 1.1," 2005.

[6] S. Millhouse, "Innovative Navigation Systems to Support Digital Geophysical Mapping," USACE-Huntsville, Washington, ESTCP Cost & Performance Report 2004. http://www.estcp.ort/documents/techdocs/UX-0129.pdf

# Appendix

*Reduction Algorithm for MPV ASI Sensor Array*

**D. D. "Skip" Snyder**
Snyder Geoscience, Inc

## 1 General

The ArcSecond, Inc (ASI) sensor array that is to be mounted on the MPV consists of 3 ASI receiver/preamplifier assemblies arrayed in the shape of an isosceles right triangle. The plane of the triangle is elevated some distance above the plane of the MPV transmitter in order to attenuate the secondary fields arising from the metal parts of the ASI assembly. A dimensioned drawing of the sensor array is provided as Figure 1 in the body of the report. In Figure 1 below, I depict the sensor array as an isometric drawing and identify several reference points.

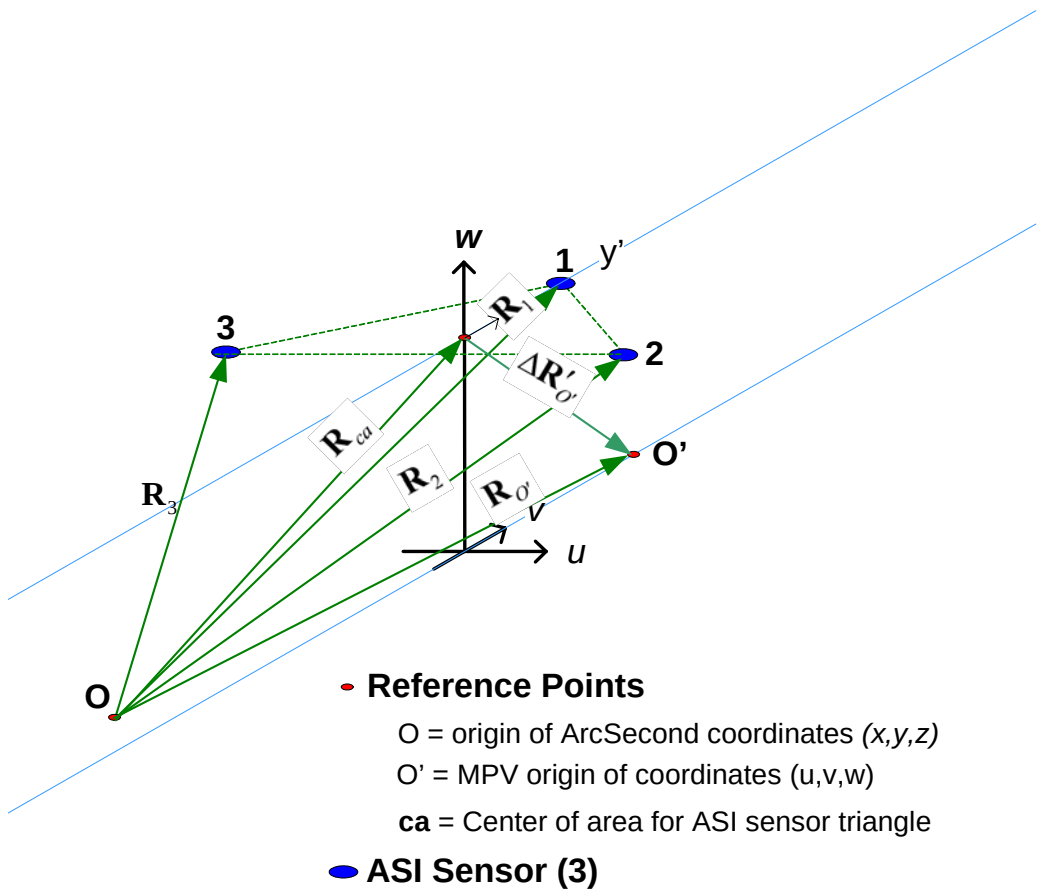


**Figure 1.** The definitions and nomenclature conventions for the ArcSecond sensor array being used in the MPV

Figure 1 identifies the three ASI receivers. The vectors $\mathbf{R}_1$, $\mathbf{R}_2$, and $\mathbf{R}_3$ represent the three positions reported by the ASI system and stored in the TEM data point. These coordinates are in the ArcSecond coordinate system. The vector $\mathbf{R}_{\mathrm{ca}}$ represents the position of the centroid of area for the triangle formed by the 3 ASI sensors. $\Delta \mathbf{R}'_{O'}$ is the offset vector from the center of area (CA) of the sensor array to the MPV reference point (i.e., the geometric center of the transmitter loop $\mathbf{O}'$). Typically, analysis of a target anomaly is carried out in a coordinate system whose origin is located at the point **O'.** Reduction of the ASI position data consists of three steps:

1. Compute attitude angles (heading, pitch, and roll) of the ASI sensor structure with respect to the ArcSecond coordinate system.
2. Compute the position of the ASI receiver array centroid. (ArcSecond coordinates) and, if necessary, correct it for an offset to an MPV reference point.

# 2 MPV Attitude Angles

Before deriving relations for the attitude angles, we must first define them. Figure 2 illustrates the definitions for the three attitude angles, heading ($\phi$), pitch ($\theta$), and roll ($\psi$). I list below their definitions in words:

1. **Heading Angle ($\phi$)**: Heading is the angle between the positive geographic or ArcSecond *y*-axis and the projection of the positive MPV *v*-axis (i.e., local *y*-axis) onto a horizontal plane. Heading is positive when measured in a clockwise direction. One should note that the definition for positive heading angle is not consistent with the right hand rule for rotation.
2. **Pitch Angle ($\theta$):** Pitch is the angle between the horizontal plane and the positive MPV *v*-axis (i.e., local *y*-axis). The pitch angle is positive when the angle of rotation is counter-clockwise when viewed from the positive *u*-axis.

3. **Roll Angle ($\psi$)**: Roll is the angle between the horizontal line the lies in vertical plane defined by the MPV *u* and *w* axes . Roll is positive when the angle of rotation is clockwise when looking toward the positive *v*-axis.

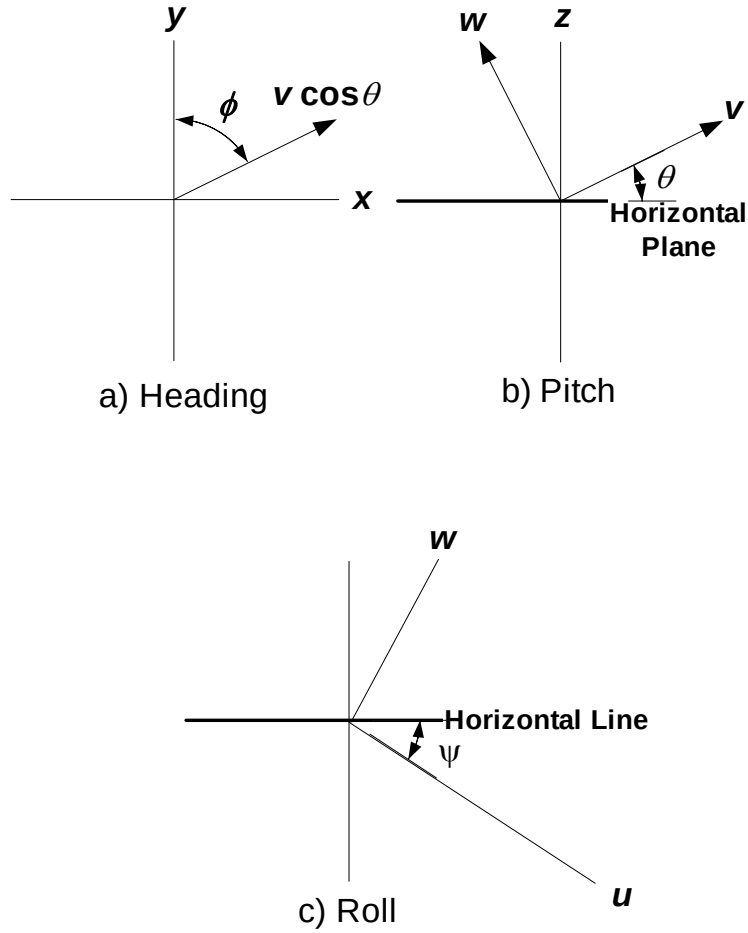


**Figure 2.** Graphic illustrations of the definitions for the elementary angles that describe the attitude of the MPV

## 2.1 Definition of Elementary Rotations

In reducing the sensor positions reported by the ArcSecond system we will be dealing with two coordinate systems: a) the ArcSecond system (*x*,*y*,*z*); b) the MPV system (*u*,*v*,*w*). The attitude angles provide the means for transforming position vectors from one system to the other. To transform from the ArcSecond coordinate system to the MPV coordinate system, we apply a sequence of elementary orthogonal transformations defined as follows:

$$\mathbf{T}_1(\phi) = \begin{pmatrix} \cos\phi & -\sin\phi & 0 \\ \sin\phi & \cos\phi & 0 \\ 0 & 0 & 1 \end{pmatrix} \tag{1}$$

$$\mathbf{T}_2(\theta) = \begin{pmatrix} 1 & 0 & 0 \\ 0 & \cos\theta & \sin\theta \\ 0 & -\sin\theta & \cos\theta \end{pmatrix} \tag{2}$$

$$\mathbf{T}_3(\psi) = \begin{pmatrix} \cos\psi & 0 & -\sin\psi \\ 0 & 1 & 0 \\ \sin\psi & 0 & \sin\psi \end{pmatrix} \tag{3}$$

Given a position vector $\bar{\boldsymbol{v}}$ expressed in the ArcSecond coordinate system, the transformation to its expression in the MPV system is

$$\bar{\boldsymbol{v}}' = \mathbf{T} \cdot \bar{\boldsymbol{v}} = (\mathrm{T}_3 \cdot \mathrm{T}_2 \cdot \mathrm{T}_1) \cdot \bar{\mathbf{v}} \tag{4}$$

To convert from a position vector expressed in the local system to its expression in the ArcSecond system, the transformation relation is

$$\bar{\boldsymbol{v}} = \mathbf{T}' \cdot \bar{\boldsymbol{v}}' = (\mathbf{T}_1' \cdot \mathbf{T}_2' \cdot \mathbf{T}_3') \cdot \bar{\mathbf{v}}', \tag{5}$$

where I am using the notation $\mathbf{T}'$ to signify the matrix transpose of $\mathbf{T}$ .

Of course, one can combine the three elementary transformation matrices into a single 3x3 transformation matrix involving all three attitude angles by performing the two matrix multiplications implied in equation equation 4. However, the terms get a little complicated and for the sake of simplicity and to avoid typographic errors, I have chosen to leave that step out.

## 2.2 Attitude Angles from 3 ASI Sensors

In the following, I develop relations for the attitude angles given the three ASI sensor position vectors, $\mathbf{R}_1$, $\mathbf{R}_2$, and $\mathbf{R}_3$. We first define 3 orthonormal vectors in the direction of the MPV coordinate axes.

$$\hat{\boldsymbol{a}} = (\mathbf{R}_2 - \mathbf{R}_3) / |\mathbf{R}_2 - \mathbf{R}_3| \tag{6}$$

$$\hat{\boldsymbol{b}} = \left(\mathbf{R}_1 - \frac{\mathbf{R}_2 + \mathbf{R}_3}{2}\right) \Big/ \left|\mathbf{R}_1 - \frac{\mathbf{R}_2 + \mathbf{R}_3}{2}\right| \tag{7}$$

$$\hat{\boldsymbol{c}} = \hat{\boldsymbol{a}} \times \hat{\boldsymbol{b}} \tag{8}$$

Since the definitions in equations 6-8 involve the 3 ArcSecond position vectors, the three unit vectors are described in the ArcSecond coordinate system. I will assume that the unit basis vectors for the ArcSecond coordinate system are $(\hat{\mathbf{i}}, \hat{\mathbf{j}}, \hat{\mathbf{k}})$.

Now, using the definitions in Section 1.1, it is easy to write relations for the heading angle and the pitch angle since those angles involve the MPV *v*-axis.

**Heading -** The unit vector $\hat{\boldsymbol{b}}$ is a vector corresponding to the direction of the *v*-axis of the MPV. Define the vector that is the projection of $\hat{\boldsymbol{b}}$ onto the horizontal plane.

$$\bar{\boldsymbol{b}}_H = b_1 \hat{\mathbf{i}} + b_2 \hat{\mathbf{j}} \tag{9}$$

The heading is the angle that the vector $\bar{\boldsymbol{b}}_H$ makes with the ArcSecond *y*-axis so it is given by the relation

$$\phi = \tan^{-1} \frac{b_1}{b_2} \tag{10}$$

**Pitch** - Again using the unit vector $\hat{\boldsymbol{b}}$, we can compute the pitch angle by recognizing that it is the that $\hat{\boldsymbol{b}}$ makes with its projection onto the horizontal plane (equation 9 above). Therefore, we can write the relation

$$\theta = \tan^{-1} \frac{b_3}{\sqrt{b_1^2 + b_2^2}} \tag{11}$$

**Roll** - Roll is a bit more difficult to calculate since it involves finding a line that is both horizontal and lies in the vertical plane defined by the MPV *u* and *w* axes. I first define an unknown unit $\hat{\boldsymbol{h}}$ vector that is in the MPV *u*-*w* plane

$$\hat{\boldsymbol{h}} = h_1\,\hat{\mathbf{a}} + h_2\,\hat{\mathbf{c}} \;=\; h_1\,\hat{\mathbf{a}} \pm \sqrt{1 - h_1^2}\;\hat{\mathbf{c}} \tag{12}$$

Since by definition, $\hat{\boldsymbol{h}}$ must also be horizontal, we must add the constraint that it be normal to a vertical vector ($\hat{\boldsymbol{k}}$)

$$\hat{\boldsymbol{h}} \cdot \hat{\boldsymbol{k}} = \mathbf{0} \tag{13}$$

When we combine equations 12 and 13 we find that there are two possible solutions corresponding to the fact that the horizontal vector $\hat{\boldsymbol{h}}$ may extend in two possible directions. I choose the solution corresponding to the '+' sign yielding the relation

$$\hat{\boldsymbol{h}} = (c_3\,\hat{\mathbf{a}} + a_3\,\hat{\mathbf{c}}) \Big/ \sqrt{a_3^2 + c_3^2} \tag{14}$$

The between the unit vectors $\hat{\boldsymbol{h}}$ and $\hat{\mathbf{a}}$ is the roll angle and it can be found using the vector relation

$$\psi = \sin^{-1}\left[\,(\hat{\boldsymbol{h}} \times \hat{\mathbf{a}}) \cdot \hat{\boldsymbol{b}}\right] \tag{15}$$

I incorporated equations 6-8 together with 10, 11, and 15 to calculate the attitude angles.

# 3 MPV Position

The position of the centroid of area ($\mathbf{R}_{\mathrm{ca}}$ in Figure 1) can be calculated by finding the mean value of the 3 sensor position vectors.

$$\mathbf{R}_{\mathrm{ca}} = \left(\mathbf{R}_1 + \mathbf{R}_2 + \mathbf{R}_3\right) \big/ 3 \tag{16}$$

But the centroid of area is not the reference position on the MPV and we would like to calculate the coordinates of that position. We know the geometry of the ASI sensor array quite well and we know where it is located with respect to the reference MPV reference point **O'** (see Figure 1). Let the vector $\mathbf{\Delta R'}_{O'}$ represent offset from the centroid of area of the sensor array with respect to the MPV reference point expressed in the MPV (i.e. *u*,*v*,*w*) coordinate system. We can transform the offset vector to its expression in the ArcSecond system if we know the three attitude angles ($\phi$,$\theta$,$\psi$) by using equation 5.

$$\mathbf{\Delta R}_{o'} = \mathbf{T'} \cdot \mathbf{\Delta R'}_{O'} = (\mathbf{T}_1{}' \cdot \mathbf{T}_2{}' \cdot \mathbf{T}_3{}') \cdot \mathbf{\Delta R'}_{O'} \tag{17}$$

The position of the MPV reference point is then easily calculated from the ArcSecond position of the centroid of area.

$$\mathbf{R}_{0'} = \mathbf{R}_{\mathrm{ca}} + \mathbf{\Delta R}_{O'} \tag{18}$$

# D Dynamic Response of the MPV Versus Speed

**TECHNICAL NOTE 2007-1**

# DYNAMIC RESPONSE OF THE MPV VERSUS SPEED

**February 12, 2007**

**In support of**

**COLD REGIONS RESEARCH AND ENGINEERING LABORATORY**
72 Lyme Rd.
Hanover, NH 03755-1290

**by**

**David C. George**
G&G Sciences Inc.
873 23 Road
Grand Junction, CO 81505
(970) 263 9714
dgeorge@ggsciences.com

# INTRODUCTION

This technical note provides results of a brief test recently completed to demonstrate dynamic acquisition of the MPV and to test, in a first-look mode, the speed and latency of the system. A corollary of the test was a first test of the ArcSecond system with actual transmitters and a dynamically moving receiver.

# MEASUREMENTS

## Experimental Setup

For these measurements, we first set up the ArcSecond transmitters at three corners a cube approximately 20m on a side. After difficulty setting up and obtaining the calibration, the system finally came alive.

We set the MPV backpack and the MPV antenna array on a PVC frame originally used for our first TEM system, the Navy's so-called AOL-1 system. This frame proved very nice because we were reasonably able to control speed and direction of the MPV antennas.

We recorded the TEM response from all cubes, all channels while moving the system past a 4 inch steel ball located about 12 inches below the MPV antennas (i.e. a very large, very strong target). We made six passes in a straight across the steel ball. Two passes were at a medium speed in both directions, two passes were at a slow speed in both directions, and two passes were at a fast speed in both directions. Speeds were from approximately 0.1 m/s to 0.5 ms.

Lastly we set the MPV statically over the target and took a static measurement of the target's response.

For all of these measurements we used a block time of 0.1 s with 9 repeats. This results in a decay time of 2.8 ms. We recorded decimated data using 0.5% windows – this causes a stored decay curve containing 601 time gates.

## Observations

We learned after the measurements that a mistake in setup resulted in ArcSecond data that was the same for two sensors. This we equivalently had only two channels of ArcSecond data. This was of little consequence because we had no plans to do any orientation calculations. One channel was sufficient to measure distance along our lines.

We learned in these measurements that the ArcSecond receivers are sensitive to battery voltage and that the receiver batteries do not last too long. By the time we completed the sixth pass across the target, the ArcSecond receivers had stopped working. That was when we discovered that if we replaced the battery, they all began working again. The result is that we have data for the purposes herein from only five lines of data. The line that is missing is the second pass on a line done at a fast speed.

After collecting the data we imported it into Oasis Montaj to make the plots shown.

Figure 1 shows a map of the coordinates observed by the ArcSecond system and reported to the TEMAcquire program. The data were recorded in six separate lines but are reported and drawn as if they are on one line. Thus, any two points that are adjacent in the data but 'discontinuous' in space will be connected by a long line.

Figure 2 shows the profiles from the Z component of cube #1, the lower of the two center cubes. The plot is a profile of the average value of a large window in the center of the decay transient versus distance along a line. Distance was computed as the ArcSecond coordinate distance from a manually selected point. The profiles are not associated with a legend. The reader can get a feel for the speed of each plot by looking at the density of data points along each profile.

Figure 3 shows the same data as shown in Figure 2 except that the abscissa is a simple sequential value for measurement number. The profiles have all been lined up manually at their peak.

Figure 4 is a plot of the transient decay curve from two cases. One case is a single data point at the peak of the profile for one of the fast-speed profiles. The other case is a stacked data point taken statically directly over the steel ball.

Table 1 shows data manually taken from the Montaj data base to show velocity for each profile. The speed was computed just for the data across the profile, from about the 3-5% level on each side of the profile.

# DISCUSSION

These data show some obvious points:

- The coordinates reported by the ArcSecond system are not consistent and 'without problems.' Further work will undoubtedly be required to be able to collect data that is precisely located using the ArcSecond system. This is not a conclusion that data that is 'good enough' cannot be collected – it is just notice that the navigation problem is likely to remain a significant problem. The noise in the coordinate data made the data that was plotted versus distance, appear significantly worse than the data that was plotted versus time.
- The data shows that there is perhaps some latency in the system but not very much. Since only one profile was collected with corresponding coordinate data, and since this data was collected at a time when we found the ArcSecond system to be about ready to quit due to a low battery, the coordinates collected for the high speed profile are uncertain and will be repeated. Speeds of these profiles varied from roughly 0.1 m/s to 0.5 m/s. It is interesting that the profiles from our slowest paced lines are the ones that show the most distortion. This likely due to our inability to keep the antenna system at a constant elevation and at a constant speed.
- For this experiment, the speed of traverse past the target did not significantly change the shape of the decay curve as demonstrated in Figure 4. There is perhaps some latency shown in the one profile at the fast speed but that statement is based only one data point and we now know that there are significant uncertainties in the coordinates. The profile shapes do not show any significant skew; but we don't expect any skew because the data are taken point by point with independence between successive points. However, for computations of target parameters, amplitude of the decay curves is more important. These experiments did not address the error in amplitude that is generated because the sensor is moving. To measure that precisely, one must take measurements where the magnitude of the anomaly is rising or falling quickly, and then compare those measurements to data that are statically collected with the antennas placed very precisely.

# CONCLUSIONS

These experiments showed our ability to collect data as we originally planned – i.e. to collect dynamic TEM data simultaneously with coordinates. However, not unexpectedly, the experiments showed that it will not be easy.

**Table 1 Speed of traverse**

| Time at beginning of anomaly (ms) | Distance at beginning of anomaly (m) | Time at beginning of anomaly (ms) | Distance at beginning of anomaly (m) | Average speed over anomaly (m/s) |
|---|---|---|---|---|
| 60422 | 1.77 | 64766 | 2.69 | 0.212 |
| 195188 | 2.99 | 201031 | 1.58 | -0.241 |
| 447904 | 1.41 | 451422 | 3.25 | 0.523 |
| 354656 | 3 | 368961 | 1.49 | -0.106 |
| 267969 | 1.45 | 281250 | 3.03 | 0.119 |

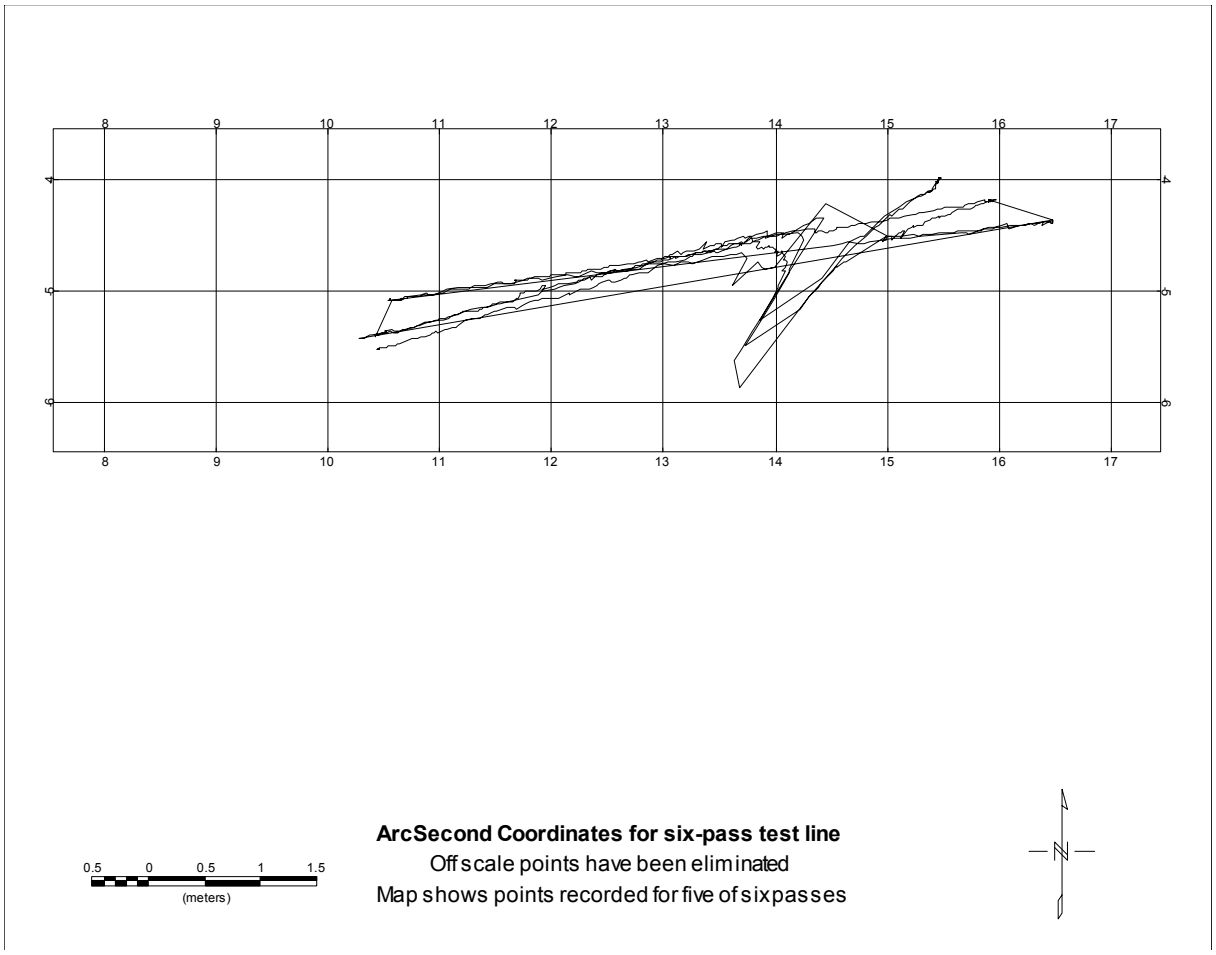


**Figure 1 Map of coordinates reported by ArcSecond system.**

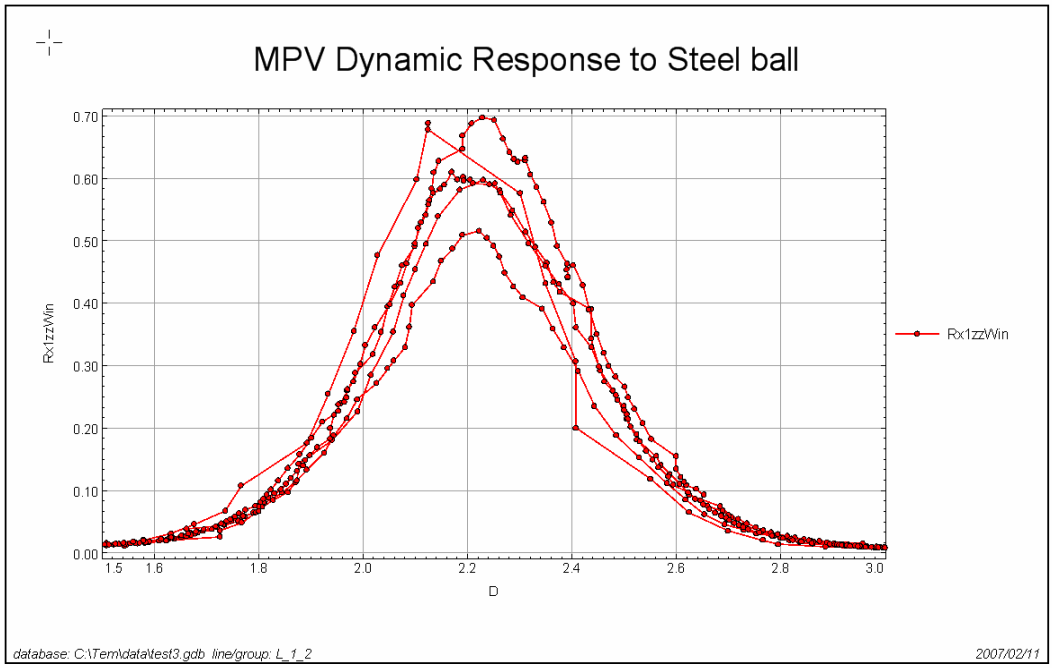


**Figure 2 Dynamic profiles over a four inch steel ball.**

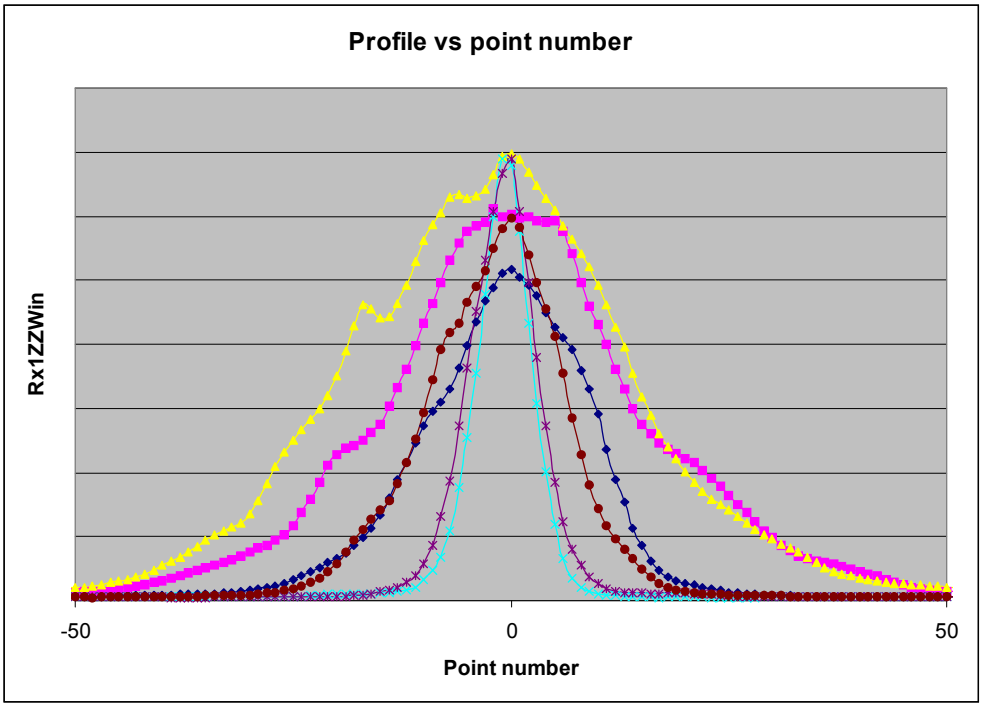


**Figure 3 Profiles like those in Figure 2, but distance is a simple sequence number. Thus the data points are an approximate plot versus time whereas Figure 2 is a plot versus distance.**

**Figure 4 Decay transients from dynamic measurement (Rx1Z) and static measurments (Rx1Z_7)**

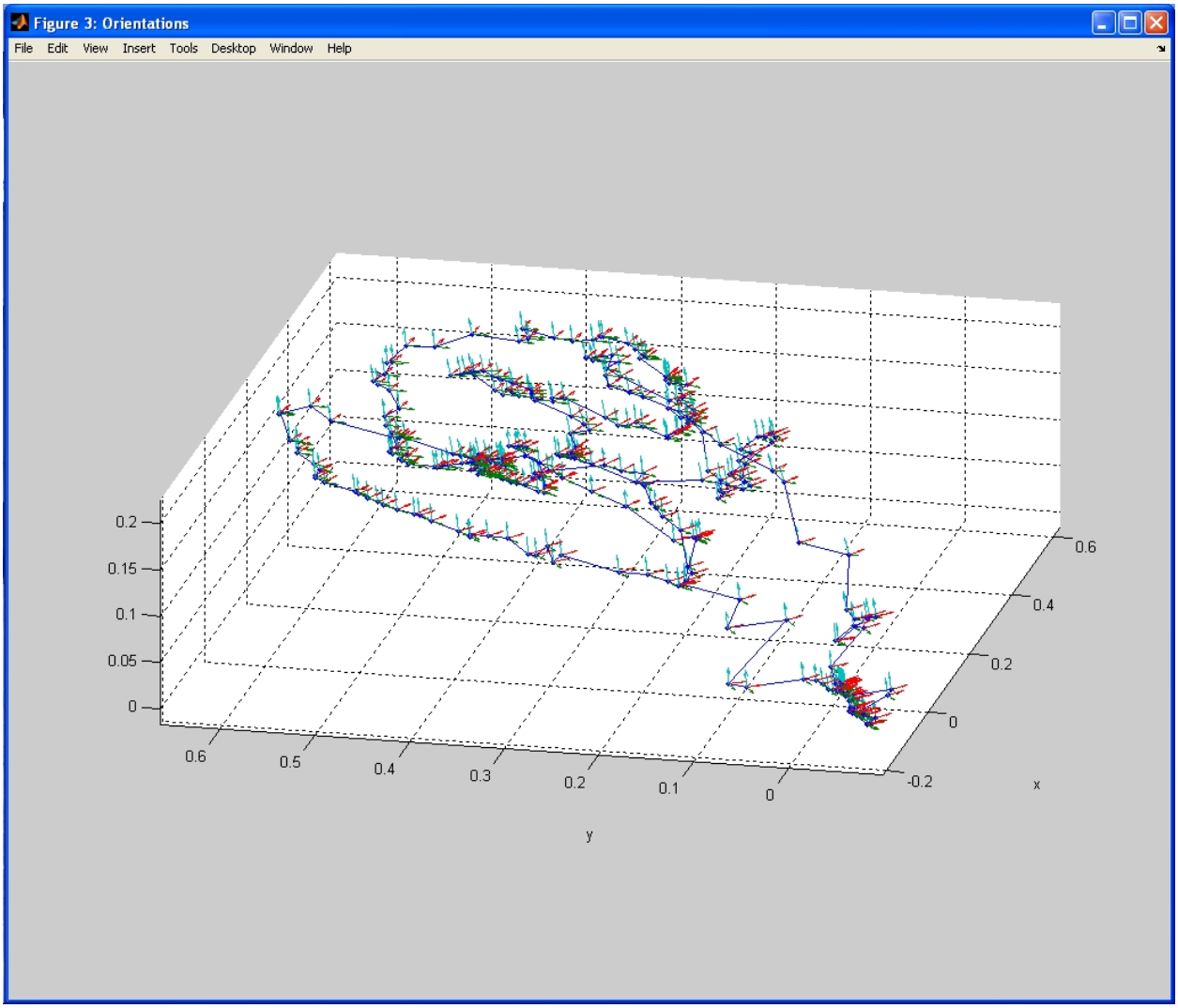


Figure A.2: Position of the MPV head for this data run of 30 seconds (300 positions). Arrows indicate tilt and rotation of MPV head.

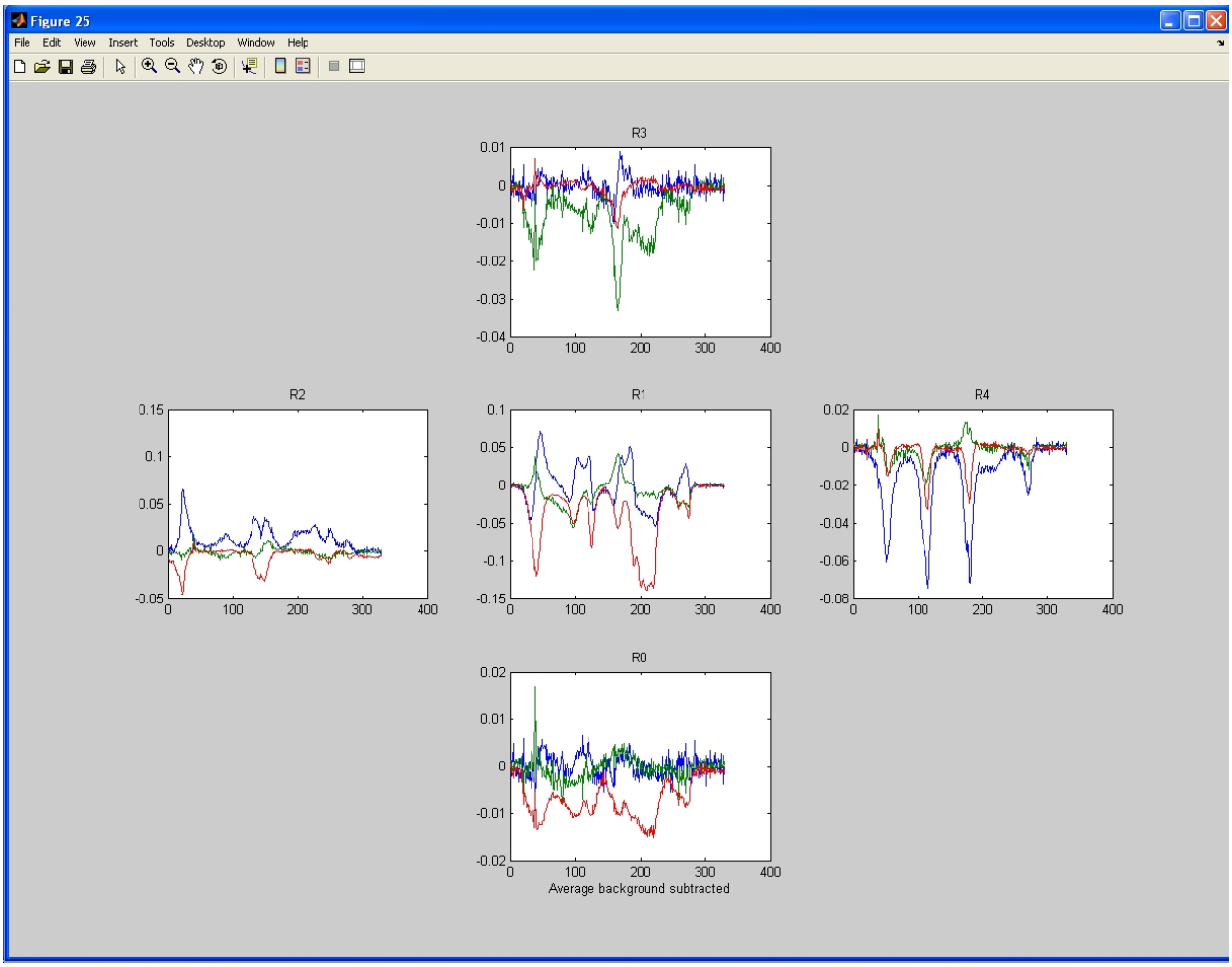


Figure A.3: $H_z$ data values for data run in Fig. A.2.

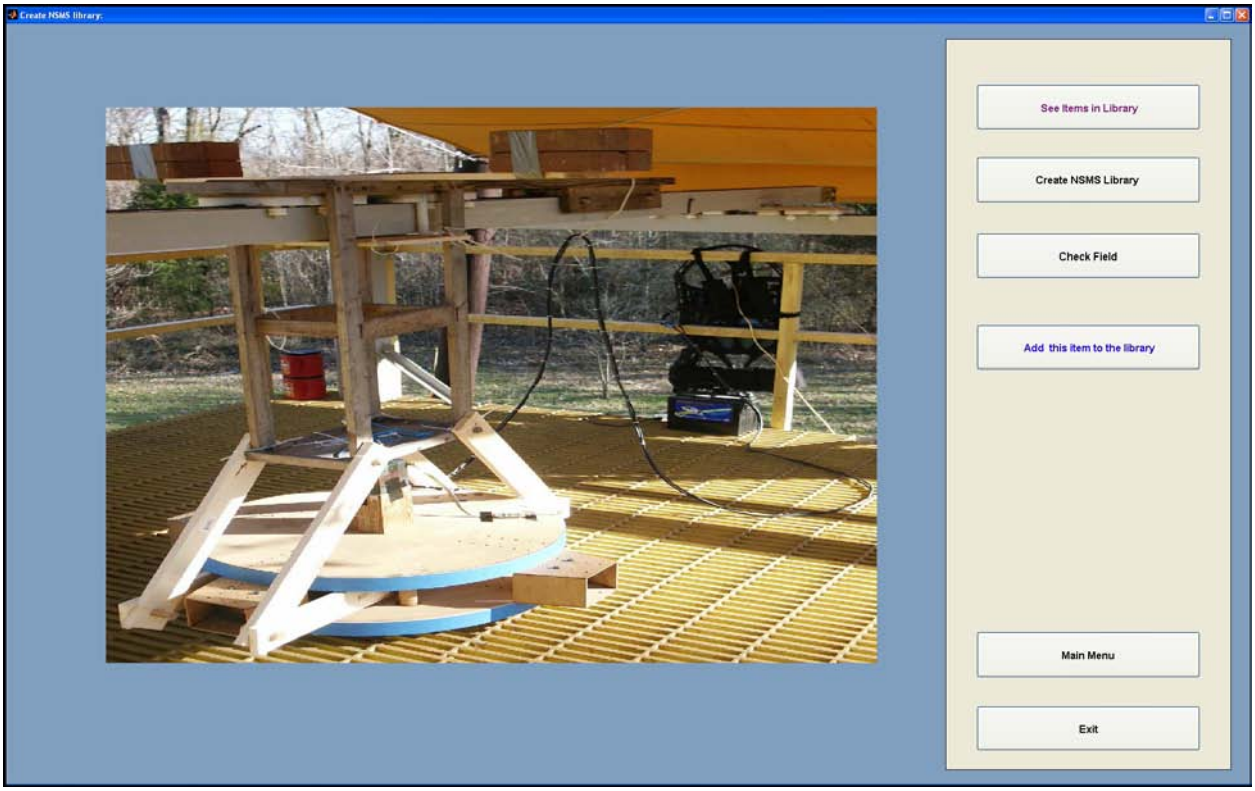


Figure A.4: Adding the current target to the library in EMI.m.

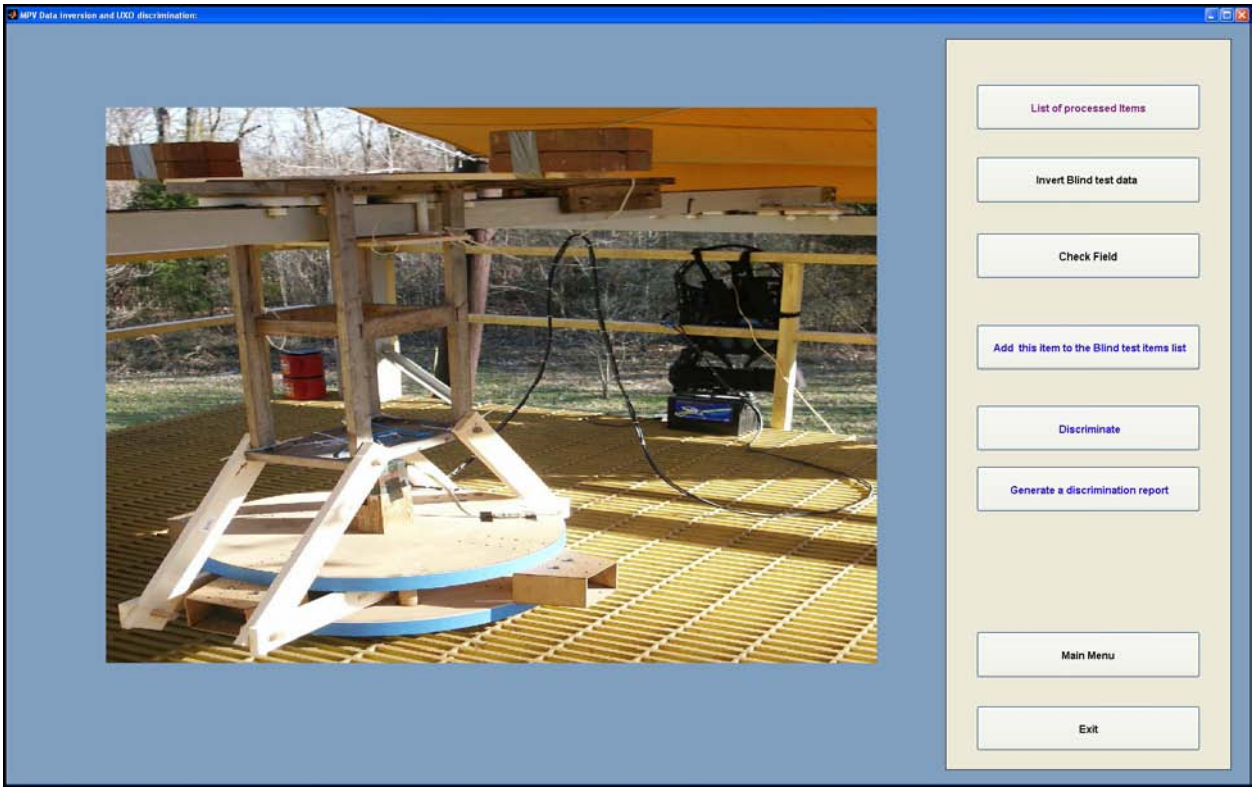


Figure A.5: Discriminate against the current library in EMI.m.

# References


[1] B. Barrow, Nagi Khadr, and H. H. Nelson. Performance of electromagnetic induction sensors for detecting and characterizing UXO. UXO Forum 1996, 1996. Williamsburg, VA. v, 16, 17, 18

[2] D. Sethi and E. Krug, editors. Guidance for Surveillance of Injuries Due to Landmines and Unexploded Ordnance. World Health Organization, Geneva, 2000. 2

[3] O. O. Bilukha, Muireann Brennan, and M. Anderson. Injuries and deaths from landmines and unexploded ordnance in Afghanistan, 2002–2006. J. Amer. Med. Assoc., 298:516–518, Aug. 2007. 2

[4] Unexploded ordnance (UXO): An overview. Federal Advisory Committee for the Development of Innovative Technologies, https://www.denix.osd.mil, Oct. 1996. 2

[5] F. S. Grant and G. F. West. Interpretation Theory in Applied Geophysics. McGraw-Hill, New York, 1965. 2

[6] E. Gasperikova, J. T. Smith, H. F. Morrison, and A. Becker. Berkeley UXO discriminator (BUD). Paper LBNL-62263, 2007. 2, 8

[7] E. Gasperikova, J. T. Smith, H. F. Morrison, A. Becker, and K.N. Kappler. UXO detection and identification based on intrinsic target polarizabilities—A case history. Geophysics, 74:B1–B8, Jan.-Feb. 2009. 2, 8

[8] D. A. Steinhurst, G. R. Harbaugh, J. B. Kingdon, T. Furuya, D. A. Keiswetter, and D. C. George. EMI array for cued UXO discrimination. ESTCP Project MM-0601 Final Report, http://www.serdp.org/Program-Areas/Munitions-Response/Land/Sensors/MR-200601/MR-200601, July 2010. 2

[9] M. D. Prouty. Draft demonstration plan: Detection and classification with the MetalMapper™ at former Camp San Luis Obispo. San Jose, CA: Geometrics, Inc. (http://www.geometrics.com), 2009. 2

[10] M. D. Prouty. MetalMapper system: Camp San Luis Obispo discrimination study. ESTCP Project MM-0603 Interim Data Report, http://www.serdp-estcp.org/Program-Areas/Munitions-Response/Land/Sensors/MR-200603/MR-200603/, July 2009. 2

[11] F. Shubitidze, J.P. Fernández, B. E. Barrowes, Irma Shamatava, and K. O'Neill. Combining NSMS and high-quality MPV-TD data for UXO discrimination. In 2008 IEEE International Geoscience & Remote Sensing Symposium, Boston, MA, July 2008. 2

[12] F. Shubitidze, B. E. Barrowes, Irma Shamatava, J.P. Fernández, and K. O'Neill. Data-derived generalized SEA applied to MPV TD data. In Applied Computational Electromagnetics Symposium (ACES), Niagara Falls, ON, Mar.–Apr. 2008. 2, 62

[13] F. Shubitidze, B. E. Barrowes, Irma Shamatava, J.P. Fernández, and K. O'Neill. Rapid and accurate estimate of the effect of magnetically susceptible soil on MPV–TD sensor data using the method of images. In Direct and Inverse Problems of Electromagnetic and Acoustic Wave Theory (DIPED–2008), Tbilisi, Georgia, 2008. 2

[14] T. M. Grzegorczyk, B. E. Barrowes, F. Shubitidze, J.P. Fernández, and K. O'Neill. Simultaneous identification of multiple unexploded ordnance using electromagnetic induction sensors. IEEE Trans. Geosci. Remote Sens., 2011. In press. 2, 50

[15] J.P. Fernández, B. E. Barrowes, K. O'Neill, Irma Shamatava, F. Shubitidze, and Keli Sun. A data-derived time-domain SEA for UXO identification using the MPV sensor. In R.l S. Harmon, J. T. Broach, and J. H. Holloway, Jr., editors, Detection and Sensing of Mines, Explosive Objects, and Obscured Targets XIII, volume 6953 of Proceedings of SPIE, pages 6953–1H, Bellingham, WA, Mar. 2008. 2, 57

[16] F. Shubitidze, B. E. Barrowes, Irma Shamatava, Juan P. Fernández, and K. O'Neill. Application of the NSMC model to multi-axis time domain EMI data. In R.l S. Harmon, J. T. Broach, and J. H. Holloway, Jr., editors, Detection and Sensing of Mines, Explosive Objects, and Obscured Targets XIII, volume 6953 of Proceedings of SPIE, page 69532, Bellingham, WA, Mar. 2008. 2

[17] B. E. Barrowes, F. Shubitidze, J.P. Fernández, Irma Shamatava, and K. O'Neill. Man-portable vector EMI instrument data characterization using the NSMS method. In R.l S. Harmon, J. T. Broach, and J. H. Holloway, Jr., editors, Detection and Sensing of Mines, Explosive Objects, and Obscured Targets XIV, volume 7303 of Proceedings of SPIE, pages 7303–0V, Bellingham, WA, Apr. 2009. 2

[18] F. Shubitidze, D. Karkashadze, J.P. Fernández, B. E. Barrowes, K. O'Neill, T. Grzegorczyk, and Irma Shamatava. Applying a volume dipole distribution model to next-generation sensor data for multi-object data inversion and discrimination. In R.l S. Harmon, J. T. Broach, and J. H. Holloway, Jr., editors, Detection and Sensing of Mines, Explosive Objects, and Obscured Targets XV, volume 7664 of Proceedings of SPIE, pages 7664–07, Bellingham, WA, Apr. 2010. 2

[19] B. E. Barrowes, K. O'Neill, T. M. Grzegorczyk, Xudong Chen, and Jin Au Kong. Broadband analytical magnetoquasistatic electromagnetic induction solution for a conducting and permeable spheroid. IEEE Trans. Geosci. Remote Sensing, 41: XXX–XXX, Sep. 2003. 2

[20] Xudong Chen, K. O'Neill, T. M. Grzegorczyk, and Jin Au Kong. Spheroidal mode approach for the characterization of metallic objects using electromagnetic induction. IEEE Trans. Geosci. Remote Sens., 45:697–706, Mar. 2007. 2

[21] T. M. Grzegorczyk, Beijia Zhang, Jin Au Kong, B. E. Barrowes, and K. O'Neill. Electromagnetic induction from highly permeable and conductive ellipsoids under arbitrary excitation: Application to the detection of unexploded ordnances. IEEE Trans. Geosci. Remote Sens., 46:1164–1876, Apr. 2008. 2

[22] J. T. Smith and H. F. Morrison. Optimizing receiver configurations for resolution of equivalent dipole polarizabilities in situ. IEEE Trans. Geosci. Remote Sens., 43:1490–1498, July 2005. 4, 43

[23] S.D. Billings, L.R. Pasion, N. Lhomme, and D.W. Oldenburg. Discrimination at camp sibert using time-domain EM. SERD-P/ESTCP Partners in Environmental Technology Symposium, Dec. 2007. 4

[24] N. Lhomme. Man-portable vector (mpv) emi sensor for full uxo characterization field tests and analysis of the man-portable vector (mpv) emi sensor. Proposal to ESTCP, FY2010. 4

[25] N. Lhomme, L. R. Pasion, S. D. Billings, and D. W. Oldenburg. Inversion of frequency domain data collected in a magnetic setting for the detection of uxo. volume 6953, pages The International Society for Optical Engineering (SPIE) –, Orlando, FL, United states, 2008. URL http://dx.doi.org/10.1117/12.780153. 5

[26] L.R. Pasion, S.D. Billings, and D.W. Oldenburg. Improving detection and discrimination of buried metallic objects in magnetic geologic settings by modeling the background soil response. Proceedings of SPIE Defense+Security, 2008. 5

[27] J.P. Fernández, B. E. Barrowes, K. O'Neill, Irma Shamatava, and F. Shubitidze. A vector handheld frequency-domain sensor for UXO identification. In R.l S. Harmon, J. T. Broach, and J. H. Holloway, Jr., editors, Detection and Sensing of Mines, Explosive Objects, and Obscured Targets XIV, volume 7303 of Proceedings of SPIE, pages 7303–0W, Bellingham, WA, Apr. 2009. 7, 76

[28] J. D. McNeill and M. Bosnar. Application of TDEM techniques to metal detection and discrimination: a case history with the new Geonics EM-63 fully time-domain metal detector. Technical Note TN-32. Missisauga, ON: Geonics LTD (http://www.geonics.com), 2000. 8, 43

[29] Ben Barrowes. Man-portable vector time domain emi sensor and discrimination processing: SERDP MM1443 - FY06 annual report. Technical report, The Strategic Environmental Research and Development Program (SERDP), December 2006. 13

[30] Ben Barrowes. Man-portable vector time domain emi sensor and discrimination processing: SERDP MM1443 - FY07 annual report. Technical report, The Strategic Environmental Research and Development Program (SERDP), December 2007. 13, 22, 68

[31] D. F. Belding and K. J. Mitchell. Foundations of Analysis. Prentice-Hall, Englewood Cliffs, NJ, 1991. 15

[32] D.D. Snyder and D. C. George. The advanced ordnance locator (AOL): A dual-mode TEM and magnetics system for detection and classification of UXO. SAGEEP, Envir. & Eng. Geophys. Soc., 2005. Atlanta, GA. 16

[33] D. D. Snyder. Technical report: Precision position and attitude measurements: An evaluation of the integration of the Arc-Second "Indoor GPS" system into the MPV. Grand Junction, CO: Snyder Geoscience, Inc., 2007. 21

[34] Itzhack Y. Bar-Itzhack and K. A. Fegley. Orthogonalization techniques of a direction cosine matrix. IEEE Trans. Aerosp. Electron. Syst., AES-5:798–804, Sep. 1969. 21

[35] Jean-Luc Boiffier. The Dynamics of Flight: The Equations. Wiley, Chichester, UK, 1998. 21

[36] N. Geng, C. E. Baum, and L. Carin. On the low-frequency natural response of conducting and permeable targets. IEEE Trans. Geosci. Remote Sens., 37:347–359, Jan. 1999. 43, 44

[37] L. Carin, Haitao Yu, y. Dalichaouch, A. R. Perry, P. V. Czipott, and C. E. Baum. On the wideband EMI response of a rotationally symmetric permeable and conducting target. IEEE Trans. Geosci. Remote Sens., 39:1206–1213, June 2001. 44

[38] L. R. Pasion and D. W. Oldenburg. A discrimination algorithm for UXO using time-domain electromagnetic induction. J. Environ. Eng. Geophys., 6:91–102, 2001. 44, 45

[39] T. H. Bell, Bruce J. Barrow, and Jonathan T. Miller. Subsurface discrimination using electromagnetic induction sensors. IEEE Trans. Geosci. Remote Sens., 39:1286–1293, June 2001. 43, 44

[40] Keli Sun, K. O'Neill, B. E. Barrowes, Juan Pablo Fernández, F. Shubitidze, Irma Shamatava, and K. Paulsen. Dumbbell dipole model and its application in UXO discrimination. In J. T. Broach, R.l S. Harmon, and J. H. Holloway, Jr., editors, Detection and Remediation Technologies for Mines and Minelike Targets XI, volume 6217 of Proceedings of SPIE, page 621706, Bellingham, WA, Apr. 2006. 43, 44

[41] Keli Sun, K. O'Neill, F. Shubitidze, Irma Shamatava, and K. D. Paulsen. Fast data-derived fundamental spheroidal excitation models with application to UXO discrimination. IEEE Transactions on Geoscience and Remote Sensing, 43(11):2573 – 2582, 2005. ISSN 0196-2892. 43, 54

[42] K. Sun, K. O'Neill, C.-C. Chen, H. S. Youn, F. Shubitidze, I. Shamatava, , and K.D. Paulsen. Highly contaminated UXO sites: combination of GPR and EMI for discrimination of clustered scatterers. SAGEEP, 2005.

[43] F. Shubitidze, K. O'Neill, I. Shamatava, Keli Sun, and K.D. Paulsen. Use of standardized source sets for enhanced EMI classification of buried heterogeneous objects. Proc. SPIE - Int. Soc. Opt. Eng. (USA), 5415(1):263 – 74, 2004. ISSN 0277-786X.

[44] F. Shubitidze, K. O'Neill, I. Shamatava, K. Sun, and K.D. Paulsen. A standardized excitation approach for classification of buried UXO. International Geoscience and Remote Sensing Symposium (IGARSS), 7:4905 – 4908, 2004.

[45] F. Shubitidze, B. E. Barrowes, K. O'Neill, I. Shamatava, J. P. Fernández, K. Sun, and K.D. Paulsen. The generalized SEA to UXO discrimination in geophysical environments producing EMI response. Proceedings of the SPIE - The International Society for Optical Engineering, 2006. 43, 54, 78

[46] B. E. Barrowes, K. O'Neill, T. M. Grzegorczyk, X. Chen, and J. A. Kong. Broadband analytical magnetoquasistatic electromagnetic induction solution for a conducting and permeable spheroid. IEEE Trans. on Geoscience and Remote Sensing, 42 (11):2479–2489, 2004. 43

[47] B. E. Barrowes, K. O'Neill, T. M. Grzegorczyk, and J. A. Kong. On the asymptotic expansion of the spheroidal wave function and its eigenvalues for complex size parameter. Studies in Applied Mathematics, 113(3):271–301, Oct. 2004.

[48] Chi On Ao, H. Braunisch, K. O'Neill, and Jin Au Kong. Quasi-magnetostatic solution for a conducting and permeable spheroid with arbitrary excitation. IEEE Trans. Geosci. Remote Sensing, 40:887–897, Apr. 2002.

[49] H. Braunisch, Chi On Ao, K. O'Neill, and Jin Au Kong. Magnetoquasistatic response of conducting and permeable prolate spheroid under axial excitation. IEEE Trans. Geosci. Remote Sensing, 39:2689–2701, Dec. 2001.

[50] X. Chen, K. O'Neill, B. E. Barrowes, T. M. Grzegorczyk, , and Jin Au Kong. Application of a spheroidal mode approach with differential evolution in inversion of magneto-quasistatic data for UXO discrimination. Inverse Problems, 20(6):27–40, 2004.

[51] F. Shubitidze, K. O'Neill, K. Sun, and I. Shamatava. Application of broadband EMI responses to infer buried object's aspect ratio. International Geoscience and Remote Sensing Symposium (IGARSS), 3:1542 – 1545, 2002.

[52] B. E. Barrowes, K. O'Neill, T. M. Grzegorczyk, and J. A. Kong. Broadband, Analytic Electromagnetic Induction (EMI) Response from Spheroidal Objects for Arbitrary Excitation. Progress in Electromagnetics Research Symposium (PIERS), October 2003. 43

[53] F. Shubitidze, B. Barrowes, J. P. Fernández, and K. O'Neill. Combined NSMC and Pseudo-Spectral Finite-Difference Method for Inverting a Buried Object Location. Symposium on the Application of Geophysics to Engineering and Environmental Problems, 2007 . 43, 67, 78

[54] F. Shubitidze, B. Barrowes, J. P. Fernández, Irma Shamatava, and K. O'Neill. NSMC for UXO discrimination in cases with overlapping signatures. SPIE, 2007. 78

[55] F. Shubitidze, B. E. Barrowes, K. O'Neill, I. Shamatava, K. Sun, and K.D. Paulsen. Total normalized surface magnetic charge for UXO discrimination. NATO Advanced Study Institute "Imaging for Detection and Identification", 23 July–5 August 2006. Ciocco, Italy.

[56] F. Shubitidze, K. O'Neill, B. Barrowes, J. P. Fernández, I. Shamatava, K. Sun, and K.D. Paulsen. Application of the normalized surface magnetic charge model to UXO discrimination in cases with overlapping signals. J. Appl. Geophys., 61(3-4): 292–303, Mar. 2007.

[57] F. Shubitidze, K. O'Neill, I. Shamatava, K. Sun, , and K. D. Paulsen. Total magnetic charge for fast screening of highly contaminated UXO sites. In proceedings of 2005 IEEE international symposium on Antennas and Propagation and USNC/CN/URSI North American Radio Science meeting, on CD, 2005.

[58] F. Shubitidze, K. O'Neill, I. Shamatava, K. Sun, and K.D. Paulsen. Total magnetic charge for fast screening of highly contaminated UXO sites. 2005 IEEE Antennas and Propagation Society International Symposium (IEEE Cat. No. 05CH37629), vol. 3A:856 – 9, 2005.

[59] F. Shubitidze, K. O'Neill, Irma Shamatava, Keli Sun, and K.D. Paulsen. Combined differential evolution and surface magnetic charge model algorithm for discrimination of UXO from non-UXO items: Simple and general inversions. Proceedings of SPIE - The International Society for Optical Engineering, 5794(Part I):346 – 357, 2005. ISSN 0277-786X. 67

[60] L. R. Pasion. A unified approach to uxo discrimination using the method of auxiliary sources. Technical report, 2006. 43, 67

[61] J. T. Smith and H. F. Morrison. Estimating equivalent dipole polarizabilities for the inductive response of isolated conductive bodies. IEEE Trans. Geosci. Remote Sens., 42:1208–1214, June 2004. 43

[62] Lev D.ovich Landau, Evgeniĭ Mikhaĭlovich Lifshitz, and Lev Petrovich Pitaevskiĭ. Electrodynamics of Continuous Media. Pergamon Press, Oxford, UK, 2nd edition, 1984. 43

[63] F. Shubitidze, K. O'Neill, Irma Shamatava, Keli Sun, and K. D. Paulsen. Fast and accurate calculation of physically complete EMI response by a heterogeneous metallic object. IEEE Transactions on Geoscience and Remote Sensing, 43(8):1736 – 1750, 2005. ISSN 0196-2892. 43

[64] Keli Sun, K. O'Neill, F. Shubitidze, Irma Shamatava, and K. Paulsen. Fast data-derived fundamental spheroidal excitation models with application to UXO identification. In R.l S. Harmon, J. H. Holloway, Jr., and J. T. Broach, editors, Detection and Remediation Technologies for Mines and Minelike Targets IX, Proceedings of SPIE, pages 855–865, Bellingham, WA, Apr. 2004.

[65] Keli Sun, K. O'Neill, F. Shubitidze, Irma Shamatava, and K. D. Paulsen. Fundamental mode approach to forward problem solutions in EMI scattering—Inferring fundamental solutions from training data. In Applied Computational Electromagnetics Symposium (ACES), Syracuse, NY, Apr. 2004. 43

[66] Keli Sun, K. O'Neill, F. Shubitidze, Irma Shamatava, and K. Paulsen. Fast data-derived fundamental spheroidal excitation models with application to UXO discrimination. IEEE Trans. Geosci. Remote Sens., 43:2573–2583, Nov. 2005. 43

[67] N. Cristianini and J. Shawe-Taylor. An Introduction to Support Vector Machines and other Kernel-Based Learning Methods. Cambridge University Press, Cambridge, 2000. 43, 57

[68] J.P. Fernández, Keli Sun, B. E. Barrowes, K. O'Neill, Irma Shamatava, F. Shubitidze, and K. Paulsen. Inferring the location of buried UXO using a Support Vector Machine. In R.l S. Harmon, J. T. Broach, and J. H. Holloway, Jr., editors, Detection and Remediation Technologies for Mines and Minelike Targets XII, volume 6553 of Proceedings of SPIE, pages 6553–0B, Bellingham, WA, Apr. 2007. 43

[69] Keli Sun, K. O'Neill, B. E. Barrowes, Irma Shamatava, J.P. Fernández, F. Shubitidze, and K. Paulsen. Data-derived SEA for time domain EMI sensing of UXO. In Progress in Electromagnetics Research Symposium (PIERS) Proceedings, page 330, Beijing, Mar. 2007. 43

[70] L. R. Pasion, S. D. Billings, D. W. Oldenburg, and S. E. Walker. Application of a library based method to time domain electromagnetic data for the identification of unexploded ordnance. J. Appl. Geophys., 61:279–291, Mar. 2007. 44

[71] F. Shubitidze, J.P. Fernández, Irma Shamatava, L. R. Pasion, B. E. Barrowes, and K. O'Neill. Application of the Normalized Surface Magnetic Source model to a blind unexploded ordnance discrimination test. ACES Journal, 25:89–98, Jan. 2010. 45, 53

[72] Y. Das, J. E. McFee, J. Toews, and G. C. Stuart. Analysis of an electromagnetic induction detector for real-time location of buried objects. IEEE Trans. Geosci. Remote Sens., 28:278–288, May 1990. 50

[73] J. R. Wait and K. P. Spies. Quasi-static transient response of a conducting permeable sphere. Geophysics, 34:789–792, Oct. 1969. 50

[74] Tibtech Innovations. Properties table of stainless steel, metals and other conductive materials. http://www.tibtech.com/conductivity.php, 2010. 50

[75] D. C. George and J. L. George. Data report: Tests of MPV at Vicksburg, February 26 to March 2, 2007. Technical Note 2007-2. Grand Junction, CO: G&G Sciences Inc. (http://www.ggsciences.com), 2007. 50

[76] J.P. Fernández, B. E. Barrowes, K. O'Neill, Irma Shamatava, and F. Shubitidze. Realistic subsurface anomaly discrimination using electromagnetic induction and an SVM classifier. EURASIP Journal on Advances in Signal Processing, 2010:305890, 2010. 53

[77] P. M. Morse and H. Feshbach. Methods of Theoretical Physics. McGraw-Hill, New York, 1953. 56

[78] George Arfken. Mathematical Methods for Physicists. Academic Press, San Diego, 3rd edition, 1985. 57

[79] J.A. Stratton. Electromagnetic Theory. McGraw-Hill, New York, 1941. 57, 63

[80] L. N. Trefethen. Numerical Methods in Matlab. SIAM, Philadelphia, 2000. 57

[81] R. C. Aster, B. Borchers, and C. H. Thurber. Parameter Estimation and Inverse Problems. Elsevier, Burlington, MA, 2005. 57

[82] Beijia Zhang, K. O'Neill, Jin Au Kong, and T. M. Grzegorczyk. Support vector machine and neural network classification of metallic objects using coefficients of the spheroidal MQS response modes. IEEE Transactions on Geoscience and Remote Sensing, 46(1):159 – 171, 2008. ISSN 0196-2892. 57, 60, 78

[83] L. R. Pasion et al. A unified approach to UXO discrimination using the Method of Auxiliary Sources. UX1446 Final Report. Vancouver, BC: Sky Research Inc./University of British Columbia, Mar. 2006. 58

[84] Optimization Toolbox for Use with Matlab. The MathWorks, Natick, MA, 2000. 59

[85] F. Shubitidze, K. O'Neill, B. E. Barrowes, Irma Shamatava, Keli Sun, Juan Pablo Fernández, and K. Paulsen. The generalized SEA to UXO discrimination in geophysical environments producing EMI response. In J. T. Broach, R.l S. Harmon, and J. H. Holloway, Jr., editors, Detection and Remediation Technologies for Mines and Minelike Targets XI, volume 6217 of Proceedings of SPIE, page 621707, Bellingham, WA, Apr. 2006. 62

[86] Irma Shamatava, F. Shubitidze, B. E. Barrowes, E. Demidenko, J.P. Fernández, and K. O'Neill. The generalized SEA and a statistical signal processing approach applied to UXO discrimination. In R.l S. Harmon, J. T. Broach, and J. H. Holloway, Jr., editors, Detection and Sensing of Mines, Explosive Objects, and Obscured Targets XIII, volume 6953 of Proceedings of SPIE, page 695353, Bellingham, WA, Mar. 2008. 62

[87] F. Shubitidze, D. Karkashadze, B. E. Barrowes, Irma Shamatava, and K. O'Neill. A new physics based approach for estimating a buried object's location, orientation and magnetic polarization from EMI data. J. Env. Eng. Geophys., 13:115–130, Sep. 2008. 64

[88] F. Shubitidze, J.P. Fernández, B. E. Barrowes, Irma Shamatava, and K. O'Neill. Normalized Surface Magnetic Source model applied to Camp Sibert data. In Applied Computational Electromagnetics Symposium (ACES), Monterey, CA, Mar. 2009. 66

[89] F. Shubitidze, B. Barrowes, I. Shamatava, J. P. Fernández, and K. O'Neill. Combining NSMC and High Quality MPV-TD Data for UXO Discrimination. Proc. IEEE Int. Geosci. Remote Sensing Symp. (IGARSS), 2008. 65

[90] F. Shubitidze, D. Karkashadze, B. Barrowes, and K. O'Neill. An analytical expression for estimating a buried object's location, orientation and magnetic polarization to support UXO discrimination. XIIth International Seminar/Workshop on Direct and Inverse Problems of Electromagnetic and Acoustic Wave Theory (DIPED), 2007. 64, 78

[91] F. Shubitidze, K. O'Neill, B.E. Barrowes, I. Shamatava, J.P. Fernandez, K. Sun, and K.D. Paulsen. Application of the normalized surface magnetic charge model to UXO discrimination in cases with overlapping signals. Journal of Applied Geophysics, 61(3-4):292 – 303, 2007. ISSN 0926-9851. 67, 78

[92] Tomoji Takasu and Akio Yasuda. Development of the low-cost RTK-GPS receiver with an open source program package RTKLIB. In International Symposium on GPS/GNSS, Jeju, Korea, Nov. 2009. 75

[93] Ben Barrowes, K. O'Neill, D.D. Snyder, D.C. George, and F. Shubitidze. New man-portable vector time domain EMI sensor and discrimination processing. UXO/Countermine Forum 2006, July 12, 2006. Las Vegas, NV. 78

[94] K. Sun, B. E. Barrowes, K. O'Neill, F. Shubitidze, I. Shamatava, J. P. Fernández, K. Sun, and K.D. Paulsen. Dumbbell dipole model and its application in UXO discrimination. Proceedings of the SPIE - The International Society for Optical Engineering, 2006.

[95] J. P. Fernández, B. E. Barrowes, K. O'Neill, F. Shubitidze, K. Sun, I. Shamatava, K. Sun, and K.D. Paulsen. Evaluation of SVM classification of metallic objects based on a magnetic-dipole representation. Proceedings of the SPIE - The International Society for Optical Engineering, 2006.

[96] Xudong Chen, K. O'Neill, T.M. Grzegorczyk, and Jin Au Kong. Spheroidal mode approach for the characterization of metallic objects using electromagnetic induction. IEEE Transactions on Geoscience and Remote Sensing, 45(3):697 – 706, 2007/03/. ISSN 0196-2892.

[97] F. Shubitidze, B. Barrowes, J. P. Fernández, Irma Shamatava, and K. O'Neill. A combined NSMC and pole series expansion approach for UXO discrimination. SPIE, 2007.

[98] J. P. Fernández, Keli Sun, B. Barrowes, K. O'Neill, Irma Shamatava, and F. Shubitidze. Inferring the location of buried UXO using a support vector machine. SPIE, 2007. 78